

Cold Spray and Tribology of Ti6Al4V and Ti6Al4V-TiC Metal Matrix Composites

Venkata Naga Vamsi Munagala

Department of Mining and Materials Engineering,
McGill University, Montreal
August 2019

A thesis submitted to McGill University in partial fulfillment of
the requirements for the degree of Doctor of Philosophy.

© Venkata Naga Vamsi Munagala 2019

Acknowledgements

First, I would like to thank my supervisor Prof. Richard R. Chromik for giving me an opportunity to join his research group. I thank him whole heartedly for his esteemed guidance, financial support as well as for sharing his valuable time and knowledge. His suggestions, and encouragement during my Ph.D. helped me to develop deep-thinking ability and expand my knowledge.

I would like to express my sincere gratitude to Prof. Thomas Scharf, for permitting me to use the high temperature tribometer equipment at University of North Texas (UNT) and for his kind support during my stay in Texas.

I must acknowledge the technical assistance and training received at McGill from Nicolas Brodusch, Stéphanie Bessette, Sriraman Rajagopalan, Monique Riendeau, Hendrix Demers, Florence Paray, Weawkamol Leelapornpisit, Liu David and Robert Paquette. I would like to thank Phuong Vo, Maniya Aghasibeig, Dina Goldbaum, Jean-Francois Alarie at the McGill Aerospace Materials and Alloy Design Center (MAMADC) for providing me access to cold spray equipment. I would like to thank my friends Priyadarshi, Lisa, Yinyin, Sara, Sima, Rohan, Nima, Tyler, Rohit, Bindu, Vikas, Ashish and many others for their priceless assistance, and support as peers.

I would also like to thank Rene Cooper from Cristal Metals, for giving me irregular Ti6Al4V and Ti powders, and Tekna for TiC powders. My research and stay in Canada wouldn't have been possible without the financial support from various funding sources including Hatch, Rio Tinto, Natural Sciences and Engineering Research Council (NSERC) of Canada, and Strategic Grants Program.

On a personal note, I would like to thank my parents, Hymavathi Devi and Krishna Mohan, my grandparents, Adilakshmi and Veerraju, my uncle, Satish Nemali and my all relatives who have been supporting me constantly at different stages of my life. I wouldn't have accomplished without your love and affection.

Finally, I would like to thank the almighty for blessing me with a beautiful life.

Abstract

Ti alloys are used in aerospace and automobile applications due to their high specific strength and corrosion resistance. However, manufacturing large components through conventional techniques leads to high production and machining costs. To overcome these challenges, cold spray (CS) is seen as a feasible and economical technique to additively manufacture and repair bulk components. In CS, coating deposition occurs through supersonic impact of powder particles in solid state. The particle temperature throughout the process is well below the melting point of the material, which prevents phase transformations and oxidation. Despite good deposition efficiency, Ti6Al4V coatings when cold sprayed using nitrogen as propellant gas are often porous.

The present thesis explores the influence of metal powder properties on the cold spray deposition, coating properties and tribology of Ti6Al4V coatings. Coatings were deposited using different feedstock powders and characterized to determine their porosity, microstructure, hardness and cohesion strength by performing mechanical tests and microscopic observations. For the same spray conditions, coatings deposited using irregular powders (IP) with equiaxed microstructure led to dense deposits with better cohesion strength compared to spherical powders (SP) with martensitic microstructure. Also, splats from IP bonded with higher adhesion strength and showed highly refined post sprayed microstructures compared to splats from SP. While Ti6Al4V coatings from IP exhibited dense microstructures and better mechanical properties, in terms of tribological performance, the porous coatings from SP showed lower wear rates compared to coatings from IP. This was due to entrapment of wear debris in the pores during wear process that decreased abrasive ploughing and lowered the wear rates.

To improve the tribological properties of Ti6Al4V, TiC powders were co-fed to the cold spray gun and Ti6Al4V-TiC metal matrix composite (MMC) coatings were fabricated. Sliding wear tests showed that the tribology of the MMCs was significantly influenced by ceramic volume fraction, coating properties, normal load and ambient temperature. For similar ceramic volume fractions, MMCs deposited with IP showed lower wear rates compared to MMCs from SP, due to the formation of tribolayers composed of Ti oxides and fragmented TiC particles. In addition, the lubricating properties of the tribolayers due to the presence of free carbon from the TiC particles led to a significant drop in CoF. Increase in normal load and ceramic volume fraction resulted in greater exposure of ceramic particles to the sliding interface and led to the formation of a more

continuous tribolayer that further decreased the wear rate and CoF. Sliding wear tests performed at different static temperatures showed that reinforcing TiC significantly improved the wear resistance of Ti6Al4V up to 200°C due to tribolayer formation. Beyond 200°C, tribo-oxidation led to the formation of oxide glaze layers that had a more profound effect in decreasing the wear and friction of both metal and composite coatings. The microscopic observations, mechanical and tribology tests helped to describe the process-structure-property-performance relationship of cold sprayed Ti6Al4V and Ti6Al4V-TiC MMCs.

Résumé

Les alliages de Ti sont utilisés dans les domaines aérospatiaux et automobiles en raison de leur haute force spécifique et leur résistance à la corrosion. Cependant, la production de grandes quantités grâce aux méthodes traditionnelles engendre des coûts élevés. Pour réduire ces coûts, la technique de pulvérisation à froid est considérée comme viable et économique pour la fabrication additive ou pour la réparation de composantes. Le dépôt de revêtement à l'aide de la technique de pulvérisation à froid est le résultat d'un impact, à vitesse supersonique, de particules de poudre à l'état solide. La température durant le processus demeure sous le point de fusion du matériau poudreux, ce qui empêche le changement de phase et l'oxydation. Malgré une haute efficacité de dépôt, les revêtements de Ti6Al4V produits à l'aide de la technique de pulvérisation à froid avec l'azote agissant comme gaz de propulsion sont généralement poreux.

La présente thèse traite de l'influence des propriétés des poudres métalliques sur le dépôt par pulvérisation à froid, des propriétés des revêtements et la tribologie des revêtements de Ti6Al4V. Les revêtements ont été déposés en utilisant différentes poudres et ont été caractérisés en déterminant leur porosité, leur microstructure, leur dureté et leur puissance de cohésion par essais mécaniques et par microscopie. Pour les mêmes conditions de dépôt, les revêtements produits avec une poudre de morphologie irrégulière (IP) ayant une microstructure équiaxe ont un dépôt plus dense avec une puissance de cohésion supérieure au résultat obtenu avec la poudre avec une morphologie sphérique (SP) et une microstructure martensitique. De plus, les particules IP ont une puissance d'adhésion supérieure et une microstructure plus affinée lorsqu'elles ont une morphologie initiale irrégulière, comparées à celles déposées avec la poudre SP. Malgré les propriétés mécaniques et la densité supérieure des revêtements IP de Ti6Al4V, en termes de performance tribologique, les revêtements poreux des revêtements SP présentaient un taux d'usure inférieur. Ceci est dû aux débris d'usure qui deviennent coincés dans les pores des revêtements SP, diminuant ainsi le labourage abrasif, ce qui réduit le taux d'usure à son tour.

Pour améliorer les propriétés tribologiques des revêtements de Ti6Al4V, une poudre de TiC a été simultanément alimentée durant le processus de pulvérisation à froid, produisant ainsi un composite à matrice métallique Ti6Al4V-TiC (MMC). Les essais d'usure ont démontré que la tribologie des MMC était significativement influencée par la fraction de volume de céramique ainsi que par les propriétés des revêtements, la force normale et la température ambiante. Pour une

fraction de volume de céramique similaire, les revêtements MMC déposés avec une poudre IP avaient un taux d'usure moindre que ceux déposés avec une poudre SP dû à la formation d'une structure tribologique par couches composées de TiC fragmenté et d'oxydes de Ti. De plus, les propriétés lubrifiantes de la structure tribologique par couches sont dues à la présence de carbone libre venant des particules de TiC, ce qui entraîne une diminution significative du coefficient de frottement (CoF). L'augmentation de la force normale et de la fraction du volume de céramique entraîne une exposition plus élevée des particules de céramique dans le revêtement, ce qui produit une structure tribologique par couches plus continue, réduisant ainsi le taux d'usure et le CoF. Les essais d'usure effectués à des températures statiques différentes ont démontré que le TiC a significativement amélioré la résistance à l'usure des revêtements de Ti6Al4V jusqu'à une température de 200 °C en raison de la formation d'une structure tribologique par couches. Au-delà de 200 °C, la tribo-oxidation a entraîné la formation d'une couche d'émaillage d'oxyde, ce qui a eu un effet plus considérable dans la diminution du taux d'usure et du CoF des revêtements métalliques et composites.

Contributions of the authors

The present thesis is manuscript based containing three publications and two other manuscripts that will be submitted in the future. The manuscripts were prepared in collaboration with researchers from other universities and research groups. A detailed contribution of each of the authors is discussed below.

Chapter 4: Influence of powder morphology and microstructure on the cold spray and mechanical properties of Ti6Al4V coatings, *Journal of Thermal Spray Technology*, 2018, 27:827 – 842. DOI: 10.1007/s11666-018-0729-8.

Venkata Naga Vamsi Munagala, Valary Akinyi, Phuong Vo and Richard R. Chromik

Venkata Naga Vamsi Munagala performed powder characterization, coating deposition, sample preparation, SEM imaging, porosity measurements, image analysis, nanoindentation, post test analysis. Valary Akinyi helped in microhardness measurements. Phuong Vo assisted in cold spray deposition of the coatings. Richard R. Chromik supervised the project and edited the manuscript.

Chapter 5: The influence of powder properties on the adhesion strength and microstructural evolution of cold sprayed Ti6Al4V single splats, *Materials Letters*, 2019, 244:58 – 61. DOI: 10.1016/j.matlet.2019.02.028

Venkata Naga Vamsi Munagala, Sara I. Imbriglio and Richard R. Chromik

Venkata Naga Vamsi Munagala performed single splat deposition, sample preparation, characterization, scanning electron microscope (SEM) imaging, image analysis, post test analysis. Sara I. Imbriglio helped in performing splat adhesion tests. Richard R. Chromik supervised the project and edited the manuscript.

Chapter 6: Sliding wear of cold sprayed Ti6Al4V coatings: Effect of coating properties and normal load. (To be submitted to “Wear”)

Venkata Naga Vamsi Munagala, Stéphanie Bessette, Raynald Gauvin and Richard R. Chromik

Venkata Naga Vamsi Munagala performed coating characterization, sample preparation, sliding wear tests, post test analysis and nanoindentation. Stéphanie Bessette performed SEM imaging. Raynald Gauvin and Richard R. Chromik supervised the project and edited the manuscript.

Chapter 7: The role of metal powder properties on the cold spray and tribology of Ti6Al4-TiC metal matrix composites. (To be submitted to “Surface and Coatings Technology”)

Venkata Naga Vamsi Munagala and Richard R. Chromik

Venkata Naga Vamsi Munagala performed coating deposition, characterization, image analysis, sample preparation, sliding wear tests, SEM imaging, post test analysis, nanoindentation. Richard R. Chromik supervised the project and edited the manuscript.

Chapter 8: High temperature friction and wear behavior of cold-sprayed Ti6Al4V and Ti6Al4V-TiC composite coatings, *Wear*, 2019, 426 – 427:357 – 369. DOI: 10.1016/j.wear.2018.11.032

Venkata Naga Vamsi Munagala, Tyler B. Torgerson, Thomas W. Scharf and Richard R. Chromik

Venkata Naga Vamsi Munagala performed sample preparation, room and high temperature sliding wear tests, SEM imaging, wear track characterization, post test analysis, nanoindentation. Tyler B. Torgerson helped in conducting high temperature sliding wear tests. Thomas W. Scharf and Richard R. Chromik supervised the project and edited the manuscript.

Table of Contents

1. Introduction.....	1
Organization of the thesis.....	4
2. Literature review	8
2.1 Coating deposition using cold spray process	8
2.1.1 Introduction to cold spray.....	8
2.1.2 Concept of critical velocity and bonding mechanisms.....	10
2.1.3 Microstructural evolution	13
2.1.4 Influence of powder properties on the cold spray of coatings.....	16
2.2 Challenges in cold spray of Ti6Al4V.....	19
2.3 Adhesion and cohesion strength.....	21
2.4 Fabrication of metal matrix composites (MMCs).....	24
2.4.1 General processing techniques	24
2.4.2 Titanium carbide (TiC) as reinforcing phase in MMCs.....	25
2.4.3 Deposition of MMCs using cold spray.....	26
2.5.1 Third bodies	29
2.5.2 Friction.....	30
2.5.3 Wear.....	32
2.5.4 Tribological circuit	33
2.5.5 Velocity accommodation modes (VAMs).....	34
2.6 Wear mechanisms	35
2.6.1 Tribo-oxidative wear	35
2.7 Tribology of TiC reinforced MMCs.....	39
2.8 Summary of literature review.....	42
3. Experimental procedure	45

3.1 Cold spray of coatings.....	45
3.1.1 Feedstock powders	45
3.1.2 Cold spray deposition	46
3.1.3 Selection of spray conditions for Ti6Al4V and Ti6Al4V-TiC composite coatings	48
3.2 Coating characterization.....	52
3.2.1 Microstructural characterization of the coatings and single splats	52
3.2.2 Microhardness testing.....	53
3.3 Splat adhesion testing.....	54
3.4 Sliding wear tests	55
3.4.1 Wear test setup.....	55
3.4.2 Wear track characterization	58
3.5 Raman spectroscopy.....	60
3.6 Nanoindentation	61
4. Influence of powder morphology and microstructure on the cold spray and mechanical properties of Ti6Al4V coatings	65
Abstract	65
4.1 Introduction	66
4.2 Experimental procedure	69
4.2.1 Feedstock powder characterization and cold spraying	69
4.2.2 Coating characterization	70
4.2.3 Coating hardness.....	71
4.3 Results	72
4.3.1 Characterization of the feedstock powders.....	72
4.3.2 Characterization of the cold sprayed coatings	75
4.3.3 Deposition efficiency and particle velocity	76

4.3.4 Coating porosity	77
4.3.4 Microstructure of the coatings	77
4.3.5 Indentation size effect on the coatings and hardness loss parameter	78
4.3.6 Calculation of hardness loss parameter	82
4.4 Discussion	86
4.4.1 General characteristics of the feedstock powders.....	86
4.4.2 Coatings characteristics	87
4.4.3 Effect of powder morphology on coating microstructure	88
4.4.4 Coating hardness and cohesive strength evaluated using multi-scale indentation	89
4.5 Conclusions	91
Acknowledgements	92
5. The influence of powder properties on the adhesion strength and microstructural evolution of cold sprayed Ti6Al4V single splats	93
Abstract	93
5.1 Introduction	93
5.2 Experimental	95
5.3 Results and discussion.....	96
5.4 Conclusions	99
Acknowledgements	99
6. Sliding wear of cold sprayed Ti6Al4V coatings: Effect of coating properties and normal load	100
Abstract	100
6.1 Introduction	101
6.2 Experimental procedure	103
6.3 Results	105
6.3.1 Coatings and their characteristics	105

6.3.2 Sliding wear tests	105
6.3.3 Characterization of the worn surfaces	107
6.3.4 Subsurface microstructure characterization and mechanical properties.....	112
6.3.5 TEM analysis of the third bodies and worn surfaces.....	117
6.4 Discussion.....	120
6.5 Summary and conclusions	126
7. The role of metal powder properties on the cold spray and tribology of Ti6Al4V-TiC metal matrix composites	127
Abstract	127
7.1 Introduction	128
7.2 Experimental	131
7.2.1 Cold spray of coatings	131
7.2.3 Sliding wear tests.....	132
7.3 Results.....	134
7.3.1 Coating deposition.....	134
7.3.2 Friction and wear of the coatings	135
7.3.3 Wear track morphology and phase analysis	137
7.3.4 Counterface analysis.....	140
7.4 Discussion	147
7.4.1 Cold spray of coatings	147
7.4.2 Tribology of the coatings.....	148
7.5 Conclusions	152
8. High temperature friction and wear behavior of cold-sprayed Ti6Al4V and Ti6Al4V-TiC composite coatings.....	153
Abstract	153
8.1 Introduction	154

8.2 Experimental procedure	155
8.2.1 Cold spray of coatings and characterization.....	155
8.2.2 Sliding wear tests.....	156
8.3 Results.....	158
8.3.1 Cold spray, characterization and properties of the coatings.....	158
8.3.2 Sliding wear of Ti6Al4V and Ti6Al4V-TiC coatings.....	159
8.4 Discussion	172
8.5 Conclusions	177
9. Global discussion.....	178
9.1 Influence of TiC reinforcement of the sliding wear of Ti6Al4V coatings.....	178
10. Concluding remarks	182
10.1 Global summary	182
10.2 Global conclusions	185
10.3 Contributions to original knowledge.....	188
10.4 Suggestions for future work	188
References.....	190
Appendix A.....	210

Chapter 1

Introduction

Titanium alloys are extensively used in aerospace, automobile, marine and biomedical applications due to their high specific strength, excellent corrosion resistance and bio-compatibility [1,2]. Ti6Al4V one of the Ti alloys is specifically used in aircraft fuselage, landing gear, wings, turbine shafts, impeller and compressor blades [1]. However, due to its poor machinability and workability [3], the production costs involved in the manufacturing and repair of large components are often too high. To reduce the production and maintenance costs, cold spray (CS) or cold gas dynamic spraying can be potentially used to additively manufacture bulk components and also repair worn parts [4–6]. CS is a novel thermal spray process in which coating, or material buildup occurs through solid state deformation of the particles. In this process, micron sized powders are accelerated to supersonic velocities ($350 \text{ m.s}^{-1} - 1200 \text{ m.s}^{-1}$) by a preheated high pressure gas stream travelling through a de Laval nozzle [7–9]. The accelerated particles impact the substrates at high velocities, undergo extensive plastic deformation and metallurgically bond to form a coating. Since the particle temperature is much lower than the melting point of the material, there are no phase transformations, oxidation and tensile residual stress build-up [7]. In addition, the peening of the incoming particles on the pre-deposited layers results in densification. Under optimised conditions, the process has the capability to achieve high build-up rates with good deposition efficiency [5,10–12].

Although CS is being used to deposit various metals like Cu, Ni, Nb etc., [10–12] deposition of dense coatings of high yield strength material like Ti6Al4V using nitrogen as propellant gas remains challenging. Previously, researchers have mostly used gas atomized or plasma gas atomized powders to deposit Ti6Al4V coatings [13–18]. The high temperatures and rapid cooling involved in the gas atomization process results in spherical powders (SP) with martensitic lath microstructure [19]. Coatings deposited using these powders with nitrogen (propellant gas) resulted in high porosity due to poor deformability of the particles [13,18]. Porosity decreases the mechanical strength of the coatings and often highly dense deposits are desired. To reduce porosity in the coatings, special techniques were used that include spraying with He, mechanical blending of powders with soft and hard particles etc. [13,15,17,20,21]. Helium accelerates particles to higher

velocities compared to nitrogen, however, the use of He is non-sustainable and uneconomical for industrial applications [22,23]. Mechanical blending of powders with hard particles like steel balls reduce porosity due to tamping during deposition but get reinforced in the final deposits as impurities. Apart from using these techniques, very less attention is given to feedstock modifications and understanding the influence of powder properties on the coating formation, mechanical properties, adhesion and cohesion strength of the final deposits.

The first goal of the thesis is to understand the influence of feedstock properties on the cold spray of Ti6Al4V and deposit dense coatings using nitrogen as propellant gas with no additional pre-treatment of the powders. This involves the fundamental concept of understanding the process-structure-property relationships in cold sprayed Ti6Al4V coatings. To achieve this objective, powders manufactured through different processing techniques were selected and characterized in terms of their flowability, surface structure, morphology and microstructure. The powders were then cold sprayed, and the coating deposition mechanisms, microstructure, mechanical properties and cohesion strength were evaluated by performing different microscopic observations and mechanical tests. The advantages of tailoring powder properties to obtain dense deposits with good cohesion strength were explored. In CS, coating buildup occurs through plastic deformation and bonding between single particles called “splats”. The microstructural transformations, bonding and deformation mechanisms that occur in single splats significantly influence the properties of bulk coatings. To understand the microstructural transformations at splat level, single particles were deposited and electron channel contrast imaging (ECCI) was performed on the cross-sections to understand the post spray microstructures. ECCI is principally based on the anisotropic angular distribution of back scattered electrons (BSEs) emitted from a polycrystalline material [11,24]. It is a powerful technique to observe crystal defects, grain size distributions over a much larger field of view compared to transmission electron microscope [11,25]. To determine the adhesion strength, splat adhesion tests were performed by starching the splats off the substrate. The microstructural observations performed on both single splats and coatings along with the cohesion and adhesion strength measurements, helped to understand the complete coating formation and characteristics, which facilitated for the future evaluation of the coating tribological properties.

Despite excellent mechanical and electrochemical properties, Ti and its alloys have poor tribological properties due to their low resistance to plastic shearing, non-protective nature of their

tribo-oxides and low strain hardening coefficient [26–29]. Literature studies have reported oxidative and abrasive wear mechanisms at low loads while delamination was observed at higher loads and sliding velocities leading to high wear rates [26]. Different surface modification techniques like laser nitriding, electron beam nitriding, laser alloying, anodizing, ion implantation were used to improve its tribological properties but these were either complex or cost ineffective [29–33]. One method of improving their wear resistance is by depositing metal matrix composite (MMC) coatings with hard particles as reinforcement. During sliding of metals or alloys, the continuous formation of debris, transfer material or mechanically mixed material, alter the localized stress state and chemistry at the interface of sliding bodies [27,34]. This often results in high friction and wear. In case of MMCs, presence of hard particles in the matrix increases the hardness, load bearing capacity and favour the formation of tribolayers that resists localized plastic deformation during wear. This results in greater wear resistance. However, the increment in wear resistance imparted by an MMC compared to an unreinforced material depends on several factors including hard phase morphology, composition, volume fraction, distribution etc. [35–37]. Studies from literature show that MMCs deposited using heat intensive processes like laser cladding, selective laser melting, plasma spraying etc., result in the formation of brittle phases, porosity, oxidation [38–44] and degrade their mechanical and tribological properties [40]. Alternatively, CS due to its ability to deposit powders in solid state, could be used to deposit MMCs both as bulk and coatings with no or minimal thermal effects. Using CS, a wide range of MMCs are deposited for mechanical, electrochemical and tribological applications [36,45–47]. However, minimal efforts are being made to understand the correlation between the feedstock properties, coating deposition and their mechanical and tribological properties.

The second objective of the thesis is to CS deposit Ti6Al4V-TiC MMC coatings using different metal powders and evaluate their tribological properties both at room and elevated temperatures. This objective primarily involves, understanding the role of powder properties on the MMC coating formation, ceramic retention, mechanical properties, and in turn their influence on the observed friction and wear behaviour. First, feedstock with different initial metal-ceramic mixtures were cold sprayed. Spherical and irregular Ti6Al4V powders that had different physical and microstructural properties were used as metal feedstock in the metal-ceramic mixtures. The coatings deposited were characterized to determine porosity, ceramic content, and hardness. To evaluate the tribological performance, dry sliding wear tests were performed on both Ti6Al4V and

Ti6Al4V-TiC composite coatings at different loads and temperatures. First, wear tests were done on Ti6Al4V coatings deposited using both spherical and irregular powders. The effect of coatings properties on the friction and wear of the coatings at different normal loads was studied. Subsequently, sliding wear tests were performed on the Ti6Al4V-TiC MMCs. For this study one set of composite coatings with similar TiC contents were selected from the coatings deposited using spherical and irregular powders along with one composite coating with highest ceramic content. The study focused on evaluating the influence of coating properties, TiC reinforcement and its content on the friction and wear behaviour of the MMCs. Finally, sliding wear tests were performed at elevated temperatures (up to 575°C) on Ti6Al4V and Ti6Al4V-TiC composite coatings. The synergetic effect of temperature and TiC reinforcement on the third bodies physical, chemical and mechanical properties were determined and co-related to observed transitions in friction and wear mechanisms.

Organization of the thesis

This thesis consists of ten chapters. The present chapter gives an overall view of the thesis and outlines the major focus of the study along with a brief introduction regarding the important aspects studied in each chapter.

Chapter 2 consists of a detailed literature review of the cold spray process, metal and composite coatings fabrication using cold spray, bonding mechanisms, microstructural evolution, influence of feedstock properties on the coatings, mechanical properties of the coatings, fundamentals of tribology, concept of third bodies and tribological behaviour of TiC reinforced MMCs.

Chapter 3 illustrates a detailed experimental procedure adopted for performing different experiments in the entire study. Although, the thesis is manuscript based with each chapter specifically describing the procedure followed to perform the experiments, a more detailed description regarding the pre-and post test sample preparations for analysis and characterization are illustrated. In addition, the sequence of steps followed to achieve the best suited spray conditions as per the requirements, specific details of the tribometer equipment and their line diagrams, method followed to obtain wear track profiles, ball wear volumes etc., are discussed.

Chapter 4 shows the influence of feedstock powder properties on the microstructure and mechanical properties of the Ti6Al4V coatings. Coatings were deposited using PGA powders of

spherical and Armstrong powders of irregular morphologies. The coatings were characterized to determine their microstructure, porosity, deposition efficiency and hardness. Electron channel contrast imaging (ECCI) was performed on the powder and coatings cross-sections to compare the pre and post spray microstructures. It was observed that the irregular morphology and deformable microstructure of the Armstrong powders led to highly dense deposits compared to PGA powder coatings. To evaluate the cohesive strength between the splats, multi-scale indentation was performed on the coatings and bulk Ti6Al4V plate. Indentation was done at different length scales (nano and micro) and a hardness loss parameter was determined that qualitatively indicated the cohesive strength between the splats. This chapter gave a complete understanding regarding the role of powder properties in determining the quality of the cold spray deposits and served as a reference to understand the tribology of Ti6Al4V coatings.

In **Chapter 5**, the adhesion strength and microstructural transformations that occur in a single Ti6Al4V powder particle at splat level was evaluated. Single splats were deposited using spherical and irregular Ti6Al4V powders at similar spray conditions and particles velocities. Splat adhesion tests were performed to determine the adhesion strength. ECCI was done on the splat cross-sections to compare the post spray microstructural transformations that occurred in spherical and irregular powders. In addition, the respective splat microstructures were also compared to their corresponding initial powder microstructures. The information obtained from both mechanical testing and microstructural observations of the splats helped to understand the advantages of using Armstrong powders for possible engineering applications in the near future.

Chapter 6 evaluated the tribological behaviour of Ti6Al4V coatings deposited using spherical and irregular powders (chapter 4). Sliding wear tests were performed at different normal loads and the coefficient of friction (CoF) and wear rates were determined. The observed differences in friction and wear mechanisms in both coatings were co-related to the coating characteristics, third bodies generation as well as flow inside the tribological circuit and wear track morphology. ECCI of the wear track cross-sections was performed to understand the wear induced microstructural changes and nanoindentation was done to generate a hardness profile across the wear track down till the unworn coating. TEM analysis was performed on the thin lamellae prepared using FIB lift out at selected locations on the wear track to specifically compare and characterize the localized deformed microstructures and chemical compositions. The mechanical, chemical and

microstructural properties of the third bodies together with the coating properties helped to understand the observed trends in friction and wear of coatings.

Chapter 7 mainly focussed on the CS deposition of Ti6Al4V-TiC MMCs and their tribological behaviour. In this chapter an attempt was made to understand the influence of metal powder properties on the CS of composite coatings and the role of TiC reinforcement as well as its content on the tribology of the coatings. Ti6Al4V-TiC MMCs were deposited using spherical and irregular Ti6Al4V powders along with TiC powders. Coatings were cold sprayed using different metal-ceramic compositions and were characterised to determine the ceramic retention, porosity and mechanical properties. The friction and wear behaviour of the coatings was evaluated by performing dry sliding wear tests at different normal loads. One set of composite coatings deposited using spherical and irregular powders with identical TiC composition along with highest ceramic retained coating were selected for tribological studies. The friction and wear behavior of the composites was co-related to the coating properties, TiC reinforcement and its volume fraction, that favoured the formation of protective tribolayers. ECCI of the wear track cross-sections helped to understand the subsurface deformation where as nanoindentation was done to evaluate the mechanical properties of the third bodies. In addition, TEM analysis was performed to understand the microstructural changes that occurred beneath the tribolayers and underneath the bare wear track (not covered with tribolayer). The microstructure, mechanical and chemical properties of the tribolayers formed due to the compaction of wear debris were used to understand the dynamic changes observed in friction and wear mechanisms.

Chapter 8 explored the high temperature tribological behaviour of cold sprayed Ti6Al4V and Ti6Al4V-TiC MMCs. Ti and its alloys used in engineering applications are subjected to service temperatures up to $\sim 600^{\circ}\text{C}$ [48], hence, sliding wear tests were performed on the coatings at different static test temperatures between $25^{\circ}\text{C} - 575^{\circ}\text{C}$. ECCI performed on the wear track cross-sections helped to understand the subsurface deformed microstructures formed due to stress transfer. Nanoindentation was done on the third bodies and unworn coatings to determine their mechanical properties. The microstructural, chemical and mechanical properties of the third bodies was used to understand the observed changes in the friction and wear mechanisms across different temperatures. In addition, the influence of TiC particle reinforcement in improving the tribological properties of Ti6Al4V at different temperatures was studied in detail.

In **Chapter 9**, a discussion comparing the tribological behaviour of Ti6Al4V-TiC MMCs and corresponding unreinforced coating deposited using the two Ti6Al4V powders (spherical and irregular) is presented. The importance of matrix properties apart from hard particle reinforcements in cold sprayed Ti6Al4V-TiC MMCs and the specific advantages of using Armstrong powders to fabricate composites for tribological applications was highlighted.

Chapter 10 outlines the summary, major conclusions based on the entire study performed in the thesis, contributions to original knowledge and the scope for a possible future work. There is one appendix showing the procedure adopted to perform the worn subsurface analysis and determine the grain size of recrystallized grains below the wear track in Chapters 6 and 7.

Chapter 2

Literature review

2.1 Coating deposition using cold spray process

2.1.1 Introduction to cold spray

Cold spray (CS) or cold gas dynamic spraying is a novel thermal spray process where micron sized particles are accelerated to supersonic velocities and impact on to substrates [8]. Upon impact, particles with velocities greater than critical velocity (V_{cr}) (defined as the minimum particle velocity required for material deposition to occur and below which the particle rebounds) undergo adiabatic shear instabilities and metallurgically bond to form a coating. The process of material deposition due to supersonic impacts was first discovered by Dr. Anatolii Papyrin and his colleagues in mid-1980s at the Institute of Theoretical and Applied Mechanics division of Russian Academy of Science in Novosibirsk while performing experiments to understand the models related to supersonic two-phase flow (gas + solid particles) inside a wind tunnel [8,9]. Subsequently, the process was further developed in the same research group to deposit different metals, alloys and demonstrated the feasibility of the process for use in different applications [8]. Unlike other thermal spray techniques like air plasma spraying, detonation gun and high velocity oxy-fuel spraying (HVOF) that involve high processing temperatures (as shown in Fig. 2.1) and melt the powder particle to develop coatings, CS uses the kinetic energy of highly accelerated particles to deform them upon impact [8]. Since the particles are not melted but deposited in solid state, the deleterious effects of oxidation, phase transformation and evaporation are minimized or eliminated. In addition, the peening of the incoming particles on the pre-deposited layers result in densification and development of compressive residual stresses [7,49–51]. Due to versatility of the process and its advantages, CS is being widely studied by many researchers all over the world to deposit metal, alloy, ceramics, polymers and composite coatings on to different substrates [5,13,47,52–68]. As a result, this process finds a wide range of applications in the fields of aerospace, marine, electronics, automobile and biomedical industries [5,6,69,70].

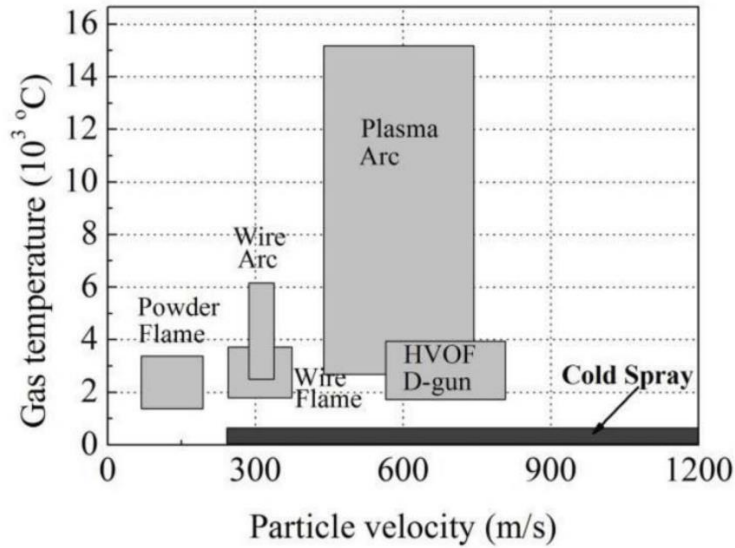


Fig. 2.1: Schematic showing the gas temperature and particle velocity in different thermal spray processes [61].

A basic CS system mainly consists of a high pressure gas supply unit, gas heater, powder feeder, de Laval nozzle and a robotic arm [8]. Prior to spraying, pressurized propellant gas is pre-heated up to 1000°C using a heater. Generally, He, N₂ or compressed air are used as propellant gases depending upon the velocity to be achieved and the nature of the material being sprayed [69,71]. The pressurised propellant gas along with the powder particles coming from a separate channel get mixed with the preheated gas stream and are injected into the inlet section of the converging-diverging de Laval nozzle. As the gas passes through the nozzle throat section, its velocity reaches the sonic velocity and in the divergent section, a rapid expansion leads to supersonic velocities between 350 m.s⁻¹ to 1200 m.s⁻¹ at the nozzle exit. The powder particles impact the substrate at such high velocities, undergo adiabatic shear instabilities and metallurgically bond to form a deposit. There are generally two types of cold spray systems (a) high pressure cold spray (HPCS) (shown in Fig. 2.2 (a)) (b) low pressure cold spray (LPCS) (shown in Fig. 2.2 (b)) [7]. The main difference between these systems is the velocity to which the particles are accelerated and the inlet gas pressure. The inlet gas pressure in LPCS is between 5 to 10 bar whereas in the case of HPCS the gas pressure is 20 to 40 bar. For HPCS, the spray particles are injected at the inlet section of the nozzle using a high-pressure gas supply whereas in LPCS the spray particles are injected at the divergent section of the nozzle. LPCS is generally portable and the powder particles are accelerated to a velocity of 300 – 600 m.s⁻¹ unlike HPCS where supersonic velocities up to 1200 m.s⁻¹ can be

achieved making it a high strain rate process, typically ranging between $10^6 - 10^9 \text{ s}^{-1}$. The LPCS is used to deposit light materials like tin, zinc [72] while a HPCS is used to deposit high strength materials like titanium, Ti6Al4V, nickel, etc.[13,66,71,73,74].

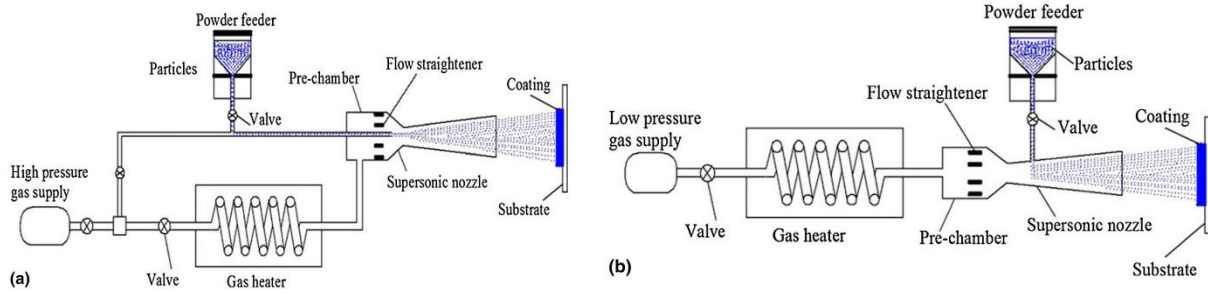


Fig. 2.2: Schematic of (a) high pressure and (b) low pressure cold spray systems [7].

2.1.2 Concept of critical velocity and bonding mechanisms

The primary requirement for any coating is its adherence to the substrate. Coating properties and its performance depend largely on the particle-substrate and interparticle bonding. Finite element analysis (FEA) and experiments were performed to understand the bonding mechanisms that occur in CS process [75–79]. Experimental results have shown that the adhesion of the particles occurs only when the particle velocity exceeds a threshold value termed as “critical velocity” [75,80]. Critical velocity depends on many factors like material density, yield strength, melting temperature, particle and substrate temperatures, particle size and oxygen content in the powder [75,80–84]. Assadi *et al.* found that an increase in material density and particle initial temperature reduce the critical velocity, whereas, an increase in yield strength and particle melting temperature increase the critical velocity [75]. They proposed a simple empirical equation to calculate the critical velocity shown below [75]:

$$V_{cr} = 667 - 14\rho + 0.08 T_m + 0.1 \sigma_u - 0.4 T_i \quad 2.1$$

In the above equation, σ_u is the yield strength, ρ is the material density, T_i is the initial particle temperature, T_m is the melting temperature. Subsequently, Schmidt *et al.* proposed a more generalized expression to theoretically calculate the critical velocity of the different materials. The equation is shown below [80]:

$$V_{cr} = \sqrt{\frac{F_1 \cdot 4 \cdot \sigma_{TS} \cdot \left(1 - \frac{T_i - T_r}{T_m - T_r}\right)}{\rho} + F_2 \cdot C_p \cdot (T_m - T_i)} \quad 2.2$$

In the above equation, F_1 and F_2 are calibration factors, σ_{TS} is the tensile strength, ρ is the material density, T_i is the impact temperature, T_r is the reference temperature (293 K), T_m is the melting temperature and C_p is the specific heat. Beyond the critical velocity the successful bonding of the particle occurs, and the bond strength increases with increase in velocity beyond critical velocity. However, when the velocity of the particle reaches a threshold where the velocity is much greater than critical velocity, erosion occurs rather than deposition. Thus, there exists a window of deposition [80] for every material where deposition occurs as shown in Fig. 2.3.

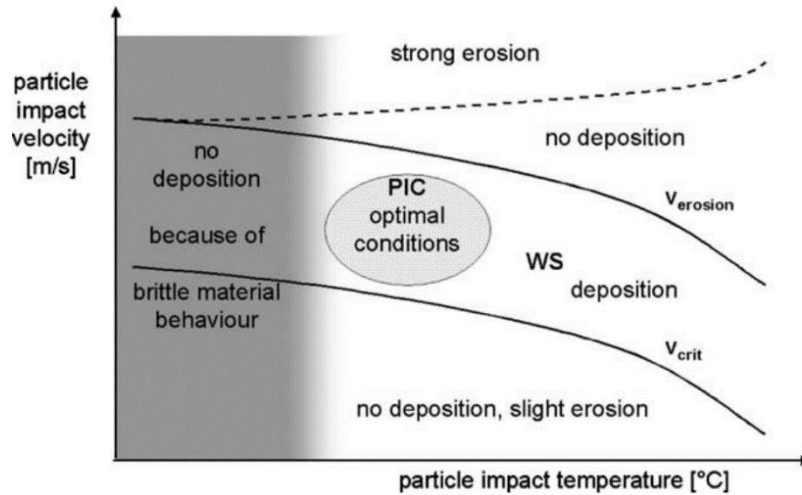


Fig. 2.3: Particle velocity over particle temperature with window of sprayability and regime of particle impact conditions [80].

The most widely accepted bonding mechanism for cold sprayed particles is “adiabatic shear instabilities (ASI)”. The concept of ASI was first proposed by Assadi *et al.* [75] and later supported by many other studies [78,79,85–88]. They performed numerical simulations and deposited single particles of copper on a copper substrate at different velocities to explore the bonding mechanism in CS. They observed that up to a particle velocity of $550 \text{ m}\cdot\text{s}^{-1}$ a normal drop in stress was observed along with an increase of plastic strain at the rate of $0.5 \times 10^9 \text{ s}^{-1}$ as shown in Fig. 2.4. Beyond $550 \text{ m}\cdot\text{s}^{-1}$ a significant break down of stress accompanied by a rapid increase in both strain and temperature was recorded. At the particle-substrate interface, temperatures close to the melting

point were observed where the material lost its shear strength and, underwent excessive deformation (due to change in deformation mechanisms from plastic to viscous flow-type). Furthermore, at such high impact velocities, strain rates in the order of 10^9 s^{-1} are experienced by the particle at the contact interface where thermal softening dominates the work hardening effects. This results in an outward viscous flow of the material called “jetting” due to the rise in interfacial temperature close to the melting point leading to ASI and subsequently bonding. The onset of ASI can be visualized by a steep rise in interfacial temperature along with strain and a sharp breakdown in stresses [75]. Since the contact time is in the order of nanoseconds, there is negligible heat transfer and the conditions are nearly adiabatic. As the particle impacts the substrate, the thin oxide layer on the particle surface is broken and removed due to the outward jetting of the material, leaving behind the fresh areas between the particle and substrate for an intimate contact and metallurgical bonding [87] as shown in Fig. 2.5.

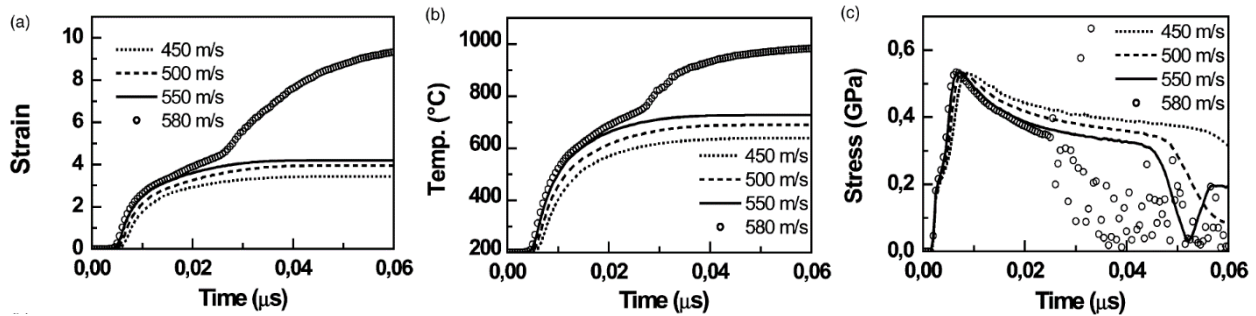


Fig. 2.4: Temporal development of (a) plastic strain (b) temperature and (c) flow stress at the critical node of a cold sprayed copper particle on a copper substrate [75].

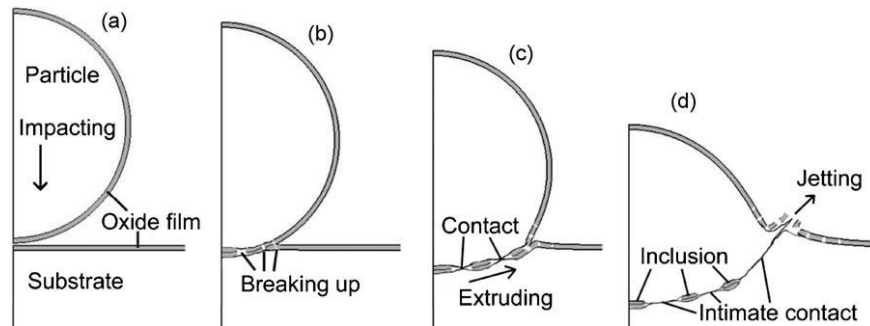


Fig. 2.5: Schematic showing the different stages of particle bonding after particle impact [87].

Apart from ASI, bonding due to mechanical interlocking of particles was reported by researchers when a hard particle was deposited on a soft substrate [76,77,89]. Studies by Hussain *et al.* have shown that when a copper particle impacted on to aluminium substrate, jetting was observed on the aluminum substrate due to its lower hardness compared to copper [76]. This resulted in the formation of lips due to jetting. The formation of lips partially encapsulated the copper particle and led to its mechanical anchorage within the substrate. The bonding through mechanical interlocking was further confirmed by the extrusion of aluminium from the substrate into the copper particles at the substrate-coating interface as shown in Fig. 2.6. Similarly, FEA simulations performed by Meng *et al.* show that mechanical interlocking was the prime bonding mechanism in case of soft particle on hard substrate impact system [77]. They found that as the particle impacts the substrate there is a significant amount of deformation in the substrate rather than the particle. This results in a crater formation in the substrate and subsequently the particle gets entrapped leading to mechanical interlocking.

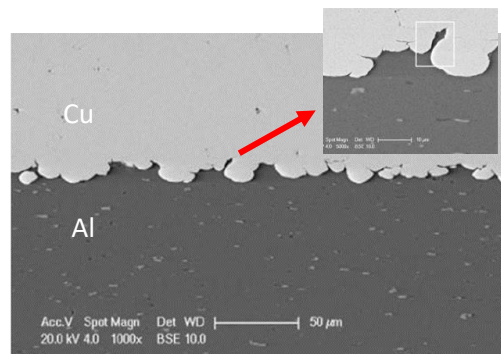


Fig. 2.6: Extrusion of aluminum substrate between copper particles leading to mechanical interlocking [76].

2.1.3 Microstructural evolution

In CS process, as the particles impact the substrate at supersonic velocities, strain rates up to 10^9 s^{-1} are experienced by the particle particularly at its periphery [75,80,85,90]. At the point of impact, a strong pressure field is generated as shown in Fig. 2.7, which is associated with a shear load, with temperatures reaching to close to melting at the interface a viscous jet is created resulting in ASI [75]. At the interface, the formation and subsequent accumulation of dislocation cells result in the formation of sub-grains and elongated sub-grains [11,64,91,92]. The progressive deformation of the elongated sub-grains lead to ultrafine grains (UFGs) [11,64,91,92]. A schematic

of the different stages that lead to grain refinement is shown in Fig. 2.8. Since a gradient of strains and temperatures are experienced by the particle, a mixture of above discussed microstructural features are observed across a single particle. Since, most of the strain is concentrated at the particle-substrate interface, UFG microstructures are observed at the interface both in particle and substrate while most of the particle retains its initial microstructure [93]. King *et al.* found the formation of UFGs at the splat-substrate interface followed by elongated submicron grains in cold sprayed Cu particle [94]. The submicron grains were followed by a microstructure that was similar to the pre-deposited copper powder microstructure. Kim *et al.* performed TEM analysis on Ti splat cross-sections deposited on steel substrates to understand the grain refinement in cold sprayed particles [85]. Ultrafine nanograins of few tens of nanometers were found along the splat-substrate interface and in the jetted region as shown in Fig. 2.9. However, away from the splat the initial microstructure of the powder particle was retained indicating that the deformation mostly concentrated at the particle interface near the impact site. Similar retention of initial microstructure away from the bonding site and formation of UFGs at the interface were reported by Lek *et al.* in Ti6Al4V particles deposited on both Ti6Al4V substrates and pre-deposited coating [92].

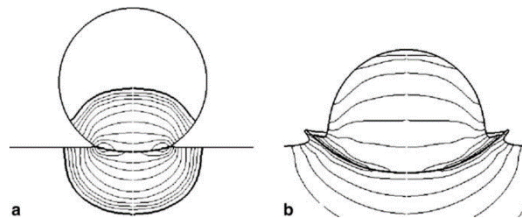


Fig. 2.7: Schematic of particle impact showing (a) pressure field generation (b) jetting due to the adiabatic shear instabilities [80].

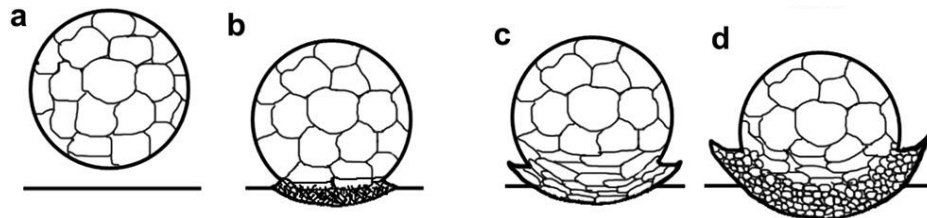


Fig. 2.8: Grain refinement mechanism that occur is a single particle (a) before impact (b) entanglement of dislocations (c) formation of dislocation cells and elongated sub-grains (d) break-up of the elongated sub grains, rotation and recrystallization to form ultra fine grains [85].

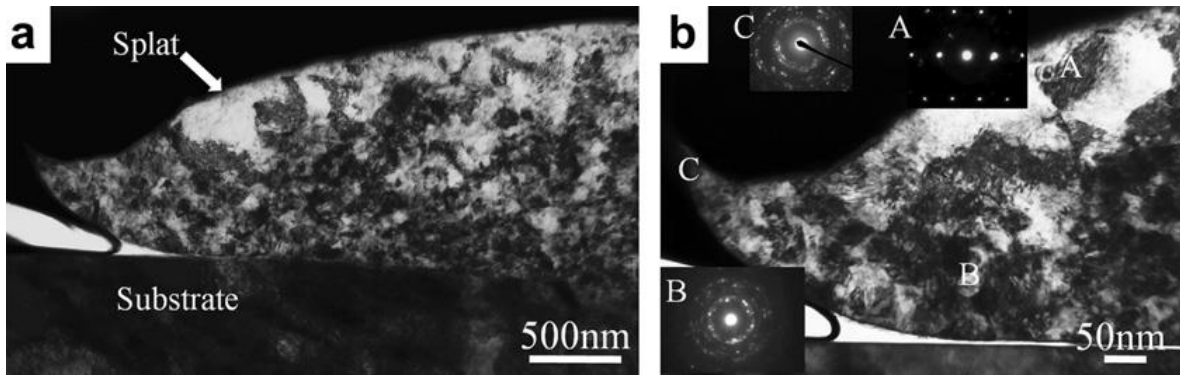


Fig. 2.9: (a) TEM image of the splat (b) selected area diffraction patterns taken at upper region of the splat – A, Splat-substrate interface – B, jetting region – C [85].

The extent of grain refinement in cold sprayed particles depends on particle velocity, particle temperature, substrate temperature, relative hardness of the particle and substrate [25,91,95,96]. Furthermore, the recrystallized regions, grain size distributions reflect the distribution of stresses and temperatures across the particle. Goldbaum *et al.* deposited single particles of Ti at different velocities and on pre-heated substrates to understand the influence of particle velocity and substrate temperature on the microstructural transformations [25]. ECCI of the splats cross-sections deposited at near critical velocity of Ti showed limited deformation with splats largely retaining the initial powder microstructure. In these splats, at the jetting region and at the splat-substrate interface UFGs of size ~ 200 nm were observed. At velocities above the critical velocity, greater extent of deformation compared to near critical velocity was observed, with UFGs of size ~ 95 nm at the splat-substrate interface. The UFGs were followed by submicron grains of size ~ 150 nm at $2 \mu\text{m}$ and 230 nm at $5 \mu\text{m}$ away from the splat-substrate interface. In this case, the recrystallized region accounted for $\sim 50\%$ of the total splat area, while the remaining portion of the spat had largely retained its initial powder microstructure. Splats deposited on preheated substrates at velocities greater than critical velocities showed greater extent of recrystallization compared to non-preheated substrates. In this case, the recrystallized area accounted for $\sim 80\%$ of the total splat area indicating that the preheating of the substrate assists in the particle deformation. Most of the above studies have widely investigated the microstructural transformation that occur due to powder and substrate pre-heating and velocity increment. However, the microstructural changes that occur in cold sprayed particle due to differences in the initial microstructure and morphologies especially in Ti alloys have not been extensively studied.

2.1.4 Influence of powder properties on the cold spray of coatings

For the same material, different feedstock manufacturing techniques and their properties such as morphology, size, oxygen content, and porosity have a significant influence on the cold sprayability and final coating properties [60,66,97,98].

Manufacturing technique

Powder manufacturing techniques determine the final microstructure and hardness of the particles which in turn influences the cold spray and coating properties [17,19,66,97,99]. Powders with hard and non-deformable microstructures often lead to poor deposits and require higher impact velocities to achieve shear instabilities [17]. Jodoin *et al.* deposited Al alloy coatings using cryomilled and plasma gas atomized (PGA) powders [97]. Their results show that the coatings deposited using PGA powders were dense while that of cryomilled powders were porous. The differences in porosity was due to the microstructure and hardness of the initial feedstock. The PGA powders were soft and had coarser grain size which favoured the particle deformation whereas the cryomilled powders were hard and had more refined grain sizes that hindered particle deformation resulting in porosity. Ti6Al4V coatings were deposited by Bhattiprolu *et al.* using gas atomized powders manufactured through PGA process and hydride de-hydride powders manufactured using hydrogenation [17]. The rapid cooling process during plasma gas atomization had resulted in martensitic lath microstructure [18] while the hydride de-hydride powders had equiaxed ' α ' grains with intermediate β -phase microstructure. Post spray characterization showed that coatings deposited using the hydride de-hydride powders had highly deformed microstructures, low porosity and adhesion strength comparable to that of gas atomized powders. The superior coating properties was co-related to the more deformable initial microstructure of the hydride de-hydride powders compared to hard martensitic microstructure.

Particle morphology

For the same spray conditions, irregular powders (IP) accelerate to higher velocities compared to SP due to higher drag force acting on the particle in the gas stream [66,97]. Higher particle velocities result in greater particle deformation and lead to dense coatings. Wong *et al.* deposited Ti coatings using spherical, irregular and sponge [66]. They found that IP were accelerated to much higher velocities compared to other powder morphologies and resulted in coatings with low

porosity. Within irregular morphology, powders with dendritic or coral surface structure also result in extremely dense coatings with high deposition efficiency compared to SP. In case of dendritic powders, while their irregular shape accelerates them to higher velocities, their dendritic surface results in multiple localized impact sites (shown in Fig. 2.10) that lead to localized adiabatic shear instabilities [54]. In addition, the presence of pores in the particle result in lower yield strength and elastic modulus [100] compared to fully dense particle and reduce the critical velocity for deposition [12,101]. This results in dense coatings at much lower inlet gas pressures and temperatures which becomes helpful in the deposition of coatings on to heat sensitive substrates.

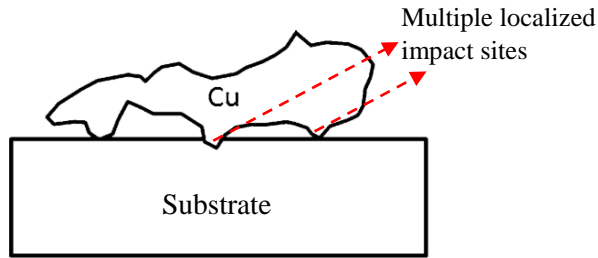


Fig. 2.10: Impact of a dendritic powder particle on a substrate [54].

Particle size

Apart from shape, particle size also has a significant influence on the ability to form adiabatic shear instabilities [80]. Smaller particles have a high surface area to volume ratio, that result in a greater amount of heat transfer from the surface and require higher particle velocities to bond. In addition, smaller particles possess higher amount of impurities and also get diverted from their path due to bow shock effect near the substrate leading to lower deposition efficiency [7]. Schmidt *et al.* calculated the critical diameter of the particles for different materials above which they successfully bond [80]:

$$d_{\text{crit}} = 36 \frac{\lambda_p}{C_p \cdot \rho_p \cdot V_p} \quad 2.3$$

In the above equation, λ_p is the thermal conductivity, C_p is the specific heat, ρ_p is the particle density and V_p is the particle velocity.

Internal porosity

Internal porosity in the powder particles assists in deformation during CS. The fracturing of pores during impact, dissipate the kinetic energy, inhibit particle rebound and increases the coating deposition efficiency [12,102]. Presence of porosity in the feedstock was proven to be particularly beneficial during the deposition of metal matrix composite coatings [62,102,103]. Coating deposition in CS occurs through deformation of powder particles but hard phase ceramics like TiC, WC, SiC do not undergo plastic deformation and are often co-deposited using a ductile matrix. However due to their inert nature, these reinforced particles do not form a bond with the matrix and tend to rebound during impact. This decreases their retention in the coatings compared to the initial feedstock. Presence of porosity in the metallic particles absorbs the kinetic energy of the incoming reinforcement particles, reducing their rebound and resulting in higher retentions. Yin *et al.* deposited WC-Co-Ni composite coatings using porous WC-Co powders with different metal-ceramic mixtures [102]. They reported that the use of porous WC-Co led to complete retention of WC which was similar to that of the initial mixture. Similarly, Lioma *et al.* deposited WC-Ni composite coatings using dense oxide reduced WC powders and porous agglomerated and sintered WC-12Co powders [103]. They found that dense WC powders fractured, rebounded during impact resulting in lower retentions while the porous powders were more deformable and lead to higher ceramic retentions.

Chemical composition

Powders having similar physical characteristics, but different chemical composition like oxygen content have a profound effect on the cold sprayability of the powders. Specifically, increase in oxygen content or oxide layer thickness, increases the critical velocity for particle deposition [81,104,105]. Powders with higher oxygen content i.e. greater thickness of oxide film on the surface, consume greater amount of impact energy to break the oxide film and expose the nascent surface for bonding. This results in lower deposition efficiencies and high porosity. Li *et al.* found that an increase in oxygen content in copper powder from 0.02 wt.% to 0.38 wt.% resulted in an increase in critical velocity from $310 \text{ m}\cdot\text{s}^{-1}$ to $550 \text{ m}\cdot\text{s}^{-1}$ [81]. Similar increase in critical velocities with oxygen content was observed in 316L stainless steel and Monel alloy powders as shown in Fig. 2.11. Furthermore, an oxide film on the powders leads to the formation of oxide debris and

pores at the splat-substrate interface in the coating [105–107]. This results in poor adhesion between the coating and substrate.

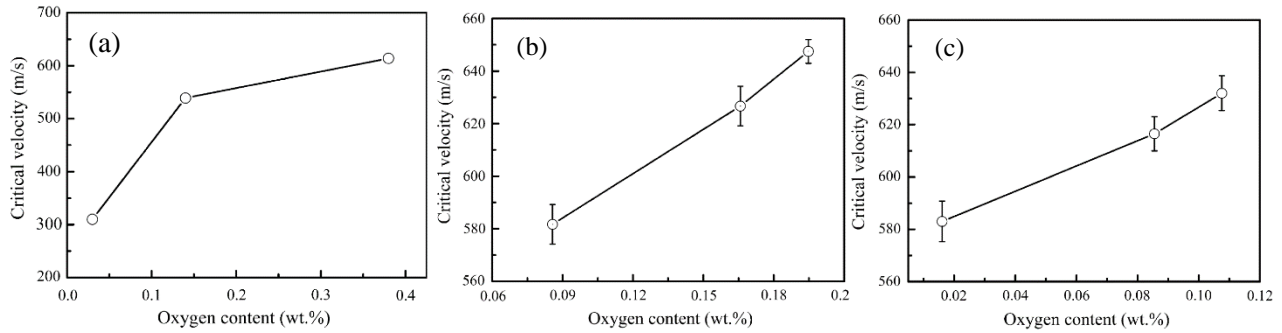


Fig. 2.11: Influence of oxygen content on critical velocity in (a) Copper (b) 316L (c) Monel alloy [81].

2.2 Challenges in cold spray of Ti6Al4V

For a material to be successfully deposited using CS it must possess some degree of ductility. Generally, soft materials with low yield strength like Cu, Zn etc. are deposited even at low particle velocities. However, to obtain good deposition efficiency, higher particle velocities must be attained [108–110]. High yield strength materials like Ti6Al4V, possess higher critical velocities and their deposition is always challenging [5,13,15,17,71]. Studies from literature have reported that cold spraying of Ti6Al4V using nitrogen as propellant gas results in significant porosity and also poor adhesion to substrate [13,17,111,112]. Phuong *et al.* reported that Ti6Al4V coatings deposited using nitrogen as propellant gas exhibited high porosity due to non-deformability of the powder particles while the coatings deposited using helium were highly dense as shown in Fig. 2.12 [13]. Helium being a monoatomic gas and due to its high compressibility index accelerates the powder particles to high velocities [22]. However, use of helium for bulk coating deposition on industrial components remains uneconomical and non-sustainable [22,23,113]. Similarly, Bhattiprolu *et al.* deposited Ti6Al4V coatings with powders manufactured using plasma gas atomization, gas atomization and hydrogenation processes [17]. The three processes resulted in powders with different microstructures. They concluded that coatings deposited using hydride dehydride powders manufactured using the hydrogenation process had resulted in coatings with low porosity compared to gas atomized powders. This was attributed to their deformable equi-axed microstructure compared to the hard martensitic microstructure exhibited by the other two powders. However, their coatings were deposited using helium as propellant gas and it is well

known that He inherently accelerates powder particles to extremely high velocities and hence it cannot be fully concluded that the powder microstructure alone resulted in highly dense deposits.

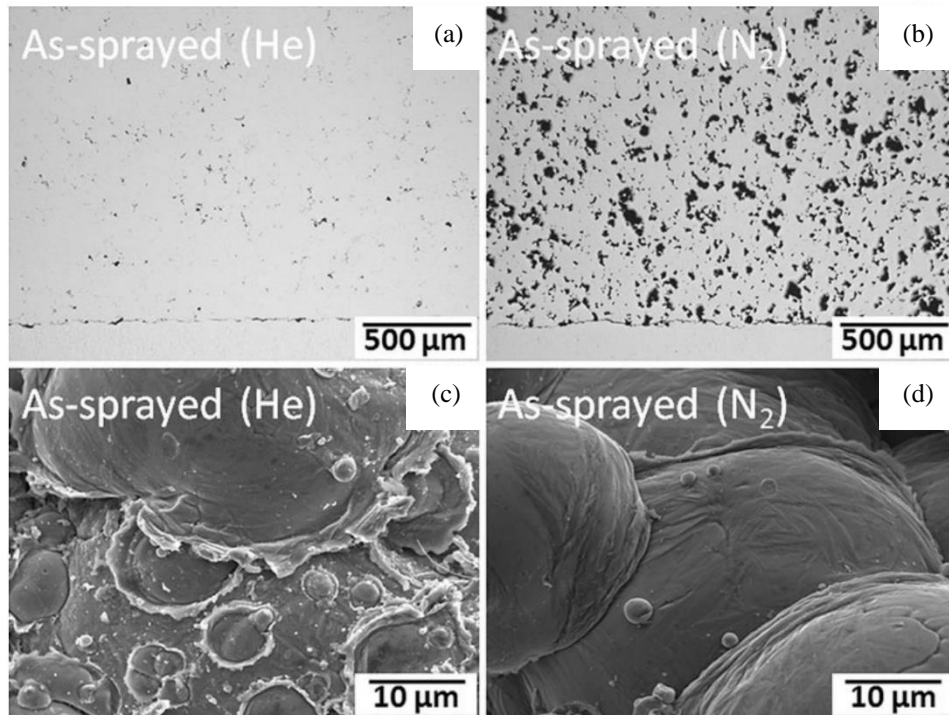


Fig. 2.12: Cross-section and top surface of the coatings deposited using helium (a) & (c) and nitrogen (b) & (d) as propellant gas [13].

To reduce porosity and improve cold sprayability, mechanical blending of Ti6Al4V powders with deformable Ti powders was done by Aydin *et al.* [15]. Presence of a small volume fraction of Ti particles in Ti6Al4V matrix resulted in the formation of a continuous network and led to densification by undergoing deformation during subsequent impact by the incoming hard particles. They found that an addition of 10 vol.% of Ti, decreased the porosity in Ti6Al4V coatings from 6.7% to 1.5%, and, a further increase in Ti vol.% did not decrease the porosity [15]. Presence of hard particles in the initial feedstock along with metal powders results in peening during deposition by the incoming hard particles on the pre-deposited coatings. This leads to coatings densification. Luo *et al.* deposited coatings by mechanically blending hard steel particle with Ti6Al4V powders [20]. They found that as the vol.% of the steel particles increased, the porosity in the coatings decreased and at 70 vol.% extremely dense coatings comparable to that of deposited using helium were obtained. However, as the percentage of the hard particles increased, the deposition

efficiency decreased and also, there was reinforcement of hard particles as impurities in the coatings.

2.3 Adhesion and cohesion strength

Good adhesion of the coating to substrate and cohesion between the splats are primary requirements of a coating. To test the adhesion strength of thermal spray coatings, mechanical tests like ASTM C633 standard, tubular coating tensile (TCT) tests were developed [14,114,115]. The standard ASTM test utilises a test rig similar to that of a tensile test in which the coatings are glued using an adhesive epoxy or glue to standard fixtures, heat cured and subsequently cooled to room temperature. The setup is mounted on a tensile machine and then pulled apart. Using this technique, Tan *et al.* determined the adhesion strength of Ti6Al4V coatings on Ti6Al4V substrates [14]. They estimated the adhesion strength of the coatings was between 65 - 70 MPa. However, the true adhesion strength of the coating could not be determined due to the failure of the epoxy which is one of the main drawbacks of the technique. Similarly, Bae *et al.* deposited Ti coatings at different velocities using nitrogen and helium as propellant gases [78]. They reported adhesion strength values between 49 MPa to 65 MPa for the coatings deposited using nitrogen. However, for the coatings deposited using helium, epoxy failure had occurred due to their high adhesion. Thus, in the above test the adhesion strength of the epoxy acts as a prime limitation in determining the true adhesion strength if the coatings are strongly bonded to the substrate. In these cases, most of the researchers report the adhesion strength of the coatings to be greater than that of the epoxy rather than giving a quantitative value.

Fundamentally, in CS process the bonding of the particles to the substrate occurs at splat level and hence, special techniques were developed to investigate the adhesion strength at splat level. Goldbaum *et al.* used a modified ball bond shear test [116] to measure the adhesion strength of Ti6Al4V and Ti splats deposited on Ti6Al4V and Ti substrates [117]. In their study, single splats were deposited at different spray conditions and velocities using nitrogen and helium as propellant gas on bare as well as pre-heated substrates. In all spray conditions, Ti splats exhibited higher adhesion strength compared to Ti6Al4V splats as shown in Fig. 2.13. This was due to the high yield strength of Ti6Al4V that makes it difficult to deform upon impact. Furthermore, an increase in particle velocity led to an increase in splat deformation and adhesion strength (shown in Fig. 2.13). Higher particle velocities result in greater strain localization and lead to better bonding

between the splat and substrate. Also, splats deposited on pre-heated substrates showed more continuous bonding and higher adhesion strength. They concluded that a combination of high particle velocities and substrate pre-heating can enhance splat-substrate bonding. To understand the adhesion at splat level, Vidaller *et al.* deposited single splats of Ti6Al4V on Al alloy, Mg alloy, Ti6Al4V and Ti substrates and performed cavitation tests to determine the bond strength [118]. They found that the ASI and splat deformation was more in Ti6Al4V splats deposited on Ti and Ti6Al4V substrates whereas in case of other two substrates there was more substrate deformation. For substrates that have almost equal or higher strength than sprayed material, shear instabilities predominantly occur on the particle side resulting in enhanced bonding. This led to the retention of more splats on Ti and Ti6Al4V substrates when compared to other substrates during cavitation tests. This illustrates that the strength of the substrate also plays an important role in determining the adhesion strength.

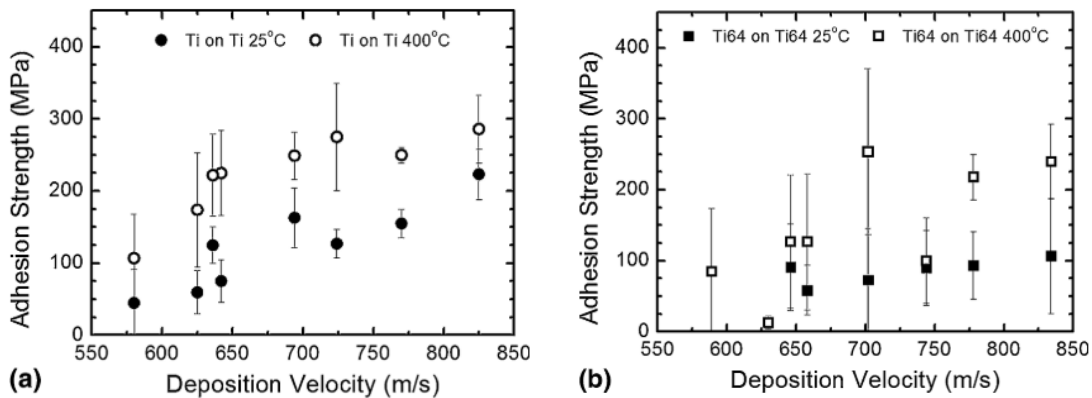


Fig. 2.13: Adhesion strength of the splats as a function of particle velocity for (a) Ti deposited on Ti substrates at 25°C and preheated to 400°C (b) Ti6Al4V deposited on Ti6Al4V substrates at 25°C and preheated to 400°C [117].

The cohesive strength signifies the bond strength between the splats in a coating. Cohesive strength between the splats broadly depends on the ability of the particle to form ASIs which in turn depends on various factors like particle temperature, particle size, its position in the jet stream, impact angle, velocity etc. [97,110,115,119–121]. Schmidt *et al.* used tubular coating tensile (TCT) test to measure the cohesive strength of copper coatings on aluminum substrates [122]. They found that an increase in process gas temperature led to greater particle deformation and enhanced the bonding between the particles. Similar, TCT tests were performed by Binder *et al.*

on cold sprayed Ti coatings deposited at different inlet gas temperatures [115] as shown in Fig. 2.14. Increase in inlet gas temperature increased the TCT strength of the coatings. This was attributed to the higher kinetic energy of the particles resulting from higher gas temperatures that led to greater deformation of the particle and improved the intersplat bonding. Also, higher gas temperatures increased the ductility of the coatings that also improved the overall coating strength. Goldbaum *et al.* proposed a multiscale indentation technique to evaluate the cohesive strength between the splats [119]. In this method, indentation was performed at two different length scales to determine the influence of indentation size effect on the coating hardness. During nanoindentation i.e. at smaller length scales, the interaction of the indenter with the defects like porosity, splat boundaries are minimum, and the determined hardness was that of the splat. However, in case of microhardness tests i.e. at larger length scales, there was a definite interaction of the indenter with macroscopic defects like porosity, splat boundaries which influence the hardness measurements. Thus, the two test methods revealed the indentation size effects in different manners. Using the hardness measurements at the two different length scales, a hardness loss parameter was determined which qualitatively indicated the cohesive strength between the splats. They found that Ti coatings deposited using nitrogen had significant hardness loss indicating a poor intersplat bonding while the coatings deposited using helium showed negligible hardness loss indicating better cohesion strength. The higher cohesion between the splats in helium deposited coatings was due to the higher particle velocities that result in greater particle deformation and better bonding. They concluded that an increase in particle velocity results in increase in cohesive strength between the splats and improves the overall strength of the coating.

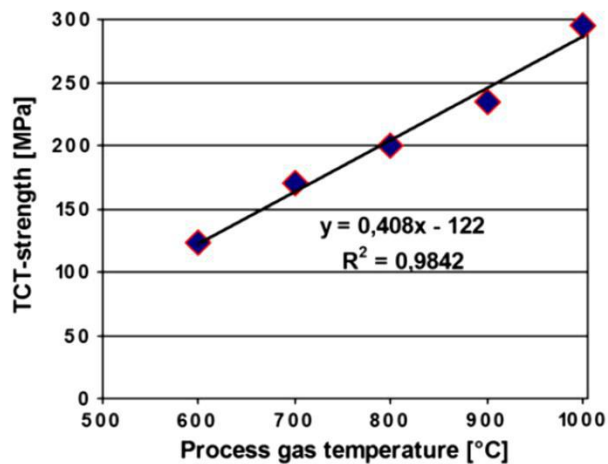


Fig. 2.14: Cohesion strength of the Ti coatings deposited as different gas temperatures [115].

2.4 Fabrication of metal matrix composites (MMCs)

2.4.1 General processing techniques

A composite material essentially consists of at least two or more chemically or physical distinct phases that combine to give properties that are not possible to obtain using a single material alone [123]. Generally, one material forms a continuous matrix while the other phase which is a fiber or a particulate, acts as a reinforcement [123]. When the matrix is a metal or an alloy, the entire system is referred as a metal matrix composite (MMC). In MMC, the metal chosen is generally a high strength or a ductile material whereas the reinforcement is of a specific property selected depending on the application. When compared to unreinforced metals, MMCs offer higher strength to-weight ratio, excellent wear resistance, improved fatigue life, higher fracture toughness, good electrical, thermal and high temperature properties [40,123–125]. Depending on the nature of reinforcement they are often classified into four types namely particle reinforced, fiber or whisker reinforced, sheet reinforced and laminated MMCs [123].

MMCs are generally manufactured using solid, liquid or gaseous processes. In solid-state processing, the metal and reinforcement powders are blended together, and the mixture is isostatically cold compacted or hot pressed to obtain MMC [123]. Liquid state processing involves combining the liquid metal with a reinforcement and allowing it to solidify to form a bulk MMC [123]. One of the types of liquid spray processing involves spray deposition, in which liquid metal is atomized and sprayed along with secondary phases to deposit MMC as coating [123]. This principle is broadly adopted in various thermal spray processes to deposit MMC coatings. In thermal spray process, the metal (matrix) is taken in the form of powder or thin wire and is melted using a plasma or electric arc as a heat source and the molten particle is accelerated to high velocities along with reinforcement phase. The particles impact the substrates and undergoes rapid solidification at high cooling rates resulting in the formation of MMC coating. Since the metal particles are melted during deposition and then solidified, the process results in porosity, residual stress buildup and phase transformations in final deposits. Recently, new techniques in thermal spray are developed to deposit MMC coatings with negligible porosity, low thermal stresses and almost no phase transformations. One such thermal spray technique is CS process that deposits powders in solid state rather than melting them [8,9] and can be broadly viewed as a solid-state deposition process to deposit MMCs. This process is used in the present study to deposit Ti6Al4V-

TiC MMCs of different ceramic compositions using morphologically and microstructurally distinct metal powders.

2.4.2 Titanium carbide (TiC) as reinforcing phase in MMCs

Titanium carbide (TiC) is a high strength, extremely hard, chemically inert refractory material with high thermal stability and excellent wear resistance. It is an interstitial carbide formed by a group IV element of the periodic table and has properties similar to other interstitial carbides (formed by group IV elements) like ZrC and HfC. These are crystalline compounds with carbon atoms occupying the interstitial sites due to their low atomic radii. Interstitial carbides have a weak metal-to-metal bond but a strong metal-carbon bond. Specifically, the interstitial carbides formed by group IV elements have a cubic close packed FCC crystal structure. The crystal structure of TiC is shown in Fig. 2.15 [126]. Mechanical properties of the interstitial carbides depend on their fabrication technique, chemical composition and volume fraction of impurities. They possess high hardness, good mechanical strength and are generally brittle in nature. Their high hardness is mainly due to the strong metal-to-carbon covalent bond and the hardness increases with increase in carbon content until an equal stoichiometric ratio is reached. However, their brittle nature results in catastrophic failure due to stress concentration around defects like voids that arise during their manufacturing. Apart from good mechanical properties, they exhibit good electrical conductivity and possess electrical resistivity slightly higher than that of metals. Despite their excellent mechanical properties, their brittle nature inhibits their usage as bulk to fabricate engineering components. However, as a reinforcement phase they are used in various metallic matrixes to fabricate MMCs both as bulk and as coatings. These MMCs possess high specific strength, hardness, wear resistance compared to unreinforced metal. Some of the typical applications of TiC reinforced MMCs include gears, bearing, cutting tools, forming tools and shafts [127]. Apart from high wear resistance, TiC specifically with carbon content >18 at% exhibits solid lubricant characteristics due to the presence of excessive carbon. This results in low friction during the wear process due to which it is especially used in the manufacture of cutting tools. Since TiC is used as a reinforcement phase in the present thesis, the physical, chemical and mechanical properties of TiC are summarized in Table 2.1 [128].

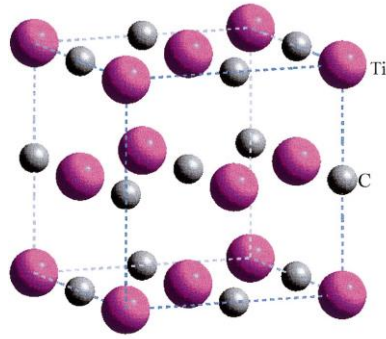


Fig. 2.15: Schematic showing the crystal structure of TiC [126].

Table 2.1 Characteristics and properties of TiC [128].

Crystal structure	Cubic close packed
Lattice parameter	0.4328 nm
Molecular weight	59.91 g.mol ⁻¹
Density	4.91 g.cm ⁻³
Melting point	3067°C
Specific heat (C _p)	33.8 J.mol ⁻¹ .K ⁻¹
Vickers hardness	28 – 35 GPa
Modulus of elasticity	410 – 510 GPa
Shear modulus	186 GPa
Bulk modulus	240 – 390 GPa
Poisson's ratio	0.191
Electrical resistivity	50 ± 10 μΩ.cm
Thermal conductivity	21 W.m ⁻¹ .°C ⁻¹

2.4.3 Deposition of MMCs using cold spray

In many engineering applications coatings deposited using one single metal or alloy don't meet the different requirements of the component and in such a scenario, deposition of MMC coatings are extremely beneficial. Unlike conventional MMC coating deposition techniques like plasma

spraying, HVOF, selective laser melting, laser cladding [40,129–131]; as discussed before, CS deposition does not possess the deleterious effect of phase transformations, oxidation of the reinforcement phase [45,132,133]. For tribological applications, MMCs using cold spray are deposited by spraying mechanically blended hard ceramic or solid lubricant powders with deformable metal powders [37,63,133–138] or by directly spraying composite powders that contain agglomerated particles of metal and second phase constituents [46,103,139,140]. In the former case, the two constituents (metal and ceramic particles) are mechanically mixed together prior to spraying, the metallic particles deform upon impact while the ceramic particles get embedded and entrapped between the pre-deposited and incoming metal particles. In the later case, composite powders have agglomerated and sintered ceramic particles inside a metal particle and when sprayed the metallic matrix deforms and forms a coating while the ceramic particles get embedded. Compared to mechanical blending, composite powders result in higher ceramic retentions, however, their deposition efficiency is low. Also, composite powders for all metal-ceramic mixtures are not readily available. Using CS process, a wide range of MMC coatings like Ni-Al₂O₃, Ti-TiC, Al-Al₂O₃, NiCr-Cr₃C₂, Ni₂₀Cr-Al₂O₃, NiCu-Al₂O₃, Cu-MoS₂, Ni-WC, Co-WC, Al-SiC, Ni-hBN, Al alloy-SiC were successfully deposited by various researchers [35,36,46,63,138,140–150].

Studies from literature on cold sprayed MMCs have shown that presence of ceramic particles in the feedstock resulting in a peening effect by the incoming particles on the pre-deposited layers during deposition. This leads to coating densification [144]. Furthermore, during coating buildup, micro asperities created by the ceramic particles increase the surface area of contact between the coating and the substrate and facilitate for better bonding [151]. Koivuluoto *et al.* observed that Al₂O₃ ceramic particle reinforcement had significantly decreased the porosity in Ni₂₀Cr coatings due to peening by the incoming ceramic particles [47]. The reduction in porosity had in turn improved the corrosion resistance of Ni₂₀Cr coatings. In terms of deposition efficiency, researchers have reported that at low ceramic volume fractions in the feedstock, an increase in deposition efficiency was observed due the micro asperities created by the ceramic particles during impact which assist metal particle bonding [36,144,152]. However, at higher ceramic volume fractions, the deposition efficiency decreased due to the significant rebound and fragmentation of ceramic particles upon impact [144]. Apart from cold sprayability, ceramic particle reinforcement also improved the hardness and mechanical strength of the coating by increasing its load bearing

capacity and resistance to plastic deformation. Previously, Irissou *et al.* deposited Al-Al₂O₃ composite coatings and found that an increase in aluminum content increased the hardness, and bond strength [144]. Increase in hardness which led to higher wear resistance of Cu-Al₂O₃ coatings compared to pure Cu coatings was observed by Triantou *et al.* [153]. Apart from improving different coating properties, presence of ceramic particles in the feedstock prevent clogging of nozzle thereby giving a chance to deposit coatings at higher gas pressures and temperatures. This led to the improvement in coating density, thickness and deposition efficiency [47].

In most of the above studies, it was found that higher ceramic retention led to better mechanical and tribological properties [154]. However, in CS due to rebound and fragmentation of ceramic particles, the retention is less compared to initial feedstock. To maximize the ceramic retention, different methods like using angular particles (shown in Fig. 2.16), finer particles, porous composite powders and mixing higher ceramic volume fractions in the initial feedstock (shown in Fig. 2.16) were adopted [35–37,103,155]. The use of angular particles led to more embedding and improved ceramic retentions due to their morphology and higher particle velocities. However, the use of angular particles as reinforcement may not be completely suitable for many engineering applications [37]. Alternatively, increase in ceramic volume fraction in the initial feedstock increase the ceramic retention. However, after a critical percentage, no significant improvement was observed. Studies from literature suggest that the use of composite or porous composite powders results in higher ceramic retentions but lead to low deposition efficiency. Also, composite powders are not available for different metal-ceramic mixtures and for all systems. Sova *et al.* found that use of finer ceramic particles led to higher retentions compared to coarser particles [155]. This was due to the fact that the finer particles led to more surface activation of the matrix resulting in higher retentions while the coarser particles resulted in more erosion of the pre-deposited metal coatings resulting in lower retentions. Furthermore, researchers have reported that higher particle velocities of the ceramic particles resulted in higher retention due to more embedding into the metallic matrix compared to lower velocities [154]. Also, the use of more deformable material as matrix led to higher retentions compared to a harder matrix [45]. Deformable matrix allows greater amount of embedding and absorbs the kinetic energy of the incoming ceramic particle while the poor deformability of the harder matrix promotes ceramic rebound and fragmentation.

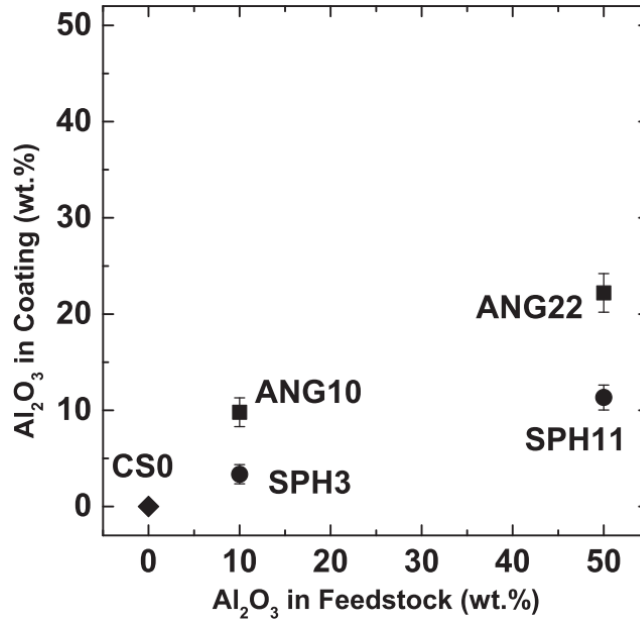


Fig. 2.16: Ceramic retention in the MMC coatings deposited using spherical (SPH) and angular (ANG) Al₂O₃ particles [37].

2.5 Fundamental Tribology concepts

2.5.1 Third bodies

Tribology is defined as the science and technology of interacting surfaces that are in relative motion [156,157]. It involves the study of friction, wear and lubrication of surfaces that are in contact. In the concept of “third bodies”, the two interacting or sliding bodies are individually referred as “first bodies” (as shown in Fig. 2.17) and together as a “tribo-pair”. The interface between the two sliding first bodies is referred as “sliding interface”. During sliding, a part of worn material from the first bodies that gets transferred on to the counter surface (shown in Fig. 2.17) and moves along with it is known as a “transfer film”. The worn material from the first bodies that forms a layer on the parent body is called the “tribofilm” (shown in Fig. 2.17) whereas “wear debris” are the loose fragmented particles that are formed during wear and ejected out of the sliding interface as shown in Fig. 2.17. A third body is a layer of tribofilm or transfer film or wear debris, which essentially separate the two first bodies that were initially in contact [158]. Third bodies are highly deformed materials and exhibit different physical, chemical and/or mechanical properties than that of first bodies [158–160]. Studies from literature show that the properties of third bodies significantly influence the tribological behavior of the material [35,36,161,162]. The formation of

stable, hard and/or lubricating tribofilms often result in low friction and wear rates compared to the materials that don't show tribofilm formation [36,45,163]. In the case of lubricated sliding contacts, a layer of lubricant forms a tribofilm whereas in unlubricated contacts, compaction of wear debris, mechanically mixed material from the first bodies contribute to tribofilm formation.

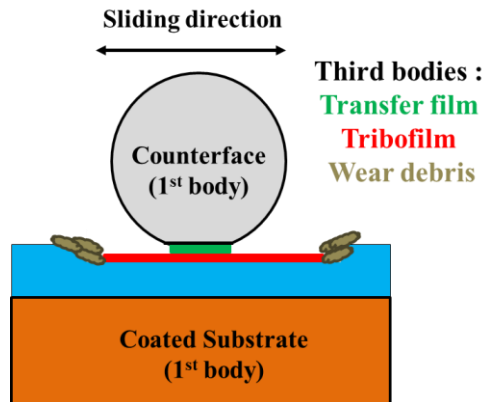


Fig. 2.17: Schematic showing third bodies.

2.5.2 Friction

The word *friction* originated from a Latin verb “fricare” which means to rub [164]. Friction is a tangential resisting force experienced by a body at the sliding interface, when moving over another. It is commonly represented by coefficient of friction (CoF or μ) and is the ratio of frictional force (F) to the normal load (W) acting on the body.

$$\mu = \frac{F}{W} \quad 2.4$$

Friction is not a material specific property and depends on many factors like physical and chemical material properties, ambient conditions, load, temperature, lubrication etc., [156,157]. Before sliding, when two first bodies come into contact under the influence of a normal load, a localized adhesion occurs between the surfaces at the multiple contact points also known as asperity junctions (shown in Fig. 2.18) [165]. At these asperity junctions, interfacial bonds (or adhesive bonds) are formed which get sheared when the first bodies start sliding [2]. The force required to shear the adhesive bonds is the frictional force due to adhesion (F_a) whereas the force required to plough the asperities through the first bodies is the frictional force (F_d) due to deformation. The adhesion and deformation forces sum up to the determine the total frictional force during sliding.

$$F = F_a + F_d \quad 2.5$$

Now using Eq. 2.4

$$\mu = \mu_a + \mu_d \quad 2.6$$

In Eq. 2.6, μ_a and μ_d are the adhesive and deformation components of CoF.

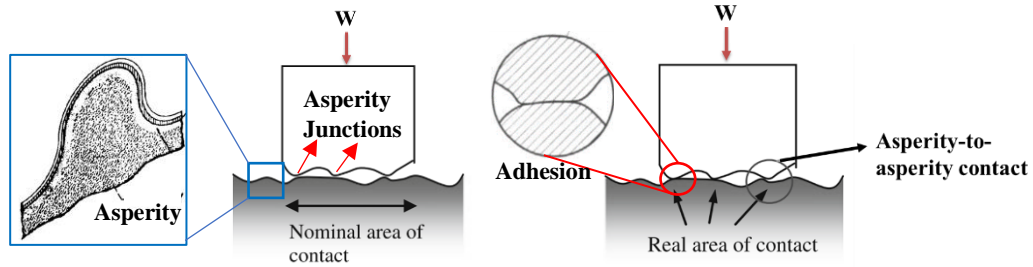


Fig. 2.18: Schematic showing contact interface between first bodies [165].

At the sliding interface, if we assume that single asperity contacts sum up to constitute the real contact area (A_r) which is just a small fraction of the nominal contact area (shown in Fig. 2.18) and all the adhesive asperity junctions have the same shear strength (τ_a) [156,157]. Then, the frictional force due to adhesion can be written as:

$$F_a = A_r \cdot \tau_a \quad 2.7$$

Using Eq. 2.4,

$$\mu_a = \frac{A_r \cdot \tau_a}{W} = \frac{\tau_a}{P_r} \quad 2.8$$

In the above equation, P_r is the mean contact pressure. Based on Eq. 2.7, to reduce the friction force due to adhesion, both contact area and shear strength should be low [166]. When a soft material is chosen as one of the first bodies to slide against a hard counterface (shown in Fig. 2.19a), the shear strength is low, but the contact area becomes large. Contrarily, for a hard surface the contact area is small, but the shear strength is high (shown in Fig. 2.19b). Thus, to have a combined effect of both low shear strength and small area of contact, soft skin on a hard substrate can potentially lead to a lower frictional force due to low adhesion (shown in Fig. 2.19c).

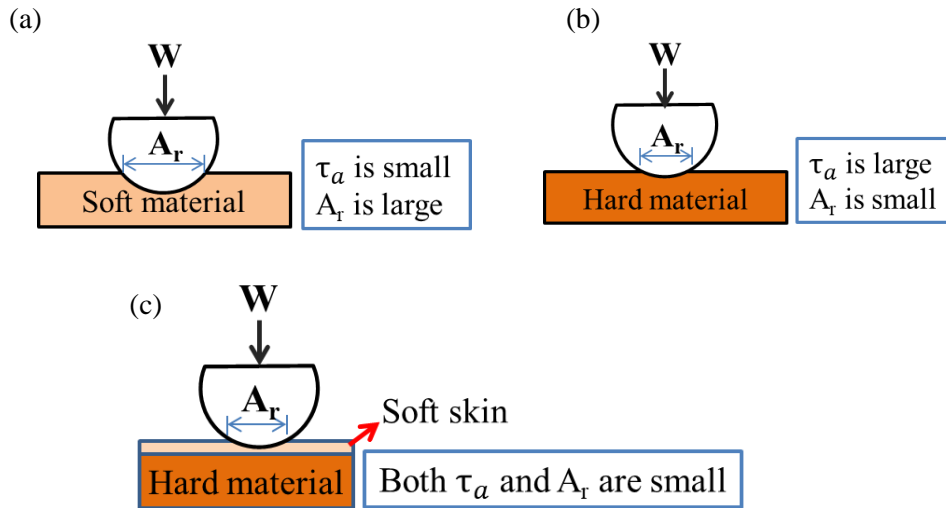


Fig. 2.19: Schematic showing the contact area and shear strength in case of (a) hard material on soft material (b) hard material on hard material and (c) hard material on hard material with soft skin. Adapted from [166].

2.5.3 Wear

During sliding, the detachment of material from one or both the first bodies and subsequent removal from the sliding interface is termed as wear. Similar to friction, wear is not a material property and depends on the first bodies physical and chemical properties, normal load, ambient conditions, temperature etc. Researchers have classified wear based on the kinematics of tribo-pair into sliding, rolling, oscillating, impact and erosive wear. Alternatively, depending on the mechanism through which wear occurs, it is divided into abrasive, adhesive, corrosive, erosive, fatigue, fretting, oxidative, electrical contact and polishing wear [165,167,168]. To quantify the material removal over a period of time, i.e. to estimate the wear rate, Archard proposed a model which is commonly known as “Archard wear relationship”. According to this model, the volume of the material removed per unit sliding distance (Q) is directly proportional to the total normal load (W) and inversely proportional to the hardness (H) of the material [156].

$$Q = \frac{K.W}{H} \quad 2.9$$

In the above equation, K is a wear coefficient that is often used to understand the severity of the wear [156]. The main assumption of the above model is that wear debris are formed, plough the material and eject out completely of the sliding interface. However, the concept of wear debris

being re-circulated into the wear track, changing the localized chemistry or transfer to the counterface is completely neglected. This model is found true for many metal-on-metal sliding contacts macroscopically, later it was found that more complex physio-chemical phenomena occur at the sliding interface that change the friction and wear behaviour of the tribo-pair [169].

2.5.4 Tribological circuit

The mechanism of third bodies generation, mechanical mixing and their circulation at the tribo-pair interface have a significant influence on the friction and wear mechanisms. A tribological circuit showing the material flow at the tribo-pair interface is shown in Fig. 2.20 [159]. During sliding, the first bodies are in relative motion while the third bodies are generated in between the first bodies. First, the detachment of the material from the first bodies to form third bodies is termed as the source flow (Q_s) and the movement of the detached material at the sliding interface is known as internal flow (Q_i). The ejecting out of the material from the sliding interface is called ejection flow (Q_e) while the reintroduction of the ejected material into the interface is known as recirculation flow (Q_r). Lastly, the permanent removal of the material from the sliding interface is called wear flow (Q_w). During sliding, the tribological circuit gets activated due to the mechanical and physio-chemical actions like shearing, pressure, oxidation etc., between the first bodies. By applying the tribological circuit to metal or composite systems, the role of third bodies in modifying the friction and wear mechanisms can be analyzed. Furthermore, by using the tribological circuit new wear models [170,171] can be developed that consider the third bodies activities at the tribo-pair interface, and more accurate predictions of the tribological properties of the sliding system can be done.

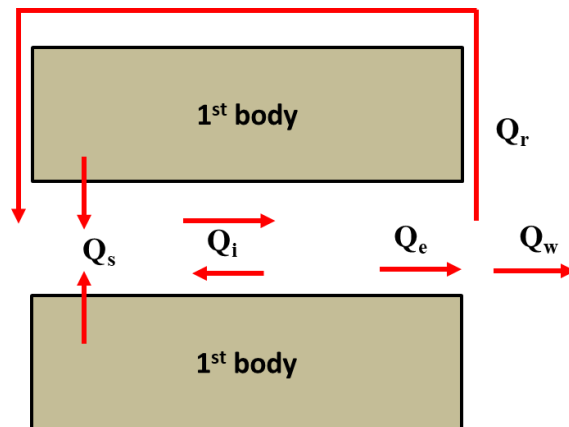


Fig. 2.20: Schematic of a tribological circuit [159].

2.5.5 Velocity accommodation modes (VAMs)

Third bodies generated at the tribo-pair interface have different chemical composition compared to that of first bodies or are of variable thickness through which they accommodate the velocity difference between the first two bodies [158,160]. Godet considered the third bodies mainly as wear debris (or particles) or a thin film of material (transferfilm or tribofilm) [158], however, Berthier *et al.* further classified them as bulk and screens [172]. A screen is an interface between the first and the third bodies that has a specific or different composition compared to first and third bodies and is a location for velocity accommodations between the first and third bodies. Berthier *et al.* illustrated that in case of dry sliding, the velocity between the two bodies can be accommodated by the third-bodies at five different sites i.e. $S_1 - S_5$ and four different modes per site through elastic deformation, fracture, shear and rolling, resulting in 20 different mechanisms as shown in Fig. 2.21. A change in VAMs may change the material flow inside the tribological circuit which in turn will influence the friction and wear behaviour of the sliding system. To summarize, third bodies physical and chemical processes such as thickening, loss of transfer film, generation of wear debris and sliding-induced chemical changes can modify wear rate and CoF depending on how they accommodate the velocity between the sliding bodies [161].

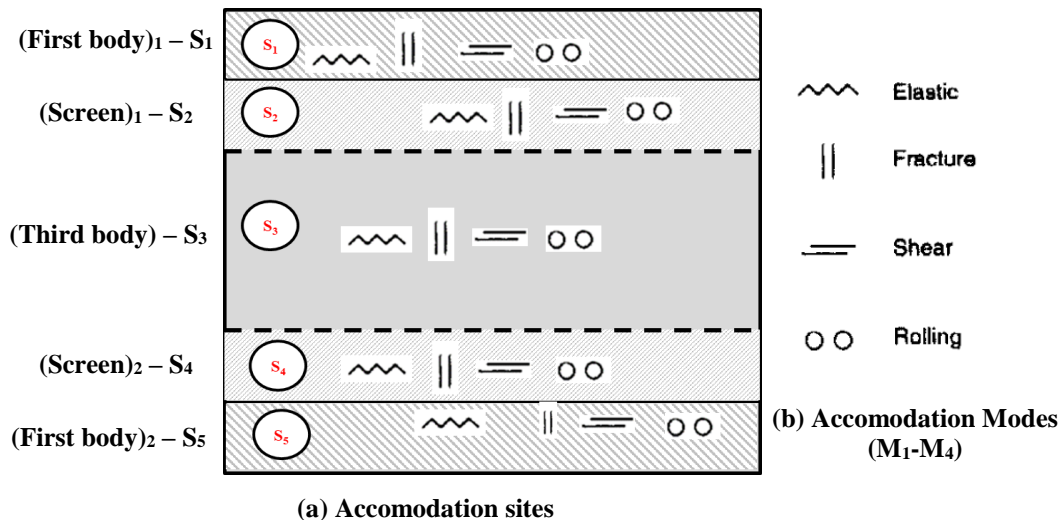


Fig. 2.21: Different velocity accommodation mode done by third bodies in sliding contacts [172].

2.6 Wear mechanisms

Wear mechanisms are broadly classified into mechanical, chemical and thermal wear depending on the type of damage [156,157]. When a material undergoes wear due to plastic deformation or by fracture it is termed as mechanical wear. Chemical reactions at the tribo-pair interface result in chemical film formation, and its degradation governs the rate of material loss from the first bodies. This type of wear is known as chemical or tribo-chemical wear. Wear governed by the localized surface melting due to frictional heating or high ambient temperatures is called thermal wear. Wear associated with mechanical damage can be further classified into abrasive, adhesive, erosive and fatigue wear [156].

Abrasive wear is characterized by material removal from the surface by hard particles that are forced to slide along with the counterface or are entrapped between the two sliding surfaces [156,157]. Adhesive wear occurs due to the shearing of localized bonded asperities, formed when two surfaces are in contact with each other [156]. The shearing of asperities sometimes results in the formation of wear debris which in turn leads to abrasive wear. Erosive wear or erosion is the surface damage caused due to the impact of hard particles that are generally carried by a gas or liquid. Fatigue wear occurs due to the cyclic loading and unloading experienced by the surface due to repeated sliding or rolling by the counterface [156,157]. In case of fatigue wear, cracks are initiated below the contact surface and propagate during repeated contact and stress cycles. In case of metal and MMC coatings, during dry sliding at both low and elevated temperatures, wear due to mechanical damage (i.e. abrasive and adhesive) and oxidation are predominantly observed [156,165]. This combination of wear mechanism and oxidation is termed as tribo-oxidative wear which will be discussed in the following section.

2.6.1 Tribo-oxidative wear

Oxidation during wear occurs due to the interaction of first bodies surface with the oxygen available in the ambient atmosphere. When two surfaces slide over each other, a combination of oxidation and wear occurs due to the fracture of asperity contact junctions and exposure of nascent surface to oxygen contained environments [156,165]. This results in the formation of an oxide layer on the surface which prevents the metal-to-metal contact ideally and reduces the friction and wear. However, the oxide layer formed is sometimes unstable due to its high or extremely low “Pilling-Bedworth ratio” (defined as the ratio of molar volume of the oxide to the molar volume

of the parent metal) [173,174] or is mechanically damaged due to repeated sliding of the countersurface. This leads to continuous exposure of freshly formed surfaces to oxidation, followed by film breakage and finally wear damage resulting in ‘tribo-oxidative wear’. Tribo-oxidative wear depends on the ambient and localized temperatures at the tribo-pair interface and is sub-divided into tribo-oxidative wear at “high” and “low” temperatures [165]. In general, ambient temperatures greater than room temperature (i.e. > 25°C) are referred as “high” temperatures where as room temperature is referred as “low” temperatures.

2.6.1.1 Tribo-oxidative wear at high temperatures

Tribo-oxidative wear at high temperatures occurs due to exposure of first bodies to high ambient temperatures or due to extremely high sliding speeds. These high temperatures readily lead to oxidation of the asperities. The oxide layer at the tip of the asperities grows until it reaches a critical thickness and spalls off as the sliding progresses. This results in the formation of wear debris and exposure of freshly formed surface to oxidation and so on. In such a scenario, wear rate depends on the rate of oxidation, critical oxide thickness and the contact area of the asperities. Quinn *et al.* proposed a mathematical model to calculate the wear rate (Q) by considering the factors responsible for tribo-oxidative wear for metallic contacts which is given by [165,175]:

$$Q = \frac{C \cdot k}{v \cdot Z_c} \cdot \frac{W}{H} = K_{ox} \cdot \frac{W}{H} \quad 2.10$$

In the above equation, C is constant that depends on the mass and density of the oxide formed, k is a parabolic rate constant calculated using the Arrhenius equation, v is the sliding velocity, Z_c is the critical oxide thickness where the spalling of the film occurs, W is the normal load, and H is the hardness. Based on the above equation and experimental results, increase in normal force increased the wear rate. However, at very high forces penetration of counterface through the oxide film occurred resulting in severe adhesive wear [156,165,176]. High sliding speeds lead to high surface heating and severe oxidation, resulting in the formation of a thick oxide film. This oxide film prevents metal-to-metal contact resulting in low wear rates. Lastly, high ambient temperatures prior to the onset on sliding led to the thermal softening of the surface material rather than oxidation resulting in adhesive wear and high wear rates. Apart from the above cases, the ability of the metal to re-oxidize also plays an important role in determining the wear rate. This mechanism is particularly important in case of reciprocating or rotary sliding contacts. During repeated sliding

the oxide film formed on the surface is partially or fully removed and the fresh surface is exposed to oxidation. In such a scenario, wear rate depends on the kinetics of oxide growth, temperature of the surface during the contact and non-contact time of the counterface [177]. Hence, high temperature tribo-oxidation is a complex mechanism which depends on the physical and chemical properties of the tribo-pair along with ambient operating conditions.

2.6.1.2 Tribo-oxidative wear at low temperatures

Tribo-oxidative wear at low-temperatures is generally found in metals when they undergo dry sliding at room temperatures and low sliding velocities [165]. At low ambient temperatures and sliding speeds, pre-oxidation of asperities does not occur prior to the start of sliding. A schematic illustrating the different steps involved in tribo-oxidative wear at low temperatures is shown in Fig. 2.18 [177]. Initially, when the two surfaces come into contact, asperity contact occurs due to adhesion (Fig. 2.22a) and subsequently, due to the onset of sliding, fracture of asperities result in the formation of metallic wear debris. The wear debris between the first bodies undergo strain-hardening, fracture, oxidation and agglomeration (Fig 2.22b). Oxidation of these wear debris occurs due to their surface exposure to atmospheric oxygen and due to the presence of high volume of surface defects. In some cases, during repetitive sliding, these oxidised wear debris plough the surface, during ejection, resulting in abrasive wear (Fig. 2.22c) or get entrapped between the first bodies and agglomerate to form a tribolayer (Fig. 2.22d). Since the tribolayers are agglomerated oxide particles, they generally possess higher hardness compared to the base metal and also have higher load bearing capacity. These hard tribolayers resist plastic deformation, prevent abrasive wear and decrease the wear rate. If the formed tribolayer is adherent and stable, low wear rate will be observed whereas if the tribolayer reaches a critical thickness or is brittle, significant cracking (Fig. 2.22e) can occur resulting in the formation of new wear debris that can further accelerate the wear process.

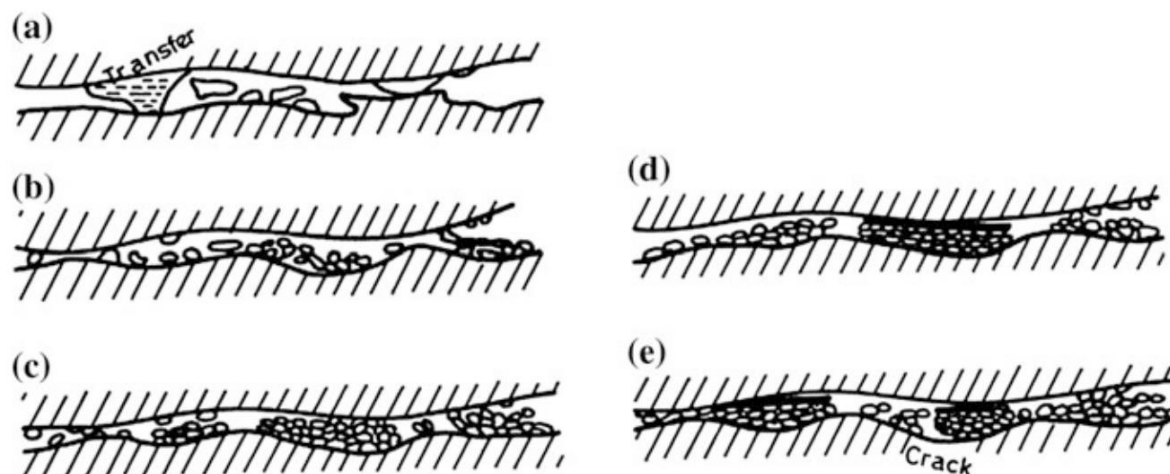


Fig. 2.22: Schematic showing the different steps that occur in tribo-oxidative wear at low temperatures [177].

Studies from literature have shown that the formation of tribolayers due to compaction of wear debris can occur both at low and high temperatures. However, their stability increases with increase in temperature and hence, lower wear rates are often observed at elevated temperatures. The improvement in tribological properties depends on both physical and chemical properties of the tribo-oxides formed at the sliding interface. Previously, Erdimer *et al.* illustrated that oxides with high ionic potentials (defined as the ratio of charge to radius of the cation) lead to greater the screening of the cations by anions [178]. This prevents the additional reactivity of the cations with other anions at the sliding interface and decreases adhesion and subsequently, friction. The CoF for different oxides and their respective ionic potential is shown in Fig. 2.23. In case of formation of two or more oxide phases at the sliding interface, the greater the differences between their ionic potentials, more stable compounds are formed which lowers the adhesion of the tribo-oxides with the counterface material and decreases the friction [179]. However, the decrease in friction due to formation of multiple oxide phases was found to be more effective at elevated temperatures compared to room temperatures. Lastly, higher CoF between the tribo-pair leads to higher magnitude of sub-surface stresses compared to lower friction [180]. This results in greater amount of subsurface deformation and can lead to the fragmentation of the tribolayer or reduce its load-bearing capacity and increase the wear rates.

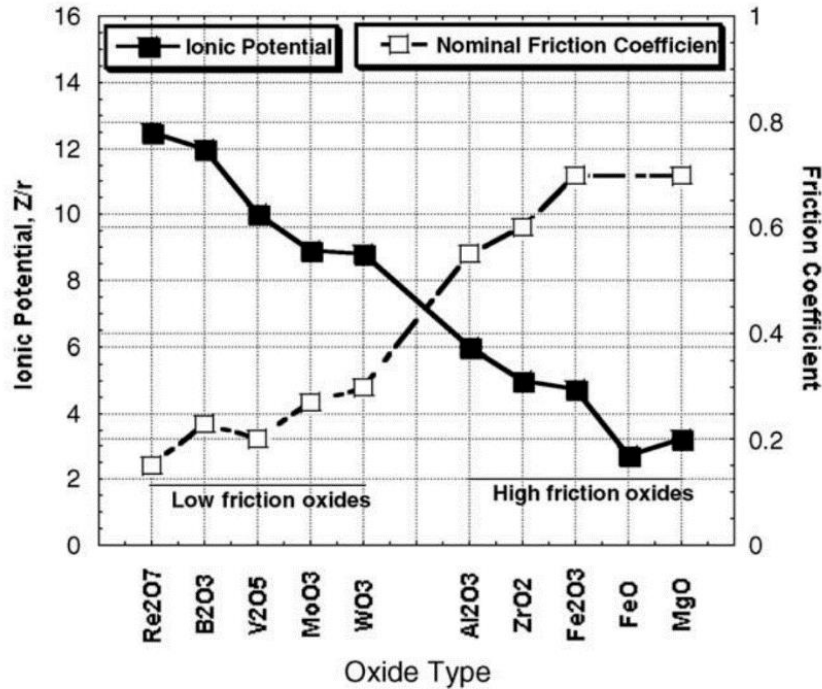


Fig. 2.23: Relation between ionic potential and coefficient of friction in different oxides [178].

2.7 Tribology of TiC reinforced MMCs

TiC as a reinforcing phase in steel, Fe, Al, Co, Ti, Ti6Al4V matrix is being extensively used due to its high hardness, low density and high temperature thermal stability [36,40,181–185]. Candel *et al.* deposited Ti based MMCs with TiC as reinforcement using laser cladding and performed sliding wear tests to evaluate their tribological properties [40]. The high heat involved in laser cladding led to the partial melting of TiC particles and formation of a heat effected zone with poor mechanical properties at the coating-substrate interface. Sliding wear test results showed that reinforcement of 30 vol.% of TiC in the matrix did not lower the wear rate in MMCs compared to unreinforced alloy, where as increase in TiC reinforcement to 60 vol.% significantly decreased the wear rate. The decrease was due to the formation of tribofilm comprising of TiC fragments and oxides of Ti that got sintered on the wear track during wear and prevented the exposure of subsurface metal. In the case of cold sprayed Ti-TiC MMC coatings deposited by Alidokht *et al.*, no phase transformations or formation of brittle phases were observed due to the ability of CS to deposit particles in solid state [36]. Sliding wear test results showed that reinforcing ~ 13.8 vol.% TiC significantly reduced the wear rates of MMC compared to unreinforced Ti. In case of Ti coatings, adhesive wear and abrasive ploughing by the wear debris resulted in high wear rates.

Contrarily, the formation of tribolayers comprising of TiO_2 and fragmented TiC particles resisted the localized shear deformation and abrasive ploughing by the wear debris resulting in lower wear rates. In addition, the TiC particles in the feedstock had free carbon at the dendritic boundaries and due to solid state deposition in CS, the reinforced TiC particles in the coating had retained free carbon. This led to lubricating effect during wear process and resulted in a significant drop in CoF. Furthermore, higher volume fractions of ceramic reinforcement in the matrix led to early formation of tribolayers and resulted in much lower wear rates and early friction drop.

In CS process, interaction time of the powder particles with the hot gas stream is less i.e. in the order of few microseconds, due to which particle temperature is well below the melting point of the material. This provides the advantage of using CS to deposit nanostructured metal and composite coatings without changing their microstructure due to thermal effects [186–188]. Kusinski *et al.* cold sprayed Ti-TiC MMCs using nanostructured powders of different compositions and evaluated their tribological properties [188]. They observed that the use of CS preserved the nanostructure of the material from powders to the coatings. To evaluate the tribological properties, Taber abrasion tests were performed on the composite coatings and were compared to steel and CoCr alloy. They found that the composite coatings exhibited lower weight loss after the tests compared to steel and CoCr samples. The higher wear resistance of composite coatings was attributed to both, the presence of ceramic particles and also to the nanostructure of the matrix that contributed to their higher hardness and resisted plastic deformation during wear.

Very few studies from literature have investigated the tribology of cold sprayed TiC reinforced MMCs. However, other thermal spraying techniques like HVOF and plasma spraying were largely used to fabricate TiC reinforced MMC coatings for tribological applications [127]. Ghazanfari *et al.* deposited Fe_3Al coatings and Fe_3Al -TiC composite coatings with different TiC contents using HVOF process and studied their sliding wear behaviour [182]. Due to the high heat involved in HVOF process, both metal and composite coatings showed the formation of oxides mostly at the splat boundaries. Wear test results showed that the composite coatings exhibited lower wear rates compared to unreinforced Fe_3Al alloy. The low wear of composite coatings was due to the presence of TiC particles that increased the hardness and facilitated the formation of oxide rich tribolayers that transformed the wear mechanisms from delamination to mild oxidative wear. Furthermore, increasing TiC content from 30 mol.% to 50 mol.% improved the wear resistance by 75% and with

further increase to 70 mol.%, wear rate decreased by an order of magnitude. The improvement in wear resistance with increase in TiC content, was both due to the increase in hardness and also to the lower mean free path between the TiC particles in MMCs at higher ceramic retentions (i.e. 50 – 70 mol.%). Lower mean free path between the ceramic particles, improved the load bearing capacity and prevented abrasive ploughing by the asperities and counterface resulting in low wear rates.

Studies from literature show that apart from TiC content, other factors like normal load, sliding velocity, temperature, ambient atmosphere significantly influence the friction and wear mechanisms [183,184,189]. These conditions essentially change the physical, chemical and mechanical properties of the third bodies formed at the sliding interface and improve or degrade the tribological performance of the MMC. Rasool *et al.* performed sliding wear tests at different loads and sliding velocities on TiC based composite coatings deposited using Tungsten Inert Gas (TiG) welding torch melting process [184]. Based on the results obtained in various test conditions, they developed wear maps showing different wear regimes and mechanisms (as shown in Fig. 2.24). Their studies illustrated that at different normal loads and sliding velocities, the wear mechanisms in composite coatings were controlled by contact stresses, temperature and oxidation phenomena. Wear maps showed that composite coatings exhibited mild and medium wear, characterized by abrasive and oxidative wear mechanisms at a different test conditions (shown in Fig. 2.24). They concluded that the presence of TiC particles in the matrix improved the hardness of the coatings that led to mild wear at low loads and sliding velocities, whereas at higher loads, tribo-oxidation played a more significant role in reducing the wear rates.

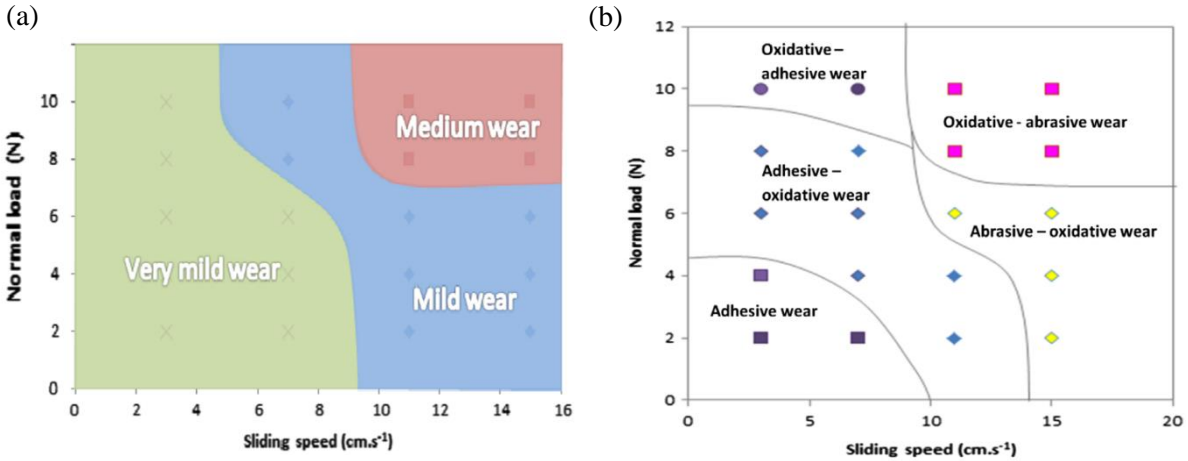


Fig. 2.24: (a) Different wear regimes and (b) corresponding wear mechanisms in TiC based composite coating [184].

2.8 Summary of literature review

CS is a feasible and versatile thermal spray process used to additively manufacture and repair parts made of Ti and its alloys. However, cold sprayed Ti6Al4V deposits show significant porosity due to low deformability of the powder particles when sprayed using nitrogen. The porosity and deposition efficiency of Ti6Al4V coatings reported by various researchers is summarized in Table 2.2. From Table 2.2, it is clear that deposition of dense Ti6Al4V (porosity < 2%) coatings using nitrogen (propellant gas) with no additional powder pre-processing, is yet to be achieved. While coatings with low porosity were deposited using helium or by mechanically blending metal powders with hard or deformable particles, these methods either involve high costs or result in impurities in the coatings. Thus, there is a need to explore alternate techniques to deposit dense Ti6Al4V coatings with good deposition efficiency and better sustainability.

Table 2.2. Porosity and deposition efficiency of Ti6Al4V coatings reported in the literature.

Researcher	Propellant gas	Porosity (%)	Deposition efficiency (%)	Feedstock
Vo <i>et al.</i> [13]	N ₂	5.0 – 12.0 %	---	Ti6Al4V
	He	< 1.0 %	---	Ti6Al4V
Aydin <i>et al.</i> [15]	N ₂	6.7 %	---	Ti6Al4V
	N ₂	6.5 %	---	Ti6Al4V + 5% Ti
	N ₂	1.5 %	---	Ti6Al4V + 10% Ti
Bhattiprolu <i>et al.</i> [17]	He	1.0 %	---	Ti6Al4V (Plasma gas atomized powders)
	He	2.0 %	---	Ti6Al4V (Gas atomized powders)
	He	2.0 %	---	Ti6Al4V (Hydride de-hydride powders)
Luo <i>et al.</i> [20]	He	2.7 %	83.7 %	Ti6Al4V
	N ₂	15.3 %	81.0 %	Ti6Al4V
	N ₂	12.0 %	76.5 %	Ti6Al4V + 10vol.% Steel particles
	N ₂	5.0 %	75.0 %	Ti6Al4V + 30vol.% Steel particles
	N ₂	2.5 %	72.0 %	Ti6Al4V + 50vol.% Steel particles
	N ₂	0.7 %	67.0 %	Ti6Al4V + 70vol.% Steel particles
Birt <i>et al.</i> [18]	N ₂	11.3 ± 6.5 %	---	Ti6Al4V
	He + N ₂	2.1 ± 4.1 %	---	Ti6Al4V
Tan <i>et al.</i> [111]	N ₂	5 %	---	Ti6Al4V
Zhou <i>et al.</i> [190]	N ₂	3% - 13%	---	Ti6Al4V
Li <i>et al.</i> [71]	Compressed air	22.3 ± 4.7 %	60.0 %	Ti6Al4V

Hard particles are reinforced in the metallic matrix to improve their mechanical and tribological properties. During sliding, the exposure of reinforced hard particles to the sliding interface, their fragmentation, and mechanical mixing of material result in the formation of third bodies.

Tribological studies from literature show that the physical, chemical and mechanical properties of the third bodies formed at the tribo-pair interface control the friction and wear mechanisms rather than the bulk properties of first bodies alone. Hence, a careful examination of the role of third bodies in modifying the friction and wear mechanism in hard particle reinforced MMCs is necessary. Furthermore, deposition of MMCs with TiC as reinforcement in a Ti alloy matrix using CS process is yet not been explored. Unlike other thermal spray processes, CS has an inherent advantage to deposit powders in solid state which prevents phase transformations and oxidation. However, there are several challenges involved in the CS deposition of MMCs in terms of achieving higher retentions, lower porosity, better sustainability, cost effectiveness, and good deposition efficiency. Thus, a comprehensive study that explores both, the cold spray of Ti6Al4V-TiC MMCs and their tribology at different test conditions and ambient temperatures is required.

Chapter 3

Experimental procedure

3.1 Cold spray of coatings

3.1.1 Feedstock powders

Metal and composite coatings were deposited using Ti6Al4V powders of spherical and irregular morphologies and TiC powders of spherical morphology. The spherical Ti6Al4V powders (Grade 5) (AP&C, Canada) were manufactured using plasma gas atomization process whereas the irregular powders (Cristal metals, USA) were manufactured using Armstrong process. The TiC powders (Tekna, Canada) were manufactured using gas atomization process. The surface morphologies of the powders (both Ti6Al4V and TiC) were characterized using a scanning electron microscope (SU3500, Hitachi, Japan) and are shown in Fig. 3.1. The powder size distribution was determined using a laser particle size distribution analyzer (LPA-920, Horiba, Japan). The characteristics of the powders are summarized in Table 3.1.

Table 3.1 Characteristics of feedstock powder used in the present thesis.

Powder	Morphology	Size distribution (μm)	D ₁₀ (μm)	D ₅₀ (μm)	Chapters
Ti6Al4V	Spherical	15 – 45	18	32	4-5-6-7-8
Ti6Al4V	Irregular	0 – 45	12	30	4-5-6-7-8
TiC	Spherical	15 – 45	26	40	7-8

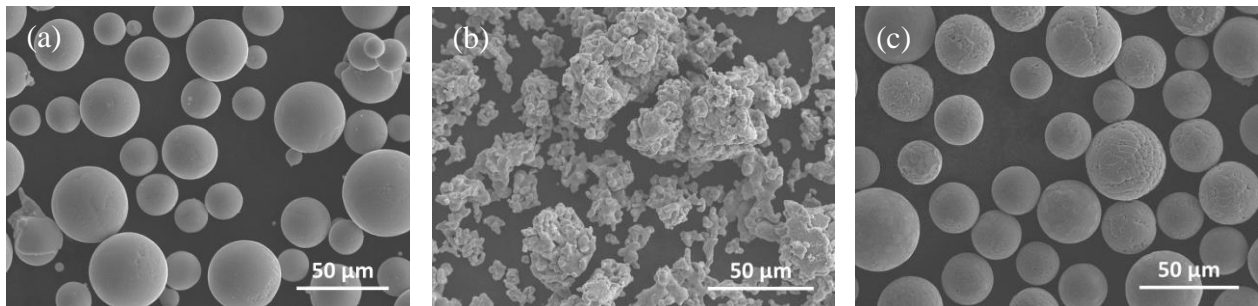


Fig. 3.1: SEM showing surface morphology of (a) spherical Ti6Al4V powders (b) irregular Ti6Al4V powders (c) TiC powders.

3.1.2 Cold spray deposition

Coatings were deposited at McGill Aerospace Materials and Alloy Design Center (MAMADC) located at NRC-CNRC Boucherville using commercially available PCS 800 and PCS 1000 (Plasma Giken system, Japan) cold spray systems. For the work in chapters 4, 6, 7 and 8, the coatings were deposited on mild steel plates of dimensions 75 x 75 x 3 mm³ using nitrogen as propellant gas. Prior to deposition the propellant gas was pressurized to 4.0 MPa and preheated to a temperature of 800°C. The cold spray test rig had a dual feeder setup provided by the manufacturer (Plasma Giken) which enabled to simultaneously inject two different powders into the mixing chamber at the inlet of the nozzle. The dual feeder setup had two hoppers with a flowmeter attached to one of the hoppers. First, the TiC powder was fed into the hopper with flowmeter, and the mass flow rate of the powder corresponding to the different feeder settings was recorded. Subsequently, the TiC powder was transferred into the other hopper (without flowmeter) and the Ti6Al4V powder was fed into the hopper with flowmeter. The mass flow rate of Ti6Al4V powder was recorded for different feeder settings. During spraying, using the feeder settings data, the mass flow rate of the powders was individually adjusted to obtain (approximately) the required metal-ceramic mixture for the deposition of composite coatings. However, to deposit Ti6Al4V coatings, the TiC powder hopper was turned off thereby allowing the flow of only Ti6Al4V powder. By using a dual feeding system, the difficulties involved in mechanical blending of powders with different densities were avoided. Before spraying, the substrates were de-greased, and grit blasted using 24 grit alumina particles to enhance the bonding between the substrate and coating. A de Laval nozzle made of WC-Co was used for all coating depositions. The nozzle was mounted on a robotic arm and the entire system was controlled using a computer console. To deposit Ti6Al4V and Ti6Al4V-TiC coatings (in Chapters 4, 6, 7 and 8), the standoff distance between the nozzle and the substrate was 40 mm and the gun traverse speed was 200 mm.s⁻¹. Deposition efficiency (DE) of the process was calculated by determining the ratio of the weight of the powder deposited (W_d) to the total weight of the powder sprayed (W_s). The equations used to calculate the weight of the powder deposited, and weight of the powder sprayed are shown below:

$$W_d = \text{Weight of the sample (after deposition)} - \text{Weight of the substrate} \quad 3.1$$

$$W_s = \frac{\text{Powder feedrate} \times \text{Distance travelled by the gun on the sample}}{\text{Gun traverse speed}} \quad 3.2$$

For the work performed in chapter 5, single splats of Ti6Al4V were deposited using spherical and irregular powders on commercially available Ti6Al4V plates (McMaster Carr, Canada) of dimensions 25 x 25 x 3 mm³. The splats were deposited using nitrogen as propellant gas that had an inlet pressure of 4.9 MPa and temperature between 650°C – 950°C. A specialized long nozzle was used to deposit particles at much higher velocities and at lower inlet temperatures compared to a conventional nozzle. The stand off distance between the nozzle and the substrate was 40 mm while the gun traverse speed was 1 m.s⁻¹. A high gun traverse speed was chosen to deposit single splats at a considerably far away distance from each other.

During the deposition process the particle velocity was measured using a commercially available Cold-SprayMeter system (Tecnar automation, Canada). The system consists of a monochromatic laser source along with a fiber optic sensing head that is aligned in perpendicular to the cold spray particle jet and mounted on a stage as shown in Fig. 3.2 [191]. The optical sensing head is equipped with two slit photomask, which is oriented in such a way that as the particle passes each slit, a light signal peak is generated due to the laser illumination. This results in a double peak signal at different time intervals by each particle. The distance between the double peaks is the time-of-flight and the distance between the slits is known. Using the above two values the velocity of the particle is determined. For each spray condition, 2000 particles were measured to plot the velocity distribution and to determine the average particle velocity.

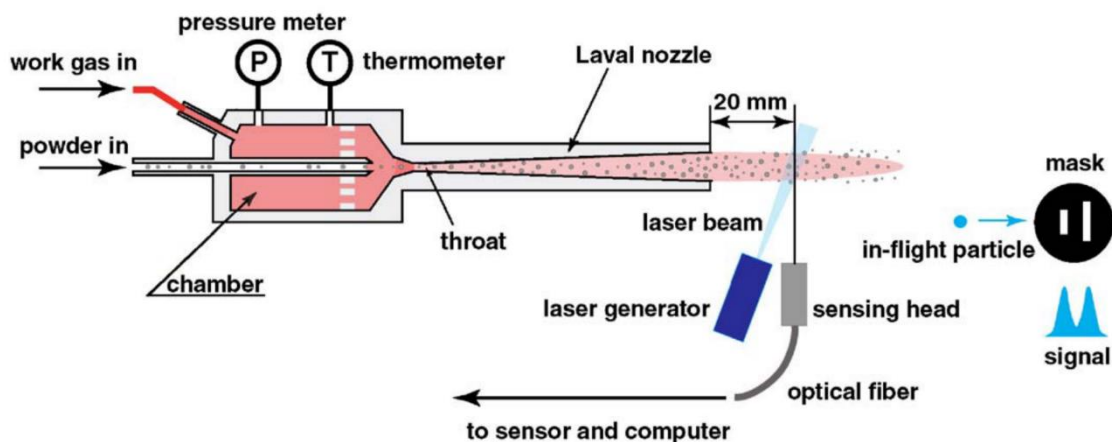


Fig. 3.2: Schematic of the cold-spray meter setup used to measure velocity of the particles at different spray conditions in the present study [191].

3.1.3 Selection of spray conditions for Ti6Al4V and Ti6Al4V-TiC composite coatings

Studies from literature reveal that CS deposition of Ti6Al4V using nitrogen as propellant gas remains challenging due to its high yield strength that limits particle deformation upon impact resulting in porosity and poor interparticle bonding [13,15]. Furthermore, the deposition of Ti based MMC coatings using Ti6Al4V as matrix is not yet explored. Also, during the deposition of MMCs using CS, ceramic particle rebound, their non-bonding nature and fragmentation act as major limitations in terms of achieving higher retentions along with good DE [74,154,155]. Hence, to deposit Ti6Al4V coatings and Ti6Al4V-TiC MMC coatings four important research questions were required to be answered: 1. What is the influence of inlet gas temperature on the porosity and DE of Ti6Al4V? 2. Can we use a high yield strength material like Ti6Al4V as a matrix to fabricate MMCs through CS process? 3. Does an increase in inlet gas temperature and pressure lead to improvement in ceramic retention? 4. Does the reinforcement of ceramic particles help to improve the coating properties?

To answer these research questions, Ti6Al4V coatings and Ti6Al4V- 20 vol.% TiC composite coatings were deposited on mild steel substrates using N₂ at gas pressures 3 – 4 MPa and temperatures 600 – 800°C. The feed rate was 20 g.min⁻¹ and the gun traverse speed was 200 mm.s⁻¹. The DE of the process was calculated and after deposition, coatings were cross-sectioned, polished and examined under a SEM (SU3500, Hitachi, Japan). The detailed procedure involved in the sample preparation (cutting, mounting and polishing) for characterization is illustrated in section 3.2.1. The results of the above experiments are presented here to understand the spray parameters optimization, and selection procedure adopted in the present thesis for further study (chapters 4, 6,7 and 8). BSE images of the coating cross-sections were taken at different locations (shown in Fig. 3.3) and were imported into ImageJ software (National Institutes of Health, USA) [192] to determine the porosity percentage and ceramic content. The properties of the coatings deposited at different gas pressures and temperatures are shown in Fig. 3.4. Ti6Al4V coatings exhibited significant amount of porosity at all spray conditions due to non-deformability of the particles. However, an increase in gas temperature led to a decrease in porosity of the coatings. It is known from literature that increase in inlet gas temperature increases the particle velocity [117]. The increase in particle velocity led to an increase in particle deformation and decreased the porosity in the coatings. Furthermore, Ti6Al4V-TiC composite coatings exhibited lower porosity

compare to Ti6Al4V coatings which was due to the peening action of the ceramic particles that led to the coating densification (as seen in Fig. 3.4b). The ceramic retention in the composite coatings was significantly less than the initial feedstock. The loss in ceramic particles could be due to rebound and their fragmentation upon impact. However, an increase in gas pressure and temperature increased the ceramic retentions and reduced the porosity in the composite coatings. The increase in ceramic retention at higher gas pressure and temperatures could be due to greater particle velocity that might have led to higher embedding of ceramic particles into the matrix or due to improve in cold sprayability of the matrix that results in greater entrapment of ceramic particles by metal particles. Nevertheless, since higher gas temperatures and pressures improved the overall properties of the coatings the highest possible spray conditions (i.e. gas pressures and temperatures) were used to deposit both metal and composite coatings. However, the feed rate was increased to deposit thick coatings for tribology tests and to avoid substrate effects during indentation at high loads.

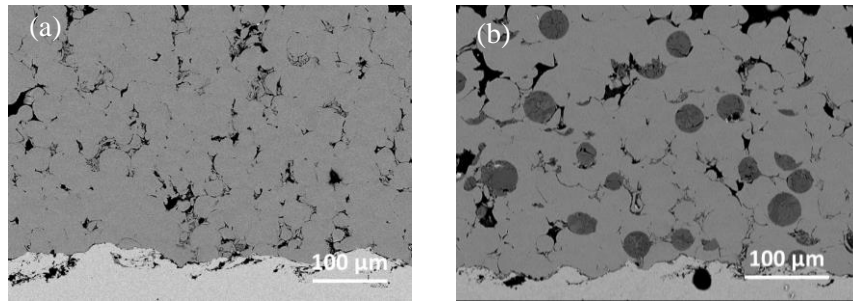


Fig. 3.3: SEM images of the (a) Ti6Al4V and (b) Ti6Al4V- TiC coatings deposited at 4 MPa – 800°C.

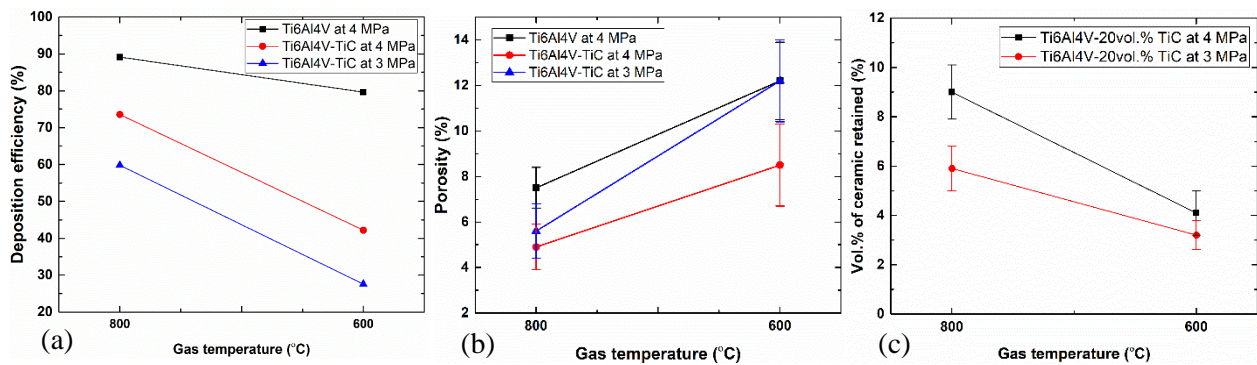


Fig. 3.4: Shows the (a) deposition efficiency (b) porosity and (c) ceramic retention in Ti6Al4V and Ti6Al4V-TiC MMCs deposited using different spray conditions.

For the above experiments, higher particle velocities must be achieved to improve the coating properties like porosity, ceramic retention and DE. Methods to improve particle velocities include spraying with helium or using higher inlet gas pressures and temperatures. However, these techniques are either non-sustainable, uneconomical or have operational difficulties. Also, using higher inlet gas temperatures might result in nozzle clogging, excessive heating of the substrate or lead to equipment damage. Alternatively, literature studies have shown that irregular morphology of the particles accelerates them to higher velocities compared to spherical particles in a gas stream due to higher drag force [97]. Also, presence of porosity in the particles is beneficial during deposition as it reduces the probability of rebound. Recently, irregular porous powders of Ti and its alloys were manufactured using Armstrong process [193]. As a part of an initial study in the present thesis, these powders of different size ranges 0 – 45 μm , 0 – 75 μm , 0 – 150 μm were evaluated to deposit Ti6Al4V and Ti6Al4V-35vol.% TiC composite coatings. The feed rate was 20 $\text{g}\cdot\text{min}^{-1}$ and the gun traverse speed was 200 $\text{mm}\cdot\text{s}^{-1}$. The SEM images of the metal and composite coatings are shown in Fig. 3.5 and the DE, porosity and ceramic retention are summarized in Table 3.2. In case of Ti6Al4V coatings, all the three size ranges led to the deposition of dense coatings with similar deposition efficiencies. However, addition of ceramic particles decreased the DE of the composite coatings due to their non-bonding nature. In case of composite coatings, all the three size ranges resulted in similar deposition efficiencies and porosity levels, however, the ceramic retention was higher in coatings deposited using finer size range powder (0 – 45 μm). Hence, this particular size range of Armstrong powders was selected in the thesis along with spherical Ti6Al4V powders to deposit metal and composite coatings. A summary of spray parameters used for the deposition of all the coatings in the present thesis are tabulated in Table 3.3.

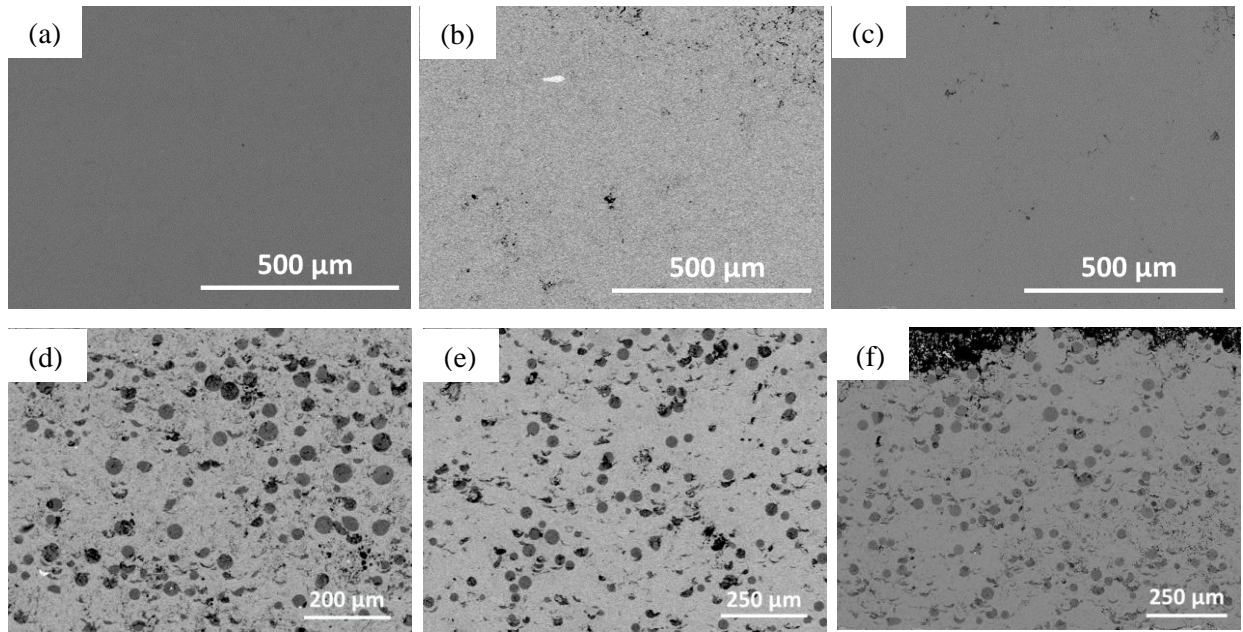


Fig. 3.5: SEM images of Ti6Al4V coatings deposited using irregular powders of size range (a) 0 – 45 μm (b) 0 – 75 μm (c) 0 – 150 μm ; Ti6Al4V-TiC coatings deposited using irregular powders of size range (d) 0 – 45 μm (e) 0 – 75 μm (f) 0 – 150 μm .

Table 3.2 Characteristics of the coatings deposited using irregular powders.

Coating	Porosity (%)	Deposition efficiency (%)	Ceramic retention (vol.%)
Ti6Al4V (0 – 45 μm)	< 1.0	90	---
Ti6Al4V (0 – 75 μm)	< 1.0	93	---
Ti6Al4V (0 – 150 μm)	< 1.0	93	---
Ti6Al4V-TiC (0 – 45 μm)	1.2 ± 0.4	72	16 ± 1.0
Ti6Al4V-TiC (0 – 75 μm)	1.2 ± 0.7	69	14 ± 0.6
Ti6Al4V-TiC (0 – 150 μm)	1.3 ± 0.5	70	12 ± 1.0

Table 3.3 Spray conditions used to deposit coatings and single splats in the present thesis.

Sample	Ti6Al4V morph- -ology	Ti6Al4V in the feedstock (vol.%)	TiC in the feedstock (vol.%)	Gas pressure and temperature	Gun traverse speed (mm.s ⁻¹)	Standoff distance (mm)	Feed rate (g/min)
Ti6Al4V coatings (Ch. 4, 6, 7)	Spherical	100	0	4 MPa – 800°C	200	40	32
Ti6Al4V coatings (Ch. 4, 6, 7, 8)	Irregular	100	0	4 MPa – 800°C	200	40	20
Ti6Al4V splats (Ch. 5)	Spherical	100	0	4.9 MPa – 950°C	1000	40	1 – 2
Ti6Al4V splats (Ch. 5)	Irregular	100	0	4.9 MPa – 600-950°C	1000	40	1 – 2
Ti6Al4V- TiC (Ch. 7)	Spherical	65	35	4 MPa – 800°C	200	40	32
Ti6Al4V- TiC (Ch. 7)	Spherical	50	50	4 MPa – 800°C	200	40	32
Ti6Al4V- TiC (Ch. 7)	Irregular	65	35	4 MPa – 800°C	200	40	20
Ti6Al4V- TiC (Ch. 7, 8)	Irregular	50	50	4 MPa – 800°C	200	40	20

3.2 Coating characterization

3.2.1 Microstructural characterization of the coatings and single splats

To observe the microstructure after deposition, the coatings were cut using a high-speed abrasive cutting saw (Buehler, USA) and then cold mounted using a conductive epoxy (containing copper filler) mixed with a hardener. The cold mounted samples were mechanically polished using SiC abrasive papers of grits 240, 320, 400, 600, 800, 1200 and subsequently using 9 μm , 3 μm and 1 μm polycrystalline diamond suspension solutions. As a final step the samples were polished using a vibrometer filled with 0.05 μm colloidal silica suspension for ~4 h. The feedstock powders cross-

sections were also polished in a similar way but a 10 ml of dil. H₂O₂ was added to colloidal silica suspension solution and manually polished rather than using a vibrometer. The polished coating cross-sections were examined in a scanning electron microscope (SU3500) equipped with a back scattered electron (BSE) and energy dispersive X-ray spectroscopy (EDS) detectors. The accelerating voltage was 10 – 15 keV, and the working distance was between 10 – 15 mm. BSE images of the coatings were taken at 10 different locations across the samples at similar magnifications. These images were uploaded into ImageJ software and the pixels associated with different contrasts were determined to calculate the area fractions of porosity and ceramic particles. In a BSE image the grey contrast represented the ceramic particles while the porosity appeared dark. The area fractions determined from different images were averaged to calculate the final average values and were considered as volume percentages. To characterize the microstructure at much finer length scales i.e. to observe the presence of highly deformed microstructures, ultrafine grains etc., ECCI [11,24] was performed on the powder and coating cross-sections using a cold field emission SEM (SU8230, Hitachi Japan).

For the work performed in chapter 5, to characterise the microstructure, single splats deposited on Ti6Al4V substrates were cut in perpendicular to the gun traverse direction using a low-speed cutting saw fitted with a diamond blade. The splat cross-sections were mechanically polished in eight pattern using 600, 800, 1000 and 1200 grit abrasive papers and subsequently using polycrystalline diamond suspension solution of 9 µm, 3 µm and 1 µm. As a final step, the specimens were polished with colloidal silica suspension of 0.05 µm mixed with 10 ml of dil. H₂O₂ solution. The eight pattern was used during mechanical polishing of the splats to avoid the edge rounding effect generally obtained at the specimen ends. To further eliminate the polishing artifacts, the samples were ion-milled using a IM300 flat milling system (Hitachi High-Technologies, Japan). ECCI of the splat cross-sections were performed using a cold field emission SEM (SU8230, Hitachi, Japan) to observe the microstructural evolution in the splats due to CS process.

3.2.2 Microhardness testing

For the work performed in chapter 4, the microhardness of the metal coatings was determined using a Vickers diamond indenter (Clark Microhardness tester, USA). Microhardness tests were performed on the polished cross-sections of the Ti6Al4V coatings and bulk Ti6Al4V plate at

different loads within a range of 25 g – 500 g and holding time of 15 s. After performing each indent, the optical image of the residual indent impression was captured at 500x magnification using an optical microscope attached to the hardness tester for subsequent analysis. At least ten indents were done and averaged, to determine the average microhardness at each load. Indentation was performed such that the distance between any two indents was at least greater than five times the length of the diagonal of the previous indent. The Vickers hardness (VH) was converted into H_{micro} (GPa) using a conversion from surface area to projected area using the equation below [119]:

$$H_{\text{micro}} \text{ (GPa)} = \frac{VH \times 9.8 \text{ m/s}^2}{1000 \times \sin 68^\circ} \quad 3.3$$

For the work performed in chapters 6, 7 and 8, the microhardness tests were done on the polished coating top surface using a Vickers microhardness tester (Buehler, USA) at 5 kg load and 15 s holding time. Indentation was done at random locations to avoid strain hardening and ceramic fracture that occur during indentation of the previous trail affecting the subsequent measurements. A high indentation load was chosen to have the indenter interact with both reinforced carbide particles and matrix material. An average of at least ten indents was done to calculate the average microhardness. For all the coatings tested, the thickness was at least ten times the indentation depth.

3.3 Splat adhesion testing

Splat adhesion testing was performed using a Micro-Combi Scratch Tester (CSM Instruments, USA) to determine the adhesion strength of the single splats. The scratch tester was equipped with a semi-circular tipped stylus of diameter 100 μm and the flat edge of the stylus was used to scratch the splats off the substrates as shown in Fig. 3.6. Prior to the testing, the optical image of the splat was captured using an optical microscope attached to the scratch tester to determine the projected area of the splat. To perform the splat adhesion test, the stylus was placed at a distance of $\sim 40 - 50 \mu\text{m}$ before the splat and was moved at a speed of $150 \mu\text{m}\cdot\text{min}^{-1}$. A normal force of 100 mN was applied on the stylus. The tangential force experienced by the stylus was recorded continuously during the test using the software provided by the manufacturer. As the stylus touched the splat, a sharp rise in tangential force ($F_{\text{T Peak}}$) was recorded followed by a sudden drop ($F_{\text{T Baseline}}$) due to splat failure. This data combined with the area of the splat was used to calculate the adhesion strength of the splats using the equation below [116] :

$$\text{Adhesion strength (MPa)} = \frac{F_{T \text{ Peak}}(\text{mN}) - F_{T \text{ Baseline}}(\text{mN})}{\text{Projected area of the splat } (\mu\text{m}^2)} \quad 3.4$$

Splats selected for performing the adhesion tests had an initial particle diameter of $\sim 30 \pm 5 \mu\text{m}$ in case of spherical powder splats and $\sim 40 \pm 5 \mu\text{m}$ for irregular powder splats, which was close to the that of the average particle size determined using the LPA. Also, the splats deposited at the middle of the spray path were considered for performing the tests to maintain the consistency with respect to the impact velocity for a particular spray condition. At least 15 splats were tested for each spray condition to determine the average adhesion strength.

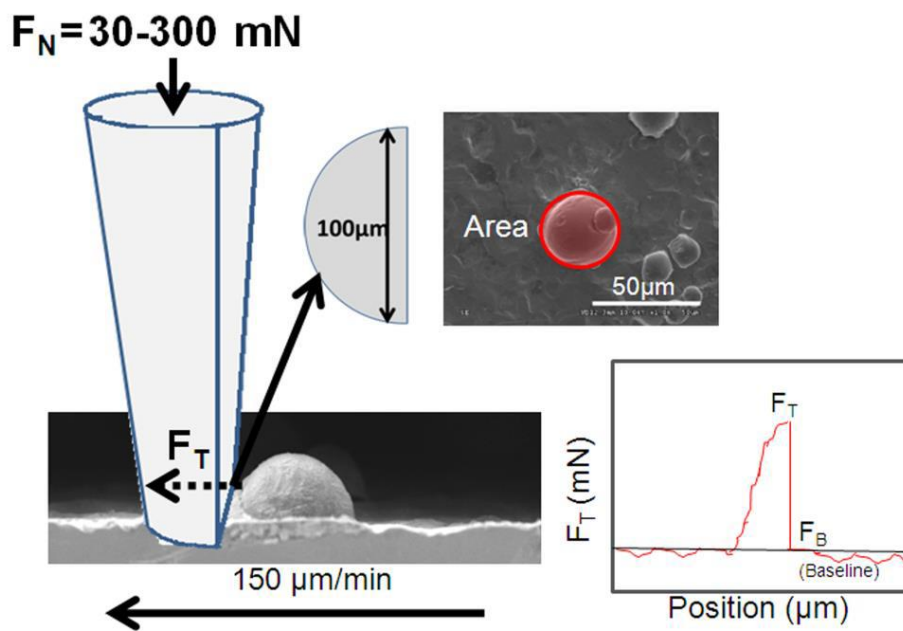


Fig. 3.6: Schematic of splat adhesion testing showing the tip shearing the splat and the corresponding force-displacement curve [117].

3.4 Sliding wear tests

3.4.1 Wear test setup

For the work in chapter 6 and 7, sliding wear tests were performed on polished coating-top surfaces using a custom-built linear reciprocating ball-on flat tribometer. The required normal load for each test was applied by placing dead weights on the loading arm of the tribometer. The reciprocating sliding speed for all the tests was $3 \text{ mm}\cdot\text{s}^{-1}$ and was provided by a motorized stage on which the

sample was mounted. The track length for all the tests was 5 mm and the total sliding distance was 10 m respectively. WC-Co spherical balls (McMaster Carr, USA) of diameter 6.35 mm were used as counterface. The counterface was tightly secured in the ball holder which was fixed to the cantilever arm as shown in Fig. 3.7 [161]. The tribometer arm with the counterface and the specimen were enclosed in a high-density polyethylene enclosure (HDPE) that was equipped with a thermohygrometer to continuously monitor the humidity. Wear tests were performed in a dry air environment (relative humidity < 2%) at 25°C. During the test, the frictional force was continuously measured using a piezoelectric sensor that was present underneath the sample holding stage, at a sampling rate between 800 Hz and 2800 Hz. The normal loads used for performing the sliding wear tests in chapter 6 were 0.5 N, 2.5 N and 5 N, while in Chapter 7 the normal loads were 0.5 N and 2.5 N respectively.

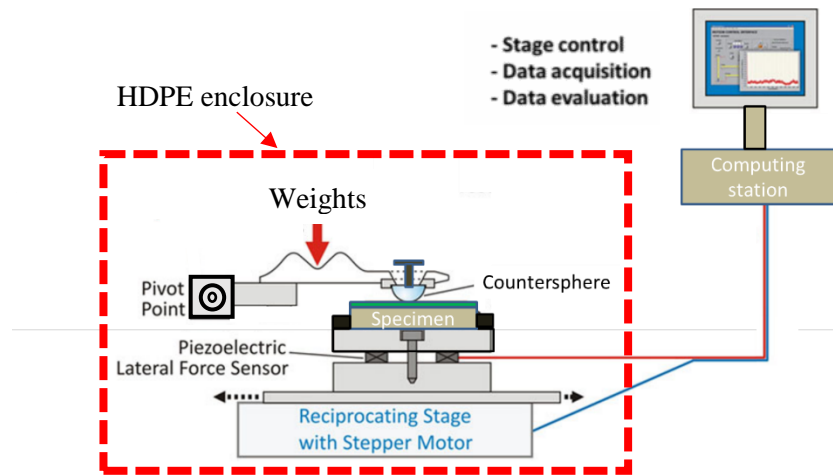


Fig. 3.7: Schematic of the tribometer used in the present study [161].

The work in chapter 8 was done in one of our collaborator’s lab at University of North Texas, Texas, USA. The sliding wear tests at room and elevated temperatures were performed using a unidirectional ball-on disc tribometer Falex ISC-450 (Falex Corporation, USA). The tribometer was equipped with a ball holder, heating stage (on which the sample was mounted), temperature controller (Honeywell, USA) and thermocouple as shown in Fig. 3.8. WC-Co balls of diameter 6.35 mm were used as counterface for all the tests. The counterface was placed in the ball holder and was fixed to the tribometer arm. The sample was mounted on the stage and the desired static test temperature was set in the temperature controller to start the heating process. The counterface

was kept in contact during the heating process and the heating rate was $\sim 10 - 15^{\circ}\text{C}\cdot\text{min}^{-1}$ for all the tests. The entire test setup i.e. the counterface, sample and thermocouple were covered by a ceramic enclosure followed by a steel enclosure to reduce the heat loss due to convective heat transfer. After the desired test temperature was reached, the system was allowed to stabilize for $\sim 15-20$ min before the test was started. The thermocouple, temperature controller and the heating stage were connected through a feedback loop wherein the temperature controller collects the data through the thermocouple and activates or de-activates the heating coil placed under the heating stage to maintain the desired static test temperature. The sliding wear tests were conducted in ambient air ($\sim 40\%$ RH) at a normal load of 2.5 N. The normal load was applied by hanging dead weights to the tribometer arm. The sliding speed was fixed at $2.1\text{ cm}\cdot\text{s}^{-1}$ and all the tests were run for a total sliding distance of 200 m. The frictional force was continuously recorded using the software provided by the manufacturer. Sliding wear tests were performed at a static test temperature of 25°C , 200°C , 400°C and 575°C respectively.

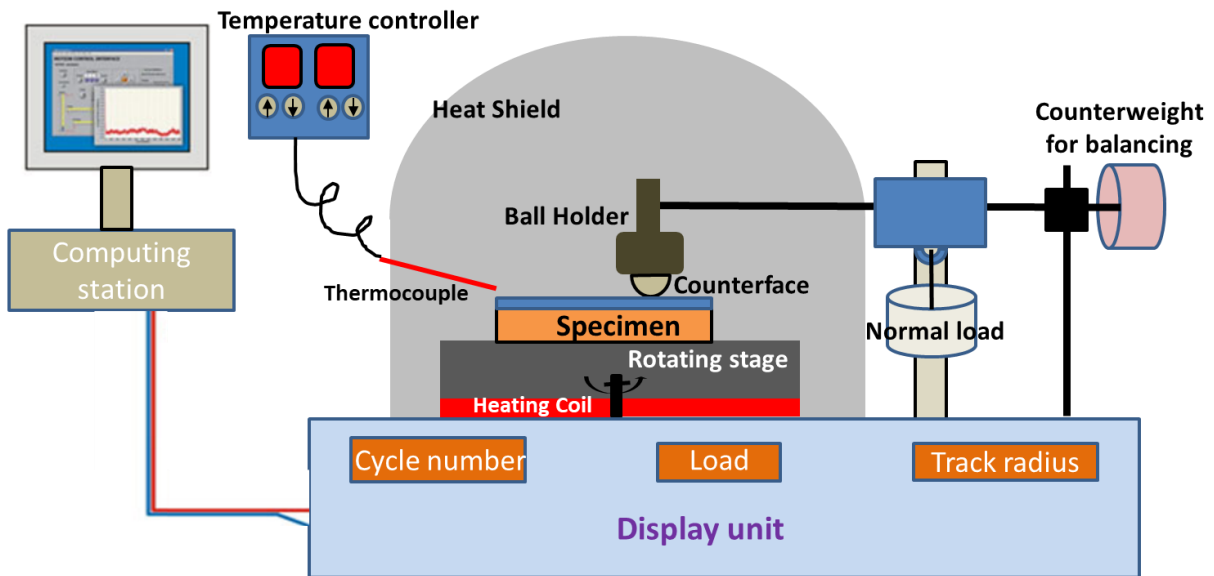


Fig. 3.8: Schematic of the high temperature tribometer used in the present study.

3.4.2 Wear track characterization

After sliding wear tests, the worn surfaces were examined under a non-contact optical profilometer (NewView 8000, Zygo corporation, USA). The surface profile of the entire wear track was generated and analyzed using the software provided by the manufacturer. The unworn surface of the coatings was considered as a reference surface and at least 35 line profiles were generated perpendicular to the wear track at different locations across the entire length as shown in Fig. 3.9. The line profiles were uploaded into Origin 2016 (Origin labs, USA) software. From the profiles, first the average surface was identified which corresponded to the unworn coating (indicated by a red line in Fig. 3.9). The area above and below the average surface was determined by integrating the profiles. Subsequently, the wear area (mm^2) was determined by calculating the difference between areas below and above the reference surface. The wear area calculated from all the profiles was averaged and multiplied with the track length (mm) to determine the wear volume (mm^3). The wear volume was normalized with load (N) and total sliding distance (m) to calculate the wear rate ($\text{mm}^3 \cdot \text{N}^{-1} \cdot \text{m}^{-1}$). Similar to wear tracks, the worn counterspheres were analyzed using the non-contact optical profilometer to determine the wear volume. The worn counterface surface profile was generated (as shown in Fig. 3.10a) and a sphere of same radius (i.e. 6.35 mm in the present study) as the counterface was fitted to flatten the surface as shown in Fig. 3.10b. The unworn surface was taken as reference and set to zero and the volume below the unworn region was determined. This volume was considered as wear volume (mm^3).

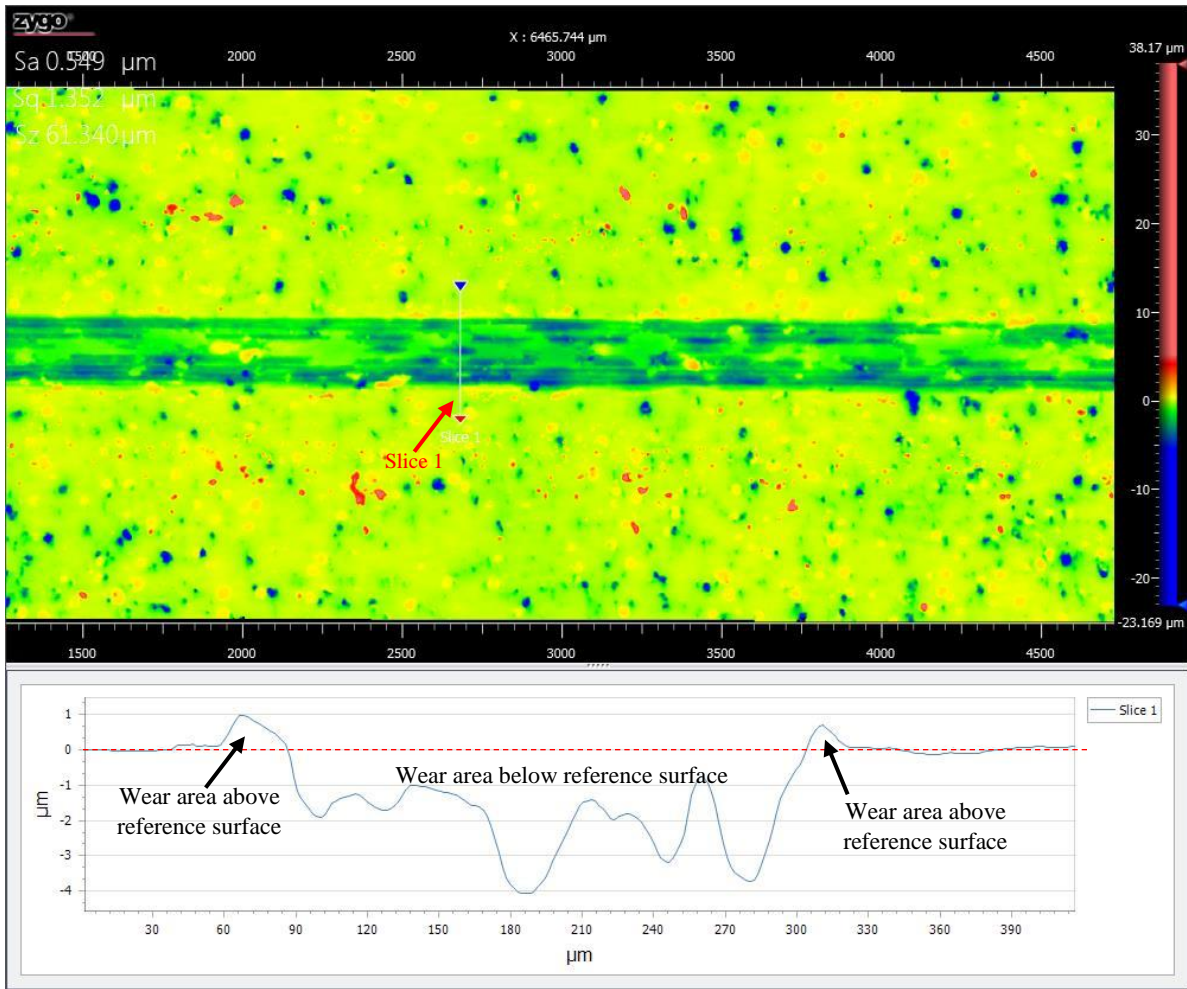


Fig. 3.9: Shows the schematic of the method used to generate line profiles across the wear track (red dotted line indicates reference surface).

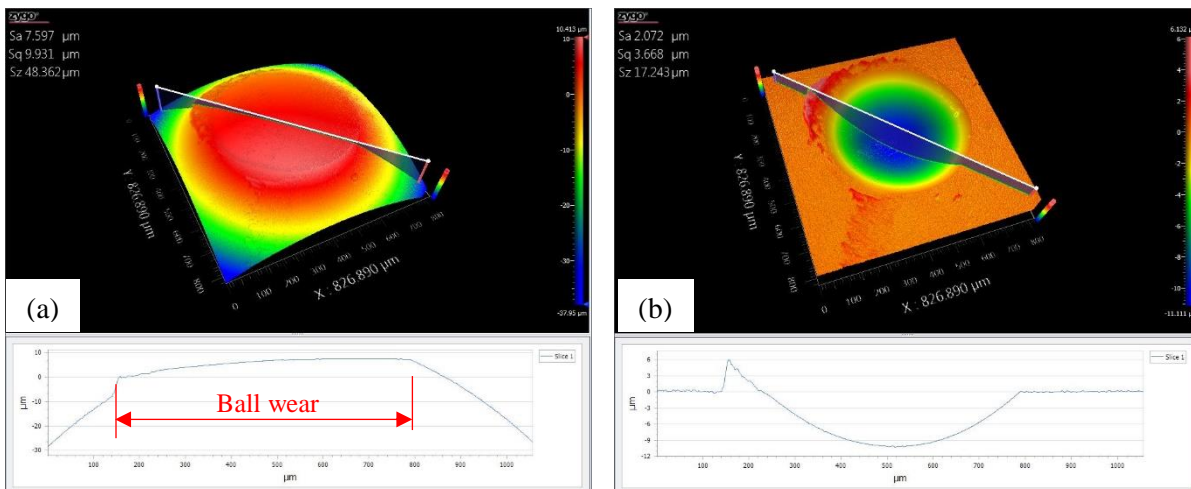


Fig. 3.10: Shows the scan profile (a) of the worn countersphere (b) of the countersphere after subtraction of the true sphere of diameter 6.35 mm.

To understand the wear mechanisms and characterize the third bodies, wear tracks and counterfaces were examined under SEM (SU3500, Hitachi, Japan). The different phases formed during the wear process were characterized using an inVia Raman spectrometer (Renishaw, UK) equipped with Ar⁺ laser source of wavelength (λ) = 514.5 nm. The subsurface analysis was performed by cross-sectioning the wear tracks using a low-speed cutting saw, cold mounting and later polishing in a similar manner as that of the coatings as illustrated previously in section 3.2.1. ECCI of the polished wear track cross-sections was performed using a cold field emission SEM (SU8230, Hitachi, Japan) equipped with a photodiode BSE and a FlatQUAD EDS detector (Bruker, USA). Furthermore, to understand the elemental distribution inside the tribofilms, EDS mapping was performed using the FlatQUAD EDS detector fitted to the cold field emission SEM. For the work performed in chapters 6 and 7, in addition to the above characterization, transmission electron microscope (TEM) lamellae were prepared using a focus ion beam (FIB) lift-out (Helios NanoLab DualBeam, FEI USA) and were subsequently observed under a cryo-STEM (Technai G2 F20, FEI, USA).

3.5 Raman spectroscopy

Raman spectroscopy was done on the third bodies to identify the phases formed during the wear process and subsequently understand the wear mechanisms. An inVia Raman microscope (Renishaw, UK) equipped with an Ar⁺ source class 3B laser of wavelength = 514.5 nm and output power of 50 mW was used to perform Raman analysis. The Raman microscope was connected to a computer interface that had Renishaw's WiRE software program installed which was used to start the spectrometer, perform lens as well as beam alignments and control the functioning of the laser. To obtain Raman spectra of different features, a laser beam of low intensity 1% - 10 % of the total intensity was exposed for a short duration of 10 – 30s to avoid sample damage due to localized heating. At least 3 trials were performed on a particular feature to check the repeatability and also to confirm that there was no thermal damage. The generated peaks corresponding to the Raman shifts were compared with the standard spectra reported in the literature to identify the tribo-chemical phases formed during wear.

3.6 Nanoindentation

Nanoindentation was performed using a Hysitron Triboindenter (TI 950, Hysitron, USA) on the coating cross-sections and third bodies to determine their mechanical properties. It is a localized and non-destructive measurement technique that enables a user to determine the mechanical properties of materials present in small quantities unlike microhardness where the interaction volume is over a few tens to hundreds of micrometers depending on the load. Furthermore, in the case of cold sprayed coatings, using nanoindentation, the interaction of the indenter with macroscopic defects like porosity, inter-splat boundaries can be minimized thus making it a powerful tool to determine the true mechanical properties of the deposits. In the present thesis, nanoindentation was performed at room temperature using a Triboindenter system equipped with a capacitive transducer, a piezoelectric scanner that permits “Imaging mode” scanning probe microscopy (SPM), and has an optical microscope.

The main component of a nanoindentation machine is the capacitive transducer that allows precise control on the loading and displacement of the indenter tip into the sample. The capacitive transducer consists of three plates as shown in Fig. 3.11 [194]. The top and bottom plates (or outer plates) are called driver plates and remain stationary. These plates carry an alternating current at 180° out of phase with respect to each other while the indenter tip is mounted on the centre plate and is suspended using springs. The opposite phases angles of the top and bottom plates create a zero electric field potential at the centre plate, and the electric field potential varies linearly with the distance between the plates. When a load is applied, a biased voltage is generated at the bottom plate which creates an electrostatic force between the plates and pulls the centre plate towards the bottom plate. The force and position of the centre plate is determined and used to generate a load-displacement curve as shown in Fig. 3.12. In the entire thesis, indentation was performed was performed using a diamond tip of Berkovich geometry as shown in Fig. 3.13 [195]. The general terminology used in nanoindentation and load-displacement curves is shown in Fig. 3.14.

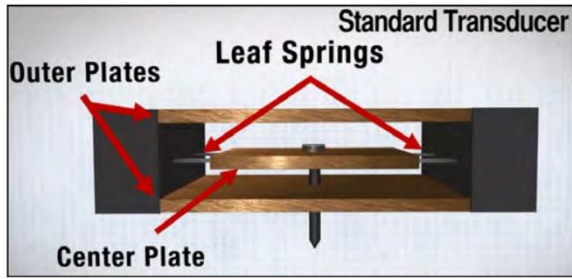


Fig. 3.11: Schematic of a capacitive transducer used for indentation in Hysitron systems [194].

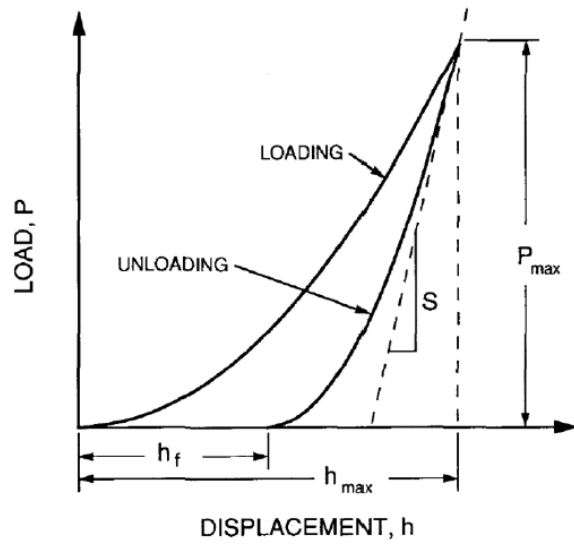


Fig. 3.12: Load-displacement curve obtained using nanoindentation technique [196].

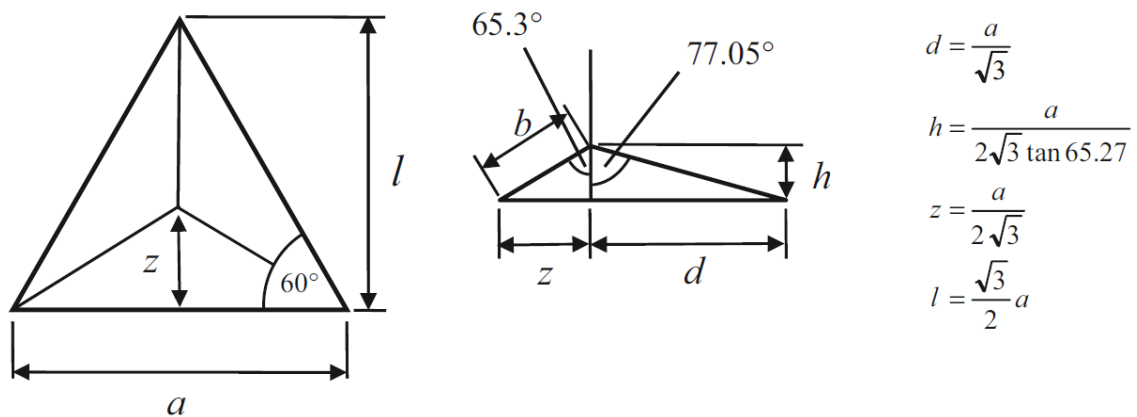


Fig. 3.13: Schematic showing the geometry and different parameters of a Berkovich tip [195].

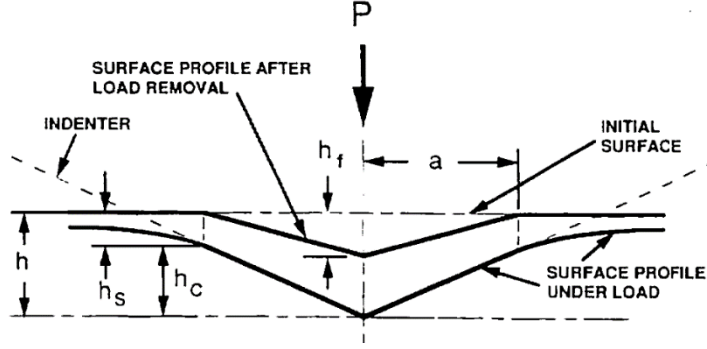


Fig. 3.14: Schematic showing an indentation section with various quantities [196].

The load-displacement curves generated were analysed using Oliver-Pharr method [196] to calculate the reduced elastic modulus and hardness using the equations explained below. The stiffness (S) of the material was determined by calculating tangent at the maximum slope of the unloading curve. The calculated stiffness was used to determine the reduced elastic modulus using the equations below [196]:

$$S = \frac{dp}{dh} = \frac{2}{\sqrt{\pi}} E_r \sqrt{A} \quad 3.5$$

$$\frac{1}{E_r} = \frac{1-\nu_i^2}{E_i} + \frac{1-\nu_s^2}{E_s} \quad 3.6$$

In the above equation, E_r is the reduced elastic modulus that is associated with the elastic moduli of the indenter (E_i) and the sample (E_s), ν_i and ν_s are the Poisson's ratio of the indenter material and the sample and A is the projected area of contact of the indentation. The projected area depends on the contact depth (h_c) of the indenter according to its tip area function which calculated using the below equation for a Berkovich indenter:

$$A = c_0 h_c^2 + c_1 h_c^1 + c_2 h_c^{1/2} + c_3 h_c^{1/4} + \dots \quad 3.7$$

In the above equation, the coefficients c_n are obtained by performing the indenter area function calibration. This was done by performing a series of indents on a standard fused quartz sample of known elastic moduli ($E = 72$ GPa) at various contact depths (by increasing the normal load). The projected area for a perfect Berkovich indenter is given by:

$$A = 24.5 h_c^2 \quad 3.8$$

whereas the remaining constants namely $c_1, c_2, c_3 \dots$ etc., depend on the defect radius (shown in Fig. 3.15) of the tip. In the Fig 3.15, R is defect radius of the tip, h_0 represents the height difference between the ideal sharp tip and the rounded (blunt) tip and h^* is the spherical portion of the round tip that will be in contact with the sample during indentation [197].

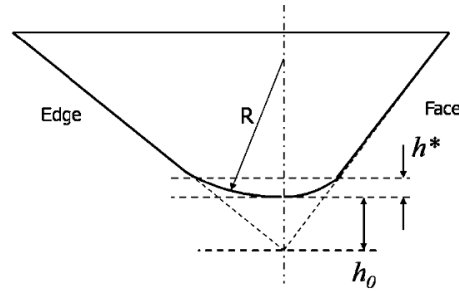


Fig. 3.15: Schematic showing the image of a truncated Berkovich tip [197].

The contact depth was calculated using the equation below:

$$h_c = h_{\max} - 0.75 \frac{P_{\max}}{S} \quad 3.9$$

In the above equation, h_{\max} is the maximum depth of indentation, P_{\max} is the maximum load. Now the hardness is determined by using the following equation:

$$H = \frac{P_{\max}}{A} \quad 3.10$$

To determine the mechanical properties of the coatings or third bodies through nanoindentation, the sample preparation forms an important step since a nearly perfect flat surface is required. Sample preparation for nanoindentation was done using the steps illustrated in section 3.2.1. For the work done in chapter 4, nanoindentation was performed on the polished cross-sections of the Ti6Al4V coatings and bulk Ti6Al4V plate at normal loads between 1 mN – 20 mN. For the work done in chapters 6, 7 and 8, to determine the mechanical properties of the third bodies, indentation was done on the polished wear track cross-sections at a normal load of 5 mN in a rectangular grid pattern starting from the subsurface up till the wear track. Subsequently, the indented samples were imaged using a cold field emission SEM and the residual indent images were matched to the corresponding load-displacement curves to precisely obtain the properties of the corresponding features. For all the indents, the loading time, holding time and unloading time was fixed at 5 s, 2 s and 5 s respectively.

Chapter 4

Influence of powder morphology and microstructure on the cold spray and mechanical properties of Ti6Al4V coatings

Venkata Naga Vamsi Munagala, Valary Akinyi, Phuong Vo, Richard R. Chromik

Adapted from a paper of the same title published in *Journal of Thermal Spray Technology*, 2018, **27**:827 – 842.

Abstract

The powder microstructure and morphology has significant influence on the cold sprayability of Ti6Al4V coatings. Here, we compare the cold sprayability and properties of coatings obtained from Ti6Al4V powders of spherical morphology (SM) manufactured using plasma gas atomization and irregular morphology (IM) manufactured using the Armstrong process. Coatings deposited using IM powders had negligible porosity and better properties compared to coatings deposited using SM powders due to higher particle impact velocities, porous surface morphology and more deformable microstructure. To evaluate the cohesive strength, multi-scale indentation was performed and hardness loss parameter was calculated. Coatings deposited using SM powders exhibited poor cohesive strength compared to coatings deposited using IM powders. Images of the residual indents showed de-bonding and sliding of adjacent splats in the coatings deposited using SM powders irrespective of the load. Coatings deposited using IM powders showed no evidence of de-bonding at low loads. At high loads, splat de-bonding was observed resulting in hardness loss despite negligible porosity. Thus, while the powders from Armstrong process lead to a significant improvement in sprayability and coating properties, further optimization of powder and cold spray (CS) process will be required as well as consideration of post-annealing treatments to obtain acceptable cohesive strength.

Keywords: Armstrong process; Ti6Al4V; Titanium alloys; Cold spray; Nanoindentation; Particle morphology

4.1 Introduction

Ti alloy Ti6Al4V is widely used in aerospace, automobile and biomedical applications due to its high strength-to-weight ratio, bio-compatibility and corrosion resistance. Various processing techniques like plasma spraying, selective laser melting and electron beam melting have been previously used to deposit Ti and its alloys as coatings.[198–201] These techniques involve high working temperatures resulting in phase transformations, tensile residual stresses and high temperature oxidation [198,200].

To overcome these challenges, a low temperature process named as cold spray or cold gas dynamic spraying is under evaluation to deposit coatings at temperatures well below the melting point of the material [46]. CS is a novel thermal spray process that involves solid-state deposition of feedstock powders. In this process, powder particles are accelerated to supersonic velocities by a pre-heated gas stream (propellant gas) using a de Laval nozzle and are subsequently impacted onto prepared substrates. The strain rates achieved in this process are typically in the range of $10^3 - 10^9$.s⁻¹ [25,202]. As the particles impact on the substrates at such high strain rates, they deform plastically resulting in coating buildup [75]. Since the CS process uses the kinetic energy of the particles for the successful deposition of the coatings, the deleterious effects of high temperature oxidation, phase transformations and/or tensile residual stresses in the coatings can be minimized or eliminated [69]. Despite numerous advantages, there are some limitations and challenges in depositing coatings using the CS process. To deposit coatings using the CS process, a material should exhibit plastic deformation and possess some amount of ductility [8,69]. Hence, brittle materials like ceramics cannot be directly deposited using the CS process and are co-deposited using a ductile matrix [69]. Furthermore, cold sprayed coatings exhibit poor tensile properties due to severe strain hardening experienced by the particles upon impact at high strain rates and require heat treatment to gain ductility [8,9,13].

Using CS, a wide range of metals, alloys and composite coatings can be deposited onto different substrates; however, deposition of high yield strength materials like Ti6Al4V are challenging [13,69,80,117]. Prior works illustrate that the high yield strength of Ti6Al4V makes it extremely difficult to CS and the resultant coatings had high porosity [13,15,16,80,203]. Vo *et al.* deposited Ti6Al4V coatings using Nitrogen (N₂) and Helium (He) as propellant gas [13]. They found that the coatings deposited using N₂ as propellant gas had significant porosity whereas coatings

deposited using He were dense. This was mainly due to the high velocities achieved by the particles with He that resulted in higher particle deformation. Tan *et al.* studied the effect of gun traverse speed on porosity and adhesion of Ti6Al4V coatings [14]. Their results illustrate that lowering the gun traverse speed from 500 mm.s⁻¹ to 100 mm.s⁻¹ reduced the porosity in the coatings from 3.2 % to 0.5 % due to greater interaction of the hot gas stream with the substrate. However, reducing the gun traverse speed resulted in a significant reduction in coating adhesion strength between the substrate and coating. Khun *et al.* deposited Ti6Al4V coatings on Ti6Al4V substrates and found that the coatings deposited using N₂ had higher porosity when compared to coatings deposited using He [16]. They also found that the dense Ti6Al4V coatings deposited using He gas exhibited superior hardness, wear and corrosion resistance compared to the coatings deposited using N₂. Their results indicated that the coating porosity had significant influence on the mechanical properties and performance of the coatings. Bhattiprolu *et al.* used He to deposit Ti6Al4V coatings from feedstock powders of different microstructures [17]. They found that coatings deposited using hydride de-hydride powders of equiaxed α microstructure had comparable adhesion strength and porosity to the coatings deposited using atomized powders with martensitic α' microstructure. Dense Ti coatings with high DE were deposited by MacDonald *et al.* using IM powders manufactured using Armstrong process [6]. They proposed that the unique morphology of the powder particles allows them to breakdown and flatten on each other upon impact resulting in dense coatings; however, with poor cohesive strength.

Single splats of Ti6Al4V onto various substrates were deposited by Vidaller *et al.* and cavitation tests were performed to understand the bond strength between the splats and the substrate [118]. Their results show that a higher hardness of the substrate compared to the spray material leads to more deformation of the splats, resulting in greater adhesion strength. Goldbaum *et al.* deposited single splats of Ti6Al4V to understand the effect of process conditions on adhesion strength [117]. Based on the results of splats adhesion tests, they found that the adhesion strength of the splats was higher when sprayed at higher velocities using He. Higher particle velocities lead to higher strain rates when particle impacts onto the substrate; thus, resulting in higher deformation. To reduce porosity in Ti6Al4V coatings, Luo *et al.*, used an in-situ shot peening process by mixing steel balls with the metal powder in the initial feedstock [20]. Peening action by these steel balls during the CS process reduced the porosity in the final coatings. An initial mixture varying from 0 % to 70 vol.% of steel balls in the initial feedstock resulted in porosity reduction from 13.7 % to

0.7 %. Based on the literature, it can be concluded that deposition of pure Ti6Al4V coatings with low porosity when sprayed using N₂ as propellant gas remains challenging. Furthermore, most of the works discussed in the above literature offered very limited or absolutely no data regarding the DE of the coatings. Thus, there is a need for a study to understand and deposit dense Ti6Al4V coatings with special emphasis on the effect of feedstock powder microstructure and characteristics on the final coating properties.

The aim of our work is to understand the influence of initial microstructure and powder morphology on the CS of Ti6Al4V coatings. In the present study, two different morphologies of powders, i.e. spherical and irregular, have been cold sprayed onto mild steel substrates. The two powders are microstructurally and morphologically distinct and were manufactured using different processing techniques. Powders were systematically characterized in terms of phases, surface structure and cross-section microstructures and were related to the coating porosity, hardness and DE. Electron channel contrast imaging (ECCI) was used to characterize the feedstock powder cross-sections and splats in the coatings to link the initial and final cold sprayed microstructures. Hardness loss parameter was calculated by performing indentation at different loads and length scales to examine the cohesive strength between the splats. Microstructure, characterization and coating properties, were used to understand the structure-process-property relationship.

4.2 Experimental procedure

4.2.1 Feedstock powder characterization and cold spraying

Ti6Al4V coatings were cold sprayed onto mild steel substrates of dimensions $75 \times 75 \times 3 \text{ mm}^3$ using a PCS 800 system (Plasma Giken, Japan) with N_2 as propellant gas. Commercially pure (CP) Ti6Al4V powders (Grade 5) of spherical morphology (SM) (AP&C, Canada) (size range: $15 \text{ }\mu\text{m}$ - $45 \text{ }\mu\text{m}$) and irregular morphology (IM) (Cristal Metals, USA) (size range: $0 - 45 \text{ }\mu\text{m}$) with average particle diameters of $31 \text{ }\mu\text{m}$ and $38 \text{ }\mu\text{m}$ respectively, were used as feedstock. The size distributions of the powders were evaluated using a laser scattering particle size distribution analyzer (LA-920, Horiba, Japan) and are shown in Fig. 4.1. The SM powders were manufactured by plasma gas atomization process and the IM powders were manufactured by Armstrong process.[19,193] The flowability and apparent density of the powders were measured as per Metal Powders Industries Federation (MPIF) standards 3 and 28 using Hall-flow and Carney flowmeter. An average of 3 measurements was taken to determine the flowability and apparent density of the powders. The specific surface area and the pore volume were determined using Brunauer-Emmett-Teller (BET) analysis i.e. gas absorption technique (TriStar 3000, Micromeritics Instrument, USA), with N_2 as absorbent. X-ray diffraction analysis for phase determination was done on feedstock powders using an X-ray diffractometer (Bruker, Germany) with $\text{Cu-K}\alpha$ as a source operated at a power of 40 kV and 40 mA . Subsequently, phase matching was performed on the generated diffractograms using the standard intensity peaks corresponding to their respective Bragg angles taken from JCPDS data card no. 00-044-1294 ($\alpha - \text{Ti}$) and 00-044-1288 ($\beta - \text{Ti}$).

Prior to CS deposition the mild steel substrates were de-greased with acetone and grit blasted using alumina to enhance the bonding between the coating and substrate. The gas pressure and temperature to deposit all the coatings were fixed at 4 MPa and 800°C , respectively. The standoff distance between the nozzle and the substrate was kept 40 mm and the gun traverse speed was $0.2 \text{ m}\cdot\text{s}^{-1}$. The in-flight particle velocities were measured using a time of flight particle diagnosis system (Coldspraymeter, Tecnar Automation, Canada). The DE of the coatings deposited was calculated by taking a ratio of the weight of the powder deposited to the weight of the powder sprayed. The weight of the powder deposited was calculated by taking the difference between the weight of the sample before and after coating deposition, whereas the weight of the powder sprayed

was determined by taking a ratio of the product of the powder feed rate and total distance travelled by the gun on the sample to the gun traverse speed.

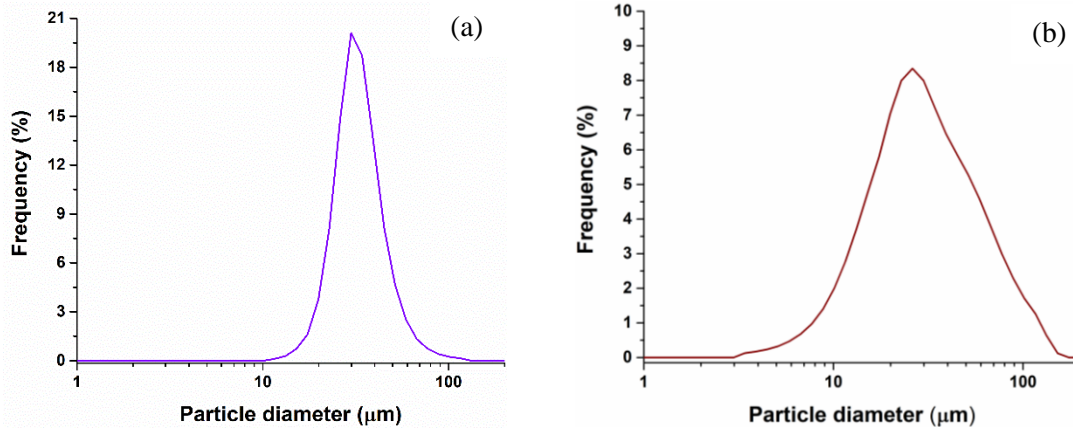


Fig. 4.1: Ti6Al4V powder size distribution of (a) SM and (b) IM.

4.2.2 Coating characterization

Coatings were cut perpendicular to the gun traverse direction, cold mounted and polished down to 0.05 μm colloidal silica suspension. These polished samples were observed under a scanning electron microscope (SEM) (SU3500, Hitachi, Japan) equipped with a back scattered electron (BSE) detector. BSE images were taken at different locations within the coating cross-section at magnifications ranging between 60x – 80x and porosity in the coatings was determined by measuring the pixels associated with the difference in contrast, from the BSE images using ImageJ software. At least 15 images were analyzed to calculate average porosity. To relate the microstructure of the initial feedstock powders and coatings, ECCI was performed on powder and coating cross-section. ECCI on the cross-sections was done using a cold field emission SEM (SU8230, Hitachi, Japan) fitted with a photodiode BSE detector. ECCI is a powerful technique to visualize crystal defects like grain boundaries, dislocations within a spatial resolution of ~1 nm. It is based on the orientations of the back scattered electrons that are emitted from a polycrystalline material due to different angular orientations of the crystals.[11,25]

4.2.3 Coating hardness

Nanoindentation was performed on the coatings using a Triboindenter (Hysitron Incorporated, USA) with a diamond Berkovich tip. Indentation was done on the coating cross-section and on a bulk CP-Ti6Al4V plate (polished in a similar manner as that of coating cross-sections) at loads ranging between 1 to 20 mN with loading and unloading segments of 5 s and holding time of 2 s to study indentation size effect. The Ti6Al4V plate had an equiaxed microstructure as shown in Fig. 4.2 with α and β phase mixtures. Nanoindentation tests were performed at the centre of the coatings away from the free surface and substrate-coating interface. The nanohardness was calculated using the load-displacement curves as described by Oliver and Pharr.[196] Microhardness tests were done using a Vickers diamond indenter (Clark Microhardness tester, USA) on the polished cross-sections of the coatings and the Ti6Al4V plate at different loads within a range of 25 g – 500 g and holding time of 15 s. An average of fifteen indents was done to calculate the final hardness at each load. Images of the residual indents were captured at 500x magnification using an optical microscope attached to the hardness testing machine. Vickers hardness (VH) was calculated by dividing the applied load by the surface area of the indent. VH (kg/mm^2) and was converted into H_{micro} (GPa) using a conversion from surface area to projected area using Eq. 4.1: [119]

$$H_{\text{micro}} \text{ (GPa)} = \frac{\text{VH} \times 9.8 \text{ m/s}^2}{1000 \times \sin 68^\circ} \quad 4.1$$

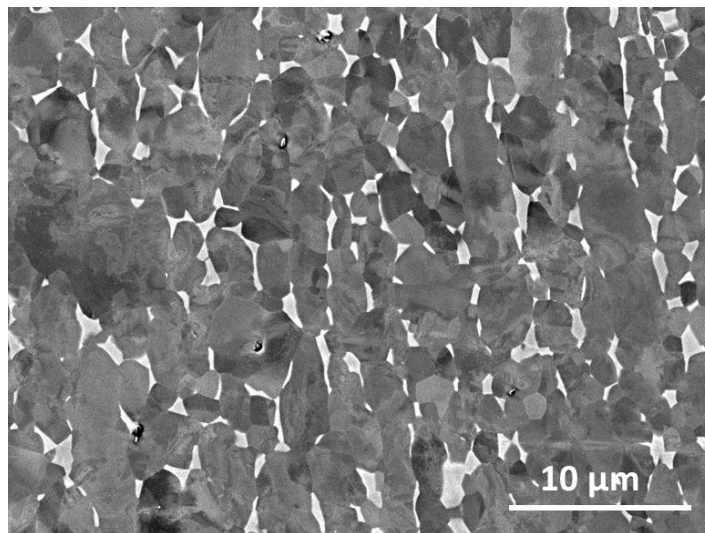


Fig. 4.2: ECCI showing cross-section of Ti6Al4V.

4.3 Results

4.3.1 Characterization of the feedstock powders

SM powders exhibited a cellular surface morphology (see Fig. 4.3a-b), which is a feature expected from the plasma gas atomization process.[19] ECCI of the cross-section of the SM Ti6Al4V powders revealed the presence of martensitic laths (Fig. 4.3c), which were formed due to rapid directional solidification resulting in martensitic bcc- β to hcp- α phase transformations.[18] A close examination of the martensitic laths indicated the presence of dislocation twins inside laths, as seen in Fig. 4.4. Martensitic structures (α') of Ti6Al4V alloy possess crystal defects and are sites for high dislocations densities such as stacking faults and dislocation twins when compared to pure α -phase.[204] In contrast, the IM powders were manufactured by the Armstrong process and showed a different surface morphology along with the presence of porosity throughout the particles (see Fig. 4.3d-e). Polished cross-sections of the IM powders showed an equiaxed alpha microstructure with a grainsize $\sim 3.2 \mu\text{m}$ (Fig. 4.3f). XRD of SM and IM powders revealed stable α -phase of Ti and there was no measurable β -Ti phase observed (due to its low volume fraction) as shown in Fig. 4.5.

The results of BET analysis are summarized in Table 4.1. The specific surface area of SM powders is less than IM powders. The flowability and apparent density of the powders are also presented in Table 4.1. SM powders had excellent flowability whereas the IM powders did not flow through the Hall-flow meter. The apparent density of IM Ti6Al4V powders was significantly lower than that of SM powders mainly due to its porous structure.

Table 4.1 Feedstock powder characteristics

Powder	Specific surface area ($\text{m}^2\cdot\text{g}^{-1}$)	Total pore volume of the pores ($\text{cm}^3\cdot\text{g}^{-1}$)	Hall flowability (s/50 g)	Apparent density ($\text{g}\cdot\text{cm}^{-3}$)
Spherical Ti6Al4V	0.046	---	40.5 ± 0.7	2.49
Irregular Ti6Al4V	0.301	59.1×10^{-5}	No flow	0.86

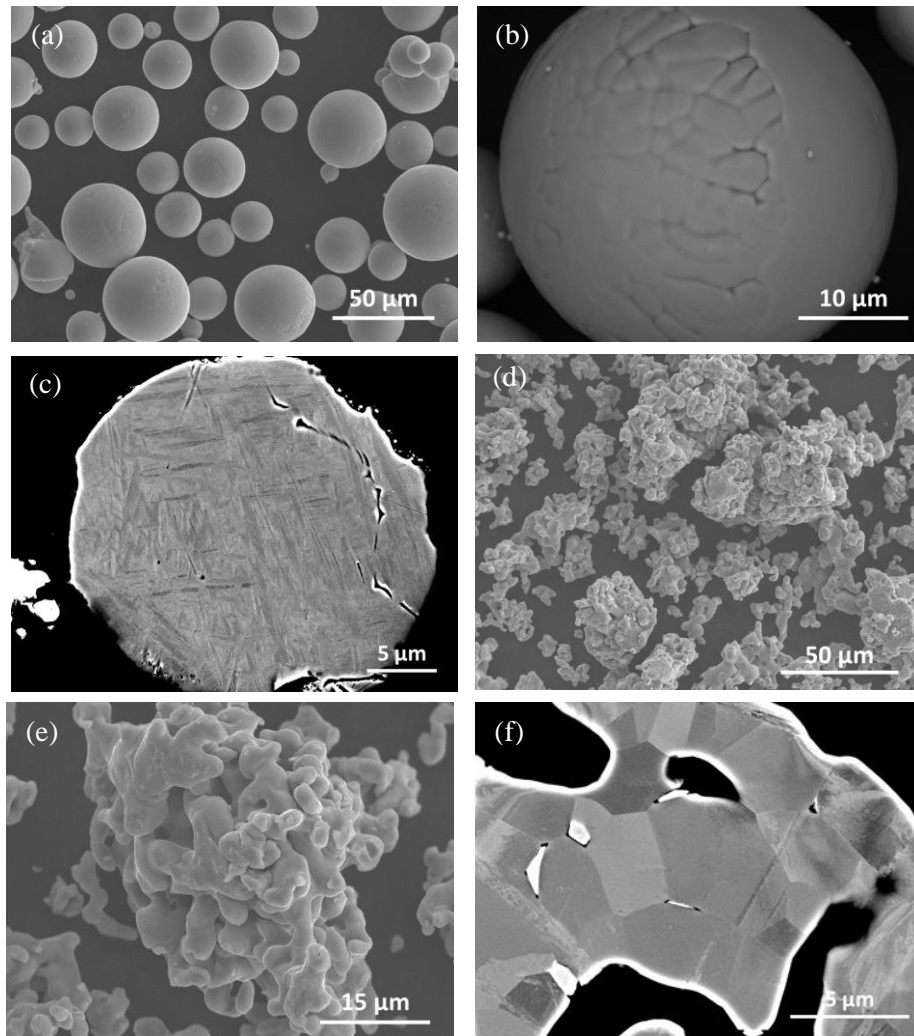


Fig. 4.3: Surface morphology of (a) & (b) SM powders (low and high magnification); (d) & (e) IM powders; ECCI of cross section of (c) SM (f) IM powders.



Fig. 4.4: ECCI of the powder cross-section of spherical Ti6Al4V powder showing dislocation twins inside the martensitic laths (features inside the white oval).

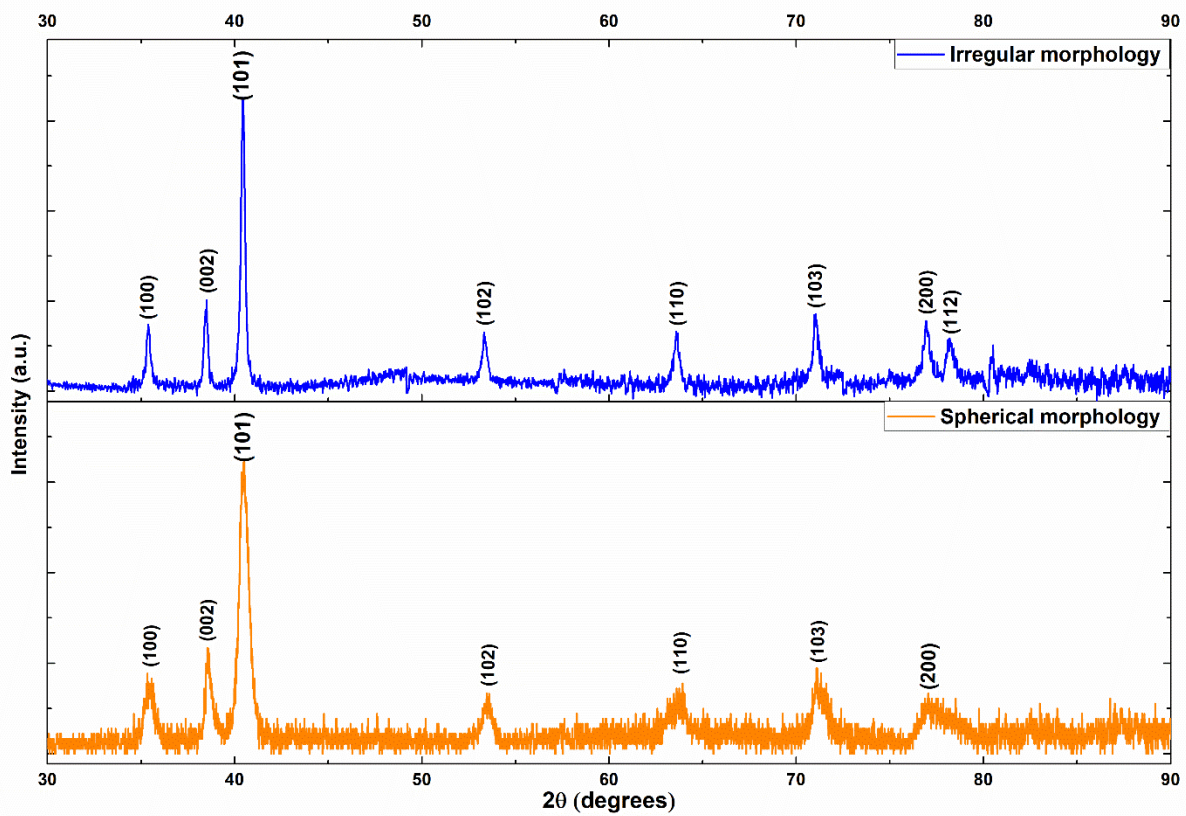


Fig. 4.5: XRD diffractograms of IM and SM Ti6Al4V.

4.3.2 Characterization of the cold sprayed coatings

4.3.2.1 Top surface morphology of the coatings

Figure 4.6 shows the top surface morphology of pure Ti6Al4V coatings cold sprayed using SM and IM feedstock powders. Ti6Al4V coatings deposited using SM powders showed evidence of adiabatic shear instabilities (ASI), by evidence of material jetting (see Fig. 4.6a). Also, most of the SM feedstock particles retained their initial morphology leading to significant gaps between deposited particles. For coatings deposited using IM powders, no conclusive evidence of ASI was found (Fig. 4.6b), which may simply be due to the complicated structure of these powders making direct observation difficult. Nevertheless, the coatings deposited using IM exhibited a denser microstructure with less evidence of gaps between the particles. Top surface porosity for coatings deposited using IM powders was mainly due to the porosity in their initial feedstock particles (Fig. 4.3d-e).

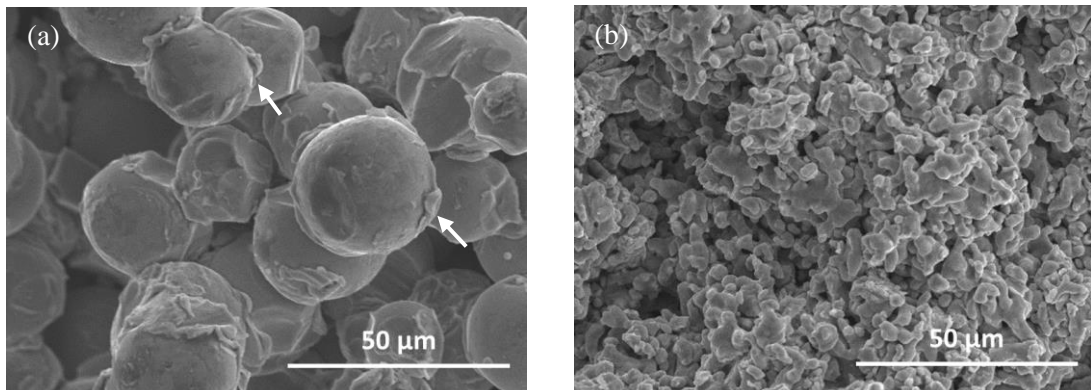


Fig. 4.6: Top surface morphology of Ti6Al4V coatings deposited using (a) SM powders (b) IM powders White arrows in (a) indicate locations with evidence of material jetting.

4.3.3 Deposition efficiency and particle velocity

Table 4.2 shows the DE of Ti6Al4V coatings deposited using SM and IM powders of similar size range. The DE of coatings deposited using IM powders was marginally greater than those deposited using SM powders due to the higher impact velocity for the similar spray conditions (i.e. gas pressure and temperature). The measured in-flight particle velocities, shown in Table 4.2 demonstrated the higher velocity of irregular particles, which is due to the higher drag force acting on the particles with IM. The drag force acting on an in-flight particle can be expressed as illustrated in Eq. 4.2: [97]

$$D = \frac{1}{2} \rho V_{\text{rel}}^2 A_p C_D \quad 4.2$$

where D is the drag force acting on the particle, ρ is the mass density of the propellant gas, V_{rel} is the relative velocity between the gas stream and the particle, A_p is the projected surface area of the particle and C_D is the drag coefficient. From Eq. 4.2, the drag force acting on the particle is proportional to the drag coefficient. For a particle in a fluid environment, the drag coefficient is a sum of frictional drag and form drag. Frictional drag coefficient of the spherical and non-spherical particles is same whereas the form drag on the IM particle is higher than spherical particle due to pressure variation around the particle [97]. This form drag depends on the morphology of the object or particle present in the fluid environment. For an irregular shaped particle, the boundary layer separation occurs at an early stage due to variation in pressure gradient on the two opposite surfaces. Hence, it experiences greater amount of drag force when compared to a spherical particle in a gas stream.

Table 4.2 Ti6Al4V coatings characteristics and particle velocity measurements.

Ti6Al4V coatings deposited using	Particle velocity (m.s⁻¹)	Porosity (%)	Coating hardness (HV_{0.5})	DE (%)	Coating thickness (mm)
SM powders	619 ± 87	13.0 ± 2.0 %	174 ± 44	85 %	2.24 ± 0.03
IM powders	732 ± 88	0.3 ± 0.1 %	197 ± 15	92 %	1.35 ± 0.01

4.3.4 Coating porosity

The porosity of Ti6Al4V coatings deposited using IM powders was significantly less compared to SM powders as seen in Table 4.2. The high porosity of Ti6Al4V coatings deposited using SM powders is mainly due to the limited deformation of the particles, as observed from the cross-section (Fig. 4.7a), and top view (Fig. 4.6a) SEM images of the coatings. Coatings deposited using irregular Ti6Al4V powders exhibited a dense microstructure with no evidence of particles retaining their initial morphology (Fig. 4.7b).

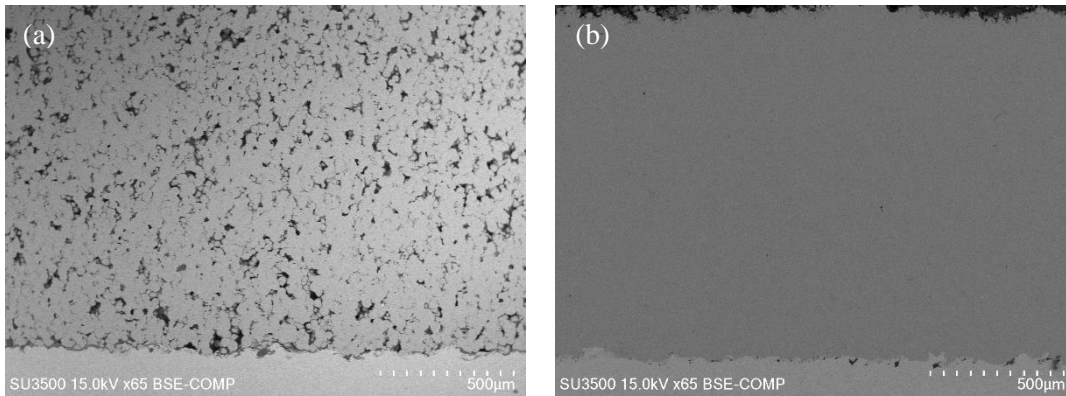


Fig. 4.7: Cross-section images of Ti6Al4V coatings deposited using (a) SM powders (b) IM powders.

4.3.4 Microstructure of the coatings

To understand the microstructure, ECCI was performed on the Ti6Al4V coatings deposited using SM and IM powders. Figure 4.8a shows an ECCI of the Ti6Al4V coating deposited using SM powders. Most of the region inside the splat showed a martensitic lath structure similar to that of the initial feedstock microstructure as previously shown in Fig. 4.3c. However, near the splat boundary nanograins were observed (see Fig. 4.8a-b). This indicates that recrystallization had taken place close to the particle boundary during the splat impact. Nanograins were observed up to $\sim 8 \mu\text{m}$ from the splat boundary, beyond which the initial martensitic lath-like microstructure of the feedstock powder was retained. Recrystallization near the splat boundaries is a result of the high strain rate and rise in localized temperature during particle impact at supersonic velocities onto the substrate or previously deposited layer. Since the rise in temperature is localized near the contact zone, recrystallization was primarily observed at splat boundaries. ECCI of the Ti6Al4V

coatings deposited using IM powders illustrates that the powder particles underwent significant amount of deformation as seen in Fig. 4.8c. Recrystallization was observed at the splat boundaries and these were followed by heavily deformed grains as we move inside the splats. This can be seen in Fig. 4.8c-d. The recrystallized region predominantly consisted of nanograins of size < 15 nm, as observed in Fig. 4.8d. Furthermore, it is worth observing that in the case of coatings deposited using SM powders initial microstructure was seen away from the splat boundaries whereas in case of coatings deposited using IM powders the initial microstructure of the feedstock particles was limitedly seen.

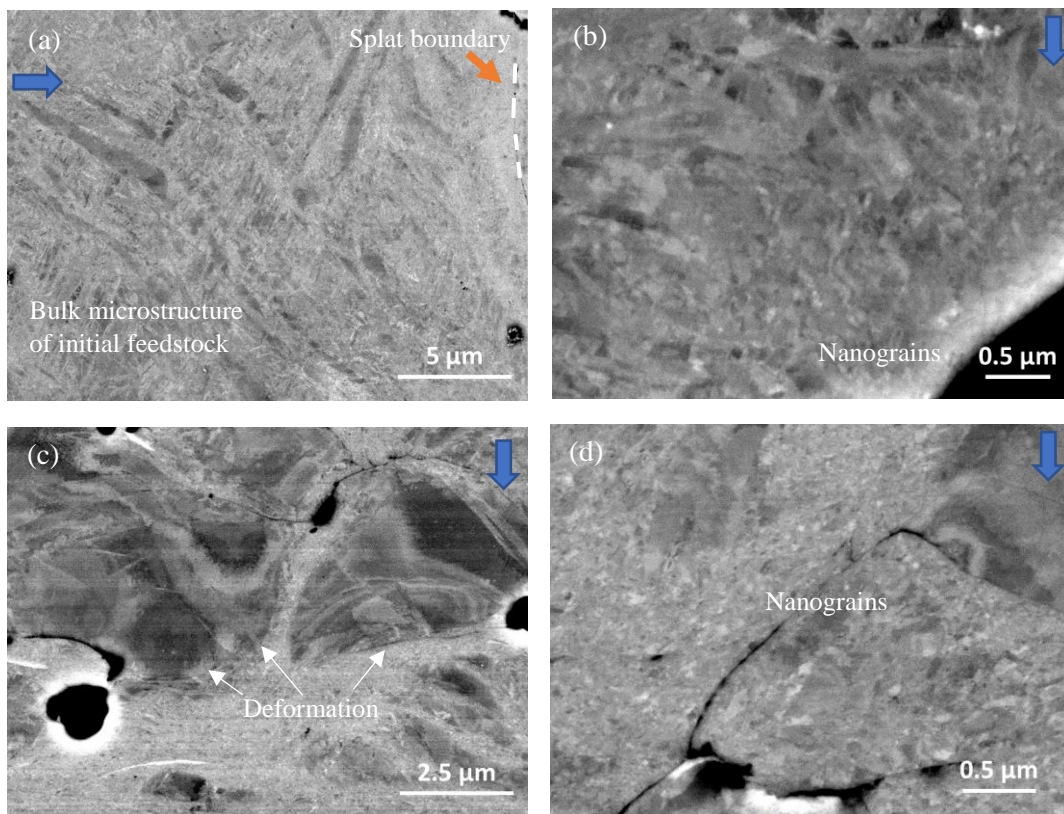


Fig. 4.8: ECCI of Ti6Al4V coating cross-sections deposited using (a) SM powder (c) IM powder and (b) & (d) high magnification images at the splat boundaries respectively; Blue arrow - indicates spray direction.

4.3.5 Indentation size effect on the coatings and hardness loss parameter

4.3.5.1 Nanohardness test results

Nanoindentation was performed on the coating cross-section and on the bulk Ti6Al4V plate at different loads ranging between 1 mN to 20 mN. With increase in indentation depth there was a general trend of decrease in hardness in both the coatings and bulk Ti6Al4V plate. The square of nanohardness as a function of inverse of indentation depth for the bulk Ti6Al4V plate and coatings is shown in Fig. 4.9a-c. This data was fit to Nix-Gao model (as per Eq. 4.3) which illustrates that the indentation size effects can be related to the geometrically necessary dislocations.[205] This model is based on law of strain gradient plasticity, and the indentation depth and hardness in this model are related using Eq. 4.3:

$$\frac{H}{H_0} = \sqrt{1 + \frac{h^*}{h}} \quad 4.3$$

In the above equation H is the nanohardness, H_0 is the hardness of the material at infinite indentation depth, h^* is a characteristic length scale and h is the indentation depth.

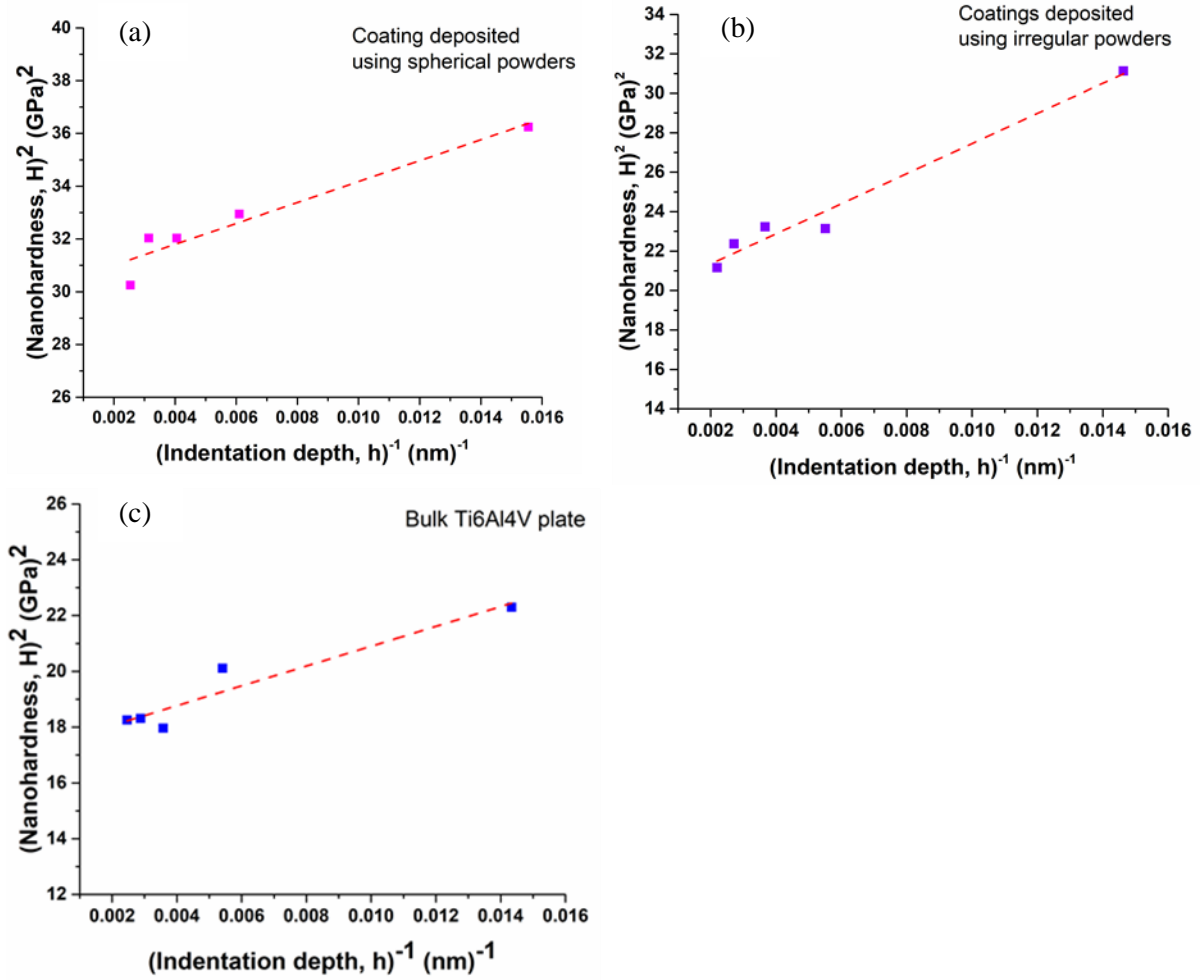


Fig. 4.9: Variation of square of hardness with inverse of indentation depth plotted according to Nix - Gao model for (a) coatings deposited using SM powders (b) coatings deposited using IM powders and (c) bulk Ti6Al4V plate.

The results of the regression fit of nanohardness to the indentation depth data as per Eq. 4.3. for the coatings deposited using SM and IM powders are shown in Table 4.3.

Table 4.3 Strain gradient plasticity parameters of bulk Ti6Al4V plate and coatings.

Sample	H_0 (GPa)	h^* (nm)
Ti6Al4V coatings deposited using SM powders	5.49 ± 0.05	13.15 ± 2.15
Ti6Al4V coatings deposited using IM powders	4.45 ± 0.01	38.54 ± 3.53
Bulk Ti6Al4V plate	4.17 ± 0.04	20.43 ± 3.62

In Table 4.3, the value of H_0 represents the “true hardness” of the material independent of the load or depth of indentation where the hardness is influenced only by statistically stored dislocations. The true hardness of the bulk Ti6Al4V plate is lower than that of the cold sprayed coatings. This could be due to the strain hardening and grain refinement in the powder particles upon impact at high strain rates during CS process. Furthermore, the true hardness of the Ti6Al4V coatings deposited using SM powders was higher than that of IM powder. This can be attributed to the initial microstructure of the two feedstock powders in which the presence of martensitic laths in SM powders would have contributed to the higher hardness.

In Eq. 3 the h^* represents the characteristic length that depends on the shape of the indenter, shear modulus and H_0 value. The lower value of h^* for coatings deposited using SM powders is mainly due to its plastic deformation resistant acicular microstructure. The values of h^* obtained here for the coatings deposited using IM powders closely match with the value of 42 nm reported by Sen *et al.* for Ti6Al4V alloy of equiaxed microstructure.[206] Also, the crystal anisotropy in the case of Ti and its alloys influences the hardness values which in turn affects the h^* . [207] However, despite these differences the h^* of bulk Ti6Al4V plate is lower than that of coating deposited using SM powders which can be due to their differences in microstructures.

4.3.5.2 Microhardness test results

Microhardness tests were performed at different loads within a range of 25 g – 500 g on the bulk Ti6Al4V plate and coatings and the hardness as a function of indentation depth is shown in Fig. 4.10. There is a decrement in microhardness with an increase in indentation depth; however, as the indentation depth increased beyond ~ 4 μm , the hardness values remained constant. This trend was observed in both the coatings and bulk Ti6Al4V plate. Furthermore, the variation in the microhardness of the bulk Ti6Al4V with indentation depth was lower when compared to CS coatings. The diagonals of the residual Vickers indents were found to be approximately between 30 μm – 75 μm at the loads where the hardness approached a constant value. At such large indentation sizes, there will be a definite interaction of the indenter with the splat boundaries and porosity present in the coatings. This indicates that microhardness tests reveal the indentation size effect in a different manner compared to nanoindentation, with greater interaction with macroscopic defects like splat boundaries and porosity.

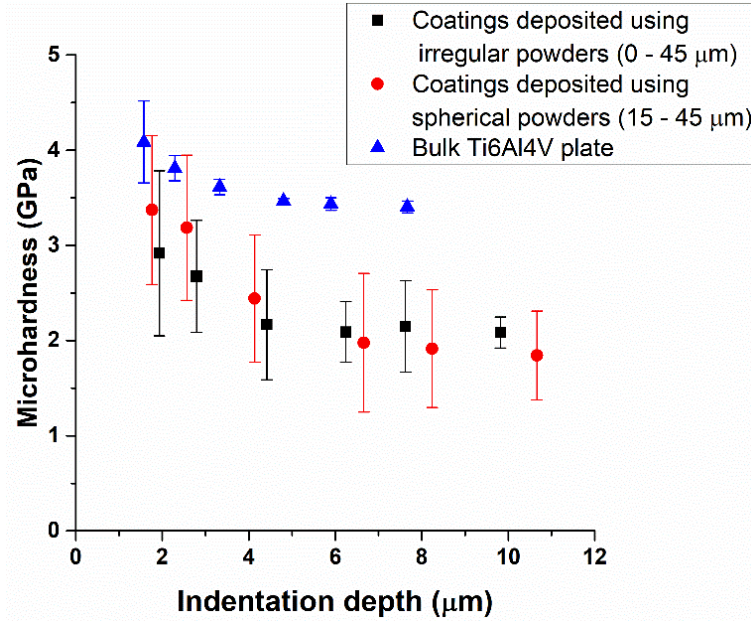


Fig. 4.10: Microhardness of bulk Ti6Al4V plate and coatings.

4.3.6 Calculation of hardness loss parameter

The hardness loss for the coatings is calculated using Eq. 4.4 as proposed previously by Goldbaum *et al.* [119]

$$\text{Hardness loss (\%)} = \frac{H_0 \text{ (GPa)} - H_{\text{plateau}} \text{ (GPa)}}{H_0 \text{ (GPa)}} \times 100 \quad 4.4$$

In Eq. 4.4, H_0 represents the true hardness of the material derived from the Nix-Gao fit (Eq. 3) to nanoindentation data and H_{plateau} is the plateau hardness of the material, which is taken as an average microhardness from the three highest loads. Hardness loss for the bulk Ti6Al4V plate and coatings deposited using the two feedstock powders are shown in Table 4.4.

Table 4.4 Hardness loss.

Sample	H_{plateau} (GPa)	Hardness loss (%)
Ti6Al4V coatings deposited using SM powders	1.91 ± 0.054	65.20 %
Ti6Al4V coatings deposited using IM powders	2.11 ± 0.029	52.58 %
Bulk Ti6Al4V plate	3.43 ± 0.025	17.74 %

The hardness loss values of CS coatings were higher than that of bulk Ti6Al4V plate. Furthermore, the hardness loss was higher in the case of Ti6Al4V coatings deposited using SM powders when compared to coatings deposited using IM powders.

To understand the reason behind the high hardness loss, despite low porosity levels (in the case of coatings deposited using IM powders), the residual indents after microhardness tests were examined under an optical microscope. Fig. 4.11 shows the images of the residual indents at the two extreme loads, i.e. 25 g and 500 g for the bulk Ti6Al4V plate and coatings. The indents on bulk Ti6Al4V plate show a perfect diamond shape of the Vickers indenter at both the loads as seen in Fig. 4.11a-b. The minor loss in hardness obtained could be due to deviations from a perfect shape of the diamond indent at low loads as shown in Fig. 4.11a. These minor deviations are mainly due to the crystal anisotropy in Ti and its alloys [207,208].

Micrographs of residual indents on cold sprayed coatings showed multiple phenomena that were not observed for the bulk Ti6Al4V plate. In the case of coatings deposited using SM powders, an interaction of the indenter with the porous regions was found at both low and high loads. De-bonding of the splats in these coatings was observed in almost all cases (Fig. 4.11c-d & g). Additionally, for some tests, there was sliding of an adjacent splat onto the residual indent due to poor bonding between the splats (Fig. 4.11d). While tests like this were not used for measurements of hardness, they provided additional evidence of the poor bonding in the coatings from SM powders. As discussed previously, the SM powders had an acicular microstructure that resists plastic deformation of the particles upon impact; thereby resulting in porosity and improper bonding between the splats. Thus, the presence of porosity and de-bonding of splats during microhardness tests led to a low plateau hardness of these coatings and resulted in high hardness loss.

In the case of coatings deposited using IM powders, there was minimum interaction of the indenter with porosity at low loads as seen in Fig. 4.11e. At higher loads, the interaction of the indenter with porosity was comparatively higher and de-bonding was observed specifically in these regions, as shown in Fig. 4.11h. Even in dense regions de-bonding of splats was found when indentation was performed at higher loads indicating poor cohesive strength between the splats (Fig. 4.11f). Poor bonding between the splats reduces the cohesive strength and results in de-bonding. However, the sliding of adjacent splats was not observed for these coatings. De-bonding of the splats during

indentation reduces the load bearing capacity thereby reducing the plateau hardness of the coatings. This explains the low hardness of coatings deposited using IM powders despite low porosity and subsequently the higher hardness loss values.

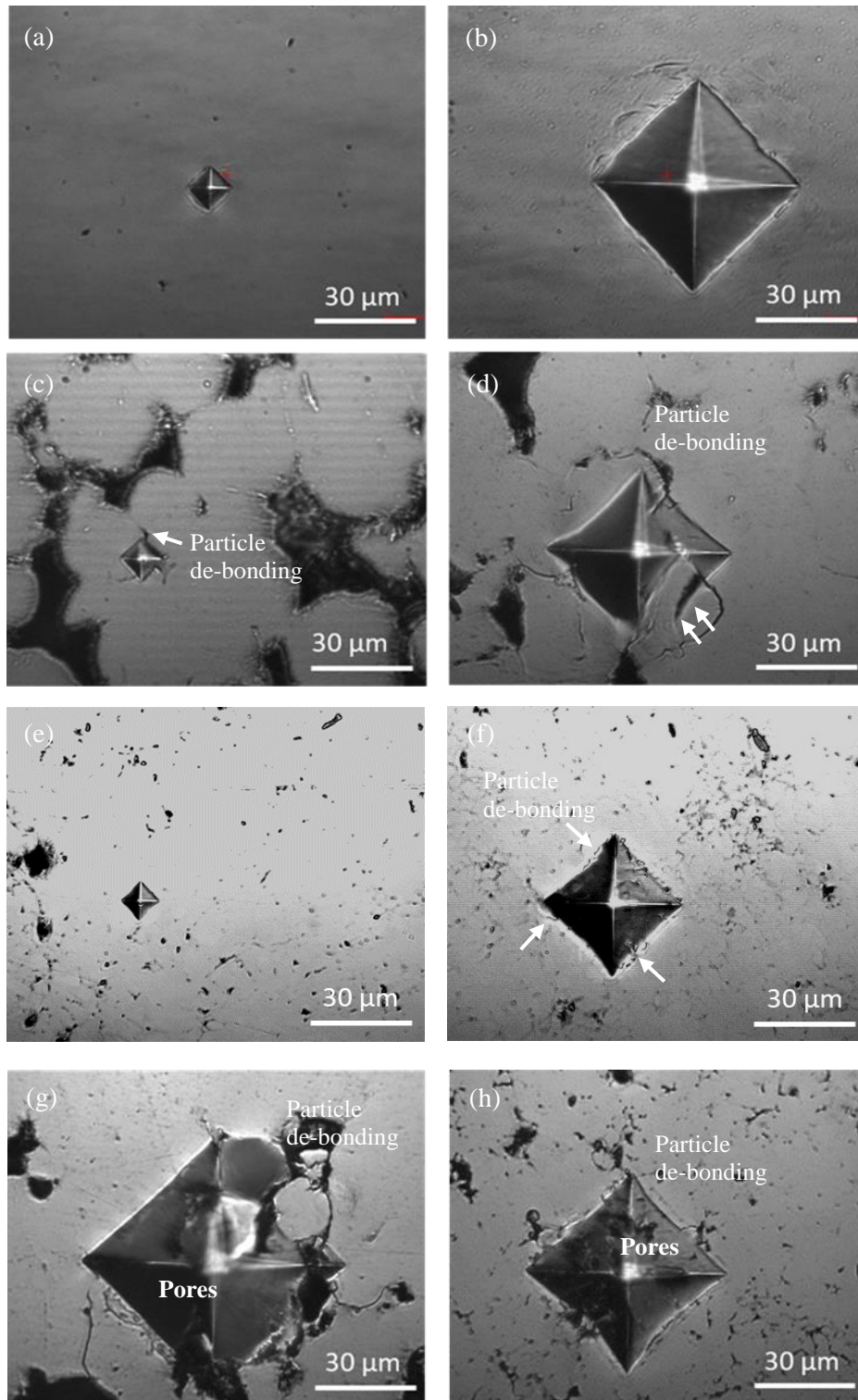


Fig. 4.11: Optical micrographs of the residual indents on (a) & (b) bulk Ti6Al4V plate at 25 g and 500 g load (c) & (d) coatings deposited using SM powders at 25 g and 500 g load (e) & (f) coatings deposited using IM powders at 25 g and 500 g load (g) & (h) porous region in the coatings deposited using SM and IM powders at 500 g load.

4.4 Discussion

4.4.1 General characteristics of the feedstock powders

Feedstock powders play an important role in the CS process since the successful deposition, microstructure and final properties of the coatings depend largely on powder initial properties. Some researchers have indicated that engineering of powders for better cold sprayability is one of the prime needs to develop and improve applications of the CS process [6,17]. One alloy system that has immediate applications for CS is Ti6Al4V, but the inherent high yield strength and melting point has made for mostly poor cold sprayability and inability to obtain a near fully dense deposit with acceptable mechanical properties. Past researchers have cold sprayed Ti6Al4V with SM powders, but attained limited success to obtain dense coatings without post heat treatments [13,15,203,209]. The most recent development for Ti and Ti6Al4V is the preparation of powders using the Armstrong process. Only a few reports have been made on this powder for CS, but some improvements are reported [6]. McDonald *et al.* deposited dense coatings of Ti using the Armstrong powders at low gas pressures and temperatures. They concluded that that unique morphology of the particles allows to deposit Ti coatings well below its critical velocity. The most common powder morphology for CS is spherical, and here we have compared spherical powders to irregular powders made by the Armstrong process.

The primary limitation in using IM powders is due to their poor flowability, which was true from their Hall flowability number. However, this did not have any significant effect on the coating characteristics like DE, porosity etc. SM powders have a good Hall flowability. The flow characteristics of the powders depend on various parameters like size, shape, interparticle friction and weight of the bulk powder [210]. The poor flowability of the IM powders can be attributed to their high interparticle friction and low apparent density. This impedes the free movement of one particle over another thereby resulting in poor flowability [210]. Another concern is that industries require no nozzle clogging or pulsating effects at the inlet of the nozzle that can often result from poor flowability and lead to waviness in the coatings [66]. However, despite their poor flowability, no pulsating effects, nozzle clogging or waviness in the final coatings was observed for the IM powders. In a high pressure CS system, pressurized N₂ gas passing through the feeder to transport the feedstock powders to the inlet of the nozzle may help counter the potential for poor flowability of the IM powders. Furthermore, while many irregular powders have been shown to be

unacceptable for CS, the unique morphology of the IM powders from the Armstrong process, with high specific surface area and complicated surface porosity may have allowed the pressurized gas to purge through them and improve their flowability in a forced gas environment.

4.4.2 Coatings characteristics

As discussed previously, high particle velocities and specific surface area enhance the particle deformation as the particle impacts the substrate. Additionally, the powder particle microstructure also plays an important role in determining the deformation of the incoming feedstock particles. Studies carried out by Murr *et al.* illustrated that Ti6Al4V alloy with acicular or martensitic lath like structure exhibits higher yield strength than lamellar and equiaxed microstructures [201]. Since in CS process, the coatings are developed by the plastic deformation of the powder particles, high yield strength materials need higher velocities to deposit coatings [80]. The SM had fine laths of α -phase leading to limited plastic deformation upon impact and a retention of most of the spherical shape. Powders of this type result in high porosity (seen in Fig. 4.7a), which has been observed by previous researchers [13,15]. In the case of IM powders, the microstructure was a more deformable equiaxed α -phase. This led to more deformation upon impact of the particles resulting in dense coatings with negligible porosity. Furthermore, IM powders had porosity (Fig. 4.3e) and also possess higher specific surface area compared to SM powders. These two aspects help for greater interaction between the particle and the hot gas stream thereby resulting in higher heat transfer [211]. An increase in particle temperature would cause thermal softening and lead to even more improvement of deformability of the IM powders.

In the past, researchers tried to engineer the powders and reduce porosity in Ti6Al4V coatings. Aydin *et al.* mixed Ti and Ti6Al4V and found that a mixture of 10 vol.% Ti to Ti6Al4V reduced the porosity from 6.7 % to 1.5 %; there was no effect with further increase in Ti% [15]. Lou *et al.* mixed different volume fractions of steel balls with Ti and Ti6Al4V powders to reduce porosity [20]. However, the resultant coatings had steel balls entrapped in the final coatings. Khun *et al.*, Bhattiprolu *et al.* and Vo *et al.* suggested that dense coatings of Ti6Al4V deposited using SM powders can only be achieved by spraying with He as propellant gas [13,16,17]. A summary of the above literature suggests that innovative techniques have been used to reduce the porosity in Ti6Al4V coatings; however, each technique had its own limitations or increased the deposition costs. In the present work, IM powders with deformable and porous structure were used to deposit

Ti6Al4V coatings. In view of the industrial requirements and cost economics, coatings were deposited using N₂ as propellant gas and no post treatments were performed. The Ti6Al4V coatings deposited using these powders were extremely dense with porosity < 1%.

Apart from deformable microstructure and high specific surface area other mechanisms may be acting as well for reduced porosity. Previously, Yin *et al.* and Lioma *et al.*, found that porosity in the particles reduced particle rebounding and resulted in dense coatings [102,103]. Their results illustrated that the fracturing of the pores as the particles make an impact, resulted in cracking thus absorbing the particle kinetic energy and reduce the probability of rebounding. Gao *et al.* reported that the coatings deposited using powder particles with high and medium porosity were dense and thick when compared to coatings deposited using powders with low porosity [62]. They concluded that optimum porosity and deformability of particles help in depositing dense coatings with continuous buildup. While no observation of particle fragmentation was made in this work, the mechanism described by previous researchers may also be partly responsible for the low porosity of the IM coatings.

4.4.3 Effect of powder morphology on coating microstructure

Comparisons of the microstructure of the coatings to the initial powders were performed with ECCI on the coating cross-sections near to the splat interface. Most of the splat microstructure in coatings from SM powders resembled that the initial feedstock particles and recrystallization was observed only close to the splat interfaces. Martensitic laths observed in the initial powder were found away from the recrystallized region indicating very limited deformation at these positions. These observations are similar to those reported previously by Goldbaum *et al.* and Kim *et al.* for SM powders of CP-Ti [25,85]. Recrystallization was observed close to the splat interface or boundaries where primarily ASI, strain localization and rise in interfacial temperatures predominantly takes place during the particle impact [85]. Since the rise in temperature is concentrated very close to the interface and the bulk of the particle remains at lower temperatures, recrystallization was observed close to the splat boundaries. The limited regions of recrystallized grains inside the splats from SM powders are a further indication of the limited deformation that took place, which led to the higher porosity and poorer mechanical properties.

ECCI of the splats in the coatings deposited using IM powders revealed a high degree of deformation with less evidence of initial feedstock microstructures. Nanograins were found along

the splat interfaces similar to that of the coatings deposited using SM powders as well as highly deformed regions adjacent to them proceeding into the splat interior. The high degree of deformation in these coatings was because of the unique particle morphology, higher impact velocities, particle temperatures and the deformability of the initial powder microstructure [6]. Previously, Schmidt *et al.* illustrated that low yield strength and high particle temperatures result in lowering the critical velocity for deposition [80]. Furthermore, higher particle impact velocities result in an increase in strain rates, total strain and higher interfacial temperatures at splat boundaries, leading to greater amounts of deformation and recrystallized regions. Additionally, a larger specific surface area and presence of pores result in a higher rate of heat transfer, thereby increasing the particle temperature and heat retention within the particle. Since Ti and its alloys have higher heat capacity compared to other metals like Zn, Cu, Pb, Sn etc., recrystallization and deformation are further enhanced by the temperature gradients across the particle interfaces, thus contributing to superior deformation [80].

4.4.4 Coating hardness and cohesive strength evaluated using multi-scale indentation

At the scale of nanoindentation, coatings with SM powders showed higher hardness than those with IM powders. This is largely due to the retention of the martensitic lath microstructure of the SM powders, which is known to have high hardness. While the IM powders formed fine scale recrystallized microstructures, the hardness of these features and the deformed particle interiors remained lower than for coatings from SM powders. At the scale of microindentation testing, Ti6Al4V coatings deposited using IM powders exhibited higher hardness compared to coatings deposited using SM powders. The improvement in the hardness can be attributed to lower porosity and better coating cohesion strength. As reported by Goldbaum *et al.* the two scales of indentation testing reveal distinctly different information on mechanical properties [119]. Nanoindentation helps for comparison of coating microstructure, while microindentation probes the effects of larger scale defects like porosity and splat boundaries.

The cohesive strength between the splats was examined through the hardness loss parameter [119]. A small hardness loss value indicates better inter-splat cohesive strength. Hardness loss was higher for CS coatings compared to bulk Ti6Al4V plate. This result is similar to what Goldbaum *et al.* observed for CS coating deposited from spherical and irregular CP-Ti powders [119]. Generally, it is not possible with cold-sprayed Ti and its alloys to observe the same mechanical properties as

their bulk counterparts. However, it should be noted that the hardness loss observed by Goldbaum *et al.* for CP-Ti at similar particle impact velocities to those obtained here was approximately 60% for both coatings deposited using spherical and irregular powders [119]. Here for Ti6Al4V, the hardness loss was around 65% and 53% for coatings deposited using SM and IM powders respectively. On one hand, this could be indicative of poor cohesive strength of the Ti6Al4V deposited using spherical powders, which would be expected considering the lower deformability of the alloy compared to the pure material. However, it may also be due to the high mechanical properties of the alloy in general. Furthermore, the marginally lower hardness loss obtained here for the coatings deposited using IM powders compare to irregular CP-Ti coatings could be due to the differences in specific surface area and porous structure of the feedstock powders that would have led to better cohesiveness between the splats. To better explain comparisons between this work and the previous study, one must turn to the examination of residual indents. Most of the features of splat debonding and interactions with porosity were observed in both studies. The only major difference found was the large scale debonding found for the SM coatings. This is the most direct comparison to the previous work as the morphology of the powder is very similar to that used by Goldbaum *et al.* and we see an increase in hardness loss for SM Ti6Al4V compared to SM CP-Ti [119]. However, turning to the coatings from IM powders, the hardness loss was lower than previously observed for CP-Ti coatings and SM powders of Ti6Al4V sprayed here. More importantly, the features observed on residual indents were much less dramatic in terms of splat debonding. There was evidence of small scale debonding events but no large scale failures at splat interfaces. Thus, despite the high hardness loss of the coatings from IM powders, they exhibited relatively better features in terms of cohesive strength compared to both the SM powders sprayed here and the previous work of Goldbaum *et al.* [119] Similar evidence of de-bonding of splats in the case of dense Ti coatings (deposited using Armstrong powders) can be seen from the indent images reported by MacDonald *et al.* [6]. They proposed that the unique morphology of the powders could have led to flattening of particles and subsequent coating build-up with low cohesive strength. Thus, the de-bonding of splats observed in the optical micrographs of the residual indents coincide with the low hardness values reported and support the high hardness loss in CS coatings when compared to bulk Ti6Al4V plate.

Hardness loss values can be a good indicator of coating tensile properties [212]. Coatings with dense microstructure and good cohesive strength between the splats exhibit better tensile

properties. Low hardness loss indicates that the coatings possess better cohesive strength and in turn show better tensile properties [212]. This can be seen from the results reported by MacDonald *et al.* in which the as-sprayed Ti coatings using the Armstrong powders had shown de-bonding of splats and poor tensile properties [6]. SEM images of the fracture surfaces after the tensile tests showed almost no evidence of metallurgical bonding between the splats indicating their poor inter-splat bonding. However, subsequent heat treatment of the coatings resulted in improvement in cohesive strength resulting in better tensile properties.

The effectiveness of powders from the Armstrong process in terms of their cold sprayability and mechanical properties of coatings were evaluated and compared to coatings from SM powders. Overall, there are clear and significant benefits imparted by the IM powders obtained from the Armstrong process for cold spraying of Ti6Al4V. However, the resulting mechanical properties are poor. While the residual indent features of the coating from IM powders was somewhat improved with no large-scale failures along splat boundaries, the mechanical properties were still clearly deficient with the spray conditions used here. Options left for researchers seeking to obtain a high quality deposit of Ti6Al4V would be to include some sample heating during deposition, which has been shown to be effective in the past or to spray with Helium (He) [17,117]. Spraying with He has clear benefits with much higher particle speeds, leading to fully dense coating with much better mechanical properties [13,16]. In fact, the hardness loss was zero for a deposit of CP-Ti with He spraying [119]. Others spraying with He have observed good mechanical properties as-deposited. However, engineers seeking applications for the Armstrong process IM powder must consider costs and sustainability. Spraying with He is not sustainable and costly. And including heating during spraying or post heat treatments is not cost friendly and may not always be practical. Thus, while this study has demonstrated significant promise for the Armstrong process IM powder, the need for other steps in manufacturing a mechanically robust deposit of Ti6Al4V by CS seem to still be required. Further research will be required to determine which steps are most effective and economically feasible.

4.5 Conclusions

Ti6Al4V coatings have been cold sprayed using SM and IM powders. A detailed characterization was performed to understand the physical and microstructural properties of the feedstock powders and were related to the coating properties. Hardness loss through multi-scale indentation was

determined to understand the cohesive strength between the splats. Based on the study following conclusions are drawn:

1. SM powders had a cellular surface structure and excellent flowability whereas IM powders had a porous structure with poor flowability. ECCI on the cross-section of the SM powders revealed a martensitic lath like structure whereas IM powders showed an equiaxed microstructure. The two different morphologies and microstructures have a significant influence on the properties of cold sprayed coatings.
2. Coatings deposited using IM powders had low porosity (< 1%), higher hardness and DE compared to the coatings deposited using SM powders. This was due to their higher particle velocity, specific surface area and more deformable microstructure compared to SM powders.
3. Multi-scale indentation was performed on the coatings and bulk Ti6Al4V plate to determine the hardness loss. Hardness loss was higher in cold sprayed coatings compared to the bulk Ti6Al4V plate due to the presence of porosity and poor cohesive strength between the splats.
4. Coatings deposited using SM powders exhibited high hardness loss due to particle de-bonding and the presence of a significant amount of porosity. Residual indents showed the adjacent particle sliding over the indent in these coatings indicating poor inter-splat bonding contributing to high hardness loss.
5. Despite low porosity, coatings deposited using IM powders exhibited hardness loss but lower than their spherical counterparts. In these coatings, de-bonding of splats resulted in hardness loss and no adjacent particle sliding on the residual indent was observed.

Acknowledgements

The authors are thankful for the technical assistance from Jean-Francois Alarie, Dina Goldbaum and Maniya Aghasibeig. The authors gratefully acknowledge the contributions of Rene Cooper from Cristal Metals for providing the irregular Ti6Al4V powders.

Chapter 5

The influence of powder properties on the adhesion strength and microstructural evolution of cold sprayed Ti6Al4V single splats

Venkata Naga Vamsi Munagala, Sara I. Imbriglio and Richard. R. Chromik

Adapted from a paper of the same title published in *Materials Letters*, 2019, **244**:58 – 61.

Abstract

The adhesion strength and microstructure of single splats significantly influence the properties of cold sprayed coatings. Here, we compare the adhesion strength and microstructural changes of Ti6Al4V spherical powder (SP) particles with a martensitic microstructure and irregular powder (IP) particles with an equiaxed microstructure deposited by cold spray (CS). Splat adhesion tests were performed to determine the adhesion strength and electron channelling contrast imaging was done for microstructural analysis of splat cross-sections. IP splats formed a continuous bonded interface with the substrate resulting in a greater adhesion strength when compared to SP splats. IP splat cross-sections revealed ultrafine grains (UFG) near the interface followed by a highly deformed microstructure. SP splat cross-sections also showed UFG at the interface but largely retained the initial microstructure in the top portion of the splat due to poor deformability. The irregular morphology of the IP led to more adherent deposits while the equiaxed microstructure resulted in highly deformed post spray microstructures.

Keywords: Adhesion; Cold spray; Microstructure; Ti6Al4V; Armstrong powders; single splats

5.1 Introduction

The cold spray (CS) process involves the acceleration of powder particles to supersonic velocities for impact onto a substrate resulting in coating buildup [79,202]. The process is widely used for the repair of worn aerospace, automobile and marine components made of Ti and its alloys, due to its versatility and ability to deposit powder particles in solid state [5]. However, Ti6Al4V coatings deposited using plasma gas atomized (PGA) powder have high porosity. Techniques to reduce

porosity include spraying with He, using mechanically blended powders or *in situ* shot peening assisted deposition [13,15,17,20]. These techniques are either complex, non-sustainable or non-economical for industrial applications.

Since coating formation relies on deformation of powder particles to form a splat, microstructural changes in splats and adhesion in splat interfaces or splat-substrate interfaces largely affect coating properties [79]. Adhesion strength measurements and microstructural analysis at splat level forms a fundamental approach to understand the bulk coating characteristics [7,25,92,116,117,213]. Post spray microstructure and adhesion strength of Ti6Al4V splats deposited using PGA powders have been studied extensively [92,117,118]. Scanning electron microscope (SEM) and transmission electron microscope images of splat cross-sections have shown that deformation and recrystallization occurs only at the splat-substrate interface, while the bulk of the particle retains its initial microstructure [18,25,92]. The low deformability of these powders results in poor bonding between the splats and porosity in the bulk coatings.

Recently, Ti and Ti6Al4V powders with irregular morphology were manufactured using an Armstrong process, which is more economical compared to the PGA process [6,193]. Cold spraying these powders produces deposits that are more dense than deposits made with PGA powders [6,73]. In our previous study [73], the cohesive strength of coatings made with PGA and Armstrong powders was evaluated by multi-scale indentation. The improvements of decreased porosity and increased cohesive strength for coatings made from Armstrong powders were tied to increased in-flight particle velocity, due to irregular morphology, and deformability, due to particle microstructure. However, the relative importance of these two factors could not be fully determined in the previous work [18]. In the present study, to better understand the candidate mechanisms for improved deposition with Armstrong powder versus PGA powders, the adhesion and microstructural transformations are studied for single irregular powder (IP) and PGA Ti6Al4V particles sprayed onto Ti6Al4V substrates at similar spray conditions and particle velocities. Splat adhesion testing [116] was done to determine the adhesion strength and ECCI was performed on the splat cross-sections to characterize the post spray microstructures.

5.2 Experimental

Single splats were deposited on Ti6Al4V substrates (McMaster Carr, Canada) using a PCS 1000 cold spray system (Plasma Giken, Japan) with nitrogen as the propellant gas. Ti6Al4V (Grade 5) powders with a spherical morphology (average diameter $\sim 31 \mu\text{m}$), manufactured using PGA, and irregular morphology (average diameter $\sim 38 \mu\text{m}$), manufactured using the Armstrong process, were used for depositing splats. The size distribution and detailed characterization of the powder particles are presented elsewhere [17]. For depositing splats using spherical powders, the gas pressure and temperature were fixed at 4.9 MPa and 950°C whereas the IP splats were sprayed at two different temperatures, 600°C and 950°C respectively, keeping the pressure constant at 4.9 MPa. The gun transverse speed was $1 \text{ m}\cdot\text{s}^{-1}$ and the in-flight particle velocity was measured using a time-of-flight particle diagnosis system (Coldspraymeter, Tecnar Automation, Canada).

After deposition, the samples were cut and polished using SiC abrasive papers up to a grit size of 1200 and subsequently with diamond suspension solution of 9 μm , 3 μm , 1 μm and finally using 0.05 μm colloidal suspension. Polished IP splat cross-sections were ion-milled using a IM300 flat milling system (Hitachi High-Technologies, Japan) to remove edge rounding induced by polishing. To observe the splat microstructure, ECCI was performed using a cold field emission SEM (SU8230, Hitachi, Japan) equipped with a photo-diode back scattered electron detector.

Adhesion strength of single splats was measured using a Micro-Combi scratch tester (CSM Instruments, USA) to perform splat adhesion testing [116]. A semi-circular tipped stylus of diameter 100 μm was mounted on the scratch tester and the flat edge of the tip was used to scratch the splats off the substrate. Prior to testing, an optical image of the splat was captured using a light optical microscope attached to the scratch tester. For all the tests, the scratch length, speed and normal force (on the tip) were 100 μm , 150 $\mu\text{m}\cdot\text{min}^{-1}$, and 100 mN, respectively. During the entire test, the tangential force experienced by the stylus was continuously recorded. As the stylus encountered the splat, a rise in tangential force ($F_{T \text{ Peak}}$) was observed followed by a sudden drop at interface failure ($F_{T \text{ Baseline}}$). This data was used to determine the adhesion strength in shear i.e. in parallel to the splat-substrate interface using Eq. 5.1 [116]. At least 15 splats were tested to determine the average adhesion strength.

$$\text{Adhesion strength (MPa)} = \frac{F_{T \text{ Peak}}(\text{mN}) - F_{T \text{ Baseline}}(\text{mN})}{\text{Projected area of the splat } (\mu\text{m}^2)} \quad 5.1$$

5.3 Results and discussion

The particle velocity and the adhesion strength of the splats are summarized in Table 5.1. At the same spray conditions (Table 5.1), the higher velocity of IP particles compared to spherical powder (SP) particles was due to the higher drag force acting on them [73,97]. The adhesion strength of IP splats was higher compared to SP splats at the same spray conditions as confirmed by an independent samples t-test (i.e. student's t-test). However, at more similar particle velocities, their adhesion strength was not different. In the t-test, the null hypothesis was rejected if the p value was less than 0.05. The higher adhesion strength of IP splats, at identical spray conditions, was due to the irregular shape that lead to higher particle velocities. For Ti6Al4V, Goldbaum *et al.* showed that higher velocities leads to more conformal bonding and higher splat adhesion strength [117].

For Armstrong powders, the irregular surface morphology enables the particles to have a large number of localized contact points and greater strain localization during particle impact [54]. Comparison of splat morphology for SP and IP is shown in Fig. 5.1. For the Armstrong IP, the localized jetting can be seen in the side view images of the splat (see Fig. 5.1b and c). Contrarily, jetting along the entire periphery was observed from the top view in SP splat (Fig. 5.1a). This is a general characteristic of cold sprayed SP particle [92,202].

Table 5.1 Particle velocity and adhesion strength of the splats.

Powder	Gas pressure (MPa)	Gas temperature (°C)	Particle velocity (m·s ⁻¹)	Adhesion strength (MPa)
Spherical	4.9	950	782 ± 152	107 ± 53
Irregular	4.9	950	865 ± 174	153 ± 48
Irregular	4.9	600	752 ± 135	109 ± 51

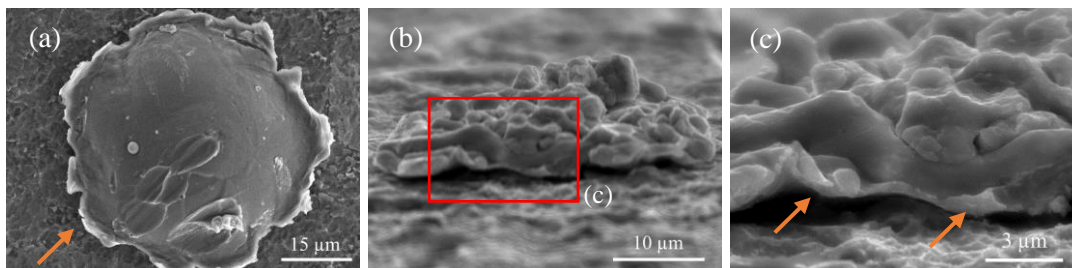


Fig. 5.1: SEM images of the splats deposited at 4.9 MPa and 950°C (a) Top view of the SP splat (b) side view of the IP splat (c) higher magnification image of IP splat; Arrow indicates jetting.

Cross-sectional splat morphology also appeared to be significantly different for both powders (Figs. 5.2 and 5.3). SP splat cross-sections showed discontinuous bonding at the splat-substrate interface with very few bonded sites (Fig. 5.2b). IP splat showed more continuous bonding with a few interface voids (Fig. 5.3b). As SP particles impact, the centre experiences the highest hydrostatic pressure leading to rebound and void formation [92,202]. Adiabatic shear instabilities at the outer edges result in bonding. [79,92] The formation of void at the centre of the spat-particle interface in SP splat can be seen in Fig. 5.2b.

The microstructural changes occurring after impact were studied by comparing splat cross-sectional microstructure and initial powder microstructures in ECCI images. Initially, SP had a martensitic lath microstructure (Fig. 5.2a) while IP had an equiaxed microstructure (Fig. 5.3a). SP splat cross-sections revealed three regions of different microstructures whereas IP splat cross-sections showed two distinct microstructures. At the interface, both SP and IP splats had ultra-fine grains (UFG). Yet, the height of the UFG region differed for IP and SP splats (Fig. 5.2e and 5.3e). In SP splat, UFG were seen up to a distance of $\sim 3 \mu\text{m}$ from the splat-substrate interface (Fig. 5.2e), followed by elongated submicron grains (Fig. 5.2d) and finally a retained martensitic lath microstructure at the top surface (Fig. 5.2c). The formation of submicron grains was due to the re-orientation of an accumulated high density of dislocations during severe plastic deformation while UFG were formed due to the progressive deformation of the particle after the creation of submicron grains [7,92]. Thus, UFG were mainly observed near the splat-substrate interface where particles experience high strain rates resulting in continuous dynamic recrystallization. Contrarily, in IP splats, UFG were seen up to a distance of $\sim 4.5 \mu\text{m}$ (Fig. 5.3d and 5.3e) followed by a heavily deformed microstructure up to the top surface of the splat (Fig. 5.3d and 5.3c). The initial microstructure was not completely retained due to the deformable equiaxed microstructure of IP in contrast to the hard martensitic lath microstructure of SP. The advantages of using these irregular powders for CS of Ti6Al4V are consistent with previous observation in full coatings. IP coatings had negligible porosity and better cohesive strength between splats compared to SP coatings [73].

Substrates also had evidence of deformation in their microstructure. Near the particle-substrate interface, substrates had recrystallized UFG. Further away from the interface, highly deformed grains were observed. The formation of UFG in the substrate for SP and IP splats can be seen in Figs. 5.2f and 5.3e. A more continuous layer of UFG was observed in the substrate of IP splats

compared to SP splats which could be due to the higher impact velocity and localized contact points of impact of the IP.

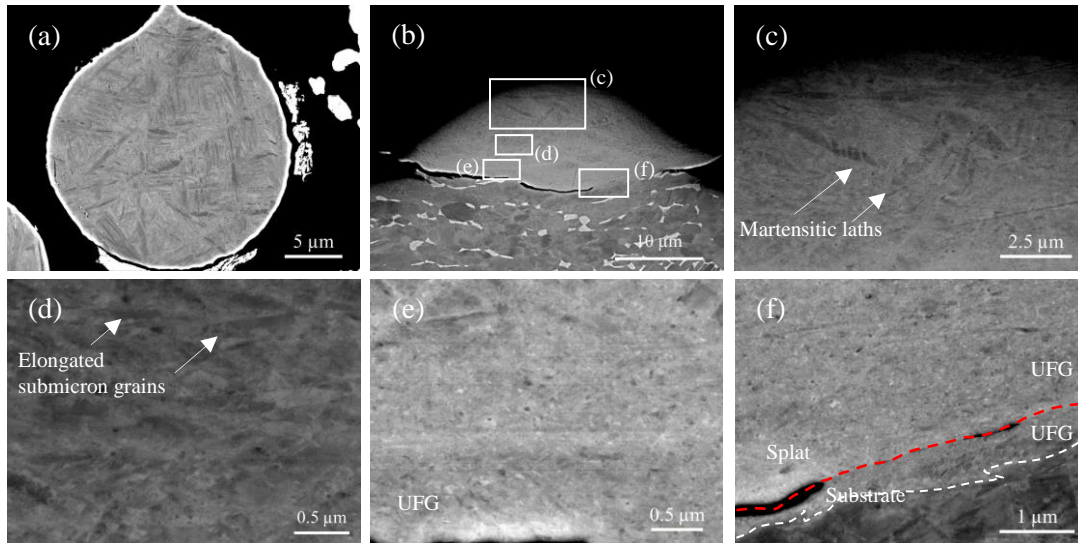


Fig. 5.2: ECCI of SP (a) particle (b) splat deposited at 4.9 MPa and 950 °C (c) top region of the splat (d) splat middle region showing sub micron grains (e) splat UFG region at the splat-substrate interface (f) splat-substrate bonded interface; Red dashed line indicates splat-substrate interface and white dashed line indicates the UFG and highly deformed region interface in the substrate.

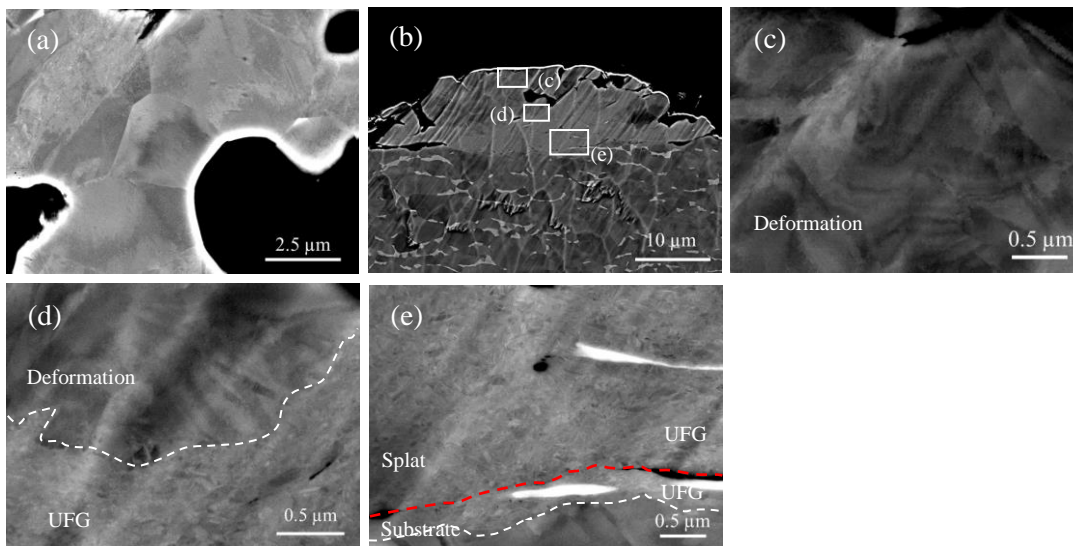


Fig. 5.3: ECCI of IP (a) particle (b) splat deposited at 4.9 MPa and 950°C (c) splat top region of the splat (d) splat middle region showing UFG + deformation (e) bottom of the splat and splat-substrate bonded interface. Red dashed line indicates splat-substrate interface and white dashed line indicates the UFG and highly deformed region interface in the substrate.

5.4 Conclusions

Splat adhesion tests along with ECCI of splat cross-sections helped to understand the adhesion strength and microstructural changes that occur in both powders. IP splats showed higher adhesion strength than SP splats. This was due to their irregular morphology that accelerates them to higher velocities at similar spray conditions. However, when sprayed at the same particle velocity, the IP splats did not show an improvement in adhesion strength compared to SP splats. These results indicate that particle velocity has more profound effect on the adhesion strength rather than microstructure. ECCI of the splat cross-sections showed greater extent of grain refinement and microstructure transformations in IP compared to SP indicating their high deformability. Lastly, for IP, when sprayed at lower gas temperatures to attain similar particle velocities as SP, both splats showed similar adhesion strength. This indicates that Armstrong manufactured irregular powders can be used to deposit Ti6Al4V coatings on to heat sensitive components with adhesion strength comparable to that of PGA powders.

Acknowledgements

The authors are thankful for the technical assistance from Maniya Aghasibeig and Jean-Francois Alarie at McGill Aerospace Materials and Alloy Design Centre (MAMADC). The authors gratefully acknowledge the contributions of Rene Cooper from Cristal Metals for providing the irregular Ti6Al4V powders. This project would also not have been possible without the financial support from the Natural Science and Engineering Research Council (NSERC) Strategic Grants Program.

Chapter 6

Sliding wear of cold sprayed Ti6Al4V coatings: Effect of coating properties and normal load

Venkata Naga Vamsi Munagala, Stéphanie Bessette, Raynald Gauvin and Richard R Chromik

This manuscript is intended to be submitted to a journal. In chapter 3, Ti6Al4V coatings were cold spray deposited using two morphologically and microstructurally distinct powders resulting in coatings with different physical and mechanical properties. In the present chapter, the influence of coating properties on the tribological behaviour of cold sprayed Ti6Al4V coatings is studied. In addition, the third bodies generation, chemical compositions and their activities at the tribo-pair interface in modifying the friction and wear mechanisms at different normal loads was investigated.

Abstract

The aim of the present study is to understand the influence of coating characteristics on the friction and wear behaviour of cold sprayed Ti6Al4V coatings. Sliding wear tests were performed at different normal loads on Ti6Al4V coatings deposited using spherical and irregular powders manufactured using plasma gas atomization and Armstrong processes. Despite low porosity and high hardness, irregular powder deposited coatings showed higher wear rates compared to spherical powder coatings. In case of irregular powder coatings, abrasive ploughing by the wear debris led to high wear rates whereas presence of porosity in spherical powder coatings, entrapped the wear debris generated during sliding and decreased the wear rate. Increase in normal load led to a decrease in wear rate and CoF in both coatings. The decrease in wear rate was due to tribo-oxidation in irregular powder coatings whereas the combined effect of entrapment of debris along with tribo-oxidation resulted in much lower wear rates in spherical powder coatings. Transmission electron microscopy (TEM) analysis showed that the third bodies filled in the pores consisted of highly deformed material with ultrafine grain microstructure and micron sized particles from the counterface while the wear track had comparatively coarse grain microstructure. Results indicated that despite low hardness of SP Ti6Al4V coatings, presence of porosity facilitated for the

entrapment of wear debris generated from first bodies which inhibited abrasive ploughing and contributed to low wear rates.

6.1 Introduction

Due to its high strength-to-weight ratio, high temperature thermal stability and excellent corrosion resistance Ti alloys especially Ti6Al4V is widely used in automobile, aerospace and marine applications [5,6,214]. However, the high costs and complex steps involved in manufacturing Ti parts due to its high reactivity and poor machinability requires alternate processes [215]. Recently cold spray (CS) or cold gas dynamic spraying is being used to deposit Ti and its alloys both as bulk and coatings [5,6,66,73]. In case of CS, micron sized particles are accelerated to supersonic velocities (600 to 1200 m.s⁻¹) to impact on to a substrate and plastically deform. Since the coating formation occurs through plastic deformation of particles rather than melting, there are no phase transformation, minimal oxidation and tensile residual stresses in the final deposits [79]. Due to the versatility of the process and high deposition rates, CS is being widely used to deposit metals, composites and nanostructures coatings on to various substrates [61,69].

Despite having numerous advantages, deposition of high yield strength materials like Ti6Al4V using nitrogen as propellant gas remained challenging in terms of achieving low porosity levels (< 2 %). Recently, Ti6Al4V powders of irregular morphology with porous structure manufactured using Armstrong process resulted in extremely dense deposits compared to conventional gas atomized powders. The formation of dense coatings was attributed to the irregular morphology that led to high particle velocities and equi-axed microstructure facilitated the particle deformation upon impact. In contrast, the hard-martensitic lath microstructure of the spherical powders (SP) inhibited their deformation and resulted in high porosity in the coatings. Although the coating characteristics and mechanical properties of the Ti6Al4V coatings deposited using the Armstrong and PGA powders are studied but their tribological properties are not yet fully explored. It is well known that the tribological properties of a coating material depend on several factors including microstructure, cohesion strength between the particles and hardness [34,216–218]. In case of pure metals or alloys, during dry sliding under the influence of a normal load, tribo-oxidation leads to the formation of continuous or islands of oxide films. The presence of oxide layer prevents metal-to-metal contact and changes the friction and wear behaviour of the tribo-pair. The oxide films grow in thickness as the sliding progresses and after reaching a critical thickness (~1 – 5 µm for

metals) they undergo fragmentation. The break down of the oxide films exposes the fresh metal underneath while the fragmented oxide particles act as abrasives resulting in ploughing and high wear rates [26,27,29,34,219,220]. While these mechanisms are observed broadly, the presence of porosity, tribo-chemical reactions, localized temperature etc. effect the third bodies generation, chemical compositions and their flow inside the tribological circuit and change the friction and wear mechanisms [48,162,174].

Previously Dubrujeaud *et al.* observed that the volume fraction of porosity in the material influences its tribological behaviour [218]. Their results showed that increase in porosity (< 20 vol.%) initially decreased the wear rates due to entrapment of wear debris into the pores while high porosity levels (> 20 vol.%) decreased mechanical strength resulting in excessive plastic deformation and high wear rates. A similar decrease in wear rates due to the presence of optimum porosity were reported by Lim *et al.* and Straellini *et al.* [217,221]. However, Ceschini *et al.* illustrated that apart from porosity volume fraction, shape of the pore also has a considerable effect on the wear resistance of the material [222]. They found that sharp pores acted as stress concentration sites and led the nucleation of microcracks that subsequently led to the formation of wear debris and increased the wear rates.

Li *et al.* found that in case of Ti alloys increase in sliding velocity and contact pressure results in tribo-oxidation and formation of an oxide rich tribolayer that changed the wear mechanisms from severe to mild wear [220]. Similarly, Farokhzadeh *et al.* reported transition in wear mechanisms from severe to mild in Ti alloys due to increase in normal load that led to greater rate of oxidation, formation of tribolayers and decreased the wear rate [34]. A summary of these studies indicates that localized features, coating characteristics and interfacial temperatures, normal load change the third bodies activities and intern change the friction and wear mechanisms.

In the present study, the tribological behaviour of cold sprayed Ti6Al4V coatings deposited using spherical and irregular powders are investigated. The influence of coating properties and normal load on the friction and wear behaviour of the coatings are studied in detail. ECCI of the wear track cross-sections were done to characterize the subsurface microstructures. TEM analysis was done at specific locations on the wear track to compare the subsurface microstructures and understand the chemical composition of the third bodies. Nanoindentation was performed to determine the mechanical properties of the third bodies.

6.2 Experimental procedure

Ti6Al4V coatings were deposited using spherical Ti6Al4V powders (AP&C, Canada) and irregular Ti6Al4V powders (Cristal metals, USA) of size ranges 15 – 45 μm and 0 – 45 μm respectively. The SP were manufactured using plasma gas atomization process while the irregular powders (IP) were manufactured using Armstrong process. The size distribution and the average particle diameter of the powders were presented in our previous publication [73]. Coatings were deposited on mild steel plates of dimensions 75 x 75 x 3 mm^3 . Prior to deposition the substrates were degreased, and grit blasted using alumina to enhance the coating-substrate bonding. Cold sprayed coatings were deposited using a PCS 800 cold spray system (Plasma Giken, Japan) with nitrogen as propellant gas. The gas stagnation pressure and temperature were 4 MPa and 800°C respectively. The standoff distance between the nozzle exit and the substrate was 40 mm and the gun traverse speed was 200 $\text{mm}\cdot\text{s}^{-1}$.

After deposition the coatings were cross-sectioned in the direction perpendicular to the gun traverse direction and cold mounted. The mounted specimens were polished using SiC abrasive papers of grit 320 to 1200 and using 9 to 1 μm polycrystalline diamond suspension and finally using 0.05 μm colloidal silica suspension solution. The polished coatings cross-sections were examined under a scanning electron microscope SU3500 (Hitachi, Japan) fitted with a back scattered electron (BSE) detector. BSE images were taken at fifteen different locations and were uploaded into ImageJ software to determine the porosity and average pore diameter. The porosity in the coatings was calculated by measuring the pixels associated with the differences in contrast. To determine the hardness of the coatings, indentation was performed on the top surface of the coatings using a microhardness tester (Buehler, USA) equipped with a Vickers diamond indenter. Indentation was performed at 5 kg load with a hold time of 15 seconds.

Sliding wear tests were performed using a custom built ball-on flat reciprocating tribometer. WC-Co balls of diameter 6.35 mm were used as counterfaces. Prior to wear testing, the top surface of the coatings was polished in a similar procedure as that of the cross-sections until the final polishing step using 0.05 μm colloidal silica suspension solution. All tests were performed in dry air environment (relative humidity < 2%) and at normal loads 0.5 N, 2.5 N and 5 N. At least 3 tests were performed at each load. The sliding speed was fixed at 3 $\text{mm}\cdot\text{s}^{-1}$, and tests were run for a total sliding distance of 10 m. The coefficient of friction (CoF) was determined by dividing the frictional

force with normal force and was continuously recorded during the entire test duration. To calculate the wear rate, the worn samples at the end of the test were analyzed using a non-contact optical profilometer (Zygo Corporation, USA) and profiles were generated across the wear tracks. At least 35 profiles were generated across the wear track and wear area was determined by integrating the profiles above and below the unworn surface (selected as reference surface). This was multiplied by track length to obtain wear volume (mm^3) and was normalized with load (N) and total sliding distance (m) to calculate the wear rate ($\text{mm}^3 \cdot \text{N}^{-1} \cdot \text{m}^{-1}$).

To understand the wear mechanisms, the worn coatings and counterfaces were examined under the SEM SU3500 equipped with BSE and EDS detectors. BSE images of the wear tracks were taken and exported into ImageJ software and the pixels associated with the contrast of the tribolayers (formed on the wear tracks) were calculated, to determine the wear track area covered with tribolayers. In addition, to determine the chemical composition of the third bodies Raman analysis was performed using an inVia Raman spectrometer (Renishaw, UK) with Ar^+ laser source of $\lambda = 514.5$ nm. To characterize the third bodies and subsurface microstructures, electron channeling contrast imaging (ECCI) was performed on the polished wear track cross-sections using FE-SEM SU8230 (Hitachi, Japan) equipped with annular photo diode backscattered electron (PDBSE) and FlatQUAD EDS (Bruker, USA) detectors. The ECCI images were exported into ImageJ software and the size of the grains was determined. At least 60 to 100 grains were measured in each region and averaged, to determine the average grain size. Nanoindentation was performed using a Triboindenter (Hysitron Corporation, USA) at a peak load of 5 mN on the wear track cross-sections to determine the mechanical properties of third bodies. The hardness and elastic modulus were determined by analyzing the load-displacement curves using Oliver and Pharr method [196]. At least 10 indents were performed on each feature to calculate the respective average values. Indentation was performed in a grit pattern starting from the unworn coating up till the worn surface. To determine the hardness of a particular feature, imaging of the residual indents was done using FE-SEM SU8230 and were subsequently matched to the corresponding load-displacement curves. TEM analysis was performed on the wear track of spherical Ti6Al4V coating at different locations to compare the subsurface microstructures. To achieve this, thin lamellae were cut using focused ion beam (FIB) (FEI Helios Nanolab 660, Thermo Fisher Scientific, USA) and were examined under a cryo-transmission electron microscope (TEM) (FEI Tecnai G2 F20, Thermo Fisher Scientific, USA).

6.3 Results

6.3.1 Coatings and their characteristics

The properties of the coatings deposited using spherical and irregular Ti6Al4V powders are summarized in Table 6.1. Spherical powder deposited Ti6Al4V coatings had significant porosity while the irregular powder coatings were dense with negligible porosity. The SEM images of the coatings were presented in our previous work [73]. The high porosity in spherical powder coatings was mainly due to the inherently hard martensitic microstructure of the particles that resulted in their poor deformability upon impact. The IP had more deformable equiaxed microstructures and their irregular morphology accelerate them to much higher velocities due to greater drag force compared to SP for similar spray conditions [97] leading to extremely dense deposits. The microhardness of the irregular powder coatings was higher compared to the spherical powder coatings due to lower porosity and better cohesive strength between the splats [73]. Contrarily, the nanohardness of irregular powder coatings was lower compared to spherical powder coatings. This was due to the equi-axed microstructure of the irregular powder coatings in contrast to the hard martensitic lath microstructure of spherical powder coatings [73].

Table 6.1 Coatings properties.

Coating	Porosity (%)	Average pore diameter (μm)	Microhardness ($\text{HV}_{5 \text{ kg}}$)	Nanohardness (GPa)
SP Ti6Al4V	13.0 ± 2.0	25	174 ± 8	5.7 ± 0.3
IP Ti6Al4V	0.3 ± 0.1	---	191 ± 12	4.8 ± 0.4

6.3.2 Sliding wear tests

6.3.2.1 Friction and wear

The CoF versus the cycle number plotted for both coatings at corresponding normal loads is shown in Fig. 6.1. The average CoF was calculated by averaging the CoF over the entire sliding distance is summarized in Table 6.2. For a given load, the average CoF for the coatings was found to be largely similar and there was a trend of decrease in CoF with an increase in normal load. In both

Ti6Al4V coatings, the CoF curve at 0.5 N load was found to be high and largely fluctuating between 0.45-0.70. As the normal load increased the CoF showed fewer fluctuations. At 2.5 N, the CoF was found to be varying between 0.35 – 0.45 and at 5 N load between 0.35 – 0.42 in both the coatings. The CoF in irregular powder coatings at 2.5 and 5 N appeared to be less fluctuating compared to SP, however, there was no significant difference in their average CoF.

The wear rate of the coatings at the end of 1000 cycles at different normal loads is shown in Fig. 6.2. Spherical powder Ti6Al4V coatings showed lower wear rates compared to irregular powder coatings at all loads. An increase in normal load from 0.5 N to 2.5 N decreased the wear rate in irregular powder coatings, and beyond 2.5 N the wear rate was almost constant. Contrarily, in case of spherical powder Ti6Al4V coatings, there was a steady decrease in wear rate with increase in normal load from 0.5 N to 5 N.

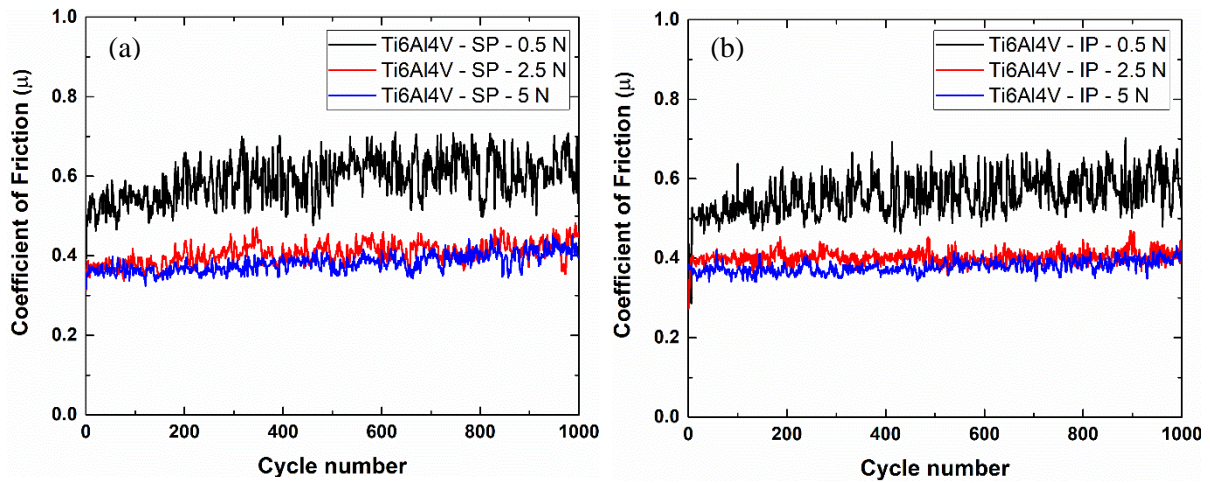


Fig. 6.1: Coefficient of friction versus sliding distance for (a) spherical powder deposited Ti6Al4V (b) irregular powder deposited Ti6Al4V coatings at different loads.

Table 6.2 Average CoF of the coatings at different loads.

Coating	0.5 N	2.5 N	5 N
SP Ti6Al4V	0.59 ± 0.05	0.41 ± 0.03	0.38 ± 0.02
IP Ti6Al4V	0.56 ± 0.05	0.40 ± 0.02	0.38 ± 0.02

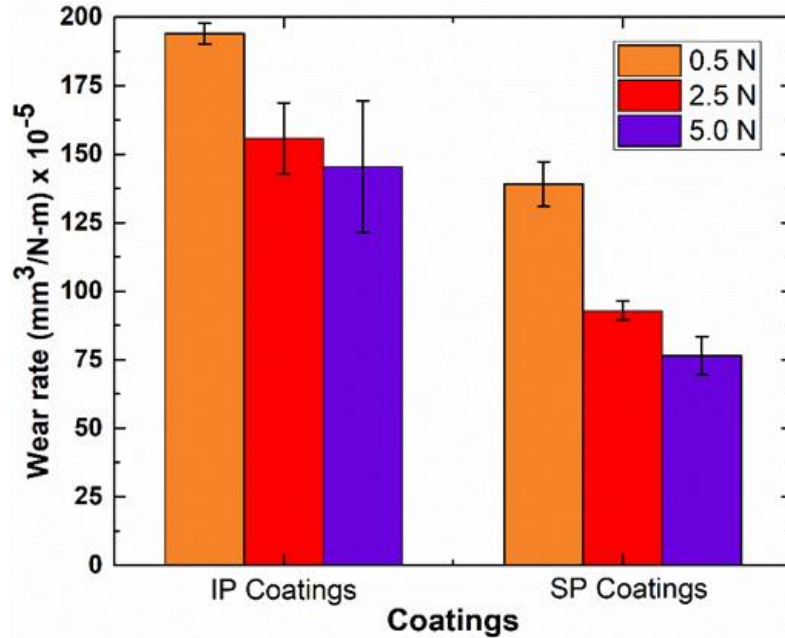


Fig. 6.2: Wear rate of the coatings at the end of the 1000 cycles.

6.3.3 Characterization of the worn surfaces

6.3.3.1 Wear track

To understand the wear mechanisms, the wear tracks were characterized using an SEM and are shown in Fig. 6.3 and 6.4. SEM images of the worn surfaces of both spherical and irregular powder coatings showed abrasive wear along with the presence of ploughing marks in the sliding direction (see Fig. 6.3a-e and 6.4a-e). The abrasive grooves were formed due to the entrapment of the wear debris between the two sliding surfaces or due to the scoring action of the counterface. Furthermore, presence of small tribolayers surrounded by wear debris were observed on the wear tracks of both coatings (see Fig. 6.3a,c,e and 6.4a,c,e). BSE images showed darker contrast at these locations compared to the wear track (see Fig. 6.3b,d,f and 6.4f) and EDS analysis performed at these locations showed higher amount of oxygen content compared to other regions of the wear track (not shown here). At 0.5 N normal load, the wear track area covered with tribolayers was ~20% and increase to ~32% at 2.5 N and to ~40% at 5 N in both the coatings. Raman analysis on the tribolayers and wear debris showed characteristic peaks corresponding to the rutile and anatase phases of TiO₂ while on the wear track no active Raman peaks were observed as shown in Fig. 6.5.

Comparing the wear track morphologies at similar normal loads, abrasive wear marks were found to be continuous over the entire wear track in irregular powder coatings while in spherical powder coatings, these were discontinuous indicating displacement of the wear debris from the sliding interface. Higher magnification SEM images of the wear tracks of spherical powder coatings showed filling of pores with wear debris along with the presence of large volumes of debris around them (at higher loads) (Fig. 6.4b, d and g). Furthermore, with an increase in normal load, the pore filling for spherical powder coatings was found to be higher and at a greater number of locations on the wear track compared to lower loads. At 2.5 N and 5 N, in addition to wear debris, portions of highly deformed material was found to be dislodged and contributed to the pore filling as shown in Fig. 6.4d and g. This indicated that at higher loads, the material adjacent to the pores underwent significant plastic deformation and as the sliding progressed, the deformed material dislodged itself from the wear track (see Fig. 6.4h) and fell into the pores along with wear debris.

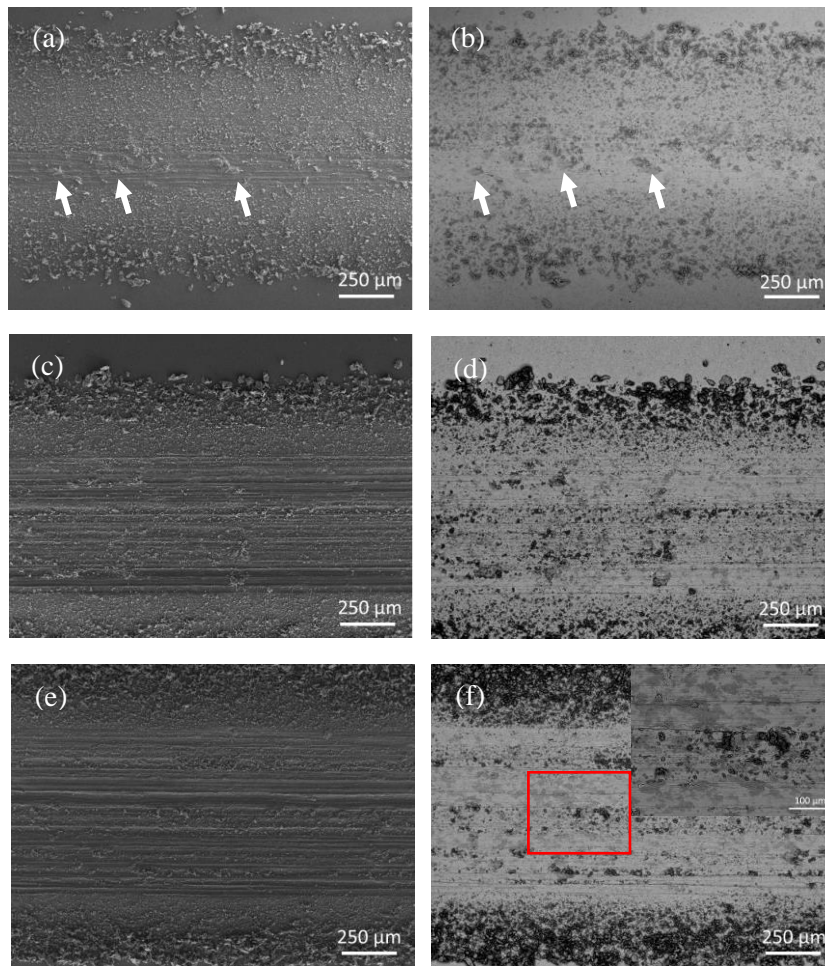


Fig. 6.3: SEM images of the wear track of IP deposited coatings tested at normal loads (a) 0.5 N (c) 2.5 N (e) 5 N and (b), (d), (f) corresponding BSE images; Inset image in (f) shows higher magnification image of region marked with red box in (e); White arrows show tribolayers.

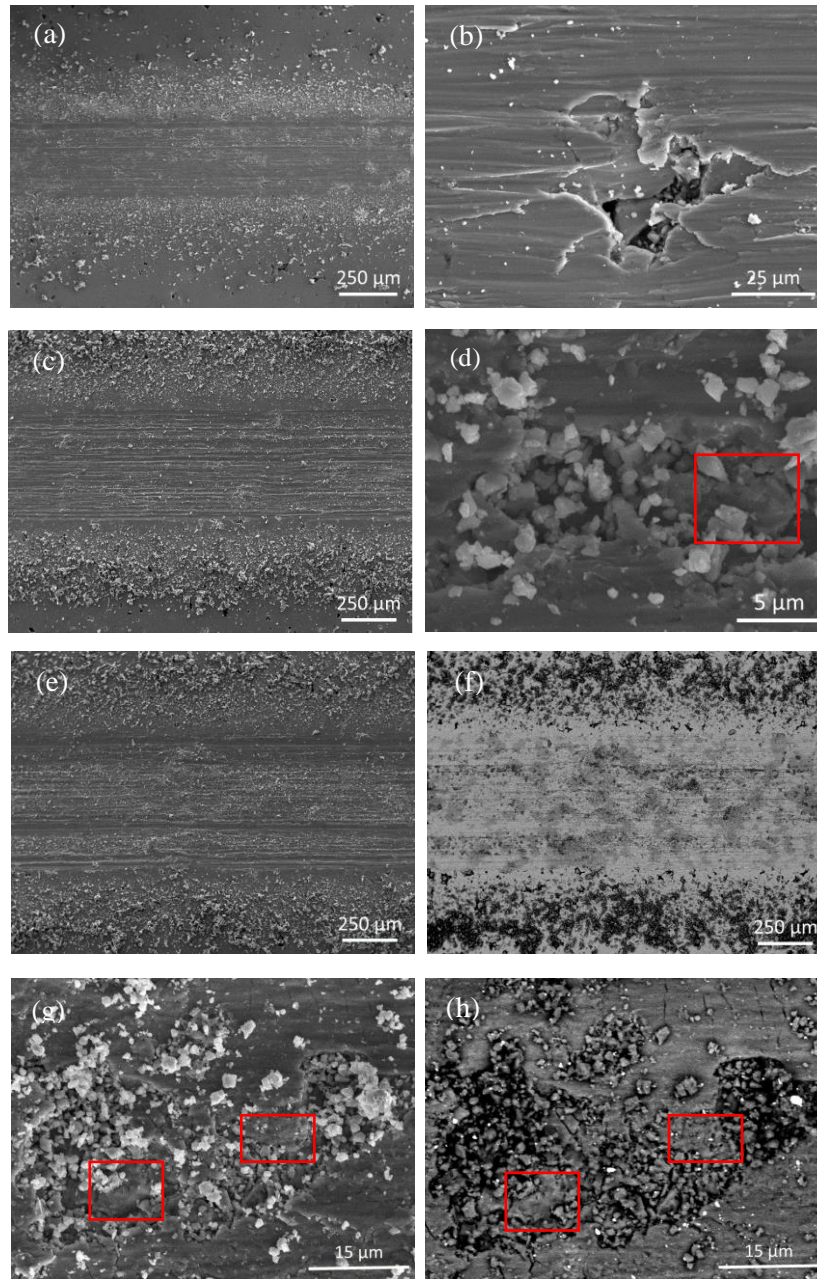


Fig. 6.4: SEM images of the wear track of SP deposited coatings tested at normal loads (a) 0.5 N (c) 2.5 N (e) 5 N and (b), (d), (g) corresponding high magnification images of the wear tracks showing pore filling; (f) and (g) BSE images corresponding to (e) and (h). Red box shows dislodged worn material inside the pore.

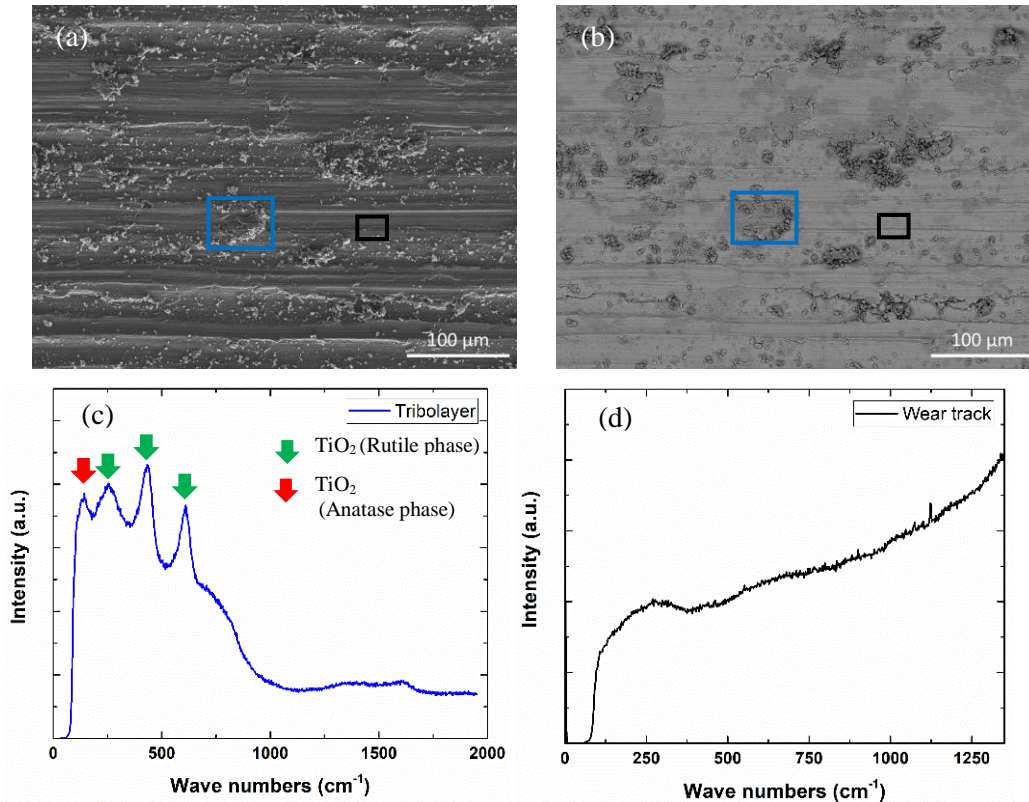


Fig. 6.5: (a) SE image (b) corresponding BSE image of the wear track (c) Raman spectra of the tribolayer (d) Raman spectra of the wear track; Boxes indicate the location where respective spectra were generated (blue box – tribolayer; black box – wear track).

6.3.3.2 Counterface

Figure 6.6a-c shows the SEM images of the counterfaces after the completion of the sliding tests at 5 N load. Both the counterfaces show the presence of thick transfer film at the contact surface along with high volume of wear debris circumscribing them. Higher magnification images of the transfer film showed layered structure along with the presence of cracks (Fig. 6.6b). The formation of thick transfer film indicated the plastic flow and material transfer from the coating, whereas the presence of cracks indicates oxidation and subsequent detachment during sliding resulting in the formation of wear debris. Similar features were observed on the counterspheres at other lower loads (not shown here).

Raman analysis was performed at different locations on the countersphere to understand the chemical compositions of the corresponding features. Raman spectra of the wear debris on both

counterspheres showed characteristic peaks corresponding to the rutile and anatase phases of TiO₂ as shown in Fig. 6.6d. This was similar to the Raman spectra of wear debris formed on the wear track (Fig. 6.5c). However, no active Raman peak was found on the thick transfer film indicating that it was composed of metallic Ti6Al4V (see Fig. 6.6e) transferred from the wear track on to the counterface during wear process.

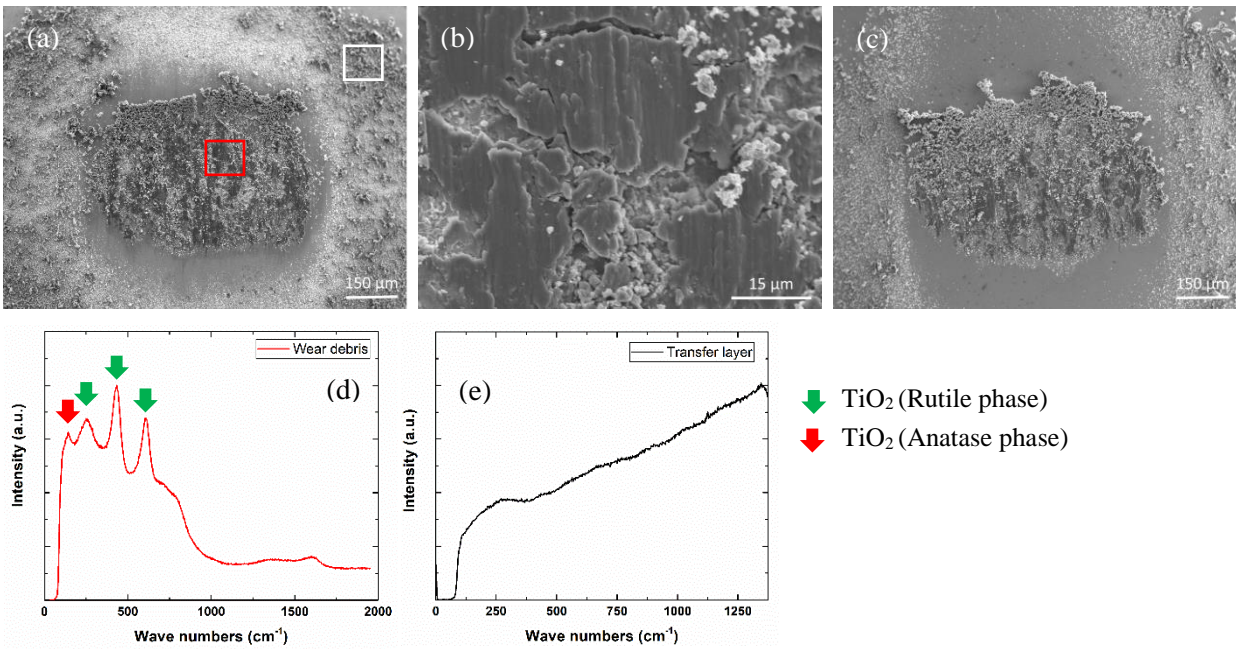


Fig. 6.6: (a) SEM images of the counterface mated with SP coating at 5 N load (b) higher magnification image taken at location indicated by red box in ‘a’ (c) SEM images of the counterface mated with IP coating at 5 N load; Raman spectra of (d) wear debris and (e) transfer layer obtained at locations shown by red and white boxes.

6.3.4 Subsurface microstructure characterization and mechanical properties

To observe the subsurface deformed microstructures, ECCI of the wear track cross-sections were performed and are shown in Fig. 6.7 and 6.8. Interparticle debonding was found below the wear track in both the coatings at all the normal loads. Particle de-bonding was more clearly visible in case of irregular powder coatings (see 6.7a) due to their dense as-sprayed microstructures while the presence of initial porosity in the spherical powder coatings inhibited the direct observation of particle debonding. Furthermore, formation of ultrafine grains (UFGs) were found beneath the

wear tracks followed by a combination of fine grains (FGs) as well as heavily deformed grains and finally the initial microstructure. The thickness of the UFG region was found to be discontinuous and depended on the normal load, presence of tribolayer, and on the coating microstructure.

Wear track cross-section of irregular powder coatings, at 0.5 N load showed the presence of UFGs below the wear track up to a distance of $\sim 3 \mu\text{m}$, followed by highly deformed grains (see Fig. 6.7b-c) and finally the initial coating microstructure. The UFGs below the wear track had an average grain size of $\sim 68 \pm 27 \text{ nm}$. Furthermore, no evidence of tribolayer on the surface was seen, which was due to its low area coverage on the wear track. At 2.5 N, formation of a thin and localized tribolayer was found on the surface of the wear track and underneath the tribolayer, UFGs of average size $\sim 72 \pm 20 \text{ nm}$ were observed up to a depth of $\sim 6.2 \mu\text{m}$ (not shown here). Wear track cross-section of the coatings tested at 5 N showed the presence of tribolayer of thickness $\sim 2.4 \mu\text{m}$ followed by a UFG region $\sim 6 \mu\text{m}$ comprising of grains of average size $\sim 95 \pm 24 \text{ nm}$ (see Fig. 6.7e-f). Higher magnification images of the tribolayer showed differences in contrast along with the presence of thin cracks and small pores (Fig. 6.7e). To understand the distribution of different elements inside the tribolayer, EDS mapping was performed at two different accelerating voltages and are shown in Fig. 6.7g-h. EDS at lower accelerating voltage (3 keV) accurately shows the distribution of oxygen while the distribution of Ti was better observed at higher accelerating voltage (8 keV). EDS mapping of the tribolayer showed the presence of oxygen rich regions corresponding to darker contrast while the brighter contrast showed the presence of high amount of Ti.

Worn cross-sections of spherical powder coatings at 0.5 N showed the presence UFGs of average size $\sim 70 \pm 20 \text{ nm}$ that extended into the wear track up to a distance of $\sim 5 \mu\text{m}$ (as shown in Fig. 6.8a-b). This was followed by fine and elongated grains (see Fig. 6.8c) and finally the initial martensitic lath microstructure of the coating (see Fig. 6.8d). At 2.5 N and 5 N, formation of tribolayers of thickness $\sim 2.2 \mu\text{m}$ and $1.4 \mu\text{m}$ (see Fig. 6.8f) respectively, was found on the wear track. At 2.5 N (not shown here), beneath the tribolayer UFGs of average size $\sim 86 \pm 27 \text{ nm}$ were observed that extended up to a distance of $\sim 4.3 \mu\text{m}$. This was followed by a mixture of fine and elongated grains and finally the initial microstructure. At 5 N, below the tribolayer the UFG region had a thickness of $\sim 8.2 \mu\text{m}$ and grains of average size $\sim 105 \pm 32 \text{ nm}$ (see Fig. 6.8g). This was followed by fine and elongated grains as shown in Fig. 6.8h and finally, the coating microstructure

(shown in Fig. 6.8i). Higher magnification images of the tribolayers at both loads showed the presence of cracks and small holes similar to that of the tribolayer formed in irregular powder coatings. EDS mapping of the tribolayer formed at 5 N load showed the presence of oxygen and titanium rich regions corresponding to the dark and bright contrasts in the tribolayer as shown in Fig. 6.8j-k.

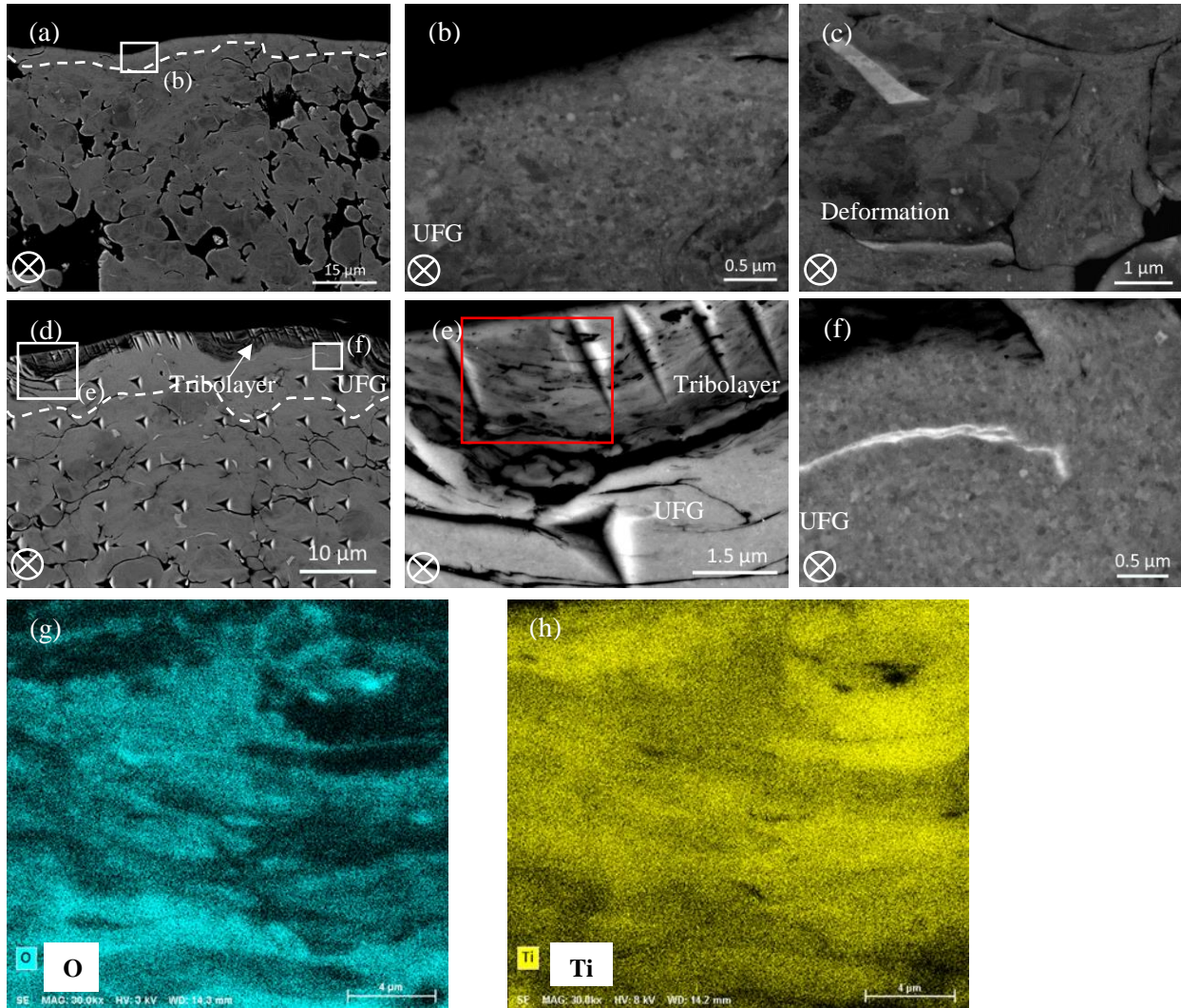


Fig. 6.7: ECCI of the wear track cross-section of irregular powder coatings (a) 0.5 N - subsurface (b) 0.5 N - near wear track (c) 0.5 N - away from wear track (d) 5 N - Subsurface (e) 5 N - tribolayer formed on the wear track (f) 5 N - below the tribolayer; (g) & (h) EDS map showing distribution of O and Ti in the tribolayer (red box). White boxes in show specific location where the ECCI was done. ⊗ – indicates sliding direction.

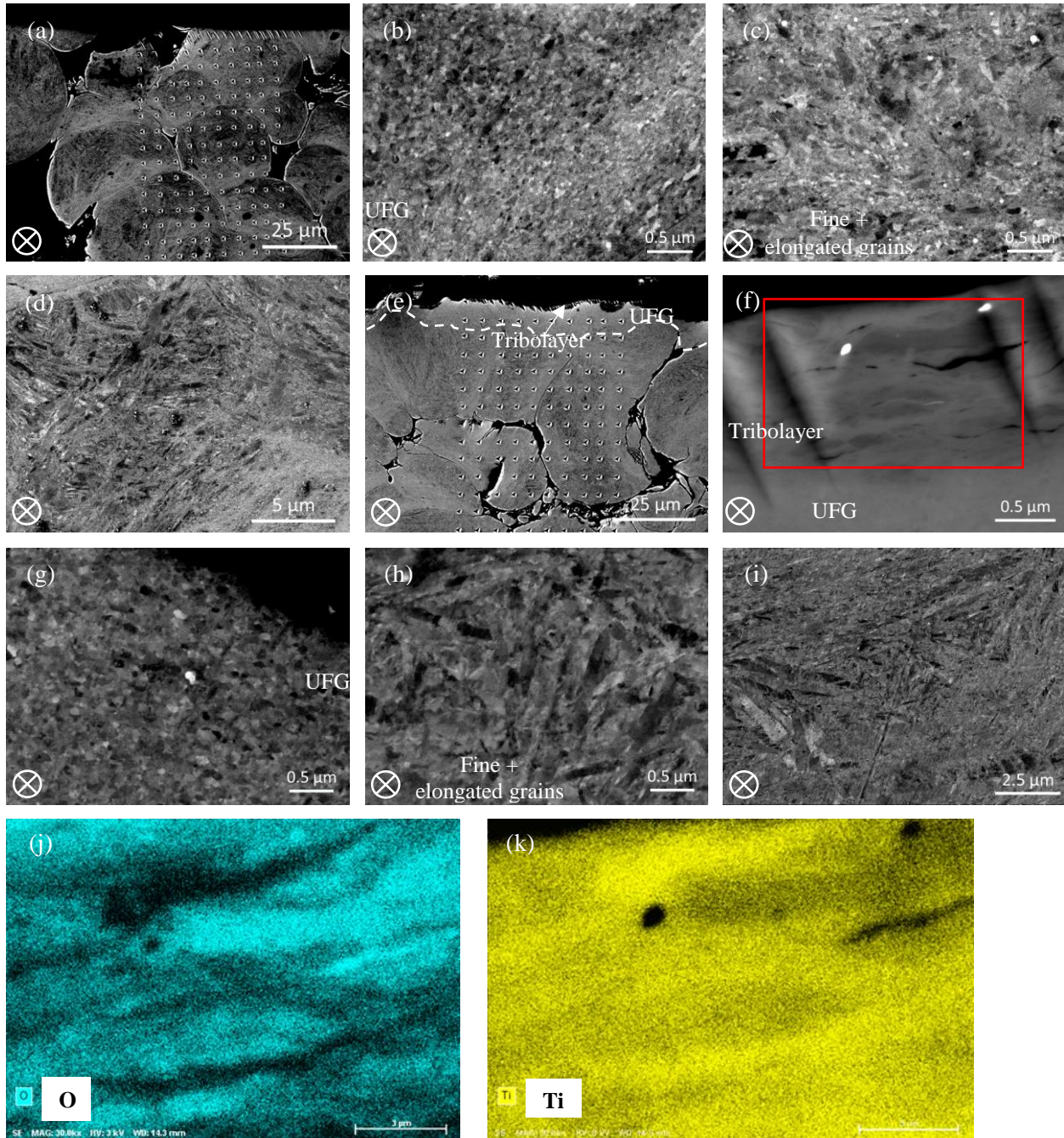


Fig. 6.8: ECCI of the wear track cross-section of spherical powder coatings tested at normal load (a) 0.5 N - subsurface (b) 0.5 N - near the wear track (c) 0.5 N – below the wear track (d) 0.5 N – away from the wear track (e) 5 N - subsurface (f) 5 N - tribolayer formed wear track (g) 5 N - below the tribolayer (h) 5 N – below the UFG region ; 5 N – away from the wear track ; (j) & (k) EDS map showing distribution of O and Ti in the tribolayer (red box). ⊗ – indicates sliding direction.

Nanoindentation was performed on the wear track cross-sections and a hardness profile as a function of the distance from the worn surface was obtained and is shown in Fig. 6.9. The surface hardness of the wear track was found to be higher compared to coatings at all loads. A trend of decrease in hardness with distance from the worn surface was observed. In both coatings, the near surface hardness of the wear tracks with tribolayer was greater than the wear tracks that did not show tribolayer presence. Comparing the hardness of the tribolayers formed on spherical and irregular coatings, no significant difference in hardness values of the were observed at corresponding normal loads which could be due to their similar chemical composition (i.e. mostly TiO₂). In addition to hardness (H), the elastic modulus (E) of the tribolayer and the near surface of the wear track (in the absence of tribolayers) was determined. This was used to calculate the ratio of hardness to elastic modulus (H/E) termed as “plasticity index” which indicates the resistance of a surface to plastic flow [223]. From Table 6.3, tribolayers exhibited higher H/E compared to worn surfaces where there was no tribolayer formation. This was mainly due to the higher hardness of tribolayers compared to worn surface of the wear tracks without tribolayers.

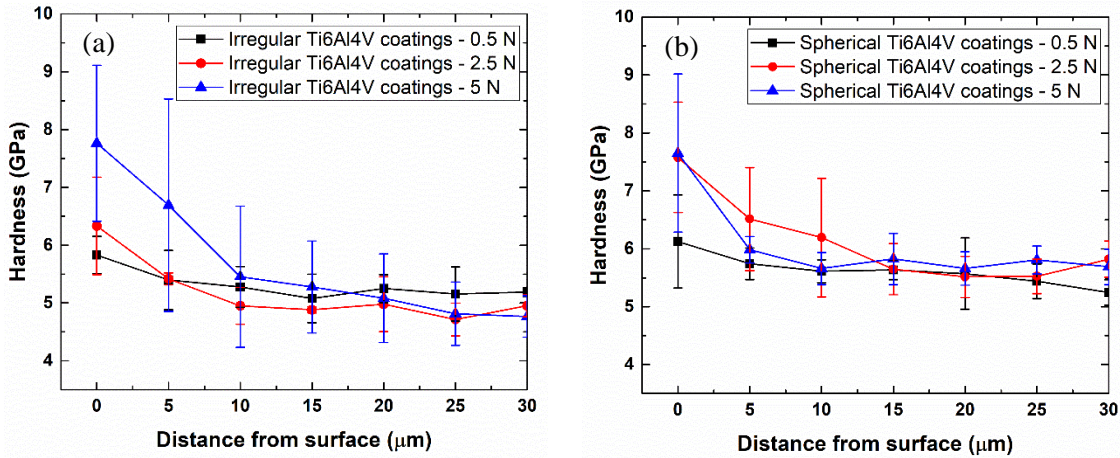


Fig. 6.9: Hardness profile of the worn cross-sections of (a) IP and (b) SP coatings.

Table 6.3 Ratio of hardness (H) to elastic modulus (E) of the worn surfaces.

Coating	H/E		
	0.5 N	2.5 N	5 N
SP Ti6Al4V	0.037 ± 0.003	0.060 ± 0.005	0.060 ± 0.008
IP Ti6Al4V	0.044 ± 0.003	0.044 ± 0.008	0.057 ± 0.012

6.3.5 TEM analysis of the third bodies and worn surfaces

The worn surface of spherical powder coatings showed two different morphologies, one being the pore filled region and another being the bare wear track. To compare the microstructures of the material inside the pore and the worn surface (away from the pore filled region), TEM analysis was performed on the cross-sectioned thin foils obtained from respective locations using FIB. The specific locations on the wear track selected for performing the thin foils are shown in Figs. 6.10a and 6.11a. TEM images of the material inside the pores showed the presence of UFG region and FG region (Fig. 6.10b). Furthermore, significant cracking was observed which could be due to its poor ductility or stresses generated during reciprocating sliding (see Fig. 6.10b). The UFG region (see Fig. 6.10c-d) appeared mostly near the worn surface and near the regions where cracks were observed. The UFG region was followed by FG region. Selected area diffraction pattern (SADP) obtained around the UFG region (Fig. 6.10c-d) showed distinct circular rings (as shown in Fig. 6.10e) indicating the grains were nanocrystalline while the SADP in the FG region also showed circular rings but were less continuous compared to the UFG region (Fig. 6.10h). This indicated that the FG region had coarser grains compared to UFG region. The d-spacing determined from the SAED patterns matched well with the corresponding d-spacing of the TiO₂ standard reflections obtained from the JCPDS card no: 021-1276 and 021-1272 and with α -Ti standard reflections from JCPDS card no: 044-1294. This indicated that the pore filled material comprised of nanocrystalline TiO₂ and α -Ti. Higher magnification images of the regions close to the wear track showed the presence of small micron sized fragmented particles embedded inside the pore filled material as seen in Fig. 6.10f. EDS analysis on the wear debris revealed characteristic peaks corresponding to W (Fig. 6.10g), which indicates the transfer of WC fragments from the counterface to the sliding interface and subsequently into the pores during wear process.

TEM analysis on the wear track (away from the pore filling region) showed the presence of a continuous layer of UFGs of thickness $\sim 3.7 \mu\text{m}$ (see Fig. 6.11b). SADP obtained over the UFG region showed continuous ring formation indicating the grains were nanocrystalline and the d-spacing calculated from these reflections matched well with the standard reflections of α -Ti obtained from JCPDS card no. 044-1294 (see 6.11c-d). The UFGs were followed by a region comprising of fine and large elongated grains as shown in 6.11e-f. SADP obtained over the FG region (Fig. 6.11d) showed less continuous rings indicating that these grains were coarser

compared to the UFG (Fig. 6.11f). Furthermore, under the wear track, unlike the pore filling region, no subsurface cracking nor embedding of WC particles were observed. Comparing Figs. 6.11c and 6.10c, the grains in the UFG region of the wear track appeared coarser compared to the UFGs observed in the pore filled region. This indicated that the pore filled material was highly deformed between the two sliding bodies before being transported into the pores.

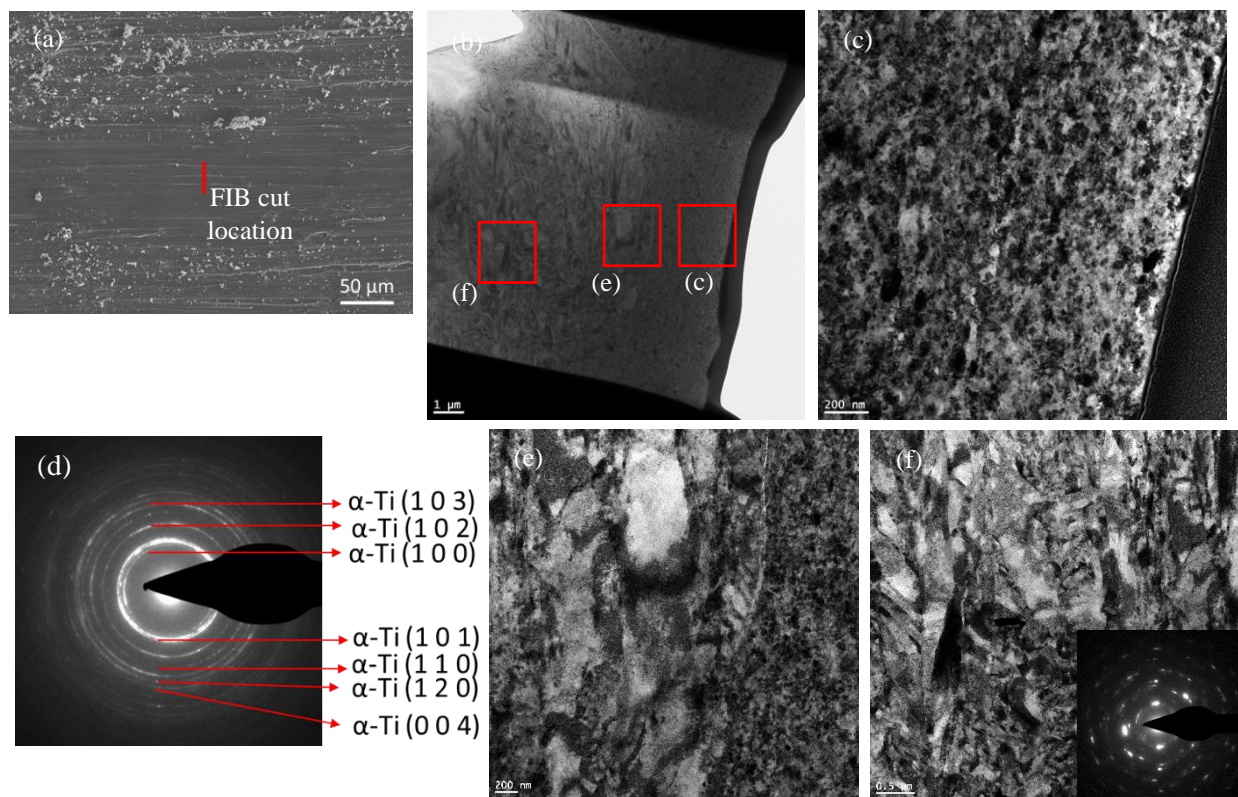


Fig. 6.11: (a) Location of the FIB cut on the wear track; TEM images of the (b) wear track subsurface (c) region near the worn surface (d) SAED pattern taken at corresponding location (e) showing the interface between recrystallized grains and deformed - elongated grains (f) region away from the worn surface i.e. into the coatings with inset image showing SAED pattern. Red boxes show the locations where higher magnification images were taken.

6.4 Discussion

The physical characteristics like porosity, second phase reinforcement, near surface microstructure of a bulk or coating material significantly influence its friction and wear behaviour [34,224,225]. These features alter the localized stresses or provide resistance to plastic shearing and in turn improve or degrade the overall tribological performance. Furthermore, the quantity or volume fraction, of these features change the third bodies activities which in turn alter the friction and wear mechanisms [36,37,218,221,225]. For example : Studies have shown that increase in porosity up to an optimum percentage decreases the wear rates due to decrease in abrasion, whereas high porosity levels reduce the mechanical strength of the material and lead to significant plastic deformation and high wear rates [218]. In addition to these, the physical conditions like the normal load, localized temperature, ambient conditions favour the formation of tribolayers which provide

localized resistance to normal and shear stresses and improve the tribological performance of the material [26,174,226,227]. In the present study, cold sprayed Ti6Al4V coatings with distinct characteristics showed different tribological behaviour during sliding at different normal loads. As it will be discussed in this section, differences in porosity in the coatings changed the third bodies generation, flow at the tribo-pair interface and changed the wear mechanisms.

A schematic showing the different wear mechanisms that occur in the two coatings are shown in Fig. 6.12. Ti6Al4V coatings deposited using spherical and irregular powders showed abrasive wear, with characteristics of ploughing by wear debris and scoring by the counterface (Fig. 6.3 and 6.4). Furthermore, formation of an adhesive transfer film at the contact surface surrounded by wear debris was observed on the counterface at all loads (Fig. 6.6a and c). The formation of adhesive transfer on the counterface sliding against Ti and its alloys was previously reported by many researchers [36,219]. This is due to the low d-bond character of Ti and its alloys that results in adhesive bonding with the counterface material. Higher magnification images of the transfer film showed the presence of brittle cracks inside them (Fig. 6.6b). This indicated that loosening, detachment of the transfer film, transfer into the sliding interface, oxidation and fragmentation occurred during the wear process. These fragments along with the worn material generated from the coating essentially constituted the wear debris. Raman analysis showed that these wear debris were predominantly TiO₂ particles (Fig. 6.5a). The high reactivity of Ti results in the formation of oxide on its surface, while its high “Pilling-Bedworth ratio”, mismatch of coefficient of thermal expansion with the underlying metal results in fragmentation during sliding [174,227,228]. These fragments get further added to the wear debris and result in three-body abrasion and high wear rates. Previously, researchers have reported that the non-protective nature of surface oxides result in abrasive ploughing and high wear rates in Ti alloys [26,27,174,220]. Despite having dense microstructures and higher hardness, irregular powder Ti6Al4V coating showed higher wear rates compared to spherical powder coating at corresponding normal loads (Fig. 6.2). The dense microstructure of irregular powder coatings supported the abrasive ploughing by the wear debris and scoring by the counterface (Fig. 6.12a). In contrast, the spherical powder coatings had internal porosity which acted as a reservoir and captured the debris during the wear process (Fig. 6.12b). This decreased the possible agglomeration and the intensity of abrasive ploughing caused by the wear debris thereby decreasing the overall wear rates. As the normal load increased, greater formation of the wear debris led to greater ploughing in irregular powder coatings (Fig. 6.3c and

6.3e) where as in spherical powder coatings, high volume fraction of porosity led to greater entrapment of the wear debris (Fig. 6.4d and 6.4g-h). Studies from literature have reported that in case of porous materials the pore size, shape and volume fraction play an important role in determining the wear behaviour of the material [217,218,221,225]. Dubrujeaud *et al.* previously observed that low porosity levels (< 10 vol.%) with a mean pore size of < 10 μm makes it difficult to entrap the debris and the pores often get closed due to plastic deformation during the wear process [218]. Contrarily, high volume of porosity > 20 vol.% leads to poor mechanical strength, inhibits complete pore filling due to excessive plastic deformation and results in high wear rates. They concluded that an optimum volume fraction of 10 – 20 vol.% porosity with a mean pore size > 12 μm ideally facilitates wear debris capture and decreases the wear rate. Here in the present study, spherical powder Ti6Al4V coatings had an average porosity of ~ 13% and mean pore size (diameter) of ~ 25 μm that favoured the pore filling mechanism and led to lower wear rates compared to dense irregular powder Ti6Al4V coatings at all loads. Additionally, presence of porosity increases the real contact area between the two surfaces during sliding and decreases the contact stress [218]. Hence for the same normal load, lower contact stress is evident in case of spherical powder coatings due to the presence of higher volume fraction of porosity compared to irregular powder coatings. Decrease in contact stress decreases plastic deformation and subsequently material removal. However, the difference in contact stress in spherical and irregular coatings due to porosity could not be calculated in the present study and would be a part of future work.

Researchers have indicated that entrapment of debris which are mostly hard oxide particles into the base material i.e. pores at the near surface of the wear track, make the localized surface to act as a composite and increase its resistance to localized shear deformation [217,218]. In the present study, TEM analysis of the pore filled material (spherical powder -Ti6Al4V) showed the presence of TiO₂ along with few micro-sized particles of WC embedded into the matrix (see Fig. 6.10c and f) while the remaining wear track did not show any presence of second phase material (Fig. 6.11b). This indicated that the pores acted as a sink for oxides (from the coating) and few hard particles from the counterface during the wear process. Contrarily, in case of irregular powder coatings, absence of porosity led to the continuous abrasive ploughing by the oxides and hard particles from the counterface, until being ejected out of the sliding interface or wear track, thus contributing to higher wear rates. In both coatings, increase in normal load led to an increase in the wear track

area covered with tribolayers due to tribo-oxidation. The formation of tribolayers due to the compaction of debris between the sliding surfaces increased the near surface hardness (Fig. 6.9) and provided localized resistance to plastic shearing thereby resulting in a decrease in the wear rate in both the coatings. However, the decrease was higher in case of spherical powder coating compared irregular powder coating. This indicated that at higher loads, while tribo-oxidation would have an influence in improving the wear resistance, specifically in spherical powder coatings, the additional pore filling mechanism also had a profound effect in decreasing the wear rates.

A sliding tribological contact led to the particle debonding and dynamic recrystallization resulting in the formation of fine, coarse and highly deformed microstructures (Fig. 6.7 and 6.8). However, the extent of grain refinement was found to be dependent on the near surface hardness of the wear tracks. Wear tracks that showed significant coverage of the worn area with tribolayers had higher near surface hardness, resulting in the formation of coarser UFGs compared to the wear tracks without tribolayers. This indicated that presence of tribolayers increased the load bearing capacity and transferred less stress to the subsurface. Furthermore, the ratio of hardness to elastic modulus of the wear tracks covered with tribolayers was higher compared to the uncovered wear tracks (Table 6.3). Higher H/E values of the tribolayers indicated that these surfaces were more resistant to plastic deformation compared to the wear tracks not covered with tribolayers. According to Irwin–Orowan fracture model [229], the fracture toughness of a material can be improved by increasing the critical stress required to fracture (i.e. increasing the hardness) and by decreasing the elastic modulus [223]. This signifies that, a material with high H/E ratio will be more resistant to fracture, compared a material with lower H/E value. Here in the present study, the higher H/E value of the tribolayers indicates that these worn surfaces were more resistant to cracking compared to wear tracks without tribolayers.

Increase in normal load from 0.5 N to 5 N decreased the CoF in both coatings due to the increased coverage on the wear track area (~ 20% to 40%) with oxygen rich tribolayers. Raman analysis on the tribolayers showed peaks mostly corresponding to the rutile phase of TiO_2 while TEM analysis (SAED pattern in Fig. 6.10e) indicated that they were crystalline in nature. Studies performed by researchers have shown that the during wear of Ti and its alloys, tribo-oxidation due to high interfacial temperatures lead to the formation of non-stoichiometric phases or Magnèli phases of

TiO₂ [230–232]. In the present study, SAED patterns (Fig. 6.10e) showed the presence of Magnèli phases in the tribolayer (Note: Pore filled region shown in Fig. 6.10a was in the tribolayer). However, a significant overlap between the diffraction patterns of the Magnèli phases, and the anatase phase of TiO₂ and α -Ti were observed. Hence, a complete confirmation regarding the presence of the Magnèli phases could not be made in the present work. However, similar formation of Magnèli phases during wear of Ti was observed previously by Woydt *et al.*, Gardos *et al.* and Erdemir *et al.* [179,230,231,233]. Literature studies illustrate that, localized high temperatures during tribological processes or bombardment of the surface with high energy ions lead to oxygen deficiency on the surface along with the formation and diffusion of anion vacancies resulting in Magnèli phases [232]. These Magnèli phases have low lattice energy crystallographic shear planes that result in low shear strength [179]. It is well known from the classical theory of Bowden and Tabor that to reduce the adhesion component of the friction, a hard material with soft skin can be used to minimize the shear strength and increase the contact pressure at the tribo-pair contact interface [36,161]. The formation of islands of tribolayers comprising of low shear strength Magnèli phases on wear track would have acted like a soft skin on hard material and decreased the CoF. Furthermore, SEM images of the worn surfaces at different loads indicate an increase in wear track width with increase in normal load (Figs. 6.3a-e and 6.4a-e). This would have led to higher contact area between the sliding surfaces which reduces the frictional force between the tribo-pair at higher loads. Thus, the combined effect of formation of low shear strength tribo-chemical oxides and increase in contact area between the tribo-pair resulted in less fluctuating and low CoF in both the coatings at higher loads.

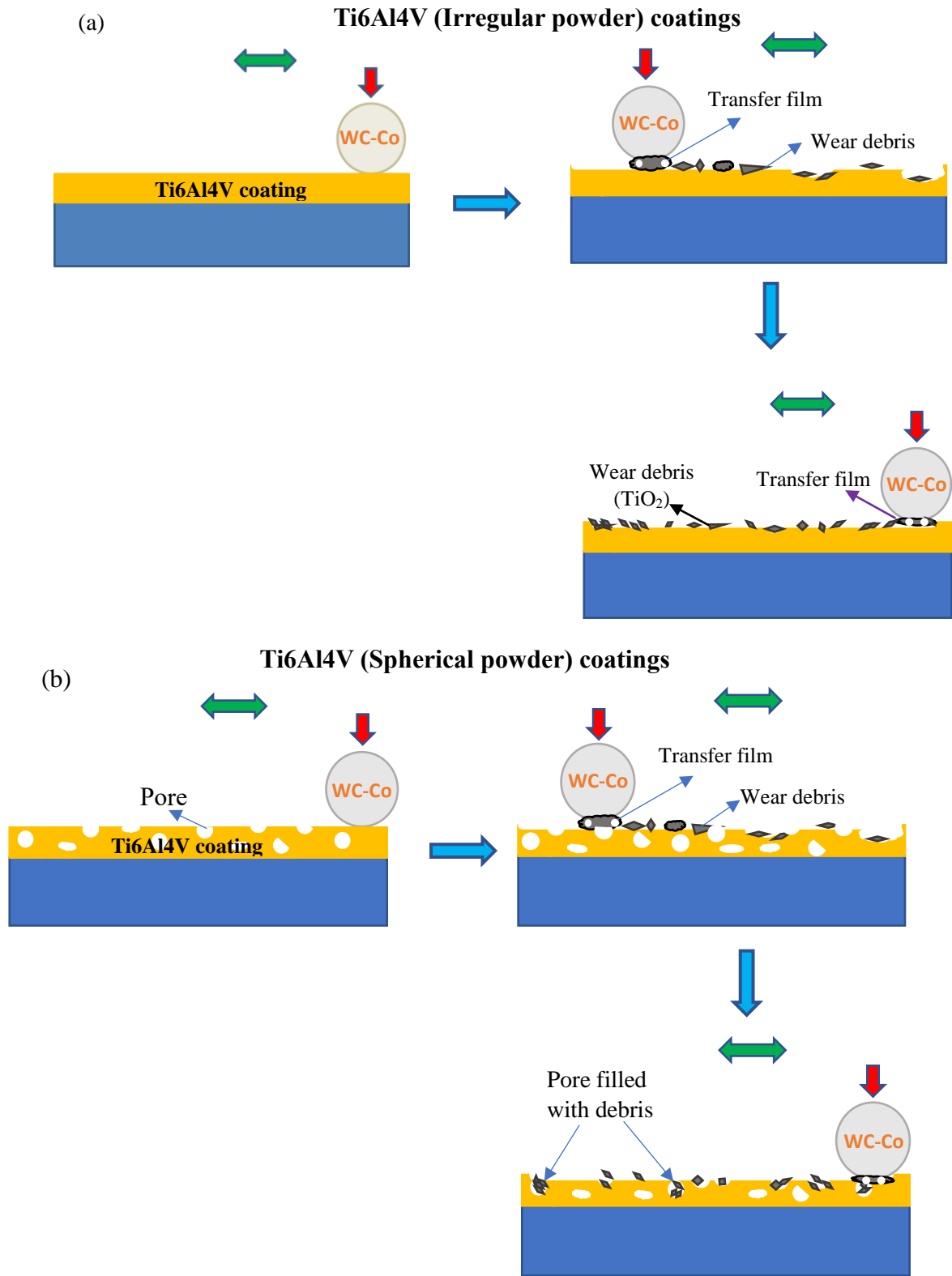


Fig. 6.12: A schematic showing the wear mechanisms in Ti6Al4V coatings deposited using (a) irregular (b) spherical powders.

6.5 Summary and conclusions

The tribological behaviour of the cold sprayed Ti6Al4V coatings deposited using powders with different morphology and microstructure, were studied at different normal loads. Spherical powder Ti6Al4V coatings, despite high porosity and lower hardness compared to irregular powder coatings showed lower wear rates at all test loads. Abrasive ploughing by the wear debris led to high wear rates in irregular powder coatings, whereas entrapment of wear debris into the pores reduced the ploughing resulting in low wear rates in spherical powder coatings. Increase in normal load from 0.5 N to 2.5 N decreased the wear rate in both the coatings, and with further increase in normal load to 5 N, no significant change in wear rate was found in irregular powder coating, whereas in spherical powder coatings a further decrease in wear rate was observed. The decrease in wear rate in irregular powder coatings was due to the tribo-oxidation that led to the greater coverage of wear track area with tribolayers, whereas the combined effect of both tribo-oxidation and higher entrapment of wear debris led to a more significant drop in the wear rates of spherical powder coatings. These results indicate that the improvement in wear resistance imparted by tribo-oxidation was limited i.e. until the normal load was increased to 2.5 N, and henceforth did not significantly influence the wear rates. Contrarily, in case of spherical powder coatings similar increase in wear track area covered with tribolayers was observed, whereas the wear rate continuously decreased with increase in normal load from 0.5 N to 5 N due to greater filling of pores with debris. These results indicate that, although porosity is detrimental to the mechanical strength of the coatings, from a tribological point of view, their presence helped to reduce the abrasive ploughing by wear debris and subsequently wear rates. Thus, the wear resistance of the Ti alloys can be improved by incorporating optimum porosity in the coatings.

Tribolayers formed on the wear tracks were mostly composed of rutile TiO₂ (crystalline) which essentially were low shear strength Magnèli phases. The formation and significant coverage of wear track area with tribolayers helped in reducing the CoF at higher loads in both coatings as they acted as a soft material with lubricating properties on a hard layer. The average CoF in both coatings was not significantly different at similar loads. This signifies that the CoF remained unaffected by the presence of porosity and the formation of tribo-oxides helped in reducing the CoF in both the coatings.

Chapter 7

The role of metal powder properties on the cold spray and tribology of Ti6Al4V-TiC metal matrix composites

Venkata Naga Vamsi Munagala and Richard R Chromik

This manuscript is intended to be submitted to a journal. In Chapter 3 and 5, it was observed that the feedstock powder characteristics have a significant influence on the coating properties which in turn influence their friction and wear performance. Also, Ti6Al4V coatings exhibited abrasive wear resulting in high wear rates. To improve its tribological properties, TiC particles are reinforced into Ti6Al4V matrix, and the friction and wear behaviour of Ti6Al4V-TiC composite coatings are studied. In addition, the influence of TiC content modifying the friction and wear mechanisms are investigated in detail.

Abstract

Ti6Al4V-TiC metal matrix composite (MMC) coatings were cold sprayed using spherical and irregular Ti6Al4V powders manufactured using plasma gas atomization and Armstrong processes. Composite coatings deposited using irregular powders (IP) showed higher ceramic retentions and lower porosity compared to spherical powders (SP) deposited coatings for all metal-ceramic mixtures. At low loads and similar ceramic contents (~15% - 16% TiC), spherical powder composites showed abrasive wear mechanisms resulting in high coefficient of friction (CoF) and wear rates. Contrarily in irregular powder composites, formation of islands of tribolayers comprising of fragmented TiC and TiO₂ particles resisted the localized shear deformation leading to low wear while the presence of free carbon in TiC particles lowered the CoF. Increase in ceramic content (23% TiC) in the coatings led to higher coverage of wear track area with tribolayers and further improved wear resistance. At higher loads, a more continuous formation of tribolayer was found on the wear track of 23% TiC composite coatings, while no significant formation of tribolayers were observed on the wear tracks of lower ceramic content MMCs. The formation of

continuous tribolayer led to extremely low CoF (~ 0.25) compared to other coatings along with low wear rate. Electron channel contrast imaging and TEM analysis of the worn subsurface under the tribolayers showed coarse-grained microstructures compared to the bare regions of the wear track (i.e. without tribolayer coverage). The formation of coarser grain microstructures indicated less stress transfer to the subsurface both due to the high hardness and lubricating nature of the tribolayers.

7.1 Introduction

To improve the tribological properties of Ti and its alloys, hard particle reinforced metal matrix composites (MMC) are fabricated as bulk or coating [36,38,95,184,188,234]. The presence of hard phases in the metallic matrix facilitates the formation of stable, continuous and coherent tribolayers that resist plastic deformation during wear process and improve the tribological performance of the material [147,163]. Traditionally MMC coatings were deposited using laser cladding, thermal spray processes like plasma spraying, high velocity oxy-fuel spraying etc. [38–40,182,185]. These processes are either complex or involve high processing temperatures resulting in phase transformations, formation of brittle intermetallic phases, oxidation, porosity and tensile residual stress buildup. For example: Candel *et al.* observed a heat affected zone with poor mechanical properties between the Ti6Al4V-TiC coating and the substrate when deposited using laser cladding technique [40]. They also found that the extensive heat due to laser irradiation led to the partial melting and dissolution of TiC particles in the Ti6Al4V matrix. To overcome these limitations, a low temperature and high velocity process known as cold spray (CS) is been recently used to deposit metal, composites and heat sensitive materials as thick coatings on to various substrates [69,73,74,143,235]. In CS, powder particles are accelerated to supersonic velocities using a de Laval nozzle for impact on to substrates [9]. At such high velocities, the particles undergo adiabatic shear stabilites and metallurgically bond to form a coating [79,236]. Since the particle temperature is well below the melting point and the coating deposition occurs in solid state, there are no phase transformations and thermal oxidation thus preserving the bulk properties of the material [69]. Furthermore, the tamping effect caused by the incoming particles on the pre-deposited layers results in coating densification [141].

CS despite being widely used for the deposition of MMCs, there are challenges involved in achieving higher ceramic retentions with good deposition efficiency and low porosity. For the

deposition of MMCs, the metal and ceramic particles are either mechanically blended or composite powders consisting of agglomerated metal and ceramic particles are used as feedstock [61,133,134]. In both cases during deposition the metal particles plastically deform, while the ceramic particles get embedded and entrapped between the metal particles [141]. However, the poor deformability of the matrix metal particles often results in high porosity and also effects the ceramic retention in the coatings. In addition, during deposition, ceramic particle rebound due to non-absorption of their kinetic energy and fragmentation due to their brittle nature often leads to low retentions compared to the initial feedstock [37,141]. The use of hard material as matrix promotes ceramic rebound due to its inability to absorb the kinetic energy of the incoming ceramic particles [45]. This leads to lower ceramic retentions. Literature studies show that porosity in the initial feedstock has a positive impact during the deposition of MMCs. Yin and Lioma *et al* found that presence of porosity in the particles led to highly dense coatings and ceramic retentions close to the initial feedstock [102,103]. This was due to fragmentation of the pores during impact that result in absorption of kinetic energy of the incoming particle and lower its probability to rebound. A summary of these studies indicate that feedstock powder properties have a significant influence in determining the characteristics of MMC coatings deposited using CS.

In case of pure metals or unreinforced materials during sliding, plastic deformation, adhesive transfer, surface oxidation, mechanical mixing during tribological interaction between the surfaces often lead to the formation of wear debris. Specifically during sliding, tribo-oxidation generally leads to the formation of an oxide film (tribolayer) that grow to a critical thickness (as sliding progresses), become unstable and finally get fragmented [237]. This exposes the underlying nascent metal to the sliding interface while the fragmented oxide particles act as abrasives and promote ploughing resulting in high friction and wear rates. Studies from literature illustrate that reinforcement of ceramic particles into the metallic matrix generally lead to better wear resistance compared to unreinforced matrix. However, under unfavourable conditions like low strength of matrix or poor bonding between metal and reinforced ceramic particles, might result in their excessive pullout from the matrix during wear and subsequently lead to high wear rates due to three body abrasion [123]. Generally, the tribological properties of MMCs are mainly influenced by cohesion between particles (metal-metal and metal-ceramic), ceramic content, ceramic particle size, morphology and their distribution in the matrix [35–37,102,123,151,224]. During sliding wear of MMCs, plastic deformation of the metallic matrix and dislodging of the reinforced

particles, their fragmentation result in the wear debris. These wear debris typically comprise of metallic or oxide particles of the matrix material and fragmented carbide particles. As the sliding progresses, the continuous formation, mechanical mixing, tribo-chemical reactions and subsequent agglomeration of wear debris under applied normal load result in the formation of tribolayers. These tribolayers are often stable and hard due to the presence of fragmented ceramic particles and resist the localized shear deformation and decrease wear. The ability of MMCs to form a tribolayers depends strongly on the ceramic particles size [224,237]. Particles with equal or less than the size of the critical oxide thickness of the matrix generally get carried with the fragmented oxide particles while the larger ceramic particles remain intact and contribute to the formation of tribolayers [224].

Previously Alidokht *et al.* illustrated that the reinforcement of WC particles in the Ni matrix increased the hardness and improved its wear resistance [134]. The improvement was attributed to the formation of tribolayers comprising of fine fragments of WC particles along with NiO that resisted the plastic flow of the matrix material. Similarly, Shockley *et al.* found that the presence of hard Al₂O₃ particles in the Al matrix led to the formation of stable tribolayers and decreased the transfer film activity (break down and re-built up) that resulted in lower friction and wear rates compared to unreinforced matrix [147]. They also concluded that increase in alumina content in the matrix led to much stable tribolayer that led to greater wear resistance compared to lower reinforcements. Sliding wear test results reported by Venkatraman *et al.* on Al, Al alloy and Al-SiC MMCs show that there exists a strong co-relation between the hardness and composition of the tribolayers and the friction and wear of the coatings [163]. Coatings that form stable and hard tribolayers show better wear resistance compared to coatings without and unstable tribolayers. Thus, from a tribological point of view the improvement in wear resistance in MMCs comes from the fact that these materials form protective tribolayers during wear that resist localized plastic flow and shear deformation caused by the counterface as well as the wear debris.

In our previous study [238], the tribological behaviour of cold sprayed Ti6Al4V and Ti6Al4V-TiC MMCs were studied at room and elevated temperatures. Based on the study it was concluded that reinforcement of carbide particles improved the wear resistance at lower temperatures whereas tribo-oxidation led to low wear of both metal and composite coatings. However, the influence of ceramic volume fraction and the influence of metal powder properties on the tribology was not

studied. Also, there is no systematic study that co-relates the influence of metal powder characteristics on the composite coating properties and their tribological behaviour. In the present study, Ti6Al4V-TiC MMCs were deposited using two morphologically and microstructurally distinct metal powders. The influence of powder characteristics on the ceramic retention and porosity of MMC coatings was studied in detail. Subsequently, sliding wear tests were performed on one set of composite coatings with similar ceramic contents (deposited using the two powders) and another with higher ceramic content at two different loads. Electron channel contrast imaging (ECCI) and transmission electron microscopy (TEM) analysis of the third bodies was performed to understand their microstructure and tribo-chemical phases formed. Nanoindentation was performed to characterise the mechanical properties of the third bodies.

7.2 Experimental

7.2.1 Cold spray of coatings

Grit blasted mild steel plates of dimensions 75x75x3 mm³ that were de-greased prior to deposition were used as substrates. In the present study, Ti6Al4V-TiC MMC coatings were deposited using two morphologically and microstructurally distinct Ti6Al4V powders along with TiC powders (spherical morphology). The Ti6Al4V powders of irregular morphology manufactured using Armstrong process had an average particle diameter ~ 38 µm while the SP manufactured using plasma gas atomization process had an average diameter ~ 31 µm. The TiC powders had an average diameter ~ 40 µm. The size distribution, microstructure and detailed characterization of the powders are reported in our previous publication [73]. Two different metal-ceramic compositions (35 vol.% TiC and 50 vol.% TiC) were sprayed using spherical and irregular Ti6Al4V powders. To deposit composite coatings, a dual feeding system with two powder hoppers that had a facility to adjust the feed rates separately was used to simultaneously feed metal and ceramic powders. This helped to avoid the problems associated with the mechanical pre-mixing of powders of different densities. The feed rates of the two powder feeders were adjusted individually to obtain the required metal-ceramic mixture. All coatings were deposited using a commercially available PCS 800 cold spray system (Plasma Giken, Japan). Prior to deposition, nitrogen (propellant gas) was pressured and preheated to 4 MPa and 800°C and was expanded through a de Laval nozzle to obtain supersonic velocities. The stand-off distance between the nozzle and the substrate was 40 mm while the gun traverse speed was 200 mm.s⁻¹.

After the deposition, the coatings were mechanically cross-sectioned in perpendicular to the gun traverse direction and cold mounted. These specimens were polished using SiC abrasive papers from 240 grit to 1200 grit and subsequently using polycrystalline diamond suspension of 9 μm , 3 μm and 1 μm . As a final polishing step, the specimens were polished using a vibrometer filled with colloidal silica suspension solution of 0.05 μm . The polished samples were examined under a scanning electron microscope (SEM) (SU3500, Hitachi, Japan) equipped with a backscattered electron (BSE) and energy dispersive spectroscopy (EDS) detectors. BSE images were taken at different locations and were uploaded into ImageJ software. The intensity threshold associated with pores and ceramic particles was adjusted to determine the area fraction of porosity and ceramic retention in the coatings. The measured area fraction was assumed as volume fraction in the present study. At least ten images were analyzed to calculate the final average values. To determine the mean free path (MFP) between the ceramic particles, random lines were drawn on BSE images and the number of particles that intersected the line, per unit length (N_l) were determined. This value together with the volume fraction of ceramic retained in the coating (v_p) was used to determine MFP (λ) using the equation below [35,239]:

$$\lambda = \frac{1-v_p}{N_l} \quad 7.1$$

The hardness of the coatings was determined by performing microhardness tests using a Vickers microhardness tester (Buehler, USA) on the polished top surface at a load of 5 kg and at a holding time of 15 s. Indentation was done at ten different locations to determine the average final hardness value.

7.2.3 Sliding wear tests

Composite coatings were polished till the last step using 0.05 μm colloidal suspension solution in a similar manner to that of the coatings cross-sections prior to wear test. Reciprocating sliding wear tests were performed in dry air environment (humidity < 2%) using a custom-built reciprocating ball-on flat tribometer. Wear tests were performed using a WC-Co spherical counterface (McMaster Carr, USA) of 6.35 mm diameter at two different normal loads 0.5 N and 2.5 N respectively. The sliding speed was 3 $\text{mm}\cdot\text{s}^{-1}$, track length was 5 mm, and the total sliding distance was 10 m. During the entire test the frictional force was recorded at a sampling rate of 800 Hz using a piezoelectric sensor placed below the stage on which the sample was mounted. To

determine the wear rate, the worn samples were examined using a non-contact optical profilometer (Zygo Corporation, USA). Wear track profiles were generated in perpendicular to the sliding direction at different locations starting from one end of the wear track to the other. At least 35 profiles were generated, and the wear area was calculated by integrating the area above and below the reference surface (unworn coating). The wear area (mm^2) was then multiplied by the track length (mm) to obtain the wear volume (mm^3) and was subsequently normalized with sliding distance (m) and normal load (N) to obtain wear rate in $\text{mm}^3 \cdot \text{N}^{-1} \cdot \text{m}^{-1}$. At least 3 wear tests were done on each coating and at every condition to determine the final average wear rate.

To understand the wear mechanisms, the worn surfaces and counterfaces were examined under SEM (SU3500, Hitachi, Japan). To identify the different phases formed during the wear process, Raman analysis was performed on the wear tracks and counterface using an inVia Raman spectrometer (Renishaw, UK) with Ar^+ laser source of $\lambda = 514.5 \text{ nm}$. To characterize the third bodies and subsurface microstructures, ECCI was performed on the polished wear track cross-sections using FE-SEM SU8230 (Hitachi, Japan) equipped with a FlatQUAD EDS detector (Bruker, USA). In addition, EDS mapping was performed at 3 keV and 8 keV accelerating voltages to understand the elemental distribution in the tribolayers. The mechanical properties of the third bodies and the subsurface were determined by performing nanoindentation on the polished wear track cross-sections using a Triboindenter (Hysitron Corporation, USA). Indentation was performed using a Berkovich tip at a peak load of 5 mN in a rectangular grid pattern starting from the unworn surface below the wear track up till the top surface. The hardness of the tribolayer and the subsurface was determined from the load-displacement curves using Oliver and Pharr method [196] and each hardness value represents an average of at least 10 indents. After indentation, the residual indents were imaged using an SEM and the corresponding indents were matched with the respective load-displacement curves to determine the hardness of a particular feature. To compare the subsurface microstructures below the tribolayers and the bare wear track, thin lamella were cut using focus ion beam (FIB) (FEI Helios Nanolab 660, Thermo Fisher Scientific, USA) and were examined under a cryo-transmission electron microscope (TEM) (FEI Tecnai G2 F20, Thermo Fisher Scientific, USA).

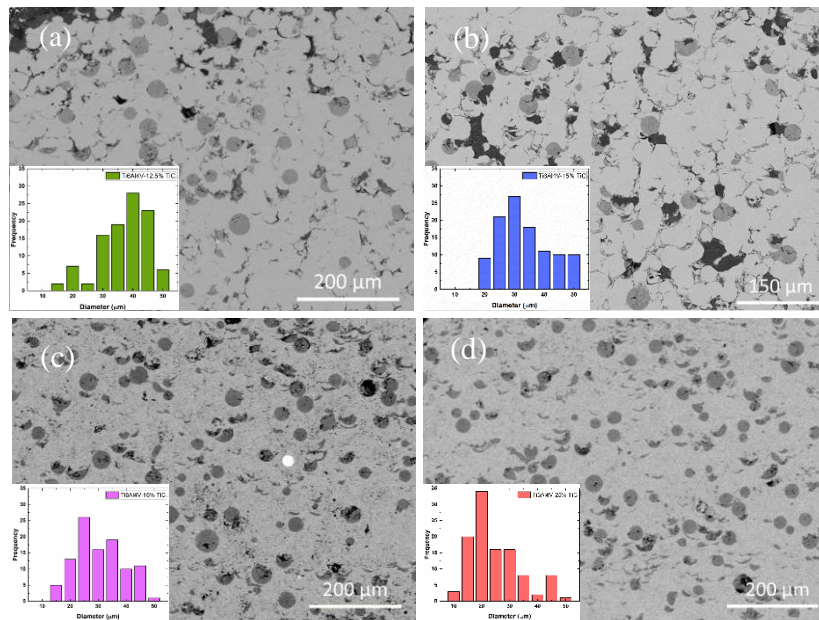
7.3 Results

7.3.1 Coating deposition

BSE images of the composite coating cross-sections along with the size distribution of the ceramic particles in the coatings are shown in Fig. 7.1. In the BSE images, the grey contrast corresponds to ceramic particles while the dark regions correspond to porosity. BSE images of the coating cross-sections show few ceramic particles fully retaining their spherical morphology along with fragments (see Fig. 7.1). Table 7.1 summarizes the ceramic content in the initial feedstock, ceramic retained in the coating, porosity, MFP and hardness of the MMCs deposited using spherical and irregular powders. From Table 7.1, composite coatings deposited using both spherical and irregular powders showed a trend of increase in ceramic retention with increase in ceramic in the initial metal-ceramic mixture. However, in all the coatings, the ceramic retention was significantly lower than the initial feedstock mainly due to the rebound of the ceramic particles upon impact. Coatings deposited using IP showed higher ceramic retentions and lower porosity compared to spherical powder composite coatings at similar initial metal-ceramic mixtures. In case of irregular powder coatings, porosity was mainly due to the empty voids created by the fragmented ceramic particles whereas in spherical powder coatings, the low deformability of Ti6Al4V powder particles led to high porosity. In both spherical and irregular powder deposited MMCs, MFP between the ceramic particles decreased with increase in ceramic retention. At similar ceramic volume fractions (i.e. 15 vol.% TiC and 16 vol.% TiC), irregular powder deposited MMC showed lower MFP compared to SP deposited MMC. This could be due to differences in ceramic retention or greater fragmentation of the ceramic particles in irregular powder MMC compared to spherical powder, as indicated by the particle size distribution histogram (see Fig. 7.1). Hardness increased with increase in ceramic retention in the coatings. This was due to the presence of higher volume fraction of ceramic particles that increase the load bearing capacity of the coatings. At similar ceramic volume fractions (i.e. 15 vol.% TiC and 16 vol.% TiC), irregular powder composite coatings showed higher hardness compared to spherical powder coatings.

Table 7.1 Coating properties.

Ti6Al4V powder	TiC vol.% (feedstock)	TiC vol.% (retained)	Porosity (%)	MFP (μm)	Hardness ($\text{HV}_5 \text{ kg}$)
Spherical	35	12.5 ± 1.2	5.1 ± 1.6	136	206 ± 14
Spherical	50	15.0 ± 1.2	5.0 ± 0.7	80	218 ± 10
Irregular	35	16.0 ± 1.0	1.1 ± 0.4	69	233 ± 8
Irregular	50	23.0 ± 1.0	1.0 ± 0.4	43	274 ± 19

**Fig. 7.1:** BSE images of the coating cross-sections of Ti6Al4V - (a) 12.5% TiC (b) 15% TiC (c) 16% TiC (d) 23% TiC; Inset images show the ceramic particle size distribution in the coatings.

7.3.2 Friction and wear of the coatings

For performing tribological studies, spherical powder deposited composite coating with 15% TiC and irregular powder deposited composite coatings with 16% TiC and 23% TiC were selected. The coefficient of friction (CoF) vs cycle number is plotted for the coatings at both loads (shown in Fig. 7.2). Spherical powder composite coating showed highly fluctuating friction behaviour at both loads. At 0.5 N normal load the CoF was found to be fluctuating between $\sim 0.48 - 0.77$ whereas at 2.5 N it was between $\sim 0.33 - 0.53$. The average CoF (0 – 1000 cycles) was found to be $\sim 0.62 \pm 0.06$ at 0.5 N and $\sim 0.44 \pm 0.03$ at 2.5 N. In contrast, irregular powder composite coatings (both 16% and 23%) at 0.5 N showed similar high CoF in the initial cycles and as the test progressed a

significant drop in CoF was observed. In case of a composite coating with 16% TiC, high CoF of ~ 0.55 (average) was seen up to 150 cycles followed by a drop to a steady state value $\sim 0.30 \pm 0.01$. In 23% TiC composite coatings, the high CoF of ~ 0.56 (average) was observed until 25 cycles, followed by a drop to a steady state value of $\sim 0.34 \pm 0.02$. Furthermore, CoF after the friction drop in both the coatings was found to be less fluctuating and henceforth did not show any subsequent rise. At 2.5 N, irregular powder composite coating with 16% TiC exhibited largely fluctuating CoF with an average value of $\sim 0.45 \pm 0.04$ which was similar to that of spherical powder 15% TiC coating. However, 23% TiC coating at 2.5 N, showed higher CoF of ~ 0.42 during the initial cycles and as the test progressed the CoF dropped to a steady state value of ~ 0.25 after 140 cycles and henceforth remained low. In case of 23% TiC coatings, the steady state CoF at 2.5 N was found to be lower and less fluctuating compared to other composite coatings.

Wear rate calculated at the end of 1000 cycles for the coatings at both the loads is shown in Fig. 7.3. First, comparing the wear rates of spherical and irregular powder composite coatings with similar ceramic retentions i.e. 15% TiC (SP) and 16% TiC (IP), at both loads irregular powder composites exhibited lower wear rates compared to SP. The difference in wear rates between the two coatings was higher at 0.5 N than at 2.5 N (see Fig. 7.3). Within the two, irregular powder deposited composites (16% and 23% TiC), higher ceramic retention led to lower wear rates at both loads. Furthermore, composite coating with 23% TiC showed extremely low wear rate even at 2.5 N normal load. Increase in normal load led to increase in wear rates in composite coatings with low ceramic contents (15% TiC and 16% TiC), where as, wear rate remained mostly low and similar in 23% TiC composite coatings (see Fig. 7.3).

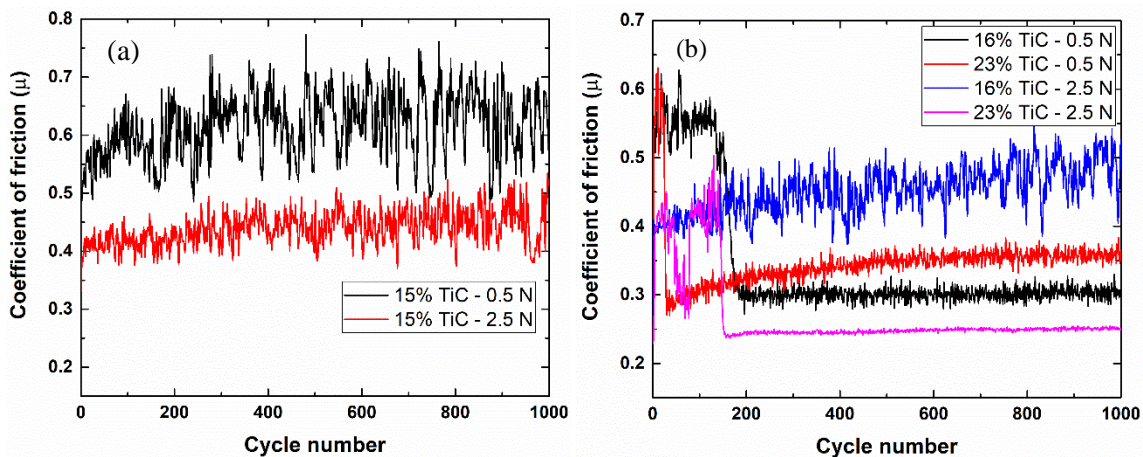


Fig. 7.2: CoF vs cycle number at respective loads (a) spherical and (b) irregular powder coatings.

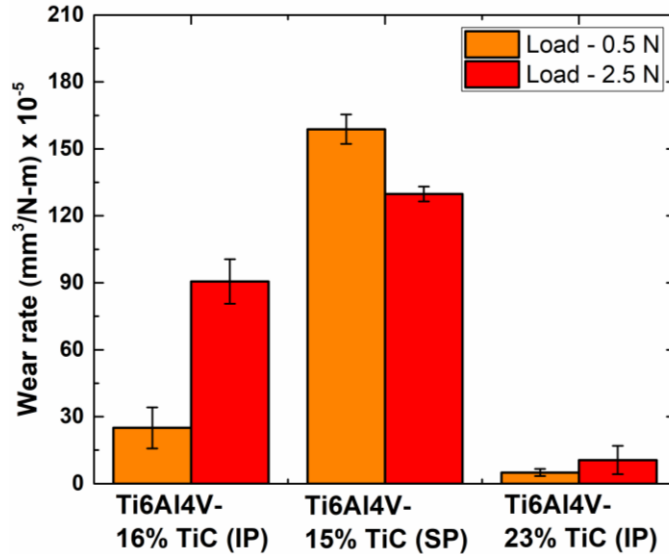


Fig. 7.3: Wear rate of the coatings calculated at the end of 1000 cycles.

7.3.3 Wear track morphology and phase analysis

The SEM images of the wear tracks are shown in Figs. 7.4-7.6. The worn surface of spherical powder composite coating (15% TiC) at 0.5 N and 2.5 N showed abrasive wear, with characteristics of ploughing by the wear debris and scoring by the counterface (see Fig. 7.4). Furthermore, at specific locations inside the wear track, evidence of splat delamination was observed, which could be due to poor intersplat bonding (see Fig. 7.4a-b). Worn surfaces of irregular powder deposited composites showed different features on the wear tracks depending on the ceramic content and normal load. At 0.5 N, both 16% TiC and 23% TiC composite coatings showed the formation of islands of tribolayers on the wear track (Fig. 7.5a-c). The tribolayers on the wear track of 23% TiC coatings were found to be covering a higher area fraction compared to 16% TiC. BSE images of the wear track showed that these tribolayers were formed around TiC carbide particles (Fig. 7.5b) and appeared to be comprised of wear debris agglomerated and sintered together (Fig. 7.5b). EDS map of the tribolayers showed the presence of oxygen and carbon along with Ti at few specific enriched locations indicating that these were oxides of Ti and fragmented TiC particles (Fig. 7.5d). At 2.5 N, 16% TiC coating showed abrasive wear with no visual evidence of tribolayer formation in lower magnification SEM images (Fig. 7.6a). However, higher magnification images of the wear tracks showed the formation of tribolayers (Fig. 7.6b) but were less compared to the wear track at 0.5 N (comparing Figs. 7.5a and 7.6a). In case of 23% TiC coating, a more continuous tribolayer compared to any other worn surface was observed on the

wear track as shown in Fig. 7.6c. However, the tribolayer did not cover the entire wear track but rather was found to be like strip that extended from one end, to the other end of the wear track.

Raman analysis performed on the Ti6Al4V and TiC particles in the unworn coating is shown in Fig. 7.7a. Raman spectra of wear debris showed characteristic peaks corresponding to rutile and anatase phases of TiO_2 along with TiC (Fig. 7.7b). This indicated that the wear debris comprised of both oxides of Ti and fragmented carbide particles. Raman analysis on the tribolayers of irregular powder composite coatings showed peaks corresponding to the rutile and anatase phases of TiO_2 along with TiC (Fig. 7.7c). In addition, Raman peaks at 1326 cm^{-1} and 1556 cm^{-1} that corresponded to the D and G peaks of carbon were observed. These peaks were significantly broad compared to spectra obtained on the initial TiC particle. However, on the wear tracks of both coatings no active Raman peaks were observed.

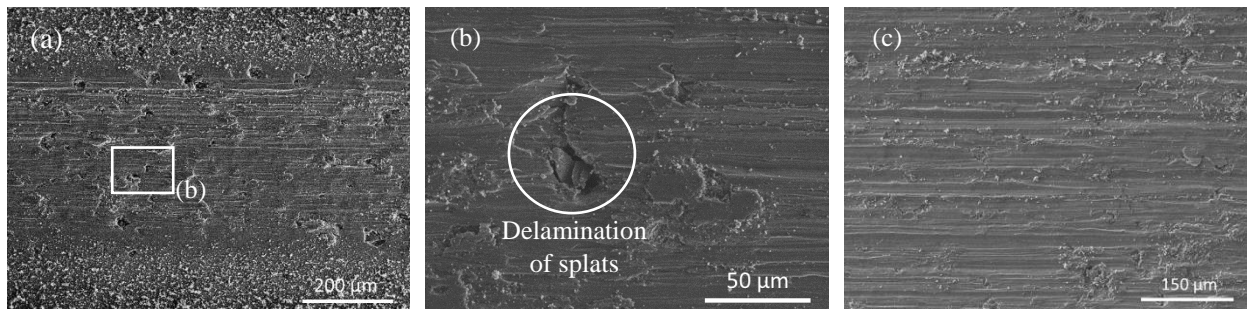


Fig. 7.4: SE images of the wear track of SP 15% TiC MMC tested at normal load (a) 0.5 N (b) Higher magnification image of the region shown in a, (c) 2.5 N.

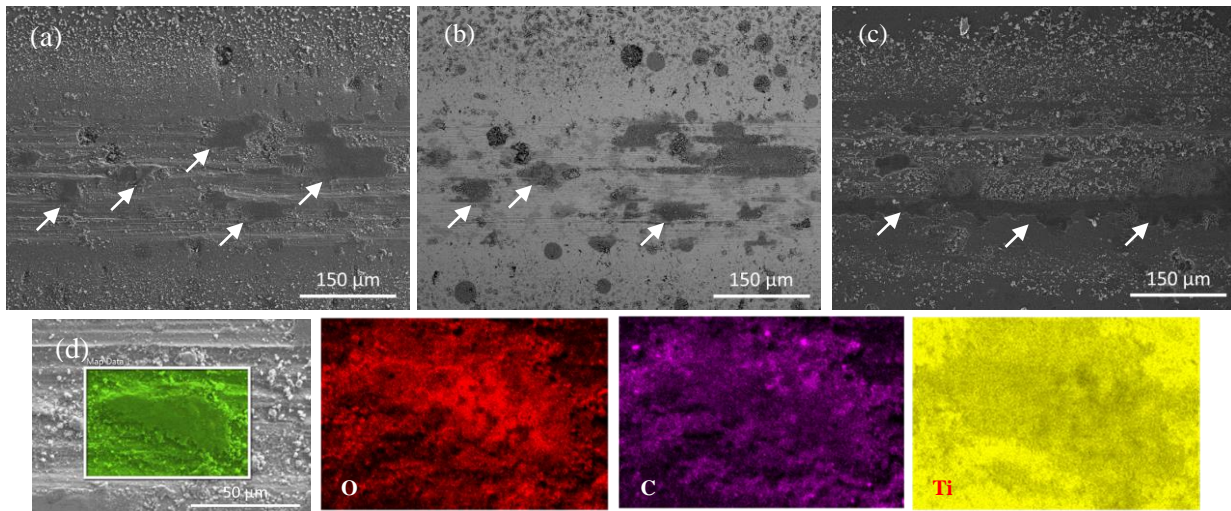


Fig. 7.5: SEM images of the wear tracks of IP composites tested at normal load 0.5 N with (a) 16% TiC (b) corresponding BSE image (c) 23% TiC (d) EDS map of the tribolayer showing O, C and Ti distributions; Arrows in the images show tribolayers.

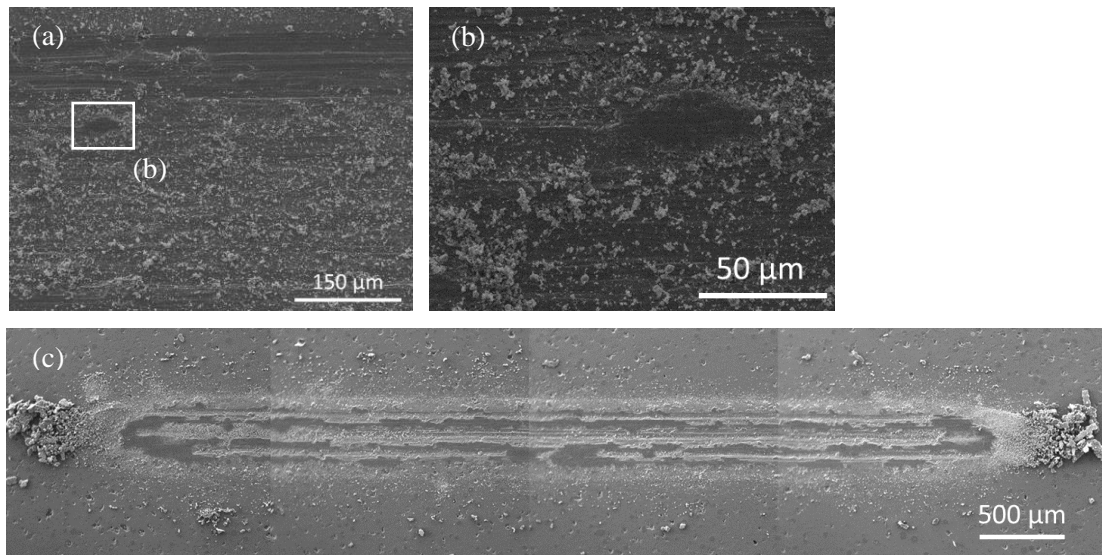


Fig. 7.6: SEM images of the wear tracks of irregular powder composites tested at normal load 2.5 N with (a) 16% TiC (b) higher magnification image of the region shown in (a); (c) 23% TiC showing more continuous tribolayer formation.

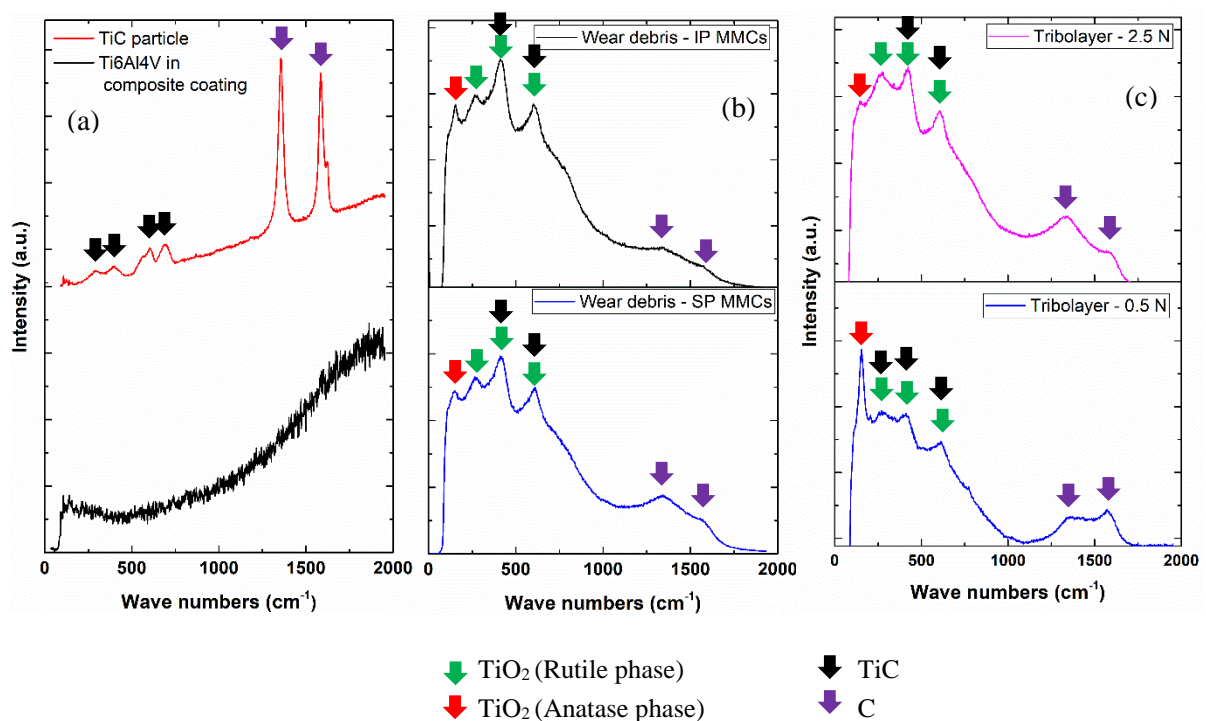


Fig. 7.7: Raman spectra of (a) Ti6Al4V and TiC particle in the coating (b) tribolayer formed at different normal loads (c) wear debris on the wear track of spherical and irregular powder deposited composites.

7.3.4 Counterface analysis

SEM images of the counterface after the completion of the sliding tests at 2.5 N load are shown in Fig. 7.8. At 2.5 N, all the counterfaces except 23% TiC coating countersphere, showed the presence of transfer film at the contact surface surrounded by wear debris (Fig. 7.8a and 7.8b). However, the transfer film and wear debris were found to be more in 15% TiC spherical powder composite coating counterface compared to 16% TiC coating. Raman analysis on the transferfilm and wear debris showed characteristic Raman peaks corresponding to both TiO_2 and TiC, indicating the presence of fragmented TiC particles in the transferfilm (Fig. 7.9a). In case of 23% TiC coatings at 2.5 N, the counterface showed negligible evidence of adhesive transferfilm at the contact surface (see Fig. 7.8c). Furthermore, at specific locations near the interface, smeared wear debris were observed along with small traces of a transferfilm. A comparison of the distance between these smeared regions on the counterface, to the tribolayers on the wear track indicated that the real contact between the wear track and the counterface occurred at these specific locations. In addition, wear debris were found to be surrounding the contact surface similar to other counterfaces. Raman analysis on the wear debris and smeared regions showed peaks corresponding to the TiO_2 and TiC (Fig. 7.9b) indicating the transfer of tribolayer material from the wear track on to the counterface. At 0.5 N, the counterfaces of all the composite coatings showed the presence of adhesive transferfilm (similar to 15% and 16% TiC mated counterfaces at 2.5 N load) comprising of oxides of Ti and fragmented TiC particles (confirmed by Raman analysis) at the contact surface surrounded by wear debris (not shown here).

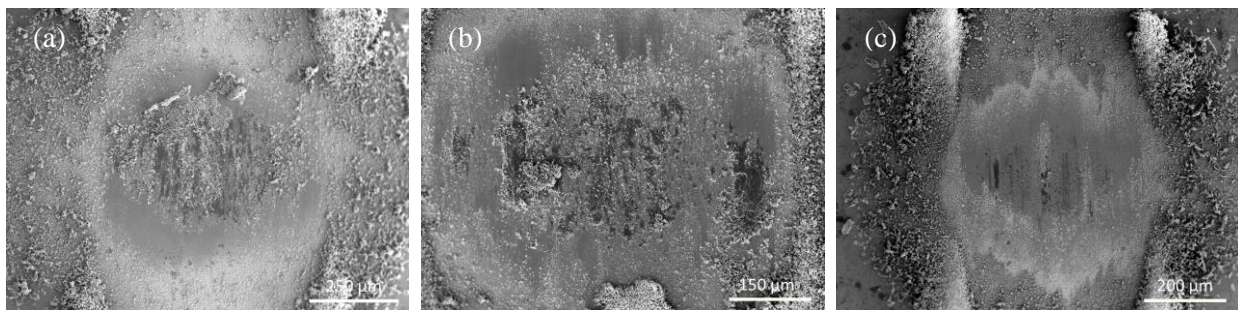


Fig. 7.8: SE images of counterfaces after the test at normal load 2.5 N mating with (a) 15% TiC (b) 16% TiC (c) 23% TiC composite coatings.

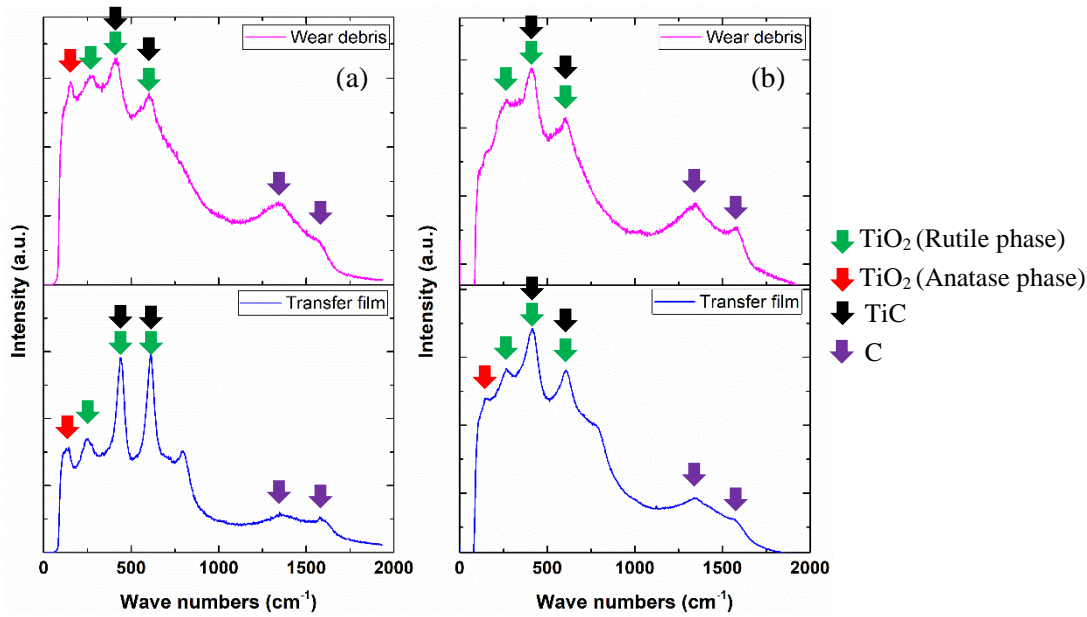


Fig. 7.9: Raman spectra of (a) transfer film and wear debris surrounding the transfer film formed on the counterface at 0.5 N (b) transfer film and wear debris surrounding the transfer film formed on the counterface mating with 23% TiC MMC at 2.5 N.

7.3.4 Subsurface analysis of the wear tracks

ECCI of the wear track cross-sections after the wear tests are shown in Fig. 7.10 and 7.11. At 2.5 N, wear track cross-sections of spherical powder composite coatings did not show the presence of tribolayers which coincided with the wear track SEM images (Fig. 7.10a). Below the wear track formation of ultrafine grain (UFG) layer of thickness $\sim 3.5 \mu\text{m}$ was observed (Fig. 7.10b) followed by a mixture of UFG and fine grains (FG) (Fig. 7.10c) and finally the martensitic lath microstructure (initial microstructure) (Fig. 7.10d). The average grain size in the UFG region was $\sim 70 \pm 20 \text{ nm}$. Similarly, at 0.5 N, UFGs of size $\sim 94 \pm 22 \text{ nm}$ were observed up to a distance of $\sim 5.2 \mu\text{m}$ followed by FGs and martensitic laths (not shown here). In case of irregular powder deposited 16% TiC composite coating at 2.5 N, tribolayer of thickness $\sim 1.6 \mu\text{m}$ was observed as shown in Fig. 7.10e. EDS map of the tribolayer clearly showed the presence of fragments of TiC particles embedded in the tribolayer along with oxygen and titanium rich regions (see Fig. 7.10j). The regions in the tribolayer with bright contrast had high amount of Ti while the dark regions were rich in oxygen. Underneath the tribolayer, an $\sim 2.7 \mu\text{m}$ thick layer of UFGs (see 7.10f-g) of average size $\sim 78 \pm 29 \text{ nm}$ were observed. This was followed by a region comprising of highly

deformed microstructures (Fig. 7.10f and h) and finally, initial coating microstructure (Fig. 7.10i). Similarly, at 0.5 N, tribolayer of thickness $\sim 1.1 \mu\text{m}$ followed by a UFG layer of thickness $\sim 3.6 \mu\text{m}$ and subsequently highly deformed and coarse grain microstructures were observed (not shown here). The UFGs has an average grain size of $\sim 108 \pm 36 \text{ nm}$. In case of 23% TiC composite coating at 2.5 N, tribolayer of $\sim 1.1 \mu\text{m}$ followed by a UFGs of size $\sim 100 \pm 30 \text{ nm}$ were observed (Fig. 7.11a-c). The UFG region was found down till $\sim 2 \mu\text{m}$ (see Fig. 7.11b) which was followed by highly deformed microstructures. Similarly, at 0.5 N, tribolayer comprising of TiC fragments embedded into fine agglomerated TiO_2 wear debris were observed (see 7.11d). The tribolayer had a thickness of $\sim 2.4 \mu\text{m}$ (Fig. 7.11d) and was followed by a layer of UFGs of size $\sim 110 \pm 52 \text{ nm}$ (Fig. 7.11e). The UFG layer of thickness $\sim 2 \mu\text{m}$ was succeeded by a mixture of coarse grain and highly deformed microstructures that extended into the coatings until the initial microstructure was observed as shown in Fig. 7.11f.

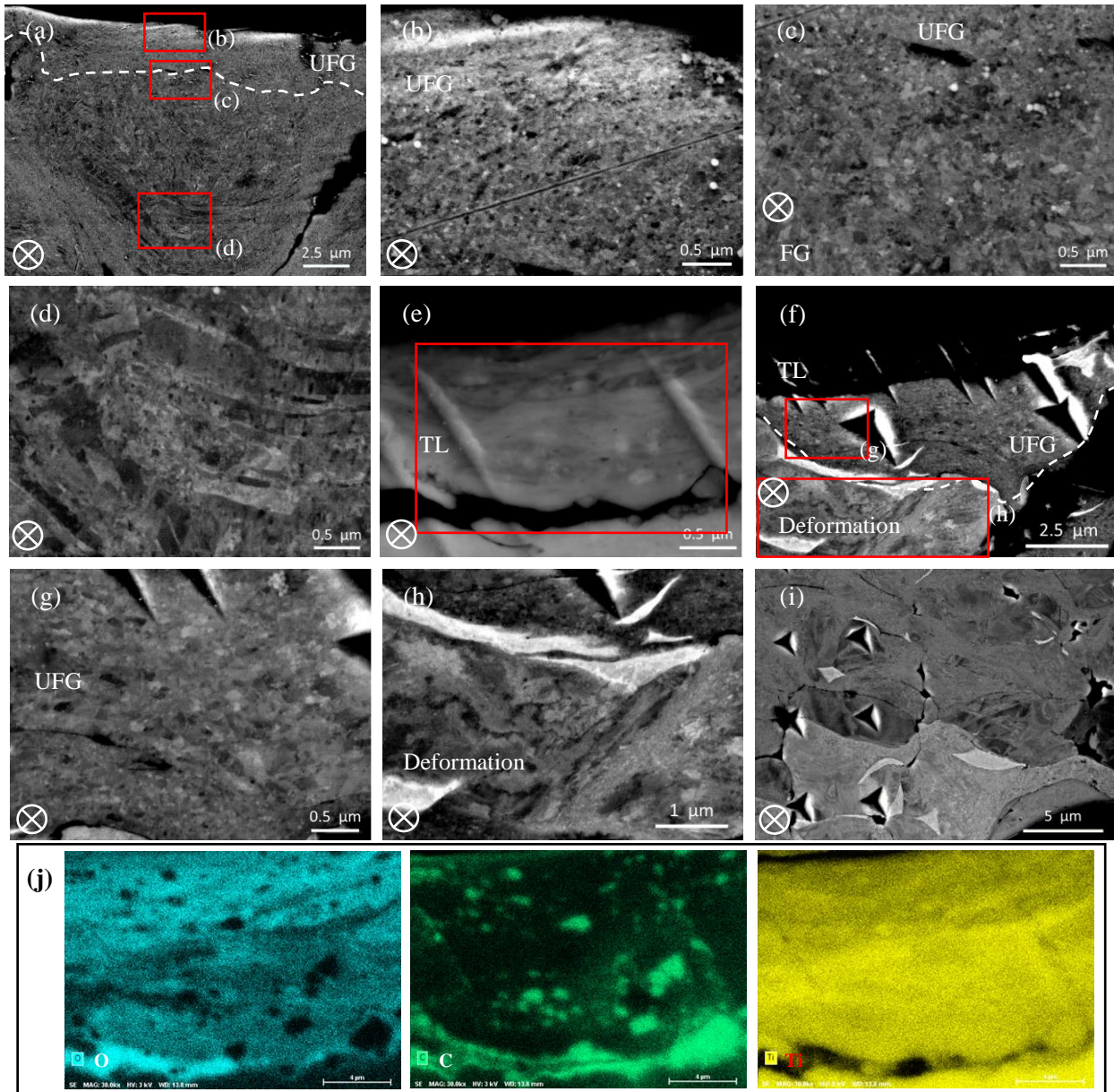


Fig. 7.10: ECCI of the wear track cross sections tested at 2.5 N normal load corresponding to spherical powder 15% TiC coatings (a) worn subsurface (b) near surface region showing UFG (b) subsurface showing UFG and FG (c) initial coating microstructure; irregular powder 16% TiC coatings - (e) tribolayer (f) region below the tribolayer (g) higher magnification image corresponding to location shown in (f) showing UFG (h) higher magnification image corresponding to region shown in (f) showing deformed microstructures (i) initial coating microstructure (j) EDS map of the tribolayer (region shown by red box in e) showing O, C and Ti distributions. ⊗ – indicates sliding direction.

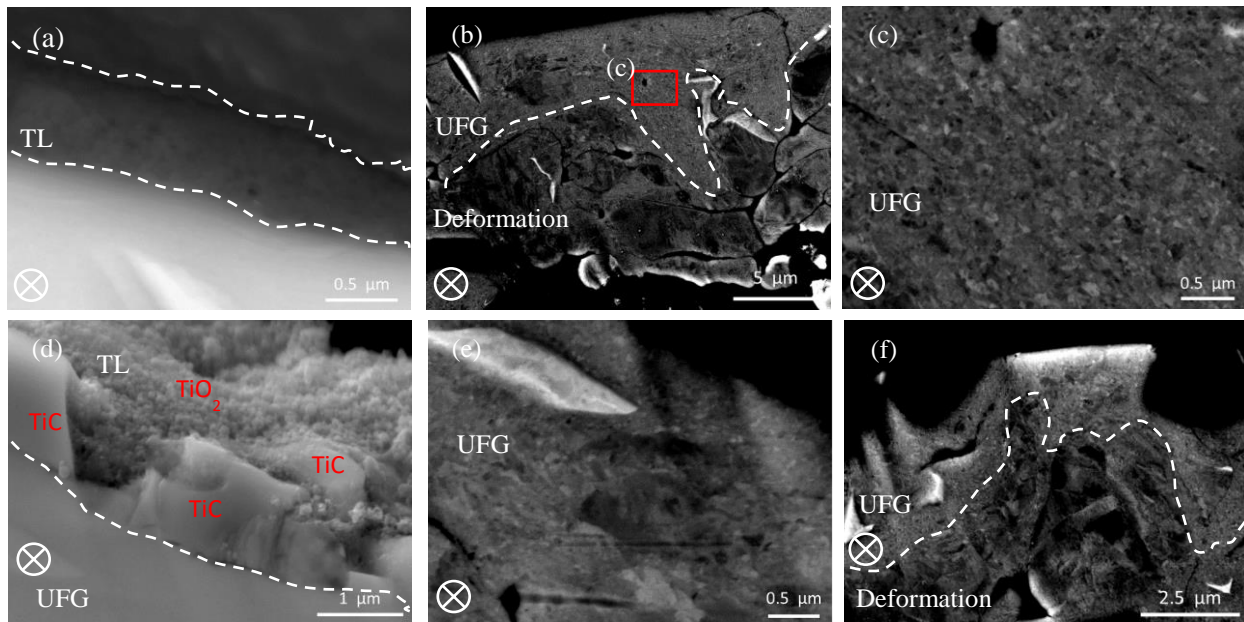


Fig. 7.11: ECCI of the wear track cross sections of Ti6Al4V-23% TiC coating tested at (a) 2.5 N showing tribolayer (b) 2.5 N - lower magnification image showing regions below tribolayer (c) 2.5 N - higher magnification image of the UFGs. (d) 0.5 N - showing the tribolayer (e) 0.5 N - region below the tribolayer (f) 0.5 N - lower magnification image showing UFG followed by highly deformed microstructures; TL – tribolayer. ⊗ – indicates sliding direction.

Figure 7.12 shows the TEM images of the worn cross-section of Ti6Al4V-23% TiC composite coating along with the specific location of the FIB cut on the wear track. From the TEM image, the tribolayer thickness was found to be $\sim 1.05 \pm 0.2 \mu\text{m}$ and cracks were observed underneath the tribolayer (see Fig. 7.12b). Furthermore, fragmented TiC particles were found to be embedded in the tribolayers and also at the regions near to the tribolayer. Furthermore, the tribolayers were found to be an agglomeration of compacted fine wear debris as seen from their bright field and dark field images respectively (Fig. 7.12c). These features were similar to those observed in the ECCI of the worn cross-sections. SAED of the tribolayer showed ring pattern indicating that they had a nanocrystalline structure (see Fig. 7.12d). The d-spacing calculated from the SAED pattern matched well with that of rutile and anatase phases of TiO_2 , indicating that the nanocrystalline tribolayer comprised of oxides of Ti. Underneath the tribolayers, elongated and highly deformed grains along with few UFGs were observed while regions away from the tribolayer showed mostly ultrafine grains (Fig. 7.12e and g). The coarse grain structure underneath tribolayers was further

confirmed by the discontinuous rings in the SAED where as region away from the wear track showed more continuous ring patterns indicating the grains were nanocrystalline to corresponding α -Ti (Fig. 7.12f and h).

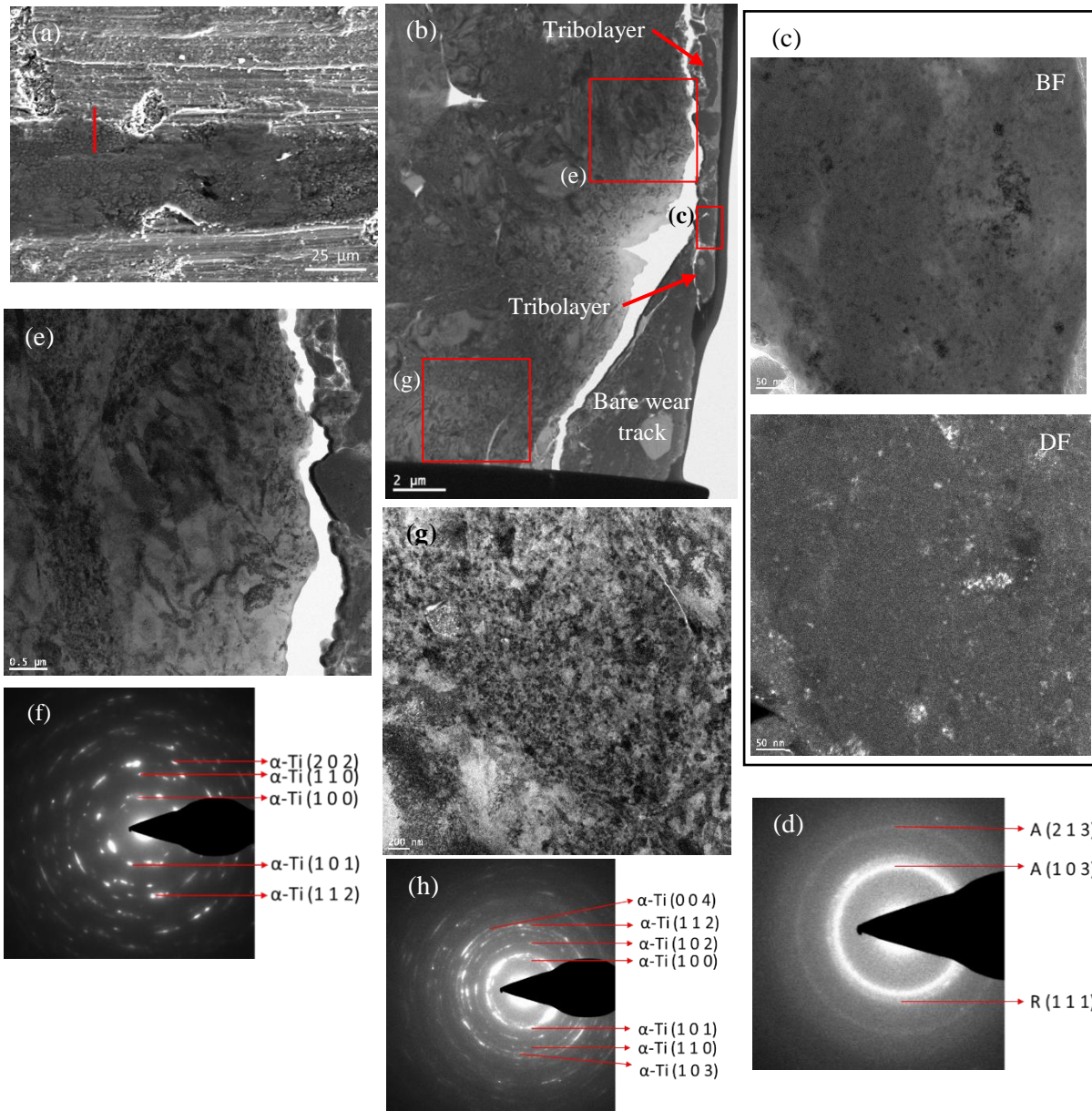


Fig. 7.12: (a) Location of FIB cut on the wear track; (b) TEM image of the subsurface cross-section (c) BF and DF image of tribolayer (d) SAED pattern of the tribolayer (e) higher magnification image of the region below the tribolayer (f) SAED pattern of the region below the tribolayer (g) higher magnification image of the region away from tribolayer (h) SAED pattern of the region away from the tribolayer; Red box in image ‘b’ shows the location where the higher magnification images were taken; A- Anatase and R – Rutile phases of TiO_2 .

Nanoindentation was performed to determine the hardness as a function of depth below the wear surface and is shown in Fig. 7.13. In case of spherical powder composite coatings, the near surface hardness (corresponding to point zero on the X-axis) represents the hardness of UFG region (Fig. 7.13a) whereas in case of irregular powder coatings it corresponds to the hardness of tribolayers (refer Fig. 7.13b). Comparing Fig. 7.13a and b, irregular powder composite coatings showed higher near surface hardness compared to spherical powder composite coatings at both loads due to the formation of tribolayers comprising of oxides of Ti along with fragmented TiC particles. In all the coatings, there was a trend of decrease in hardness with an increase in distance from the worn surface. However, this trend was more clearly seen in irregular powder composite coatings. The variation of hardness with depth from the surface matched with the corresponding features such as UFG, FG and deformed layer that extended below the worn surface. In case of the irregular powder composite coatings, the hardness values approached to a stable coating hardness values at $\sim 10 \mu\text{m}$ below the tribolayer while in spherical powder composite coatings it appeared that the hardness values approached to that of the coatings at $\sim 15 \mu\text{m}$ from the worn surface. This indicated that the stress transfer was greater in case of spherical powder composites which could be due to the absence of tribolayers.

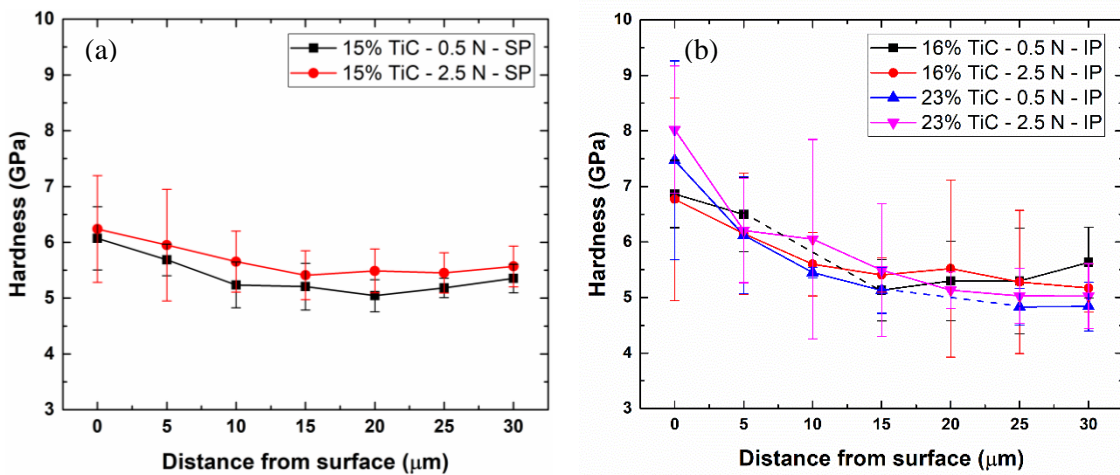


Fig. 7.13: Hardness profile of the worn cross-sections of (a) spherical and (b) irregular powder composite coatings tested at respective normal loads.

7.4 Discussion

The mechanical and tribological properties of MMCs depend largely on the volume fraction of the reinforcements, distribution and hence, high ceramic retentions are often desired [35–37,46]. During the CS deposition of MMCs, ceramic rebound, fragmentation often reduce ceramic retentions [36,37,45,47] especially when hard or high strength materials are used as matrix. In the present study, Ti6Al4V-TiC MMC coatings cold sprayed using two metal powders of different morphology and properties resulted in different ceramic retentions, and tribological properties. As it will be discussed, although higher ceramic retentions resulted in better wear resistance, the properties of the matrix also have a significant effect in determining the tribological behaviour of the coatings.

7.4.1 Cold spray of coatings

MMC coatings deposited using SP had higher porosity and lower ceramic retentions compared to IP deposited coatings for the same initial metal-ceramic mixtures (Table 7.1). The inherent hard martensitic lath microstructure of the SP led to their poor deformability, resulting in porosity. Compared to unreinforced Ti6Al4V coatings (porosity ~13 %) as reported in our previous study [73], the porosity in composite coatings was less and it decreased with increase in ceramic volume fraction in the initial feed stock. This was due to the tamping effect caused by the incoming ceramic particles resulting in coating densification [47,67,141]. Contrarily, the highly deformable equi-axed microstructure of the IP particles and higher impact velocities led to dense coatings (Fig. 7.1d-e). In all the composite coatings the ceramic retention was much lower (< 50%) compared to the initial metal-ceramic mixture due to the rebounding and fragmentation of the ceramic particles upon impact [240]. Ceramic retention in cold sprayed coatings occurs mainly through embedding and entrapping of ceramic particles [45,151]. The embedding of the ceramic particles depends on the hardness of the matrix and its ability to reduce the probability particle rebound. The irregular powder had a deformable equi-axed microstructure and retained porosity on the top surface of the coatings [73]. It has been reported previously by researchers that presence of porosity absorbs the kinetic energy and reduces particle rebound during CS deposition [102,103]. This led to the greater embedding and less probability for a ceramic particle to rebound when compared to spherical powder coatings resulting in higher retentions. Increase in ceramic retention, increased the load bearing capacity of the matrix and hardness of the coatings (refer Table 7.1). At the similar volume

fraction, due to high particle deformability and low porosity, irregular powder composites showed marginally higher hardness compared to spherical powder composites.

7.4.2 Tribology of the coatings

A schematic of the wear mechanisms that occur in spherical and irregular powder deposited composites is shown in Fig. 7.14. Ceramic content and matrix properties significantly influenced the friction and wear behavior of the coatings [45,123]. At 0.5 N load, comparing the spherical and irregular powder composite coatings with similar ceramic contents i.e. 15 vol.% and 16 vol.%, irregular powder coatings showed lower wear rate and low steady state CoF compared to spherical powder coatings (Fig. 7.2). Worn surfaces of spherical powder composites showed abrasive ploughing by the wear debris, which were mostly fragmented TiC and TiO₂ particles (Fig. 7.4a). These abrasive plough marks were similar to that of unreinforced Ti6Al4V coatings as reported in the literature [26,27]. This indicated that the reinforcing ceramic particles did not change the wear mechanisms significantly in these coatings. The continuous formation of wear debris, their fragmentation and ploughing (Fig. 7.14a) during ejection from the sliding interface resulted in high CoF along with large fluctuations (Fig. 7.2a). In addition, delamination of splats was observed on the wear track of these coatings which could be due to weak intersplat bonding (Fig. 7.4b). It was observed in our previous work that Ti6Al4V coatings deposited using these SP had poor cohesive strength between the splats due to limited deformability of the particles [73]. Additionally, the presence of TiC particles would have further hampered the intersplat bonding resulting in delamination during sliding. Compared to spherical powder coatings, the irregular powder coatings had better intersplat bonding due to deformable microstructure and higher inflight particle velocities [73]. This prevented the delamination of the splats and supported the formation tribolayers on the wear tracks due to the presence of TiC particles. These tribolayers were formed around TiC particles and were an agglomeration of highly deformed wear debris comprising of TiO₂ particles and fragments of TiC (Fig. 7.5 and Fig. 7.14b). The tribolayers had higher hardness compared to the near surface hardness of the wear tracks not covered with tribolayers. The formation of hard tribolayers on the wear track resisted the localized shear deformation, reduced the source flow from the underlying matrix and decreased the wear rates [35,36,162]. Raman analysis on the tribolayers, in addition to TiO₂, and TiC showed the presence of broad D and G peaks of carbon. The peaks appeared to be broad compared to the TiC particle in the initial coating

and resembled glassy carbon (Fig. 7.7a-b). The presence of fragmented TiC particles with glassy carbon in the tribolayers provided easy shear for the counterface during sliding resulting in lower CoF. However, during initial cycles (i.e. before friction drop) the CoF in irregular powder composites was mostly similar to spherical, which could be due to similar abrasive wear mechanisms. As the sliding progressed the compaction of wear debris between the first bodies led to the formation of tribolayers resulting in friction drop in irregular powder MMCs. Similar observations were made by Alidokht *et al.* during in situ sliding wear tests of Ti coatings reinforced with TiC particles with high carbon content [36].

Increase in ceramic content in irregular powder coatings from 16% to 23%, led to the higher area coverage of the wear track area with tribolayers. Higher volume fractions led to greater and faster exposure of the reinforced phase to the sliding interface and led to the early formation of tribolayers as indicated by the early drop in CoF (Fig. 7.2b). Furthermore, the presence of tribolayers was observed inside and mostly along the outer edge of the track unlike 16% TiC composites where the tribolayers were mostly inside the wear track. These differences could have resulted in minor changes in the steady state CoF after the friction drop. Furthermore, the early formation of tribolayers in 23% TiC coatings resisted shear deformation and abrasive ploughing by the wear debris at a much early stage, resulting in lower wear rates compared to 16% TiC.

During the wear process, the tribological performance of a material, is governed by its ability to form a wear resistance tribolayer [45,163,238]. At 2.5 N, no tribolayers were observed on the wear track of 15% TiC composite coating, whereas minor evidence of tribolayers were observed in 16% TiC coating (Fig. 7.6b). The absence of significant amount of tribolayers led to abrasive wear in both coatings (Fig. 7.4c and 7.6a). However, the irregular powder deposited composite showed lower wear rate compared to spherical powder composite, which could be due to its higher hardness. The formation of tribolayers, coverage on the wear track and their role in reducing the friction and wear rates, are influenced by a ceramic volume fraction. Irregular powder composites with 23 vol.% TiC showed the formation of tribolayers at both loads. Specifically, at 2.5 N, tribolayers on the wear tracks were found to be highly continuous compared to lower loads resulting in very low average CoF of ~ 0.25 along with low wear rates (Fig. 7.2b and 7.6c). Prior to the friction drop, the CoF was similar to 16% TiC composite coatings indicating similar wear mechanisms initially. As the sliding progressed due to higher ceramic content and high load,

greater pulling out of the TiC particles, their fragmentation along with TiO₂ particles resulted in the formation of highly continuous tribolayer (Fig. 7.6c). This also resulted in lower transfer of material from the coatings as indicated by the minimal transfer film formation on to the counterface when compared to composites with lower reinforcements (Fig. 7.8). The absence or extremely low coverage of the worn surface with tribolayer in 15% and 16% TiC coatings could have led to the scoring by the counterface, progressive formation of wear debris and abrasive ploughing during sliding. This led to highly fluctuating CoF with no friction drops. Contrarily, the formation of a stable tribolayer in 23% TiC coating first led to the significant drop-in friction. Secondly, its highly continuous nature led to minimal exposure of the matrix resulting in lower third bodies activities and hence, lower fluctuations in CoF after the drop (Fig. 7.2b).

The absence of tribolayers on the wear tracks also affected the subsurface microstructure. The grains underneath the wear tracks i.e. in the UFG region were finer compared to the grains formed under the tribolayers, indicating greater stress transfer to the subsurface due to the absence of tribolayers (Fig. 7.12e and g). While the formation of tribolayers might have largely contributed to lower stress transfer due to their high hardness, it is also reported that presence of friction between sliding surfaces changes the stress field at the contact interface [165,180,241]. During sliding in addition to the compressive normal stress due to normal load, presence of friction induces two additional stresses at the contact surface. First, it induces shear stress in the sliding direction and second, a normal stress, that changes from compressive at the initial contact region of the counterface to tensile at the end of the contact [165,241]. The magnitude of these stresses are proportional to the CoF i.e. a lower CoF between the sliding surfaces will lead to lower shear and normal stresses at the contact interface. In the present study, the formation of lubricating tribofilms on the wear tracks of irregular powder coatings would have resulted in lower near surface and subsurface stresses compared to wear tracks without tribolayers. This could have led to lower grain refinement below the tribolayers compared to the wear tracks without tribolayers. Thus, the formation of hard and lubricating tribofilms on the wear track surfaces decreased the CoF, wear rate and also led to lower subsurface stresses resulting in an overall improvement in tribology of the composite coatings.

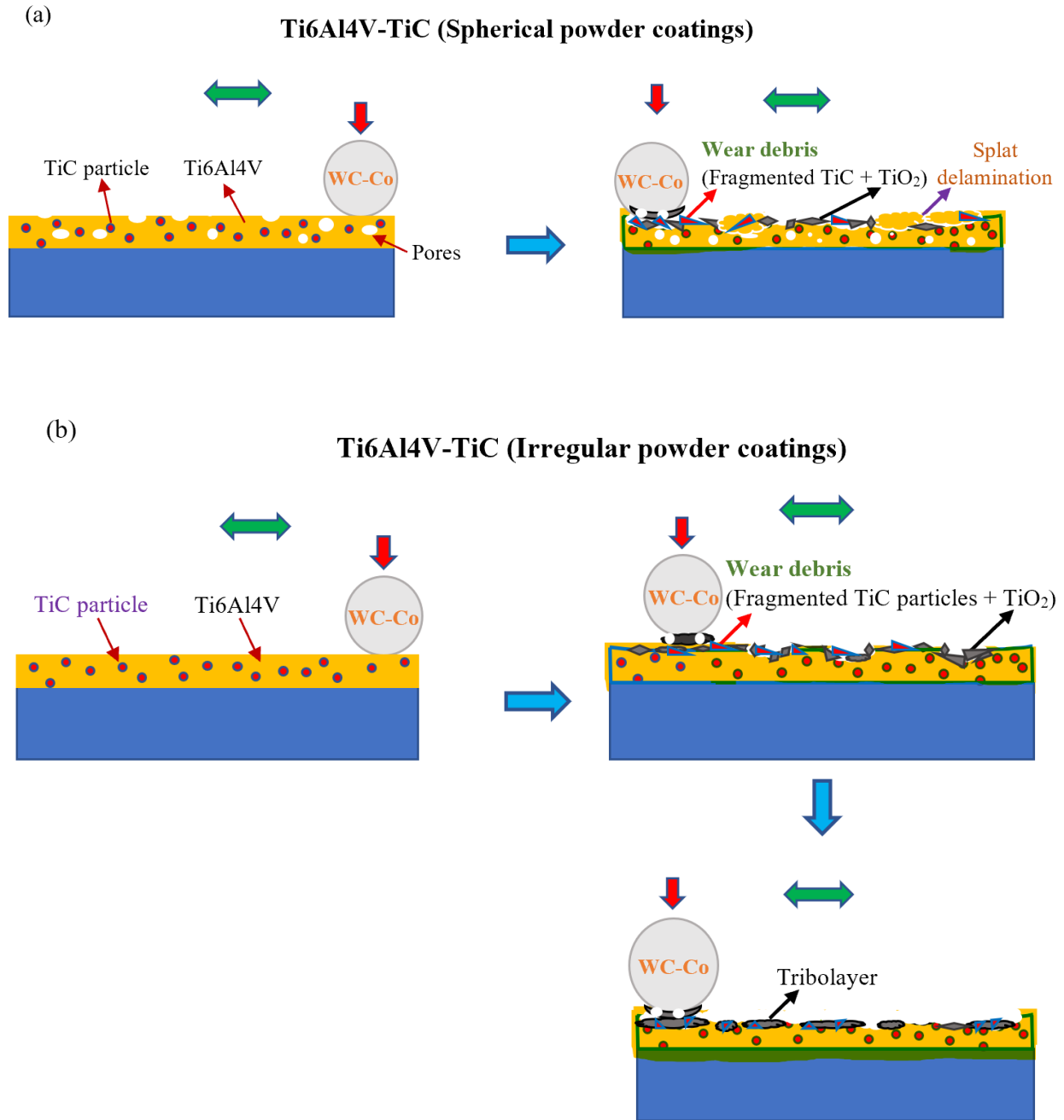


Fig. 7.14: A schematic showing the wear mechanisms in Ti6Al4V-TiC MMCs deposited using (a) spherical (b) irregular powders.

7.5 Conclusions

In the present study, Ti6Al4V-TiC composite coatings were CS deposited using spherical and irregular Ti6Al4V powders and their tribological behaviour was evaluated. Based on the results following conclusions were drawn:

1. Composite coatings deposited using IP showed higher ceramic retentions and lower porosity when compared to SP at similar initial metal-ceramic mixtures. This was due to the more deformable equiaxed microstructure and presence of pores in the feedstock powders that contributed to the higher deformation of the matrix and lowered the probability of ceramic particle rebound during deposition.
2. At low loads i.e. 0.5 N, formation of tribolayers comprising of oxides of Ti and fragmented TiC particles were observed on the wear tracks of irregular powder coatings that led to a drop in CoF and low wear rates. The formation of tribolayers showed twin effect of both resisting the localized deformation and facilitated for the easy shear of the counterface during sliding. However, the ease of formation of tribolayers was highly dependent on the TiC content in the coatings with higher carbide retention favoured their early formation.
3. In case of spherical powder composite coatings, delamination of splats due to their poor bonding did not support the formation of tribolayers. This led to the continuous abrasive ploughing by the wear debris resulting in high friction and wear rates.
4. At higher loads i.e. 2.5 N, formation of tribolayers depended on the TiC content in the coatings. Highly continuous tribolayers were observed on the wear track of 23% TiC composite coating whereas no significant tribolayers were observed on the wear tracks of 15% and 16% TiC coatings. In case of 23% TiC coating, higher ceramic content resulted in greater dislodging of TiC particles from the matrix and led to the formation of a highly continuous tribolayer. This resulted in highly stable and low CoF along with low wear rates.
5. Fragmentation of carbide particles during wear and their reinforcement in the tribolayers contributed to their higher hardness, while the presence of free carbon led to their lubricating nature. These two properties resulted in a composite effect by reducing the magnitude of stress transfer to the subsurface resulting in the formation of coarse grains along with lesser extent of subsurface deformation compared to the wear tracks without tribolayers.

Chapter 8

High temperature friction and wear behavior of cold-sprayed Ti6Al4V and Ti6Al4V-TiC composite coatings

Venkata Naga Vamsi Munagala, Tyler B. Torgerson, Thomas. W. Scharf, Richard. R. Chromik

Adapted from a paper of the same title published in *Wear*, 2019, **426 – 427**:357 – 369.

Abstract

The poor wear resistance of titanium and its alloys often results in galling and high wear rates. One method to improve their wear resistance is by hard secondary phase reinforcement to create a metal matrix composite, which can be utilized in the bulk or as a coating. In the present study, Ti6Al4V coatings and Ti6Al4V-TiC metal matrix composite coatings were deposited on mild steel substrates using cold spray process and their dry sliding wear behaviour was studied over a static temperature range of 25–575°C. Tests were performed using a unidirectional ball-on-disc tribometer with WC-Co sphere as the counterface at a load of 2.5 N and sliding velocity of 2.1 cm.s⁻¹. Wear rate and coefficient of friction (CoF) decreased with an increase in temperature and composite coatings exhibited higher wear resistance at all temperatures. Below 200°C, abrasive wear characterized by ploughing by wear debris resulted in high wear of Ti6Al4V coatings, whereas formation of tribolayers led to lower wear of composite coatings. At elevated temperatures (> 200°C), oxide glaze layers formed on both coatings were composed of WO₃, TiO₂ and CoWO₄. Electron channel contrast imaging of the wear track cross-sections showed no splat debonding, less extent of recrystallization and larger grain sizes (at 575°C) in composite coatings compared to Ti6Al4V.

Keywords: Cold spray, Metal matrix composites, Sliding wear, Ti6Al4V, Tribo-oxides

8.1 Introduction

During wear, metal matrix composite (MMC) coatings form tribolayers that are often beneficial and improve tribological properties in comparison to a pure metal coating of the same material as the matrix [45,61,147,148,163,242]. Tribolayers form due to the agglomeration of third bodies that are generated from one or both of the mating surfaces (first bodies) during wear [36,134,158,243]. The presence of tribolayers, which often have different properties than the first bodies, alter the contact conditions and tribology of the system [158,163]. Alidokht *et al.* and Torgerson *et al.* studied the sliding wear of cold sprayed Ni and Ni-WC composite coatings and found that the reinforcement of WC in Ni matrix facilitated the formation of tribolayers during dry sliding wear which improved the wear resistance compared to pure Ni coatings [134,242]. To enhance the tribological properties of Ti6Al4V, Zhang *et al.* artificially sprinkled TiO₂ and Fe₂O₃ nanoparticles during the sliding wear tests to accelerate the formation of tribolayers [244]. They concluded that a minimum mixture of TiO₂-50 vol.% Fe₂O₃ was required to form tribolayers that increase the load bearing capacity and thus reduce the wear rate. Studies performed by Du *et al.* on wear behavior of NiCr/Cr₃C₂ - NiCr/hBN coatings show that presence of hBN improved the wear resistance and reduced the CoF compared to NiCr/Cr₃C₂ [245]. They reported that formation of a surface layer with embedded hBN particles, reduced the adhesion between the mating surfaces and improved tribological properties. Based on the above studies, the hard phase or solid lubricant changed the kinetics of tribolayer formation and also imparted better properties and wear resistance.

The nature of tribolayers formed on metals and MMCs will change with temperature. Other than mechanical mixing, tribo-oxidation with the atmosphere and tribochemical reactions between the two first bodies are the main mechanisms for tribolayer formation. At elevated temperatures, tribolayers are often referred as glaze layers since they are compacted layers of tribo-oxides comprising of third bodies from either one or both the mating surfaces. In terms of Ti alloys, Cui *et al.* studied the sliding wear behavior of Ti6Al4V coatings in a temperature and load range of 20–400°C and 50–250 N, respectively [227]. They found that an increase in temperature up to 200°C increased the wear rate with abrasive and adhesive wear resulting in severe wear. Beyond 200°C, the wear rate decreased due to the formation of protective tribolayers resulting in mild wear. Wang *et al.* performed sliding wear test on Ti alloys within a range of 25–600°C with steel as counterface [48]. They reported a transition in wear mechanisms between 300–400°C from

predominantly abrasive to oxidative wear, which significantly decreased the wear rate. The change in wear mechanism and improvement in wear resistance was attributed to the continuous formation of hard tribolayers (or oxide glaze layers) comprising of Ti and Fe-based oxides. In addition, similar results of improvement in wear resistance of a Ti alloy sliding against steel counterface due to the formation of tribolayer beyond 200°C was reported by Chen *et al.* [246] The studies mentioned above illustrate that below ~ 300°C, Ti alloys exhibit severe abrasive wear due to the inability of their tribo-oxides to coalesce and form protective tribolayers, while the tribolayer formation occurs only beyond ~ 300°C.

Thus, Ti alloys show different friction and wear mechanisms with changes in temperature due to the formation of tribolayers of different chemical compositions based on the elements present at the tribo-pair interface. Furthermore, the sliding wear of Ti6Al4V based MMC coatings at elevated temperatures is not extensively studied in the literature. The aim of the present study is to understand the tribological behavior of cold sprayed Ti6Al4V and Ti6Al4V-TiC MMC coatings over a temperature range of 25-575°C. The effects of temperature and TiC reinforcement in modifying the friction and wear mechanisms was investigated in detail. Electron channel contrast imaging (ECCI) was done on the wear track cross-sections to characterize the third bodies and subsurface microstructures. In addition, nanoindentation was performed on the third bodies to determine their hardness.

8.2 Experimental procedure

8.2.1 Cold spray of coatings and characterization

Irregular Ti6Al4V (Cristal Metals, USA) and spherical TiC (Tekna, Canada) powders of size range: 0 – 45 µm and 15 – 45 µm were cold sprayed to deposit Ti6Al4V and Ti6Al4V-TiC MMC coatings. The size distribution, average particle diameter and microstructure of the two feedstock powders were reported in previous publications [36,73]. Coatings were deposited on to mild steel plates (substrate) of dimensions 75×75×3 mm³ using a high pressure cold spray system PCS 800 (Plasma Giken, Japan). Prior to deposition the substrates were de-greased and grit blasted using alumina to enhance the coating-substrate bonding. Nitrogen (N₂) was used as propellant gas with pressure and temperature fixed at 4 MPa and 800°C for all the coatings. The standoff distance between the nozzle and substrate was 40 mm and the gun traverse speed was 0.2 m.s⁻¹. The CS

system used was equipped with a dual feeding system in which Ti6Al4V and TiC powders were fed into two separate hoppers. During the deposition of Ti6Al4V coatings, Ti6Al4V powder was fed through the nozzle whereas for the deposition of composite coatings both hoppers (i.e. dual feeding system) were activated. The feed rate of the hoppers was adjusted separately to get the required initial metal-ceramic mixture at the inlet of the nozzle.

Deposition efficiency (DE) of the coatings was determined using Eq. 8.1-8.3. After CS deposition, coatings were cut perpendicular to the gun traverse direction, cold mounted and polished down till 0.05 μm using colloidal silica suspension. The polished samples were characterized using a scanning electron microscope (SEM) SU3500 (Hitachi, Japan) equipped with a back scattered electron (BSE) detector. BSE images were taken at different locations across the sample cross-section and were uploaded into ImageJ software and the pixels associated with their respective contrast was calculated to determine the porosity and ceramic retention percentages. At least 15 images taken at various locations were analysed to calculate the final average values in each case.

$$\text{DE (\%)} = \frac{\text{Weight of the powder deposited (W}_d\text{)}}{\text{Weight of the powder sprayed (W}_s\text{)}} \quad 8.1$$

$$W_d = \text{Weight of the sample (after coating)} - \text{Weight of the substrate} \quad 8.2$$

$$W_s = \frac{\text{Powder feedrate} \times \text{Distance travelled by the gun on the sample}}{\text{Gun traverse speed}} \quad 8.3$$

Microhardness tests were performed on the polished coating surface at random locations using a Vickers microhardness tester (Buehler, USA) at 5 kg load and 15 s holding time. This indentation load was chosen to have the indenter interact with the reinforced carbide particles along with the matrix. An average of 10 indents was done to calculate the average hardness.

8.2.2 Sliding wear tests

Dry sliding wear tests on the coatings were performed using a unidirectional ball-on disc tribometer Falex ISC-450 (Falex Corporation, USA). The tribometer was equipped with a heating stage (on which the sample was mounted), a temperature controller (Honeywell, USA) and a thermocouple. The thermocouple, temperature controller and the heating stage were connected through a feedback loop wherein the temperature controller collects the data through the thermocouple and activates or de-activates the heating coil placed under the heating stage to

maintain the desired static test temperature. WC-Co balls of diameter 6.35 mm were used as counterface for all the tests. The sliding wear tests were conducted in ambient air (~40% RH) under a normal load of 2.5 N (~0.8 GPa initial maximum Hertzian contact stress), which was chosen to be below the ~0.9 GPa yield strength of Ti6Al4V alloy. The sliding speed was fixed at 2.1 cm.s⁻¹ and all the tests were run for a total sliding distance of 200 m to observe the steady-state friction behavior. At least two sliding tests were performed on each coating at every temperature up to 400°C while for test at 575°C only one test was done due to constraints from the experimental setup. Coatings used for the wear tests were polished using 400 to 1200 grit SiC abrasive paper, subsequently using 9 μm, 3 μm, 1 μm diamond suspension solution and finally using 0.05 μm colloidal silica suspension. Sliding wear tests were performed at 25°C, 200°C, 400°C and 575°C static test temperatures for both Ti6Al4V and Ti6Al4V-TiC composite coatings. The above temperature range was chosen since Ti and its alloys are widely used in aerospace applications where they are subjected to elevated temperatures up to ~ 600°C [48]. The coefficient of friction (CoF) for the entire test duration was recorded using the software supplied by the manufacturer. Generally, in a sliding wear test there is a running-in period characterized by either sharp rise or fall in CoF followed by a steady state regime where the CoF converges approximately to a stable value. In the present study, the average CoF was calculated by averaging the CoF after it had reached steady state. The steady state regime was chosen based on the criteria that the CoF did not abruptly rise or fall beyond a value of ± 0.05 for the subsequent sliding distance till the end of the test. For all the coatings the steady state was found to be lasting for at least 150 m after the initial running-in period. To calculate the wear rate, wear tracks were analyzed under a non-contact optical profilometer (Zygo Corporation, USA) and profiles were generated across the wear tracks. A minimum of 35 profiles were used to calculate the wear area (by integrating the profiles above and below the surface), that was subsequently averaged and multiplied with the total track length to determine the final wear volume (mm³). The wear volume was normalized with load (N) and total sliding distance (m) to calculate the wear rate (mm³.N⁻¹.m⁻¹). Profilometry was performed on the worn counterface using a non-contact optical profilometer to calculate the wear volume. The worn counterface was fitted with a sphere of same radius and was flattened to determine the volume below the unworn region (reference surface). The volume below the unworn region was considered as wear volume.

The worn surface and counterface after the wear tests were characterized using an SEM SU3500 equipped with an energy-dispersive X-ray spectroscope (EDS) and BSE detectors. Raman analysis was also performed on the wear tracks and counterface using an inVia Raman spectrometer (Renishaw, UK) with Ar⁺ laser source of $\lambda = 514.5$ nm. To characterize the subsurface microstructure, ECCI was performed on the wear track cross-sections using a FE-SEM SU8230 (Hitachi, Japan) equipped with a BSE detector. Nanoindentation was performed on the wear track cross-sections using a Triboindenter (Hysitron Corporation, USA) at a peak load of 5 mN using a Berkovich tip. The hardness of the tribolayer and the subsurface was determined from the load-displacement curves using Oliver and Pharr method [196] and each hardness value represents an average of 5 to 10 indents. Indentation was done in a grid pattern on the wear track cross-sections from the unworn coating up to the worn surface. Subsequently, the residual indent images were matched with the corresponding pre-indent images and load-displacement curves to obtain the required features of interest.

8.3 Results

8.3.1 Cold spray, characterization and properties of the coatings

Ti6Al4V and Ti6Al4V-TiC coatings were cold sprayed and the DE, porosity, ceramic retention, hardness and thickness values are summarized in Table 8.1. From Table 8.1, the DE of composite coating was significantly less than Ti6Al4V coatings mainly due to the non-bonding nature of the ceramic particles. Fig. 8.1a and 8.1b show the BSE images of the cross-section of the Ti6Al4V and Ti6Al4V-TiC composite coatings. In the BSE images of the composite coatings (Fig. 8.1b), the grey contrast of the spherical and fragmented particles corresponds to the ceramic particles whereas the dark spots correspond to porosity (shown by white arrows in Fig. 8.1b). BSE images reveal that the Ti6Al4V coatings were dense with negligible porosity whereas the composite coatings showed evidence of some porosity due to the fragmentation of ceramic particles. Ceramic retention in the composite coatings was found to be lower compared to the initial feedstock. Initially, a mixture of 50 vol.% of metal and ceramic were cold sprayed and only 23 vol.% was retained in the coatings that correspond to 46% of ceramic in the initial feedstock. The hardness of the composite coatings was higher compared to pure Ti6Al4V coatings (Table 8.1) due to the presence of ceramic particles that increase the load-bearing capacity.

Table 8.1 Coating characteristics.

Coating	Deposition efficiency (%)	Porosity (%)	Ceramic in the initial feedstock (vol.%)	Ceramic retention (vol.%)	Hardness (HV)	Thickness (mm)
Ti6Al4V	92	0.3 ± 0.1	---	---	191 ± 12	1.7 ± 0.04
Ti6Al4V-TiC	42	1.0 ± 0.4	50	23	274 ± 19	1.0 ± 0.06

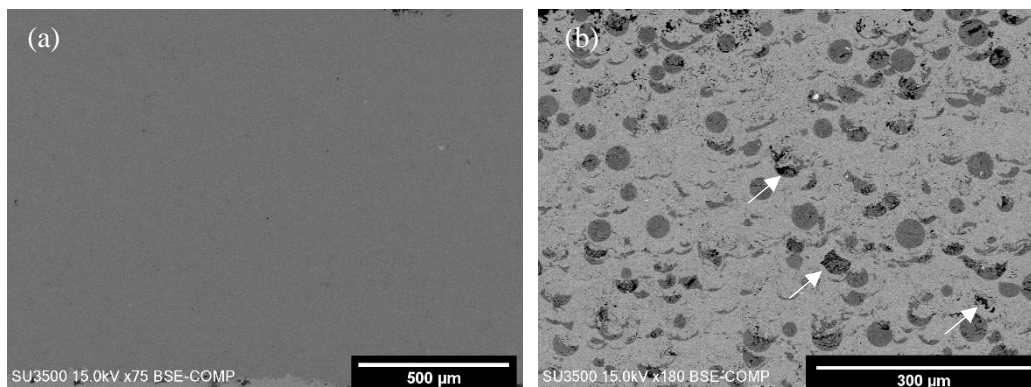


Fig. 8.1: SEM images of (a) Ti6Al4V (b) Ti6Al4V-TiC composite coating. White arrows indicate porosity due to ceramic fragmentation.

8.3.2 Sliding wear of Ti6Al4V and Ti6Al4V-TiC coatings

8.3.2.1 Friction and wear behavior of the coatings

Figure 8.2a shows the wear rates of Ti6Al4V and Ti6Al4V-TiC composite coatings at different test temperatures. There was a trend of decreasing wear rate with increased temperature in both the coatings. At all test temperatures, the composite coating had a lower wear rate compared to Ti6Al4V coating (see Fig. 8.2a). For example, composite coating exhibited approximately 7 times lower wear rate compared to Ti6Al4V coating at 25°C (room temperature). At higher temperatures (400°C and 575°C), composite coating showed negative wear rate (i.e. material gain on the wear track was recorded due to the transfer from the counterface). For the Ti6Al4V coatings, there was some amount of wear that occurred irrespective of the temperature. However, the difference in the wear rates between Ti6Al4V and the Ti6Al4V-TiC composite coating became less as the test temperature increased (see Fig. 8.2a).

Figure 8.2b shows the average CoF of the Ti6Al4V and Ti6Al4V-TiC composite coatings. The average CoF was between 0.25 – 0.45 for both coatings at all test temperatures. To check the hypothesis that the average CoF of Ti6Al4V and composite coatings at all the temperatures was statistically different, an independent samples t-test (i.e. student's t-test) was performed with the probability (p) value to accept null hypothesis (i.e. there is no significant difference between the means) greater than 0.05. T Test results showed that the average CoF was different both in pure Ti6Al4V and composite coatings at all temperatures. For the case of Ti6Al4V coatings, the average CoF increased initially and then decreased with temperature, whereas in the composite coatings the average CoF decreased with an increase in temperature. Above 200°C, the Ti6Al4V-TiC coating exhibits lower CoF than Ti6Al4V coating.

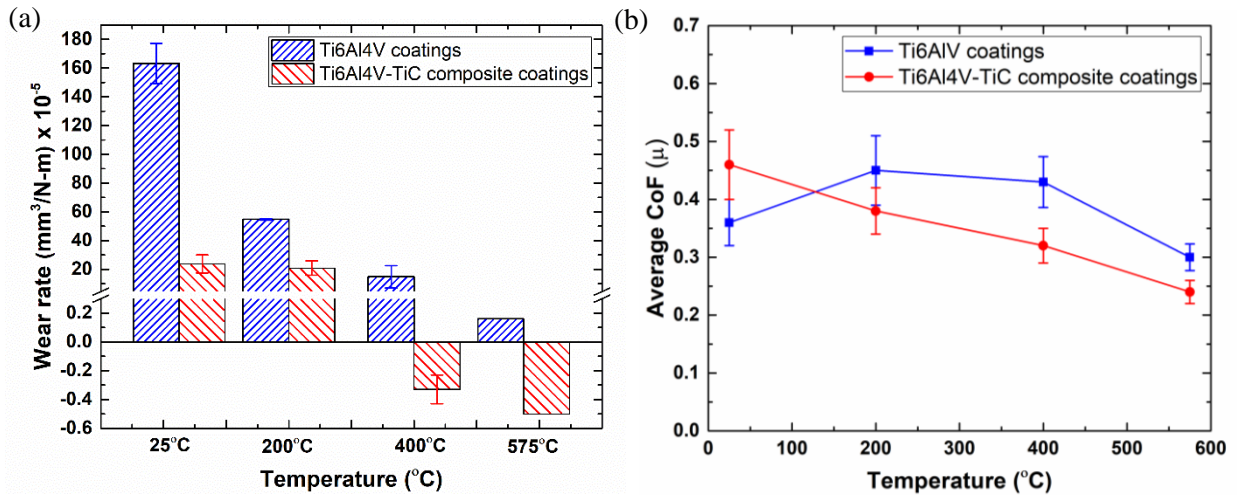


Fig. 8.2: (a) Wear rate (b) average CoF of the coatings.

8.3.2.2 Wear track morphology

The worn surface morphology of the coatings after sliding wear tests at different temperatures are shown in Fig. 8.3 and 8.4. Worn surface of Ti6Al4V coating at 25°C showed abrasive wear with grooves aligned in the sliding direction (Fig. 8.3a). These grooves were formed due to the scoring action caused by the entrapped wear debris and the counterface during sliding. Additionally, wear debris were found to be displaced on either side of the track along with few patches inside the track as seen in Fig. 3a. A similar abrasive wear mechanism was found at 200°C (Fig. 8.3c). However,

at 200°C the grooves were found to be deeper (see Fig. 8.3c) compared to 25°C. At 400°C and 575°C, the wear tracks are characterized by different features compared to 25°C and 200°C. These wear tracks are covered with a compact tribolayer (or glaze layer) indicating a change in wear mechanisms (see Fig. 8.3e and g). However, apart from tribolayers, abrasive grooves in the sliding direction were still visible on the wear track at 400°C, but to a lesser extent as compared to 200°C. Furthermore, a uniform coverage of the wear track with tribolayer was found at 575°C (Fig. 8.3g) with no evidence of abrasive wear.

Figure 8.4 shows the wear track morphology of the composite coatings at different test temperatures. At 25°C, tribolayers were found to be covering the entire wear track (see Fig. 8.4a). Additionally, minor abrasive grooves formed due to ploughing by the wear debris were found on the wear track, which is a characteristic of abrasive wear. Similarly, at 200°C, tribolayers along with abrasive grooves were found on the wear track, however the area covered by the tribolayer at this temperature was less compared to 25°C (Fig. 8.4c). At 400°C and 575°C, the wear track was covered with a tribolayer (or glaze layer) similar to Ti6Al4V coatings (Fig. 8.4e and 8.4g). Along with tribolayers, a few shallow wear scars along the direction of sliding were found on the wear track. At 400°C, the tribolayer was partially covering the wear track (Fig. 8.4e), whereas at 575°C, the tribolayer was found to be covering the entire wear track (Fig. 8.4g).

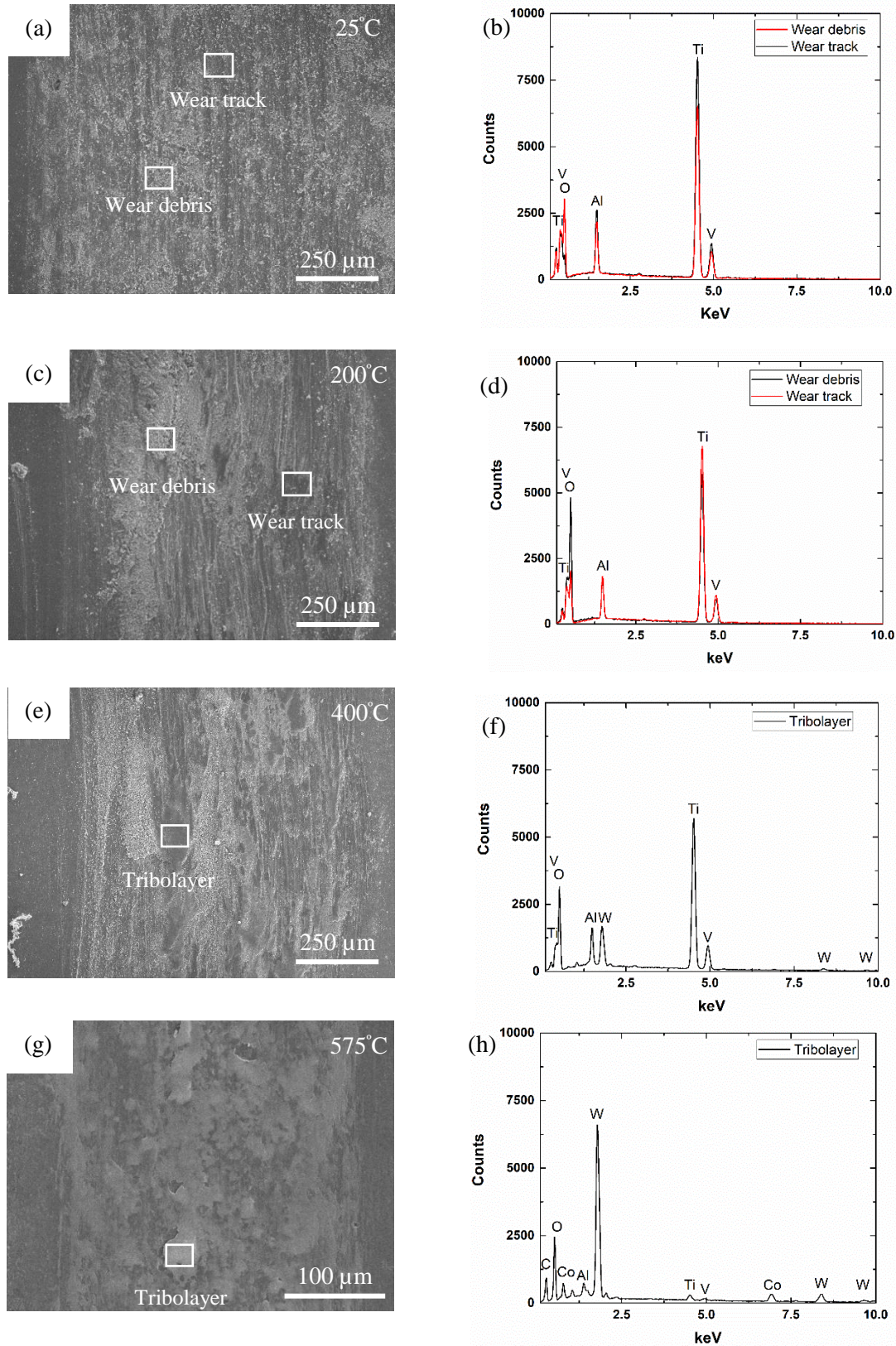


Fig. 8.3: SEM images of wear track of Ti6Al4V coatings tested at (a) 25°C (c) 200°C (e) 400°C (g) 575°C and (b), (d), (f), (h) EDS spectra taken at respective positions on the wear tracks.

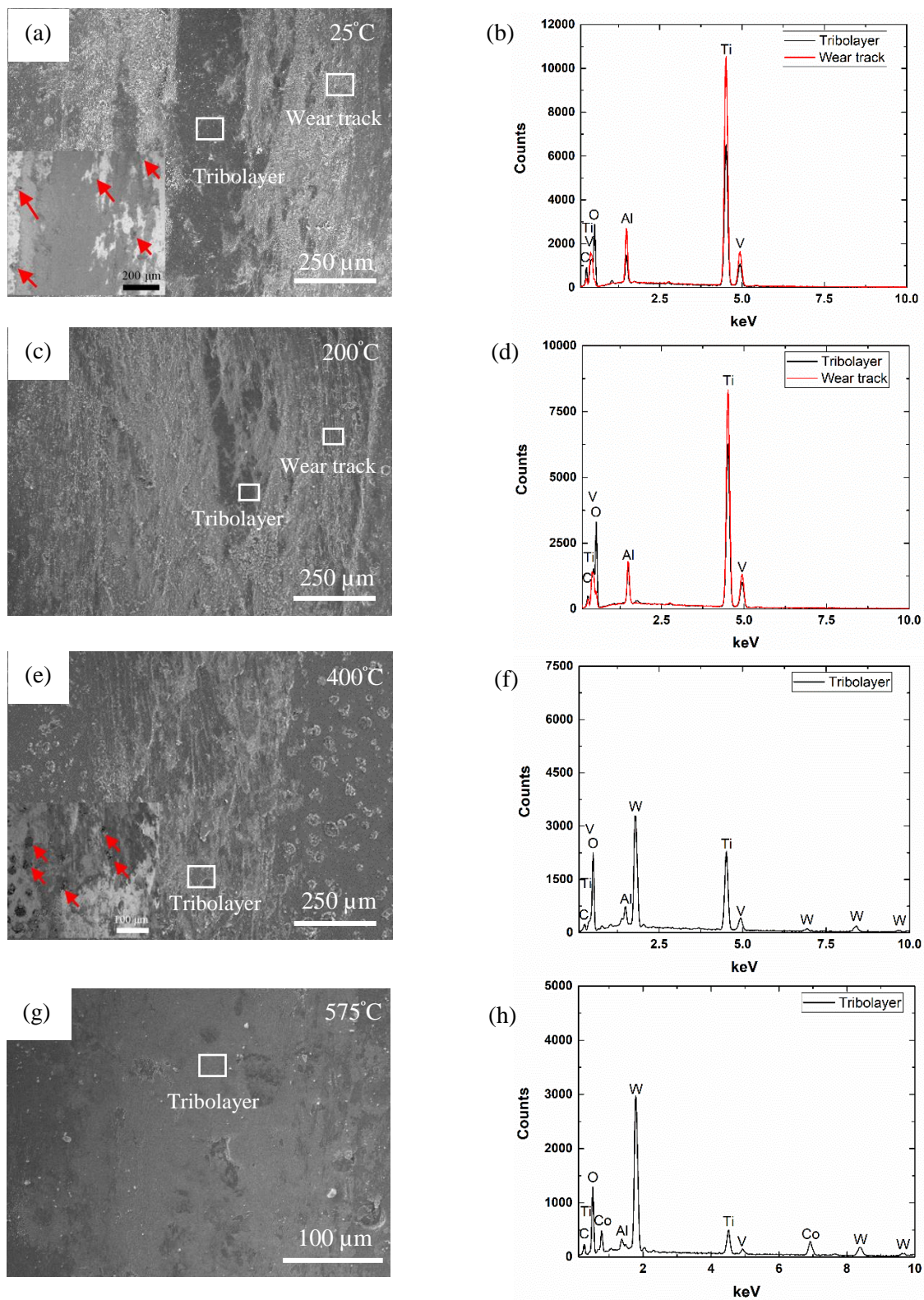


Fig. 8.4: SEM images of wear track of Ti6Al4V-TiC coatings tested at (a) 25°C (c) 200°C (e) 400°C (g) 575°C and (b), (d), (f), (h) EDS spectra taken at respective positions on the wear tracks. Inset images in (a) and (e) show BSE image of tribolayers with arrows showing fragmented TiC particles.

8.3.2.3 Wear track chemical analysis

EDS analysis on the wear track of Ti6Al4V coating at 25°C and 200°C revealed the presence of Ti, Al, V and O both on the wear track as well as on wear debris (Fig. 8.3b and 8.3d). However, the amount of oxygen content in the wear debris and wear track increased with an increase in temperature due to greater oxidation. At 400°C, W was also found along with Ti, Al, V and O in the tribolayers (see Fig. 8.3f). The W in the tribolayer was due to the transfer of the WC-Co ball material during the wear process. Furthermore, as the test temperature increased to 575°C, W, C and Co were also found along with Ti, Al, V and O on the wear track that was covered with tribolayer (see Fig. 8.3h).

In contrast, EDS analysis on the wear track of composite coatings showed the presence of different elemental compositions with increasing test temperatures. EDS of the worn surface of the composite coatings at 25°C and 200°C showed the presence of Ti, Al, V, O and C on the tribolayers and wear track (Fig. 8.4b and 8.4d). However, the amount of C and O detected was higher on the tribolayers as compared to the wear track (see Fig. 8.4b and 8.4d). At 400°C and 575°C, EDS analysis on the tribolayer also revealed the presence of W, and additionally Co (only at 575°C), due to WC-Co ball transfer, along with Ti, Al, V, O and C (Fig. 8.4f and 8.4h). Furthermore, C content on the wear track decreased as the temperature increased due to limited exposure of TiC carbide particles as they were masked by the oxide-rich tribolayers. However, at 575°C, the higher C content could be due to the transfer of material from the counterface. Compared to Ti6Al4V coatings, composite coatings showed higher amount of W at 400°C and Co at 575°C correspondingly, indicating more material transfer from the ball.

To identify the tribo-chemical phases formed, Raman analysis was performed on the wear track and tribolayers at the respective test temperatures and the resultant peaks corresponding to the Raman shift were matched with those reported in the literature [36,247–249]. Raman analysis on the wear debris of the Ti6Al4V coatings tested at 25°C and 200°C showed characteristic peaks at 143 cm⁻¹, 270 cm⁻¹, 405 cm⁻¹ and 609 cm⁻¹ corresponding to rutile and anatase phases of TiO₂ (Fig. 8.5a and 8.5b). However, on the wear track at 25°C and 200 °C, no peaks were detected (Fig. 8.5a and 8.5b) and was similar to the Raman spectra of as-sprayed coating (Fig. 8.5a), whereas at 400°C, peaks corresponding to TiO₂ were observed. Tribolayers formed at 400°C revealed peaks at 870

cm^{-1} and 1583 cm^{-1} corresponding to WO_3 and C (Fig. 8.5c) respectively, along with TiO_2 . At 575°C , a sharp peak at 885 cm^{-1} corresponding to CoWO_4 (Fig. 8.5c) was observed on the tribolayers in addition to TiO_2 and WO_3 .

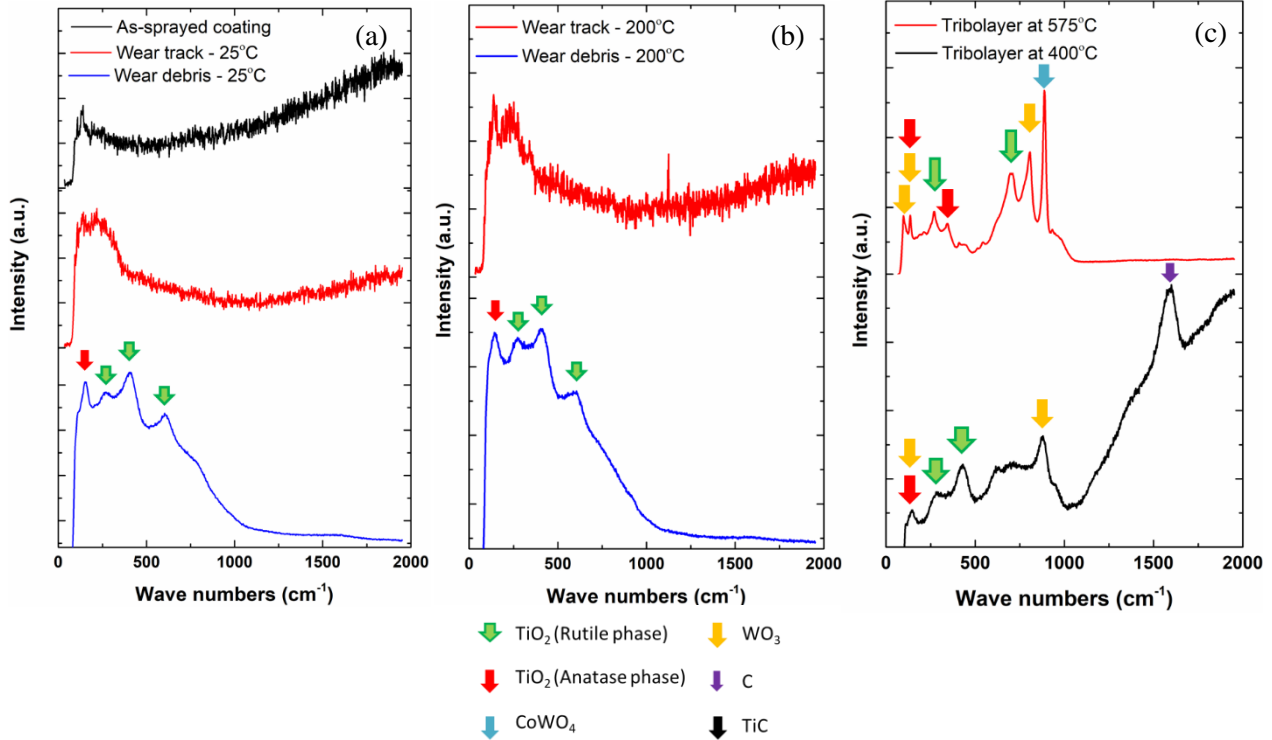


Fig. 8.5: Raman spectra of Ti6Al4V coatings corresponding to (a) as-sprayed coating, wear track and wear debris at 25°C (b) wear track and wear debris at 200°C (c) tribolayer at 400°C and 575°C .

Raman analysis on the tribolayer and wear track of composite coatings revealed distinct phases with an increase in test temperatures. At 25°C and 200°C , tribolayers on the track showed peaks corresponding to TiO_2 along with TiC (Fig. 8.6b). However, the carbon peaks corresponding to a Raman shift of 1335 cm^{-1} (D-band) and 1583 cm^{-1} (G-band) were significantly broad and different compared to the peaks observed in the initial TiC particle (see Fig. 8.6a). Wear debris on the side of the 25°C wear tracks showed the presence of TiC and TiO_2 phases indicating that the debris were predominantly the oxide particles of Ti and exposed TiC particles (Fig. 8.6b). At 400°C , the wear debris showed peaks corresponding to TiO_2 whereas the tribolayer showed additional peaks of WO_3 along with TiC (Fig. 8.6c). The tribolayer covering the wear track at 575°C showed an additional high-intensity sharp peak of CoWO_4 along with TiO_2 , TiC and WO_3 peaks (Fig. 8.6c).

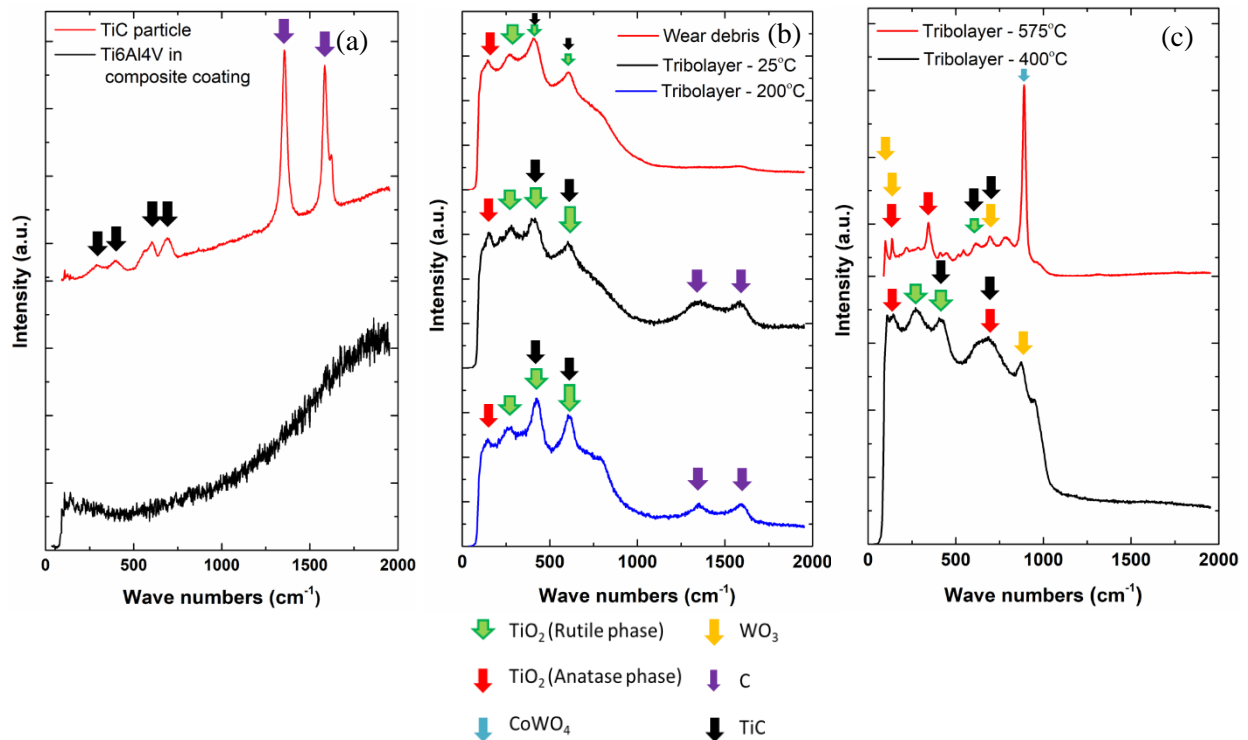


Fig. 8.6: Raman spectra of (a) as-sprayed composite coating (TiC particle and Ti6Al4V matrix); worn composite coatings corresponding to (b) tribolayers at 25°C, 200°C and wear debris (c) tribolayer at 400°C and 575°C.

8.3.2.4 Counterface analysis

The WC-Co counterfaces after the sliding test were examined under SEM and optical profilometer to characterize the worn morphology and to determine the wear volume. At 25°C and 200°C, there was no observable ball wear. However, at 400°C and 575°C, there was ball wear for counterfaces used in wear tests on both coatings. The volume of material worn from the ball after the sliding wear tests at different temperatures are summarized in Table 8.2. For tests on both coatings, the wear volume of the counterface was higher at 400°C compared to 575°C.

Counterfaces sliding on the Ti6Al4V coatings for tests at 25°C (Fig. 8.7a) and 200°C (not shown here) showed the coverage of the contact surface with the wear debris and transfer layer. Raman analysis on the wear debris showed characteristic peaks corresponding to TiO₂ (Fig. 8.7d) whereas on the transfer layer, no active Raman peak was found indicating the transfer of Ti6Al4V on to the ball. As the test temperature was increased to 400°C, wear scar was found on the counterface with wear debris at its circumference as seen in Fig. 8.7b. Raman analysis on the wear debris revealed

peaks corresponding to TiO_2 along with WO_3 as shown in Fig. 8.7e, similar to the phases found on the tribolayer of the wear track. At 575°C , minimal wear was observed on the ball (Fig. 8.7c) corresponding to the low ball wear volume reported in Table 8.2. Furthermore, scattered wear debris were found at the contact interface, with few at the point of contact, which could have occurred during the wear process. Raman peaks corresponding to CoWO_4 , WO_3 and TiO_2 were observed on the wear debris as shown in Fig. 8.7f.

Table 8.2 Wear volume of the counterface.

Coating	Temperature ($^\circ\text{C}$)	Wear volume (μm^3) $\times 10^4$
Ti6Al4V and Ti6Al4V-TiC	25°C and 200°C	No wear
Ti6Al4V	400°C	92 ± 6
Ti6Al4V-TiC	400°C	120 ± 13
Ti6Al4V	575°C	0.3 ± 0.1
Ti6Al4V-TiC	575°C	1.2 ± 0.5

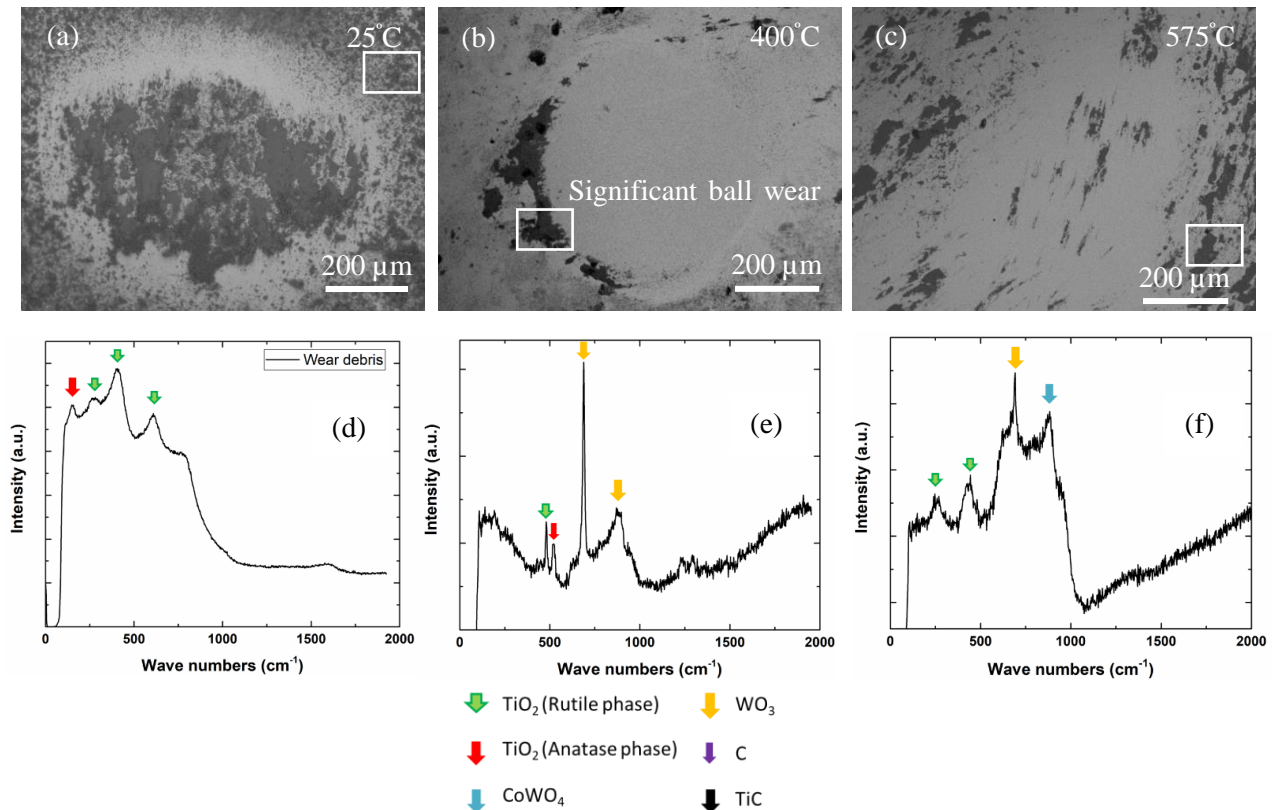


Fig. 8.7: SEM images of the counterfaces used on Ti6Al4V coatings at (a) 25°C (b) 400°C (c) 575°C ; (d), (e) and (f) Raman spectra at corresponding places shown with a box.

Figure 8.8 shows the SEM images of the counterfaces used for sliding tests on composite coatings at different temperatures. At 25°C (see Fig. 8.8a) and 200°C (not shown here), formation of transfer film and wear debris at the contact surface was found on the counterface. Raman analysis on the transfer film formed at the contact interface showed characteristic peaks corresponding to TiO₂ and TiC (see Fig. 8.8d) whereas scans on the wear debris showed peaks corresponding to TiO₂. As the temperature increased to 400°C, the wear scar (see Fig. 8.8b) showed significant wear of the counterface surrounded by wear debris. Raman analysis on the wear debris revealed characteristic peaks corresponding to TiO₂, TiC and WO₃ (Fig. 8.8e). At 575°C, the ball wear significantly reduced compared to that of 400°C where no visible wear scar was found in the SEM image. Additionally, wear debris were found to be aligned in the sliding direction as seen in Fig. 8.8c. Raman peaks on the debris showed an additional phase of CoWO₄ along with TiO₂, TiC and WO₃ (Fig. 8.8f) similar to Ti6Al4V coatings at 575°C. However, the volume fraction of wear debris found were low compared to previous temperatures indicating less transfer of material from the coating.

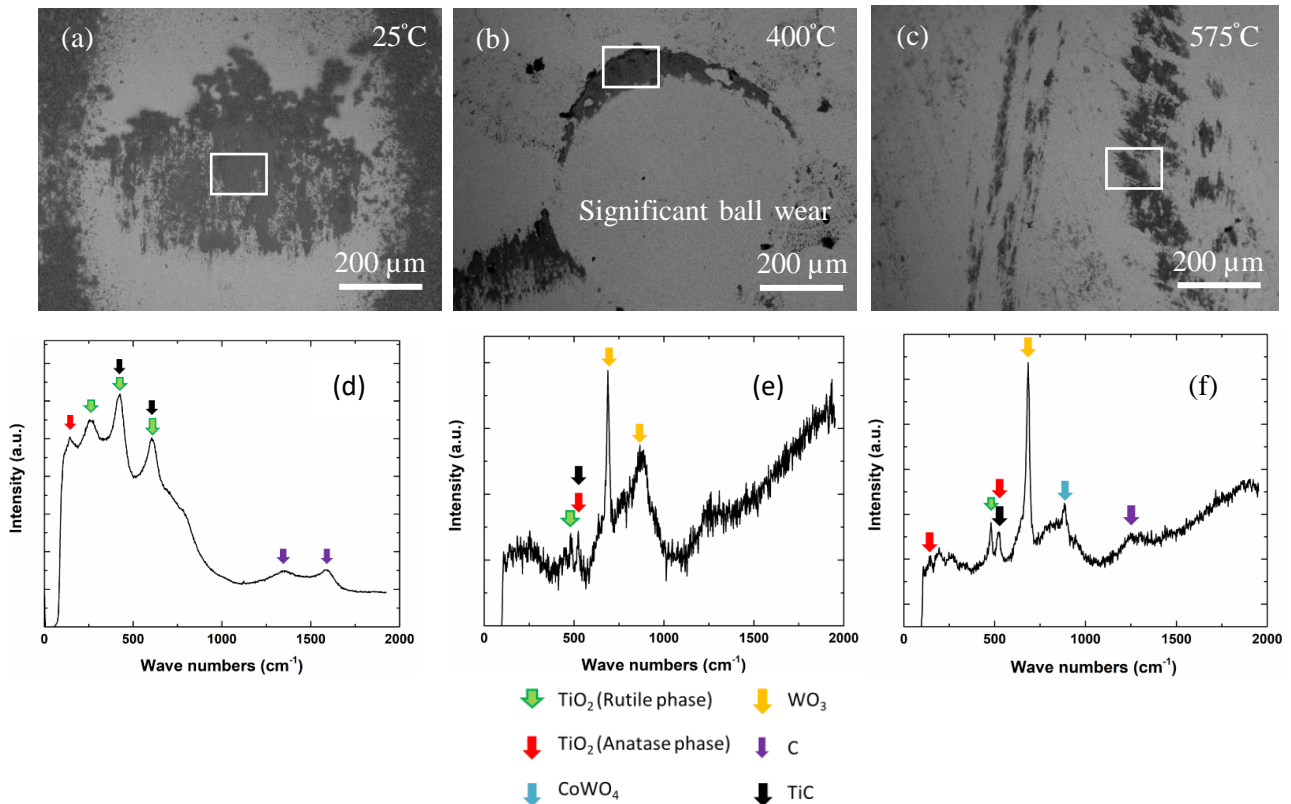


Fig. 8.8: SEM images of the counterfaces used on composite coatings at (a) 25°C (b) 400°C (c) 575°C; (d), (e) and (f) Raman spectra at corresponding places shown with a box

8.3.2.5 Subsurface analysis

Figures 8.9 and 8.10 show the ECCI of the cross-sectional wear track subsurface of the Ti6Al4V and composite coatings tested at different temperatures. For the Ti6Al4V coatings at 25°C, there were no observable tribolayers, while underneath the wear track, debonding of splats (see Fig. 8.9a) was seen up to ~ 600 µm into the coating due to the transfer of stress to the subsurface during wear. The initial static maximum Hertzian contact stress in the case of Ti6Al4V was ~ 0.8 GPa and the maximum stress point was ~ 19 µm below the contact surface. At 200°C, discontinuous tribolayers were observed due to compaction of wear debris. Below the tribolayers, ultrafine-grained region up to a depth of ~ 2.5 µm and recrystallized regions were seen (Fig. 8.9b and 8.9c). As the temperature was increased to 400°C and 575°C, a more continuous tribolayer was found on wear track (Fig. 8.9d and 8.9g). Tribolayer was of ~ 10 ± 1.8 µm at 400°C and ~ 3.5 ± 0.5 µm at 575°C with cracks inside them (see Fig. 8.9d and 8.9g). At 400°C, underneath the tribolayer ultrafine-grained region of ~ 1.5 µm thickness was observed followed by a recrystallized region (Fig. 8.9f). In contrast, at 575°C below the tribolayer ultrafine grains were not seen, however, microcrystalline grains of grain size ~ 0.8 µm (see Fig. 8.9h), similar to the grain size in the thermally cycled region (i.e. region away from the wear track) were observed. Additionally, debonding of the splats were observed at all test temperatures below the wear track and tribolayers, however the extent of debonding decreased as the temperature increased (Fig. 8.9).

In the case of the composite coatings, tribolayers were observed at all test temperatures due to the presence of stabilizing TiC particles. At 25°C, tribolayer of ~ 8.2 ± 2.7 µm was found on the wear track with no evidence of splat debonding beneath the tribolayers. Composite coatings at 200°C showed discontinuous tribolayers of thickness ~ 7.5 ± 2.7 µm as seen in Fig. 10c, that coincides with the SEM image of the wear track morphology. This was followed by ultrafine grains up to a depth of ~ 2 µm and subsequently by recrystallized region (Fig. 8.10d). At 400°C, a tribolayer of thickness ~ 2.5 ± 0.4 µm (Fig. 8.10e) was observed and below it similar to Ti6Al4V coatings, ultrafine-grained region was found up to a thickness of ~ 2 µm with few fragments of carbide particles, followed by recrystallized grains that extended into the coating (see Fig. 8.10f). At a test temperature of 575°C, a thin tribolayer (Fig. 8.10g) was observed with recrystallized grains of size ~ 1.5 µm underneath as seen in Fig. 8.10h.

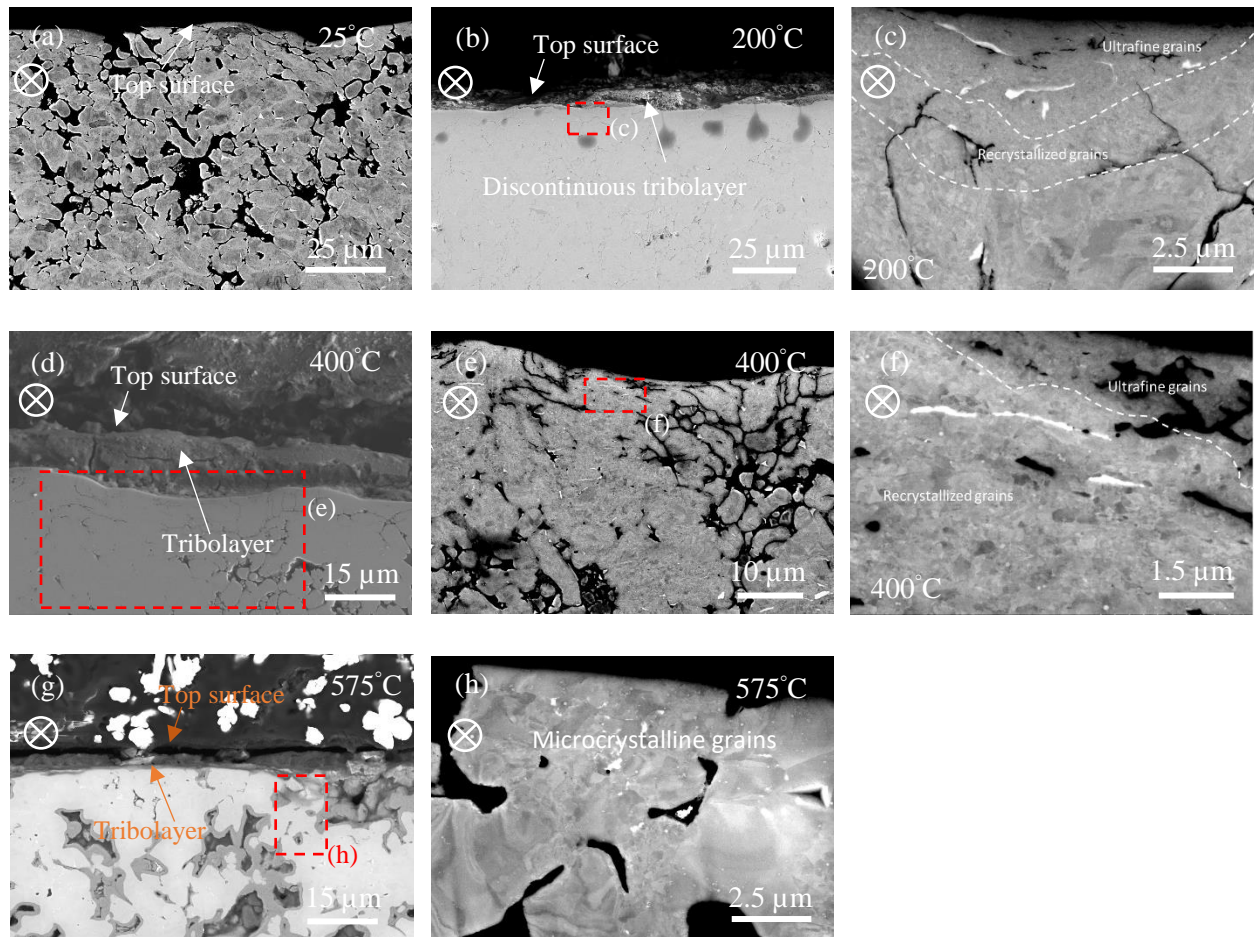


Fig. 8.9: SEM images of tribolayers of Ti6Al4V coatings at (a) 25°C (b) 200°C (d) 400°C (g) 575°C and (c), (e), (f) and (h) ECCI of the subsurface respectively. The red box in the SEM images shows the sub-surface region where the ECCI was done. ⊗ – indicates sliding direction.

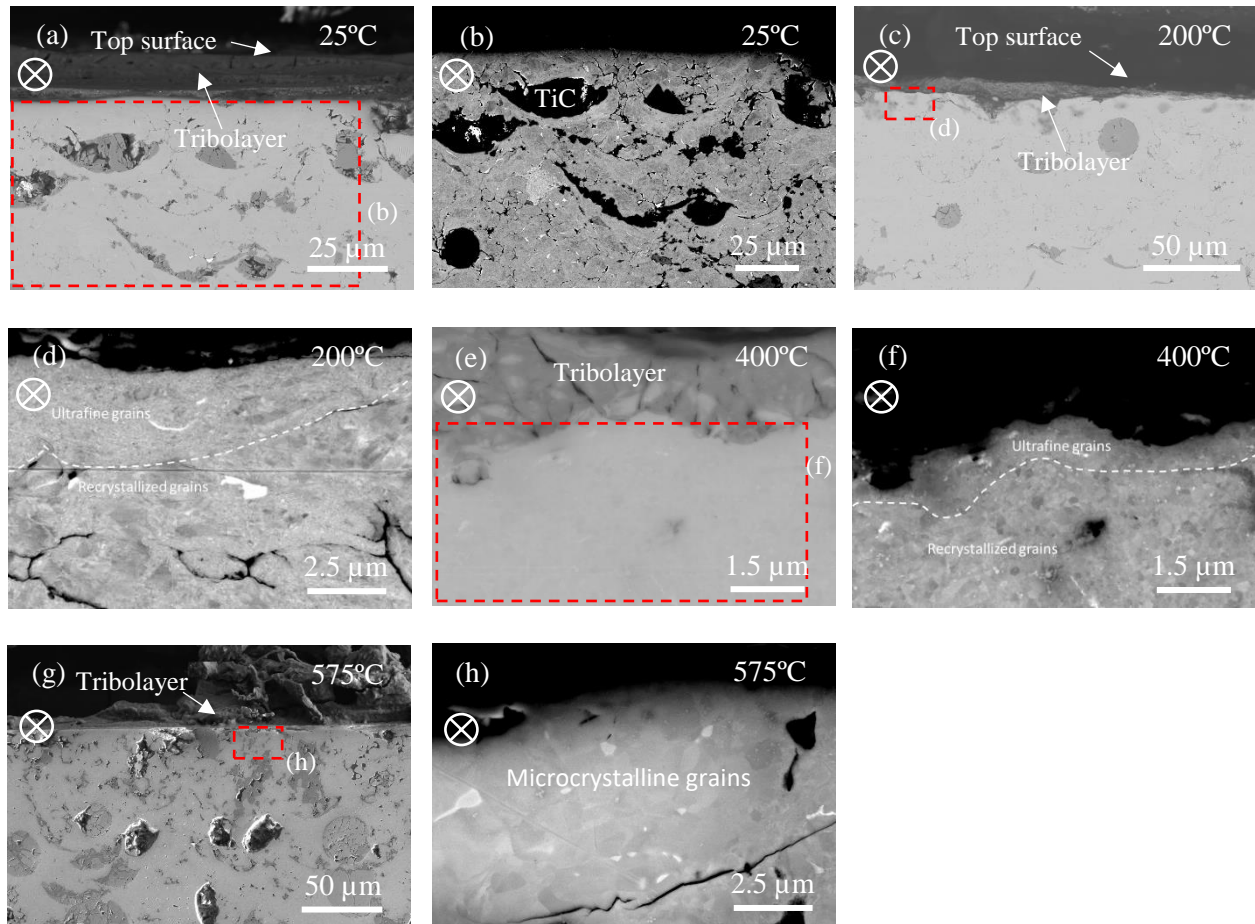


Fig. 8.10: SEM images of tribolayers of composite coatings at (a) 25°C (c) 200°C (e) 400°C (g) 575°C and (b), (d) and (f) ECCI of the subsurface respectively. The red box in the SEM images shows the sub-surface region where the ECCI was done. ⊗ – indicates sliding direction.

Hardness of the tribolayers and the unworn coating at different test temperatures is shown in Fig. 8.11. Tribolayers were formed on the wear tracks of Ti6Al4V-TiC composite coatings at all test temperatures and in Ti6Al4V coatings at elevated temperatures (> 200°C). Below 200°C, no stable and continuous tribolayers were formed on the wear tracks on the Ti6Al4V coatings, hence the hardness of the subsurface underneath the wear track (i.e. ultra fine grain region) was plotted in Fig. 8.11. The hardness of the tribolayers for both coatings was higher than the unworn surfaces at all test temperatures. At the lower two test temperatures (25 and 200°C), the tribolayer hardness was similar, with the tribolayers on the composite coating being harder than for Ti6Al4V coatings. This was also true for 400°C and at all three of the lower test temperatures there was sufficient coating wear that fragmented TiC particles were likely incorporated into the tribofilms, leading to

higher hardness. Also of note, at 400 °C and 575 °C the hardness of tribofilms for both coatings (see Fig. 8.11) become harder than at lower temperatures. In both cases, this is due to oxidation and glaze layer formation. At 575 °C, the tribolayers of both Ti6Al4V and composite coatings showed similar hardness, which was the highest measured, and was connected to oxide glaze layer formation with minimal wear of the coatings.

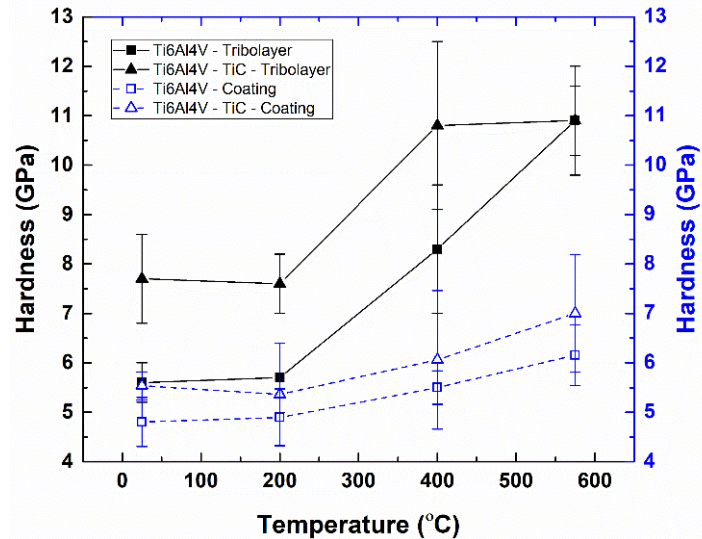


Fig. 8.11: Hardness of the tribolayer and coating at different static test temperatures.

8.4 Discussion

MMCs, used as bulk materials or coatings, are designed to resist mechanical stresses better than the pure metal or alloy used as the matrix. From a tribological standpoint, the hard particles provide load support to resist the hydrostatic and shearing stresses at the interface of a sliding contact. However, recent research has also shown that the hard particles modify local stress states or accelerate the formation of wear-resistant tribofilms [36,45,74,250]. These tribofilms are often formed by oxidative wear of the matrix material but can also incorporate some of the hard particles. The chemical and mechanical mixing that forms these tribofilms may be modified by changes in ambient temperature. In this study of Ti6Al4V and Ti6Al4V-TiC coatings, the hard particles were effective in the manner described above and changes in the tribofilm composition with temperature were linked to changes in the wear mechanisms and wear rates. As will be discussed below, the wear mechanisms and the properties of third bodies were changed by temperature, with the TiC in the composite coating making the processes distinctly different from the pure Ti6Al4V coating.

A schematic of the wear mechanisms occurring in Ti6Al4V and Ti6Al4V-TiC composite coatings at lower ($< 200^{\circ}\text{C}$) and higher ($> 200^{\circ}\text{C}$) test temperatures is shown in Fig. 8.12. Up to 200°C , Ti6Al4V coatings showed high wear rates compared to composite coatings due to abrasive wear caused by the trapped wear debris at the interface (see Fig. 8.3a and 8.3c). The wear debris were composed of oxides of Ti that acted like abrasive particles during sliding wear, resulting in material ploughing until getting displaced to either side of the wear track (Fig. 8.12a and Fig. 8.3a). Additionally, the formation of an adhesive transfer film of Ti6Al4V on the counterface was observed at both the test temperatures (Fig. 8.7a), due to the low d-bond character of Ti and its alloys [36,251]. Along with the transfer film, wear debris were found around the transfer film (on the counterface). At 25°C , no tribolayers were formed, whereas at 200°C , minor evidence of tribolayer formation due to compaction of wear debris was observed on the wear track. However, the tribolayers were non-protective and their poor resistance to the localized deformation induced by the counterface during sliding led to the transfer of stress to the subsurface [36]. This resulted in de-bonding of particle-particle interfaces underneath the wear track (see Fig. 8.9a). Similar evidence of loose, non-adherent and non-protective tribolayer formation, which led to high wear of Ti and its alloys up to 200°C was reported by Straffelini *et al.*, Cui *et al.*, Molinari *et al.*, Chen *et al.* and Mao *et al.* [26,27,174,227,246] Furthermore, the high affinity of Ti and its alloys towards oxygen results in the early formation of oxides. However, its high “Pilling-Bedworth ratio” results in internal stresses in the oxide layers (that are further enhanced during the wear process) and the mismatch for the coefficient of thermal expansion between the oxide layer and subsurface material result in their breakage [174,227,228]. These fragmented oxide debris further act as abrasive particles and accelerate the wear process resulting in high wear rates.

Reinforcement of TiC ceramic particles into Ti6Al4V matrix improved the wear resistance. This was due to the formation of tribolayers on the wear track (Fig. 8.12b) and could also be due to the improvement in the hardness of the coating making it resistant to plastic deformation. Previously, Alidokht *et al.* reported the formation of tribolayers around TiC particles in Ti-TiC MMC coatings and illustrated that their reinforcement in the metallic matrix offered resistance to plastic deformation during sliding [36]. Candel *et al.* also found that the presence of TiC particles in Ti6Al4V matrix resulted in the formation of tribolayers that decreased the friction and wear of the MMC coatings [40]. Similar tribolayers composed of fragmented oxide debris of Ti and TiC particles were found on the wear track of composite coatings at both 25°C and 200°C (see Fig.

8.4a). Formation of tribolayers on the wear track offered resistance to localized plastic shearing and thus improved the wear resistance of the coatings. Studies performed by Venkataraman *et al.* illustrated that the presence of hard tribolayer resulted in mild wear with lower wear rates in Al based composites compared to the pure Al where there was no evidence of tribolayer [163]. Similar improvements in wear resistance due to the formation of tribolayers were reported by Torgerson *et al.*, Shockley *et al.*, Alidokht *et al.*, Zhang *et al.* and Cui *et al.* [37,134,227,242,244]. Thus, reinforcing TiC ceramic particles in the Ti6Al4V matrix facilitated the formation of the protective tribolayers and their presence in the form of fragments in the tribolayers (Fig. 8.12b) offered resistance to localized plastic deformation during sliding wear, leading to improved wear resistance [36,40].

Beyond 200°C, oxide glaze layers formed on the wear tracks of both coatings were composed of TiO₂, WO₃ and CoWO₄ (only at 575°C) and significantly improved the wear resistance compared to lower temperatures. At elevated temperatures (> 200°C), a similar mechanism for the formation of tribolayers in Ti and its alloys were reported by Cui *et al.*, Wang *et al.* and Chen *et al.* [48,227,246]. Furthermore, composite coating showed almost no wear in addition to material gain on the wear track by material transfer from the counterface, which resulted in negative wear rates. Additionally, the glaze layers of composite coatings showed relatively uniform coverage compared to Ti6Al4V coatings. The formation of WO₃ and CoWO₄ (only at 575°C) phases in the glaze layers was due to the oxidation and wear of the WC-Co counterface, resulting in the transfer of material onto the wear track (see Fig. 8.7 and 8.8). Prior studies have shown that WC-Co composites exhibit high wear resistance up to 200°C, while beyond this temperature, oxidation results in significant wear along with the formation of oxides of W and Co [248,249,252]. This was consistent with the observations made in this study, where ball wear occurred only beyond 200°C and hence no oxides of W and Co were detected on the wear tracks at 25°C and 200°C (Fig. 8.5 and 8.6).

The tribolayer hardness of composite coatings was found to be higher compared to Ti6Al4V due to the presence of fragmented TiC particles; however, at 575°C, tribo-oxidation lead to limited pulling out and subsequent fragmentation resulting in similar hardness. Ultrafine recrystallized grains were found beneath the glaze layers in both coatings up to 400°C. The formation of ultrafine region was due to dynamic recrystallization that occurs due to stress transfer during the wear process. In contrast, at 575°C, micron sized grains were observed underneath the glaze layers that

were similar to the thermally cycled region (i.e. region away from the wear track) indicating recrystallization had occurred prior to the start of wear tests at this temperature. However, the average grain size beneath the glaze layer was higher in the composite coatings compared to Ti6Al4V indicating these coatings were more resistant to subsurface deformation.

The average CoF in Ti6Al4V and Ti6Al4V-TiC coatings decreased with an increase in temperature. Below 200°C, the average CoF of Ti6Al4V and composite coatings did not vary significantly with temperature. However, as the test temperature was increased to 400°C and 575°C, the formation of new phases changed the tribo-chemistry resulting in a decrease in CoF. Erdemir *et al.* proposed that higher ionic potential of the oxides result in greater screening of the cations by the anions and prevent their additional reactivity with the other available atoms which reduces the adhesion and thereby the CoF [178,179]. At 400°C, WO₃ was detected on the wear track of both coatings, which has a high ionic potential of ~ 8.3 and exhibits CoF within a range of 0.25 – 0.33 [179]. However, the decrease in CoF was more significant in the case of composite coatings due to a higher amount of W transferred from the counterface with more uniform coverage over the entire wear track (Fig. 8.4d). Additionally, abrasive grooves were observed on the wear track of Ti6Al4V coatings even at 400°C which could have led to a higher CoF despite the presence of WO₃ (see Fig. 8.3c). Similar trends of a decrease in CoF due to the presence of WO₃ on the wear track was reported by Geng *et al.* and Mi *et al.* [248,249,252]. With a further increase in test temperature to 575°C, CoWO₄ was additionally found on the wear track along with TiO₂ and WO₃. Previously, Erdemir *et al.* illustrated that the large differences in the ionic potentials of the chemical species result in lower CoF [179]. Their observations revealed that CoWO₄ (that exists as CoO-WO₃) had an ionic potential difference of 6.9 and exhibited CoF in the range of 0.2 – 0.47 at temperatures between 573 K – 1072 K. This coincides with the low CoF values observed in our study where the formation of CoWO₄ significantly decreased the CoF in both coatings at 575°C.

Thus, reinforcement of TiC ceramic particles favoured the formation of wear resistant tribolayers at lower temperatures unlike the pure Ti6Al4V coating, whereas, tribo-oxidation led to the formation of oxide glaze layers comprising of WO₃ and CoWO₄ at elevated temperatures that reduced the CoF and wear for both coatings.

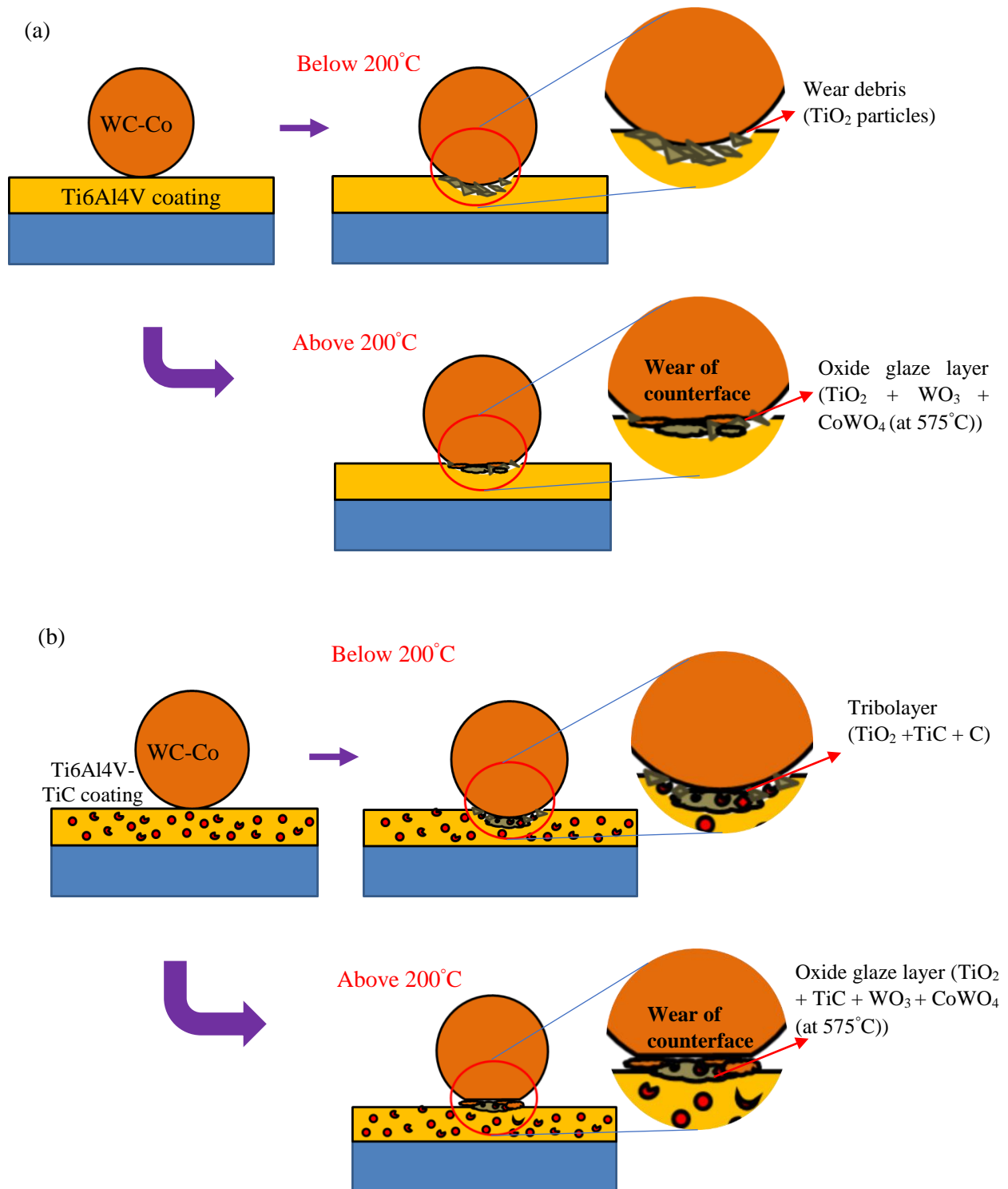


Fig. 8.12: Schematic showing the third bodies chemical compositions and wear mechanisms in (a) Ti6Al4V and (b) Ti6Al4V-TiC MMC coatings at different static test temperatures.

8.5 Conclusions

Ti6Al4V and Ti6Al4V-TiC MMC coatings were deposited using CS process and their high temperature sliding friction, wear behavior, tribochemical phase formation and wear mechanisms were studied in detail. Based on the results following conclusions were drawn:

1. At lower test temperatures, abrasive grooves along the sliding direction were observed in Ti6Al4V coatings whereas tribolayers were found on the wear track of composite coatings. This indicated that the reinforced TiC ceramic particles favoured the formation of tribolayers that resist localized deformation and result in low wear of composite coatings compared to Ti6Al4V.
2. The wear rate of Ti6Al4V and Ti6Al4V-TiC composite coatings was lower at elevated temperatures. This was due to a transition in wear mechanisms to tribo-oxidation that led to oxide glaze layers composed of TiO₂, WO₃ and CoWO₄ phases on the wear track. Glaze layers were partially formed by wear and oxidation of the WC-Co counterface followed by adhesive transfer to the wear track. Even with this material transfer, the Ti6Al4V coatings showed a measurable positive wear rate. The composite coating, with reinforced TiC, showed a negative wear rate, indicating minimal true wear of the coating and mostly glaze layer formation.
3. Interparticle de-bonding was seen underneath the tribolayers of Ti6Al4V coatings due to the transfer of stress to the subsurface, while the formation of tribolayers comprising of oxides of Ti and TiC particles increased their load bearing capacity and prevented de-bonding in composite coatings.
4. Average CoF decreased with increasing temperature in both coatings. Below 200°C, the CoF of Ti6Al4V and Ti6Al4V-TiC composite coatings did not vary significantly with temperature. However, at elevated temperatures, formation of glaze layers composed of oxides of W and Co reduced the adhesion and decreased the CoF.

Acknowledgements

The authors are thankful for the technical assistance from Phuong Vo, Maniya Aghasibeig and Jean-Francois Alarie at McGill Aerospace Materials and Alloy Design Centre (MAMADC). The authors gratefully acknowledge the contributions of Rene Cooper from Cristal Metals for providing the irregular Ti6Al4V powders.

Chapter 9

Global discussion

The present thesis is a manuscript based and the chapters from 4 – 8 are presented as separate studies. There are few comparisons that can be made but are not highlighted in the manuscripts. A global discussion on the influence of coating properties and TiC reinforcement on the tribological behaviour of Ti6Al4V coatings deposited using both spherical and irregular powders are discussed below:

9.1 Influence of TiC reinforcement of the sliding wear of Ti6Al4V coatings

The CoF and wear rate of Ti6Al4V and Ti6Al4V-TiC MMCs deposited using spherical Ti6Al4V powders is shown in Fig. 9.1. At 0.5 N normal load, the CoF of the Ti6Al4V-15% TiC MMCs was found to be highly fluctuating and similar to Ti6Al4V as shown in Fig. 9a. Despite higher microhardness (see Tables 6.1 and 7.1), the wear rate of the composite coatings was higher compared to Ti6Al4V. Similarly, at 2.5 N, the CoF of the MMC was not significantly different compared to unreinforced alloy and the wear rate was also higher. This indicated that embedding TiC particles into Ti6Al4V matrix in case of spherical powder coatings did not improve its tribological properties. Comparing the SEM images of the wear tracks (shown in Figs. 6.4 and 7.4) of Ti6Al4V and Ti6Al4V-TiC MMCs, both surfaces showed abrasive grooves in the sliding direction due to ploughing by wear debris and scoring by the counterface. Furthermore, evidence of splat delamination was observed in case of MMCs (shown in Fig. 7.4b) which could be due to their poor intersplat bonding as observed in spherical powder deposits (see Fig. 4.11). In case of Ti6Al4V coatings, the presence of optimum porosity (> 10 vol.%) and pore size entrapped the wear debris (Fig. 6.4b and d), decreased the abrasive wear and hence wear rate. Contrarily, low volume fraction (~ 5 vol.%) of porosity in the composite coating would have inhibited the complete entrapment of wear debris that led to abrasive ploughing. Raman spectra showed that the wear debris were TiO₂ particles in Ti6Al4V whereas in case of composite coating they were both TiO₂ and fragmented TiC particles (as shown in Fig. 7.7b). This indicated that as the test progressed the continuous dislodging of the TiC particles from the matrix caused abrasion along with TiO₂ particles rather than forming protective tribolayers leading to higher wear rates compared to Ti6Al4V. Increase in normal load led to the decrease in wear rate in both Ti6Al4V and Ti6Al4V-

TiC MMCs as shown in Fig. 9.1b. However, the decrease was greater in Ti6Al4V coating and it exhibited lower wear rates compared to composite. This was due to the dual effect of tribo-oxidation and wear debris entrapment in Ti6Al4V whereas the sole effect of tribo-oxidation marginally decreased the wear rate in composite coating. These results indicate that despite the presence of TiC particles and high hardness of MMCs, its tribological properties were low compared to unreinforced coatings, mainly due to the poor bonding between the metallic matrix particles.

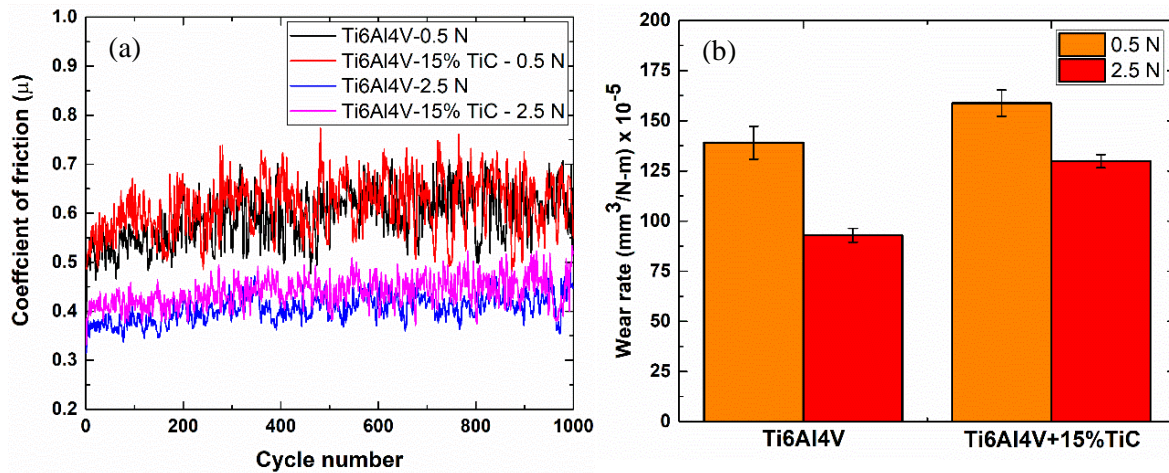


Fig. 9.1: (a) CoF and (b) wear rate of Ti6Al4V and Ti6Al4V-15% TiC coatings deposited using spherical Ti6Al4V powders.

Comparing the tribological behaviour of irregular powder deposited Ti6Al4V and Ti6Al4V-TiC MMCs at 0.5 N normal load, the steady state CoF (after friction drop) and wear rate of composite coatings was less compared to unreinforced coating as shown in Fig. 9.2a-c. During the initial sliding cycles, CoF between Ti6Al4V and composite coatings was found to be similar indicating similar wear mechanisms, however, as sliding progressed a significant drop was observed followed by a less fluctuating steady stage regime. Increase in ceramic reinforcement further decreased the wear rate and also led to an early drop in CoF indicating that the volume fraction of the reinforcement played a role in determining the tribology of the coatings. Comparing the worn surface morphologies of Ti6Al4V and Ti6Al4V-TiC MMCs, abrasive ploughing by the wear debris and scoring by counterface was observed in Ti6Al4V (Fig. 9a-c) whereas islands of tribolayers were observed on the MMCs wear tracks (shown in Fig. 7.5a-c). Abrasive wear in Ti and its alloys occurs due to the non-protective nature of the tribolayers and their low resistance to

plastic shearing [26,27,174,227,246]. Contrarily in case of composite coatings, formation of hard tribolayers comprising of agglomerated debris of TiO_2 and fragmented TiC particles, resisted the localized plastic deformation and prevented abrasive ploughing by wear debris. The tribolayers were mostly formed around TiC particles (see Fig. 7.5b) indicating that their reinforcement improved the load bearing capacity of Ti6Al4V and its resistance to plastic shearing caused by the wear debris and counterface. The degree of improvement in tribological properties imparted by the tribolayers depends on its physical and chemical compositions [35,36,45]. Apart from their high hardness the tribolayers had lubricating properties due to the presence of free carbon in the TiC particles that acted as a soft skin on a hard substrate and provided easy shear to the counterface and led to the friction drop. As the normal load increased to 2.5 N, no significant coverage of the wear track area with tribolayers was observed in case of 16vol.% TiC composite coating and the CoF was similar to Ti6Al4V coatings as shown in Fig. 9b. This indicated that similar wear mechanisms took place in both coatings and that the volume of reinforcement was not enough to support the formation of protective tribolayers. However, the higher hardness of MMCs resisted deformation and led to their lower wear rates compared to Ti6Al4V (refer Table 6.1 and 7.1). Increase in reinforcement to 23vol.% led to the formation of a highly continuous tribolayer (shown in Fig. 7.6c) compared to other coatings, which resulted in a drop in CoF to a much lower value as seen in Fig 9b. The subsequent sliding of the counterface on the tribolayer prevented wear of the underlying matrix (confirmed by the negligible amount of transferfilm on the counterface) and resulted in extremely low fluctuations in CoF after the drop (see Fig. 9.2b) along with low wear rates (see Fig. 9.2c). Furthermore, both at 0.5 N and 2.5 N, the near surface hardness of the wear tracks with tribolayers was higher compared to the worn surfaces without tribolayers due to the presence of TiO_2 and fragmented TiC particles. The hybrid characteristics of high hardness and lubricating nature of the tribolayers [165,180,241] led to lower stress transfer to the subsurface during sliding. This prevented splat de-bonding and excessive grain refinement underneath the wear tracks of composite coatings compared to unreinforced alloy.

Thus, the reinforcement of TiC ceramic particles was found to be effective in case of MMC coatings deposited using IP due to their better cohesive strength that initially supported the formation of protective tribolayers. From a tribological point of view, the ability of these powders to retain more ceramic particles in the final coatings and form lubricating tribolayers can be highly

rewarding for engineering applications where both low friction and high wear resistance are prime requirements.

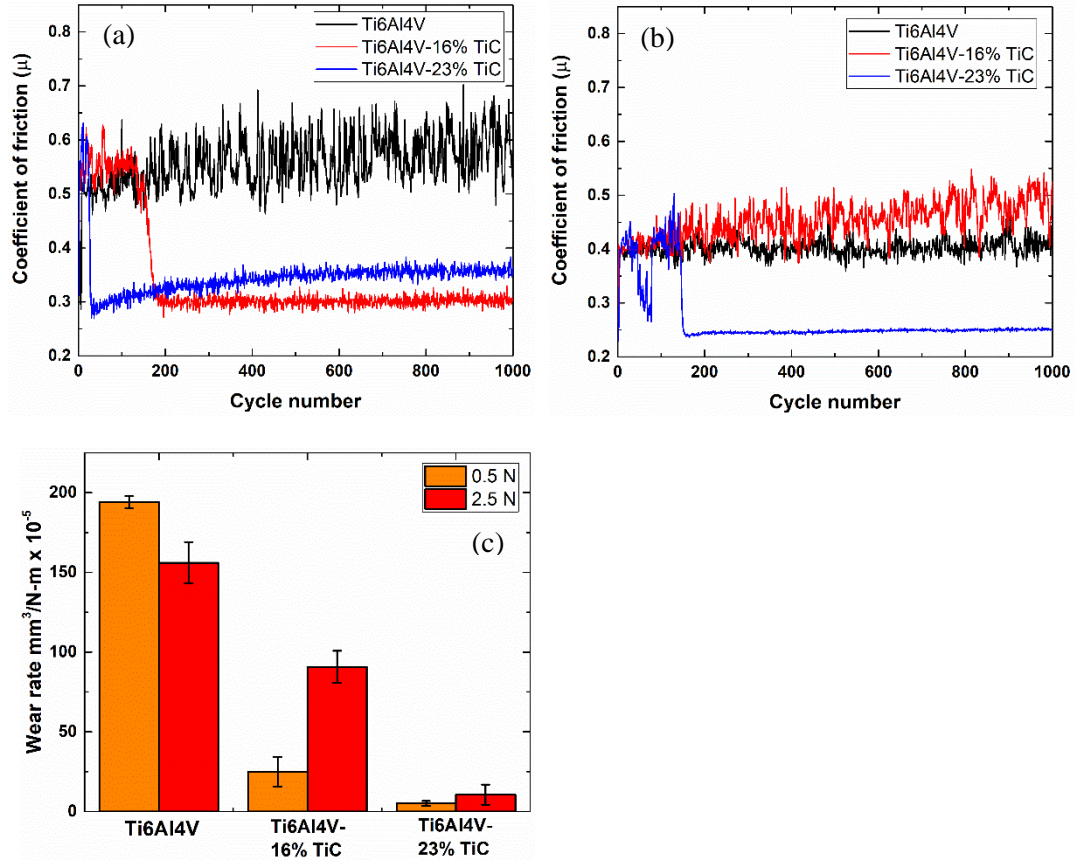


Fig. 9.2: (a) CoF at 0.5 N normal load (b) CoF at 2.5 N normal load and (c) wear rate of Ti6Al4V and Ti6Al4V-TiC coatings deposited using irregular Ti6Al4V powders.

Chapter 10

Concluding remarks

10.1 Global summary

Feedstock powder properties have a significant influence on the physical, mechanical and tribological properties of the cold sprayed deposits. The use of Armstrong process manufactured Ti6Al4V powders with internal porosity, irregular morphology and equi-axed microstructure led to highly dense coatings with better cohesive strength compared to plasma gas atomized (PGA) SP. Furthermore, splat adhesion tests also showed higher adhesion strength for the irregular powder deposited splats compared to spherical powder splats at similar spray conditions. The irregular morphology accelerates the particles to higher velocities due to greater drag force whereas the equi-axed microstructure assists in the particle deformation. ECCI of the irregular powder splat cross-sections revealed complete microstructural transformation (no evidence of particle initial microstructure) along with the formation of ultra fine grains (UFG) at the particle-substrate interface indicating their high degree of deformability whereas in spherical powder splats, bulk of the region had retained the martensitic lath microstructure (similar to initial powder). This poor deformability of the single particles resulted in porosity in the full coatings. Apart from porosity, this also led to high amount of particle debonding both at low and high indentation loads indicating poor cohesive strength whereas the high deformability of the irregular powder particles led to coatings with better cohesive strength. In addition, irregular powder splat cross-sections showed the formation of localized adiabatic shear instabilities and multiple bonded locations at the splat-substrate interface due to their irregular surface whereas lower particles velocities of SP led to a large fraction of unbonded locations at the splat-substrate interface resulting in weak adhesion.

Sliding wear of cold sprayed Ti6Al4V coatings showed that, presence of porosity significantly influences the tribological properties. Despite high hardness, irregular powder coatings exhibited higher wear rates compared to spherical powder coating at all test loads (i.e. 0.5 N to 5 N). The highly dense irregular powder deposited coatings favoured the continuous material removal through abrasive ploughing by the wear debris during sliding. Contrarily, presence of pores in spherical powder coatings acted as locations for wear debris entrapment and prevented continuous

abrasive ploughing, resulting in lower wear rate. As the normal load increased from 0.5 N to 5 N, tribo-oxidation led to the formation of tribolayers on the irregular powder coating wear tracks. This led to a marginal decrement in wear rates. However, in case of spherical powder coatings, along with tribo-oxidation, increase in load led to higher entrapment of wear debris at a greater number of locations on the wear track. The effect of these two factors led to a much greater decrease in wear rates compared to irregular powder coatings. TEM images of the pore filled region showed the presence of micron sized particles of WC transferred from the counterface along with oxides of Ti, where as at the wear track subsurface away from the pores showed ultra fine nanocrystalline grains of α -Ti followed by elongated micro-sized grains. This indicated that along with TiO_2 particles the wear debris also had few WC fragments that contributed to the abrasive ploughing and entrapment of these debris, prevented excessive abrasive ploughing. CoF in both coatings showed similar trends of decrease with increase in normal load. At 0.5 N normal load the CoF was found to be largely fluctuating due to the third bodies formation and their flow inside the tribological circuit. However, as the normal load increased to 2.5 N and 5 N, tribo-oxidation led to greater coverage of wear track with tribolayers resulting in a decrease in CoF. Dynamic recrystallization due to stress transfer during wear process led to the formation of UFGs, FGs and highly deformed microstructures underneath the wear tracks. However, the average grain size in the UFG region was found to be coarser below the tribolayer compared to the grains below the worn regions not covered with tribolayer. This indicates that the presence of tribolayers increased the near surface hardness of the wear tracks and transferred less stress to the subsurface resulting in lower grain refinement.

The friction and wear behaviour of Ti6Al4V-TiC MMCs showed dependence on both coating properties as well as TiC content. At 0.5 N normal load, formation of islands of tribolayers were observed on the wear tracks of irregular powder deposited composite coatings (both 16vol.% and 23vol.% TiC) which led to a low CoF (steady state) and wear rates compared to Ti6Al4V coatings deposited using same powders. Contrarily in spherical powder deposited composite, delamination of splats due to the poor cohesion between the particles and continuous abrasive ploughing by the wear debris similar to unreinforced Ti6Al4V coatings was observed. This also led to high friction and wear rates compared to irregular powder composites with similar TiC content. SEM images of the wear tracks of irregular powder composites showed tribolayer formation around TiC particles indicating that their reinforcement prevented the localized deformation of the matrix. At

2.5 N normal load, formation of a more continuous tribolayer compared to lower loads was observed in composite coatings with 23vol.% TiC due to greater exposure of TiC particles to the sliding interface. This resulted in low wear rates and CoF compared to other composite coatings. Furthermore, at this load both composite coatings deposited using SP with ~ 15vol.% and IP with ~ 16vol.% TiC content did not show significant formation of protective tribolayers resulting in abrasive wear and high wear rates. However, within the two coatings, irregular powder composite showed lower wear rate due to its higher hardness and also better cohesion between the splats. It was noted that despite similar volume fraction of reinforcement tribolayer formation was observed only of the wear track of irregular powder composites. This indicates that the better cohesion between the metal particles prevented delamination during initial sliding cycles and provided mechanical support to the formation of tribolayers. EDS mapping and Raman analysis showed that the tribolayers comprised of TiO₂ along with fragments of TiC and the additional presence of free carbon in TiC particles. These tribolayers resisted localized plastic flow and the presence of free carbon contributed to the easy shear of the counterface thereby providing a hybrid effect of both lower friction and wear. TEM analysis of the worn subsurface showed the presence of coarser grains under the tribolayers whereas under the worn surface (not covered with tribolayer), only UFGs were observed. This indicated that the formation of tribolayers on the wear track comprising of fragmented TiC particles, and the presence of free carbon led to lower transfer of stress to the subsurface resulting in lower grain refinement.

To understand the synergetic effect of TiC reinforcement and temperature on the tribology of Ti6Al4V coatings, sliding wear tests were performed at different static tests temperatures up to 575°C. At all test temperature composite coatings exhibited lower wear rates compared to Ti6Al4V coatings. Specifically, beyond 200°C composite coatings showed negative wear rates due to additional material gain from the counterface. The low wear of composite coatings was mainly due to the formation of tribolayers of different chemical compositions at different test temperatures. At lower test temperatures (< 200°C), the tribolayers composed of TiO₂ and fragmented TiC particles that resisted the localized shear deformation and improved the wear resistance whereas in case of Ti6Al4V coatings abrasive ploughing by the wear debris led to high wear rates. At elevated temperatures (> 200°C) tribo-oxidation led to formation of oxide glaze layers comprising of oxides of W and Co along with Ti on the wear track of both Ti6Al4V and Ti6Al4V-TiC MMCs. This resulted in low wear rates in both coatings compared to lower test

temperatures. However, the presence of TiC particles led to minimal wear of the composite coatings and greater volume of material transfer from the counterface resulting in negative wear rates. ECCI of the worn cross-sections showed the formation of UFG below the worn surfaces in both coatings up to 400°C due to stress transfer to the subsurface. However, at 575°C, tribo-oxidation and formation of oxide glaze layers led to the lower stress transfer to the subsurface and showed no evidence of grain refinement in both the coatings. Apart from significantly improving the wear resistance of the coatings, the presence of WO₃ and CoWO₄ phases in the oxide glaze layers lowered the adhesion between the sliding surfaces and decreased the CoF in both coatings at elevated temperatures.

10.2 Global conclusions

Ti6Al4V and Ti6Al4V-TiC metal matrix composites (MMCs) were fabricated using CS process. It was observed that feedstock powder properties had significant influence on the coating microstructure, mechanical and tribological properties. Ti6Al4V coatings deposited using Armstrong process manufactured IP with equi-axed microstructure were dense compared to coatings deposited using plasma gas atomized SP with martensitic lath microstructure. The irregular morphology of the Armstrong powders helped to accelerate the particles to higher velocities compared to SP due to greater drag force whereas the deformable microstructure assisted in particle deformation. Contrarily, the hard martensitic lath microstructure of the SP inhibited particle deformation and led to high porosity. Presence of porosity and the poor deformability of the particles significantly influenced the cohesion strength of the coatings. Inter-particle debonding and sliding of the adjacent splats (at high loads) were observed during indentation in spherical powder coatings due to their poor cohesion strength. Despite extremely dense microstructure, the irregular powder coatings also showed de-bonding at higher loads but to a much lesser extent compared to spherical powder deposits. These results indicated that, although dense coatings were deposited using IP with better cohesion strength compared to SP, there is a need for additional process optimization or heat treatment to further improve the cohesion strength between the particles.

Splat adhesion tests performed on single particles revealed that at similar spray conditions, IP bonded with higher adhesion strength compared to SP. While at similar particle velocities no significant difference in their adhesion strength was observed. This indicated that although the

equi-axed microstructure assisted in particle deformation, particle velocities had a more profound effect in determining the particle adhesion strength. In addition, the dendritic surface of IP led to multiple contact points resulting in localised ASIs and multiple bonded locations (at splat-substrate interface), which could have contributed to greater particle adhesion. ECCI of the irregular powder splat cross-sections revealed the formation of ultrafine and fine grains with no retention of feedstock microstructure, whereas the spherical powder splats had retained most of the initial martensitic lath microstructure, and the microstructural transformations were observed only at the splat-substrate interface. This indicated that the equi-axed microstructure and higher particle velocities of the IP helped for particle deformation with along with the formation of highly refined post spray microstructures.

Sliding wear tests performed on Ti6Al4V coatings showed that despite dense microstructure and high hardness, irregular powder coatings exhibited higher wear rates compared to spherical powder coatings at all test loads. The high wear of irregular powder coatings was due to the abrasive ploughing by the wear debris and counterface scoring during sliding process. Contrarily, presence of pores in spherical powder coatings led to the entrapment of wear debris, minimized the ploughing and reduced the wear rates. Increase in normal load led to tribo-oxidation and increased the area covered with tribolayers. This decreased wear rates in both the coatings. Specifically, in spherical powder coatings, along with tribo-oxidation, pore filling by wear debris increased with increase in normal load. The combined effect of both tribo-oxidation and pore filling led to much lower wear rates in spherical powder coatings compared to irregular powder coatings. Thus, it can be concluded that although porosity decreased the hardness and cohesion strength of the spherical powder coatings, with respect to tribology, presence of porosity decreased the abrasive wear, and lowered the wear rate. CoF in both coatings decreased with increase in normal load and was not significantly different at similar loads. The decrease in CoF was due to the increase in wear track area coverage with tribolayers that were composed of low shear strength Magnèli phases. This signifies that tribo-oxidation had a more profound effect in determining the CoF of Ti6Al4V coatings rather than the coating microstructure and mechanical properties.

The tribological behaviour of Ti6Al4V-TiC MMCs was significantly influenced by coating properties, ceramic volume fraction and normal load. At similar TiC volume fractions, irregular powder MMCs showed low wear rates and CoF compared to spherical powder MMCs due to the

formation of hard tribolayers with lubricating properties. Tribolayers were formed due to agglomeration of TiO_2 particles and fragmented TiC which resisted shear deformation and lowered the wear rates, where as the presence of free carbon in TiC particles decreased the friction. Contrarily, wear tracks of spherical powder MMCs showed abrasive wear mechanisms and splat delamination due to poor inter-splat bonding between the matrix particles. This indicated that the poor cohesive strength of the coatings deposited using SP did not support the formation of tribolayers, and the continuous ploughing by the TiO_2 and fragmented TiC particles led to high friction and wear rates. Increase in TiC volume fraction and normal load in irregular powder MMCs accelerated the formation of tribolayers and also contributed to the higher area coverage on the wear track. This resulted in much lower wear rates and early drop in CoF to a much lower value with less fluctuations. In addition to higher wear resistance, the formation of hard tribolayers with lubricating properties led to lower subsurface stresses and resulted in the formation of coarser grains compared to the wear tracks without tribolayers.

Sliding wear tests performed at different temperatures (25°C - 575°C) showed that Ti6Al4V-TiC MMCs had higher wear resistance compared to unreinforced Ti6Al4V coatings at all temperatures. However, a greater improvement in the wear resistance of Ti6Al4V due to TiC reinforcement was found at lower test temperatures ($< 200^\circ\text{C}$) compared to elevated temperatures ($> 200^\circ\text{C}$). At lower temperatures, the presence of TiC particles favoured the formation of hard tribolayers in MMCs and decreased the wear rates, where as in Ti6Al4V coatings, abrasive ploughing by wear debris resulted in high wear rates. At elevated temperature, tribo-oxidation led to the wear and transfer of material from counterface on to the wear tracks of both coatings resulting in the formation of oxide glaze layers comprising of TiO_2 , WO_3 and CoWO_4 tribo-chemical phases. The formation of glaze layers significantly decreased the wear rates in both Ti6Al4V and Ti6Al4V-TiC MMC coatings. Nevertheless, the reinforcement of fragmented TiC particles in the glaze layers during wear, further led to a marginal improvement in the wear resistance of MMCs compared to Ti6Al4V at elevated temperatures. In addition to improved wear resistance, the presence of tribo-chemical phases (WO_3 and CoWO_4) in the glaze layers decreased the adhesion between the sliding surfaces and lowered the friction in both coatings.

10.3 Contributions to original knowledge

1. For the first time, Ti6Al4V powders manufactured using Armstrong process were cold sprayed to deposit dense coatings (porosity < 2%) using nitrogen as propellant gas. The advantages and limitations of using Armstrong powders that are more economical and sustainable compared to plasma gas atomized (PGA) powders was demonstrated.
2. The influence of feedstock powder characteristics on the adhesion strength and post spray microstructural transformations were studied. The ability of Armstrong powders to deposit highly adherent coatings at much lower gas temperatures compared to PGA powders enables them to be used for spraying on to heat sensitive materials was highlighted.
3. Ti6Al4V-TiC MMCs were cold spray deposited for the first time using different metal powders. The specific advantages of using Armstrong powders to deposit Ti6Al4V-TiC MMC coatings with higher ceramic retention and lower porosity compared to PGA powders were explored.
4. A study comparing the friction and wear behaviour of the Ti6Al4V-TiC MMC coatings with similar TiC content, deposited using spherical and irregular Ti6Al4V powders was performed. The importance of using MMCs with better cohesion strength between the metallic matrix particles for tribological applications was discussed. In addition, the effect of TiC content on the tribology of the MMC coatings at different normal loads was evaluated.
5. For the first time the sliding wear behaviour of cold sprayed Ti6Al4V coatings and Ti6Al4V-TiC MMCs was evaluated at different temperatures. Through this study, the temperature up to which the TiC reinforcement can effectively improve the tribological performance of Ti6Al4V was explored.
6. A third body approach was extensively used to understand the sliding wear behaviour of cold sprayed Ti6Al4V and Ti6Al4V-TiC MMC coatings both at low and elevated temperatures. The physical, chemical, microstructural and mechanical properties of the third bodies were correlated to the observed changes in friction and wear mechanisms.

10.4 Suggestions for future work

1. Despite having extremely dense microstructures IP deposited Ti6Al4V coatings exhibited greater hardness loss compared to bulk Ti6Al4V. Hence, there is a need for a comprehensive study to identify methods to improve the cohesive strength between the splats. In this aspect,

performing heat treatment at different temperatures and understanding its effect on the cohesive strength of the splats would be an interesting study.

2. The ceramic particle size and morphology play an important role in determining the cold sprayability, mechanical and tribological properties of the MMCs. In this dissertation, spherical TiC particles were used as a reinforcement phase. It would be interesting to deposit MMCs using irregular TiC particles and perform sliding wear tests to understand their influence of TiC morphology on the friction and wear of the coatings.
3. MMCs when put into service in various aerospace, marine or mining applications, are often subjected to solid particle erosion (SPE) due to the impact of hard abrasive particles. It would be useful to study the influence of TiC reinforcement and its content on the SPE behaviour of MMCs. In addition, a systematic work to understand the influence of erodent velocity, size, angle of impact could help to evaluate the performance of the coatings under different conditions.
4. Ti and its alloys are known for their excellent corrosion resistance due to the formation of a highly stable passive film. The reinforcement of secondary phases like ceramic particles could improve or degrade its corrosion resistance depending on the ability of the coatings to form a passive film. Hence, evaluating the aqueous corrosion behaviour of the Ti6Al4V-TiC MMCs with special emphasis on the TiC content, would be a fertile area to explore as a part of future study.
5. In the present study, the tribological properties of Ti6Al4V coatings and Ti6Al4V-TiC MMCs were studied in dry sliding conditions. It would be interesting to explore the friction and wear behaviour of the coatings under lubricated sliding conditions.
6. Worn surfaces of composite coatings showed the formation of islands of tribolayers that had lubricating properties while abrasive ploughing marks observed on the wear track. It would be interesting to perform microtribology tests using a spherical indenter probe at these two regions separately and determine the CoF of each of these features. The data could be used to develop a mathematical model co-relating the wear track area covered by tribolayer and its contribution in decreasing the overall CoF.

References

- [1] R. Boyer, G. Welsch, E.W. Collings, *Materials Properties Handbook: Titanium Alloys*, ASM International, Materials Park, OH, USA, 1994.
- [2] G. Lütjering, J. Williams, *Titanium*, 2nd ed., Springer: Berlin, 2007.
- [3] S. Ali, N. Polytechnique, V. Songmene, T. Sup, *Machining of Titanium Alloys*, 2014.
- [4] V.K. Champagne, D. Helfritsch, *Critical Assessment 11: Structural repairs by cold spray*, *Mater. Sci. Technol.* 31 (2014) 627–634.
- [5] P. Vo, D. Goldbaum, W. Wong, E. Irissou, J.G. Legoux, R.R. Chromik, S. Yue, *Cold-spray processing of titanium and titanium alloys*, Elsevier Inc., 2015.
- [6] D. MacDonald, R. Fernández, F. Delloro, B. Jodoin, *Cold spraying of Armstrong process titanium powder for additive manufacturing*, *J. Therm. Spray Technol.* 26 (2017) 598–609.
- [7] M.R. Rokni, S.R. Nutt, C.A. Widener, V.K. Champagne, R.H. Hrabe, *Review of relationship between particle deformation, coating microstructure, and properties in high-pressure cold spray*, *J. Therm. Spray Technol.* 26 (2017) 1308–1355.
- [8] V.K. Champagne, *The cold spray materials deposition process: Fundamentals and applications*, Woodhead Publishing Limited, 2007.
- [9] A. Papyrin, V. Kosarev, S. Klinkov, A. Alkimov, V. Fomin, *Cold Spray Technology*, Elsevier, 2007.
- [10] S. Kumar, M. Ramakrishna, N.M. Chavan, S. V. Joshi, *Correlation of splat state with deposition characteristics of cold sprayed niobium coatings*, *Acta Mater.* 130 (2017) 177–195.
- [11] Y. Zhang, N. Brodusch, S. Descartes, R.R. Chromik, R. Gauvin, *Microstructure refinement of cold-sprayed copper investigated by electron channeling contrast imaging*, *Microsc. Microanal.* 20 (2014) 1499–1506.
- [12] X.T. Luo, Y.J. Li, C.J. Li, *A comparison of cold spray deposition behavior between gas atomized and dendritic porous electrolytic Ni powders under the same spray conditions*, *Mater. Lett.* 163 (2016) 58–60.
- [13] P. Vo, E. Irissou, J.G. Legoux, S. Yue, *Mechanical and microstructural characterization of cold-sprayed Ti-6Al-4V after heat treatment*, *J. Therm. Spray Technol.* 22 (2013) 954–964.
- [14] A.W.Y. Tan, W. Sun, Y.P. Phang, M. Dai, I. Marinescu, Z. Dong, E. Liu, *Effects of traverse*

- scanning speed of spray nozzle on the microstructure and mechanical properties of cold-sprayed Ti6Al4V coatings, *J. Therm. Spray Technol.* 26 (2017) 1484–1497.
- [15] H. Aydin, M. Alomair, W. Wong, P. Vo, S. Yue, Cold Sprayability of Mixed Commercial Purity Ti Plus Ti6Al4V Metal Powders, *J. Therm. Spray Technol.* 26 (2017) 360–370.
- [16] N.W. Khun, A.W.Y. Tan, K.J.W. Bi, E. Liu, Effects of working gas on wear and corrosion resistances of cold sprayed Ti-6Al-4V coatings, *Surf. Coatings Technol.* 302 (2016) 1–12.
- [17] V.S. Bhattiprolu, K.W. Johnson, O.C. Ozdemir, G.A. Crawford, Influence of feedstock powder and cold spray processing parameters on microstructure and mechanical properties of Ti-6Al-4V cold spray depositions, *Surf. Coatings Technol.* 335 (2018) 1–12.
- [18] A.M. Birt, V.K. Champagne, R.D. Sisson, D. Apelian, Microstructural analysis of cold-sprayed Ti-6Al-4V at the micro- and nano-Scale, *J. Therm. Spray Technol.* 24 (2015) 1277–1288.
- [19] A.M. Birt, V.K. Champagne, R.D. Sisson, D. Apelian, Microstructural analysis of Ti-6Al-4V powder for cold gas dynamic spray applications, *Adv. Powder Technol.* 26 (2015) 1335–1347.
- [20] X.T. Luo, Y.K. Wei, Y. Wang, C.J. Li, Microstructure and mechanical property of Ti and Ti6Al4V prepared by an in-situ shot peening assisted cold spraying, *Mater. Des.* 85 (2015) 527–533.
- [21] H. Zhou, C. Li, G. Ji, S. Fu, H. Yang, X. Luo, G. Yang, C. Li, Local microstructure inhomogeneity and gas temperature effect in in-situ shot-peening assisted cold-sprayed Ti-6Al-4V coating, *J. Alloys Compd.* 766 (2018) 694–704.
- [22] O.C. Ozdemir, C.A. Widener, D. Helfrich, F. Delfanian, Estimating the effect of helium and nitrogen mixing on deposition efficiency in cold spray, *J. Therm. Spray Technol.* 25 (2016) 660–671.
- [23] D. MacDonald, S. Rahmati, B. Jodoin, W. Birtch, An economical approach to cold spray using in-line nitrogen–helium blending, *J. Therm. Spray Technol.* 28 (2019) 161–173.
- [24] D.C. Joy, D.E. Newbury, D.L. Davidson, Electron channeling patterns in the scanning electron microscope, *J. Appl. Phys.* 53 (1982).
- [25] D. Goldbaum, R.R. Chromik, N. Brodusch, R. Gauvin, Microstructure and mechanical properties of Ti cold-spray splats determined by electron channeling contrast imaging and nanoindentation mapping, *Microsc. Microanal.* 21 (2015) 570–581.

- [26] A. Molinari, G. Straffelini, B. Tesi, T. Bacci, Dry sliding wear mechanisms of the Ti6Al4V alloy, *Wear*. 208 (1997) 105–112.
- [27] G. Straffelini, a Molinari, Dry sliding wear of Ti-6Al-4V alloy as influenced by the counterface and sliding conditions, *Wear*. 236 (1999) 328–338.
- [28] R.S. Magaziner, V.K. Jain, S. Mall, Investigation into wear of Ti-6Al-4V under reciprocating sliding conditions, *Wear*. 267 (2009) 368–373.
- [29] K.G. Budinski, Tribological properties of titanium alloys, *Wear*. 151 (1991) 203–217.
- [30] S.R. Shepard, N.P. Suh, The effects of ion implantation on friction and wear of metals, *J. Lubr. Technol.* 104 (1982) 29.
- [31] E. Roliński, Surface properties of plasma-nitrided titanium alloys, *Mater. Sci. Eng. A*. 108 (1989) 37–44.
- [32] M. Ignatiev, E. Kovalev, I. Melekhin, I.Y. Smurov, S. Sturlese, Investigation of the hardening of a titanium alloy by laser nitriding, *Wear*. 166 (1993) 233–236.
- [33] S. Yerramareddy, S. Bahadur, The effect of laser surface texturing on the tribological behavior of Ti-6Al-4V, *Wear*. 157 (1992) 245–262.
- [34] K. Farokhzadeh, A. Edrissy, Transition between mild and severe wear in titanium alloys, *Tribol. Int.* 94 (2016) 98–111.
- [35] S. A. Alidokht, S. Yue, R.R. Chromik, Effect of WC morphology on dry sliding wear behavior of cold-sprayed Ni-WC composite coatings, *Surf. Coatings Technol.* 357 (2019) 849–863.
- [36] S.A. Alidokht, V.N.V. Munagala, R.R. Chromik, Role of third bodies in friction and wear of cold-sprayed Ti and Ti–TiC composite coatings, *Tribol. Lett.* 65 (2017).
- [37] J.M. Shockley, S. Descartes, P. Vo, E. Irissou, R.R. Chromik, The influence of Al₂O₃ particle morphology on the coating formation and dry sliding wear behavior of cold sprayed Al-Al₂O₃ composites, *Surf. Coatings Technol.* 270 (2015) 324–333.
- [38] T. Yamaguchi, H. Hagino, Y. Michiyama, A. Nakahira, Sliding wear properties of Ti/TiC surface composite layer formed by laser alloying, *Mater. Trans.* 56 (2015) 361–366.
- [39] F. Wang, J. Mei, H. Jiang, X. Wu, Laser fabrication of Ti6Al4V/TiC composites using simultaneous powder and wire feed, *Mater. Sci. Eng. A*. 445–446 (2007) 461–466.
- [40] J.J. Candel, V. Amigó, J.A. Ramos, D. Busquets, Sliding wear resistance of TiCp reinforced titanium composite coating produced by laser cladding, *Surf. Coatings Technol.* 204 (2010)

- 3161–3166.
- [41] A. Datye, S. Koneti, G. Gomes, K.H. Wu, H.T. Lin, Synthesis and characterization of aluminum oxide-boron carbide coatings by air plasma spraying, *Ceram. Int.* 36 (2010) 1517–1522.
- [42] H. Wang, W. Xia, Y. Jin, A study on abrasive resistance of Ni-based coatings with a WC hard phase, *Wear.* 195 (1996) 47–52.
- [43] A. Salman, B. Gabbitas, D.L. Zhang, Titanium based composite coatings deposited by high velocity oxygen fuel (HVOF) and plasma spraying methods, *Key Eng. Mater.* 551 (2013) 127–132.
- [44] K. Van Acker, D. Vanhoyweghen, R. Persoons, J. Vangrunderbeek, Influence of tungsten carbide particle size and distribution on the wear resistance of laser clad WC/Ni coatings, *Wear.* 258 (2005) 194–202.
- [45] R.R. Chromik, S.A. Alidokht, J.M. Shockley, Y. Zhang, Tribological coatings prepared by cold spray, in: *Cold-Spray Coatings*, 2018: pp. 321–348.
- [46] D.E. Wolfe, T.J. Eden, J.K. Potter, A.P. Jaroh, Investigation and characterization of Cr₃C₂-based wear-resistant coatings applied by the cold spray process, *J. Therm. Spray Technol.* 15 (2006) 400–412.
- [47] H. Koivuluoto, P. Vuoristo, Effect of ceramic particles on properties of cold-sprayed Ni-20Cr+Al₂O₃ coatings, *J. Therm. Spray Technol.* 18 (2009) 555–562.
- [48] L. Wang, Q.Y. Zhang, X.X. Li, X.H. Cui, S.Q. Wang, Severe-to-mild wear transition of titanium alloys as a function of temperature, *Tribol. Lett.* 53 (2014) 511–520.
- [49] T. Suhonen, T. Varis, S. Dosta, M. Torrell, J.M. Guilemany, Residual stress development in cold sprayed Al, Cu and Ti coatings, *Acta Mater.* 61 (2013) 6329–6337.
- [50] V. Luzin, K. Spencer, M.X. Zhang, Residual stress and thermo-mechanical properties of cold spray metal coatings, *Acta Mater.* 59 (2011) 1259–1270.
- [51] D. Boruah, B. Ahmad, T.L. Lee, S. Kabra, A.K. Syed, P. McNutt, M. Doré, X. Zhang, Evaluation of residual stresses induced by cold spraying of Ti-6Al-4V on Ti-6Al-4V substrates, *Surf. Coat. Technol.* 374 (2019) 591–602.
- [52] X.L. Zhou, A.F. Chen, J.C. Liu, X.K. Wu, J.S. Zhang, Preparation of metallic coatings on polymer matrix composites by cold spray, *Surf. Coatings Technol.* 206 (2011) 132–136.
- [53] Y. Wang, B. Normand, N. Mary, M. Yu, H. Liao, Microstructure and corrosion behavior of

- cold sprayed SiCp/Al 5056 composite coatings, *Surf. Coatings Technol.* 251 (2014) 264–275.
- [54] A. Ganesan, M. Yamada, M. Fukumoto, Cold spray coating deposition mechanism on the thermoplastic and thermosetting polymer substrates, *J. Therm. Spray Technol.* 22 (2013) 1275–1282.
- [55] G.J. Yang, C.J. Li, F. Han, W.Y. Li, A. Ohmori, Low temperature deposition and characterization of TiO₂ photocatalytic film through cold spray, *Appl. Surf. Sci.* 254 (2008) 3979–3982.
- [56] H.Y. Lee, Y.H. Yu, Y.C. Lee, Y.P. Hong, K.H. Ko, Thin film coatings of WO₃ by cold gas dynamic spray: A technical note, *J. Therm. Spray Technol.* 14 (2005) 183–186.
- [57] R. Lupoi, W. O'Neill, Deposition of metallic coatings on polymer surfaces using cold spray, *Surf. Coatings Technol.* 205 (2010) 2167–2173.
- [58] A.S. Alhulaifi, G.A. Buck, W.J. Arbegast, Numerical and experimental investigation of cold spray gas dynamic effects for polymer coating, *J. Therm. Spray Technol.* 21 (2012) 852–862.
- [59] Y. Xu, I.M. Hutchings, Cold spray deposition of thermoplastic powder, *Surf. Coatings Technol.* 201 (2006) 3044–3050.
- [60] P.C. King, M. Jahedi, Relationship between particle size and deformation in the cold spray process, *Appl. Surf. Sci.* 256 (2010) 1735–1738.
- [61] W. Li, H. Assadi, F. Gaertner, S. Yin, A review of advanced composite and nanostructured coatings by solid-state cold spraying process, *Crit. Rev. Solid State Mater. Sci.* 8436 (2018) 1–48.
- [62] P.H. Gao, Y.G. Li, C.J. Li, G.J. Yang, C.X. Li, Influence of powder porous structure on the deposition behavior of cold-sprayed WC-12Co coatings, *J. Therm. Spray Technol.* 17 (2008) 742–749.
- [63] I. Smid, A.E. Segall, P. Walia, G. Aggarwal, T.J. Eden, J.K. Potter, Cold-sprayed Ni-hBN self-lubricating coatings, *Tribol. Trans.* 55 (2012) 599–605.
- [64] C. Borchers, F. Gärtner, T. Stoltenhoff, H. Assadi, H. Kreye, Microstructural and macroscopic properties of cold sprayed copper coatings, *J. Appl. Phys.* 93 (2003) 10064–10070.
- [65] N. Cinca, M. Barbosa, S. Dosta, J.M. Guilemany, Study of Ti deposition onto Al alloy by

- cold gas spraying, *Surf. Coatings Technol.* 205 (2010) 1096–1102.
- [66] W. Wong, P. Vo, E. Irissou, A.N. Ryabinin, J.G. Legoux, S. Yue, Effect of particle morphology and size distribution on cold-sprayed pure titanium coatings, *J. Therm. Spray Technol.* 22 (2013) 1140–1153.
- [67] H. Koivuluoto, P. Vuoristo, Effect of powder type and composition on structure and mechanical properties of Cu + Al₂O₃ coatings prepared by using low-pressure cold spray process, *J. Therm. Spray Technol.* 19 (2010) 1081–1092.
- [68] H. Koivuluoto, A. Milanti, G. Bolelli, L. Lusvarghi, P. Vuoristo, High-pressure cold-sprayed Ni and Ni-Cu coatings: improved structures and corrosion properties, *J. Therm. Spray Technol.* 23 (2013) 98–103.
- [69] A. Moridi, S.M. Hassani-Gangaraj, M. Guagliano, M. Dao, Cold spray coating: review of material systems and future perspectives, *Surf. Eng.* 30 (2014) 369–395.
- [70] P. Cavaliere, *Cold-spray coatings: Recent trends and future perspectives*, Springer, 2018.
- [71] W.Y. Li, C.C. Zhang, X. Guo, J. Xu, C.J. Li, H. Liao, C. Coddet, K.A. Khor, B.W. Li, C.C. Zhang, X. Guo, J. Xu, C.J. Li, H. Liao, C. Coddet, K.A. Khor, Ti and Ti-6Al-4V coatings by cold spraying and microstructure modification by heat treatment, *Adv. Eng. Mater.* 9 (2007) 418–423.
- [72] A. Małachowska, M. Winnicki, M. Stachowicz, M. Korzeniowski, Metallisation of polycarbonates using a low pressure cold spray method, *Surf. Eng.* 34 (2018) 251–258.
- [73] V.N.V. Munagala, V. Akinyi, P. Vo, R.R. Chromik, Influence of powder morphology and microstructure on the cold spray and mechanical properties of Ti6Al4V coatings, *J. Therm. Spray Technol.* 27 (2018) 827–842.
- [74] S.A. Alidokht, P. Vo, S. Yue, R.R. Chromik, Cold Spray Deposition of Ni and WC-Reinforced Ni Matrix Composite Coatings, *J. Therm. Spray Technol.* 26 (2017) 1908–1921.
- [75] H. Assadi, F. Gärtner, T. Stoltenhoff, H. Kreye, Bonding mechanism in cold gas spraying, *Acta Mater.* 51 (2003) 4379–4394.
- [76] T. Hussain, D.G. McCartney, P.H. Shipway, D. Zhang, Bonding mechanisms in cold spraying: The contributions of metallurgical and mechanical components, *J. Therm. Spray Technol.* 18 (2009) 364–379.
- [77] F. Meng, D. Hu, Y. Gao, S. Yue, J. Song, Cold-spray bonding mechanisms and deposition efficiency prediction for particle/substrate with distinct deformability, *Mater. Des.* 109

- (2016) 503–510.
- [78] G. Bae, S. Kumar, S. Yoon, K. Kang, H. Na, H.J. Kim, C. Lee, Bonding features and associated mechanisms in kinetic sprayed titanium coatings, *Acta Mater.* 57 (2009) 5654–5666.
- [79] T. Schmidt, H. Assadi, F. Gärtner, H. Richter, T. Stoltenhoff, H. Kreye, T. Klassen, From particle acceleration to impact and bonding in cold spraying, *J. Therm. Spray Technol.* 18 (2009) 794–808.
- [80] T. Schmidt, F. Gärtner, H. Assadi, H. Kreye, Development of a generalized parameter window for cold spray deposition, *Acta Mater.* 54 (2006) 729–742.
- [81] C.J. Li, H.T. Wang, Q. Zhang, G.J. Yang, W.Y. Li, H.L. Liao, Influence of spray materials and their surface oxidation on the critical velocity in cold spraying, *J. Therm. Spray Technol.* 19 (2010) 95–101.
- [82] C.-J. Li, W.-Y. Li, H. Liao, Examination of the critical velocity for deposition of particles in cold spraying, *J. Therm. Spray Technol.* 15 (2006) 212–222.
- [83] J. Lee, S. Shin, H.J. Kim, C. Lee, Effect of gas temperature on critical velocity and deposition characteristics in kinetic spraying, *Appl. Surf. Sci.* 253 (2007) 3512–3520.
- [84] M. Yu, W.Y. Li, F.F. Wang, X.K. Suo, H.L. Liao, Effect of particle and substrate preheating on particle deformation behavior in cold spraying, *Surf. Coatings Technol.* 220 (2013) 174–178.
- [85] K.H. Kim, M. Watanabe, J. Kawakita, S. Kuroda, Grain refinement in a single titanium powder particle impacted at high velocity, *Scr. Mater.* 59 (2008) 768–771.
- [86] G. Bae, Y. Xiong, S. Kumar, K. Kang, C. Lee, General aspects of interface bonding in kinetic sprayed coatings, *Acta Mater.* 56 (2008) 4858–4868.
- [87] W.Y. Li, W. Gao, Some aspects on 3D numerical modeling of high velocity impact of particles in cold spraying by explicit finite element analysis, *Appl. Surf. Sci.* 255 (2009) 7878–7892.
- [88] S. Kumar, G. Bae, C. Lee, Influence of substrate roughness on bonding mechanism in cold spray, *Surf. Coatings Technol.* 304 (2016) 592–605.
- [89] M. Jahedi, S.H. Zahiri, C. Lee, G. Bae, P.C. King, An Experimental and Finite Element Study of Cold Spray Copper Impact onto Two Aluminum Substrates, *J. Therm. Spray Technol.* 19 (2009) 620–634.

- [90] J. Vlcek, L. Gimeno, H. Huber, E. Lugscheider, A Systematic Approach to Material Eligibility for the Cold-Spray Process, *J. Therm. Spray Technol.* 14 (2005) 125–133.
- [91] Y. Zou, W. Qin, E. Irissou, J.G. Legoux, S. Yue, J.A. Szpunar, Dynamic recrystallization in the particle/particle interfacial region of cold-sprayed nickel coating: Electron backscatter diffraction characterization, *Scr. Mater.* 61 (2009) 899–902.
- [92] J.Y. Lek, A. Bhowmik, E. Liu, X. Song, J.Y. Lek, P.J. Buenconsejo, Y.M. Lam, A.W.Y. Tan, F. Li, W. Sun, C.B. Boothroyd, W. Zhai, Understanding the microstructural evolution of cold sprayed Ti-6Al-4V coatings on Ti-6Al-4V substrates, *Appl. Surf. Sci.* 459 (2018) 492–504.
- [93] P.C. King, S.H. Zahiri, M. Jahedi, Focused ion beam micro-dissection of cold-sprayed particles, *Acta Mater.* 56 (2008) 5617–5626.
- [94] P.C. King, S.H. Zahiri, M. Jahedi, Microstructural refinement within a cold-sprayed copper particle, *Metall. Mater. Trans. A Phys. Metall. Mater. Sci.* 40 (2009) 2115–2123.
- [95] V.N.V. Munagala, S.I. Imbriglio, R.R. Chromik, The influence of powder properties on the adhesion strength and microstructural evolution of cold sprayed Ti6Al4V single splats, *Mater. Lett.* 244 (2019) 58–61.
- [96] N. Brodusch, R.R. Chromik, Y. Zhang, S. Descartes, J.M. Shockley, R. Gauvin, The effect of submicron second-phase particles on the rate of grain refinement in a copper-oxygen alloy during cold spray, *J. Therm. Spray Technol.* 26 (2017) 1509–1516.
- [97] B. Jodoin, L. Ajdelsztajn, E. Sansoucy, a. Zúñiga, P. Richer, E.J. Lavernia, Effect of particle size, morphology, and hardness on cold gas dynamic sprayed aluminum alloy coatings, *Surf. Coatings Technol.* 201 (2006) 3422–3429.
- [98] D. Poirier, P.G. Keech, J.D. Giallonardo, J.-G. Legoux, B. Blais, P. Vo, Powder Development and Qualification for high-performance cold spray copper coatings on steel substrates, *J. Therm. Spray Technol.* 28 (2019) 444–459.
- [99] V.S. Bhattiprolu, G.A. Crawford, Microstructural evolution and mechanical behavior of heat treated Ti-6Al-4V powders, *Metallogr. Microstruct. Anal.* 7 (2018) 761–768.
- [100] J. Banhart, Manufacture, characterisation and application of cellular metals and metal foams, *Prog. Mater. Sci.* 46 (2001) 559–632.
- [101] X.T. Luo, Y.J. Li, C.X. Li, G.J. Yang, C.J. Li, Effect of spray conditions on deposition behavior and microstructure of cold sprayed Ni coatings sprayed with a porous electrolytic

- Ni powder, *Surf. Coatings Technol.* 289 (2016) 85–93.
- [102] S. Yin, E.J. Ekoi, T.L. Lupton, D.P. Dowling, R. Lupoi, Cold spraying of WC-Co-Ni coatings using porous WC-17Co powders: Formation mechanism, microstructure characterization and tribological performance, *Mater. Des.* 126 (2017) 305–313.
- [103] D. Lioma, N. Sacks, I. Botef, Cold gas dynamic spraying of WC–Ni cemented carbide coatings, *Int. J. Refract. Met. Hard Mater.* 49 (2015) 365–373.
- [104] W.Y. Li, C.J. Li, H. Liao, Significant influence of particle surface oxidation on deposition efficiency, interface microstructure and adhesive strength of cold-sprayed copper coatings, *Appl. Surf. Sci.* 256 (2010) 4953–4958.
- [105] K. Kang, S. Yoon, Y. Ji, C. Lee, Oxidation dependency of critical velocity for aluminum feedstock deposition in kinetic spraying process, *Mater. Sci. Eng. A.* 486 (2008) 300–307.
- [106] K. Balani, A. Agarwal, S. Seal, J. Karthikeyan, Transmission electron microscopy of cold sprayed 1100 aluminum coating, *Scr. Mater.* 53 (2005) 845–850.
- [107] R.C. McCune, W.T. Donlon, O.O. Popoola, E.L. Cartwright, Characterization of copper layers produced by cold gas-dynamic spraying, *J. Therm. Spray Technol.* 9 (2000) 73–82.
- [108] Z.H. Wang, C.X. Li, Y. Bai, Y. Li, G.S. Huang, X.B. Li, Corrosion behavior of low pressure cold sprayed Zn-Ni composite coatings, *J. Alloys Compd.* 719 (2017) 194–202.
- [109] H. Koivuluoto, A. Coleman, K. Murray, M. Kearns, P. Vuoristo, High pressure cold sprayed (HPCS) and low pressure cold sprayed (LPCS) coatings prepared from OFHC Cu feedstock: Overview from powder characteristics to coating properties, *J. Therm. Spray Technol.* 21 (2012) 1065–1075.
- [110] D.L. Gilmore, R.C. Dykhuizen, R.A. Neiser, T.J. Roemer, M.F. Smith, Particle velocity and deposition efficiency in the cold spray process, *J. Therm. Spray Technol.* 8 (1999) 576–582.
- [111] A.W.Y. Tan, W. Sun, A. Bhowmik, J.Y. Lek, I. Marinescu, F. Li, N.W. Khun, Z. Dong, E. Liu, Effect of substrate surface roughness on microstructure and mechanical properties of cold-sprayed Ti6Al4V coatings on Ti6Al4V substrates, *J. Therm. Spray Technol.* (2019).
- [112] A.W.Y. Tan, A. Bhowmik, F. Li, N.W. Khun, J.Y. Lek, Z. Dong, W. Sun, I. Marinescu, E. Liu, Effect of coating thickness on microstructure, mechanical properties and fracture behaviour of cold sprayed Ti6Al4V coatings on Ti6Al4V substrates, *Surf. Coatings Technol.* 349 (2018) 303–317.
- [113] S. Adachi, N. Ueda, Effect of cold-spray conditions using a nitrogen propellant gas on AISI

- 316L stainless steel-coating microstructures, *Coatings*. 7 (2017) 87.
- [114] W. Han, E.F. Rybicki, J.R. Shadley, An improved specimen geometry for ASTM C633-79 to estimate bond strengths of thermal spray coatings, *J. Therm. Spray Technol.* 2 (1993) 145–150.
- [115] K. Binder, J. Gottschalk, M. Kollenda, F. Gärtner, T. Klassen, Influence of impact angle and gas temperature on mechanical properties of titanium cold spray deposits, *J. Therm. Spray Technol.* 20 (2011) 234–242.
- [116] R.R. Chromik, D. Goldbaum, J.M. Shockley, S. Yue, E. Irissou, J.G. Legoux, N.X. Randall, Modified ball bond shear test for determination of adhesion strength of cold spray splats, *Surf. Coatings Technol.* 205 (2010) 1409–1414.
- [117] D. Goldbaum, J.M. Shockley, R.R. Chromik, A. Rezaeian, S. Yue, J.G. Legoux, E. Irissou, The effect of deposition conditions on adhesion strength of Ti and Ti6Al4V cold spray splats, *J. Therm. Spray Technol.* 21 (2012) 288–303.
- [118] M.V. Vidaller, A. List, F. Gaertner, T. Klassen, S. Dosta, J.M. Guilemany, Single Impact Bonding of Cold Sprayed Ti-6Al-4V Powders on Different Substrates, *J. Therm. Spray Technol.* 24 (2015) 644–658.
- [119] D. Goldbaum, J. Ajaja, R.R. Chromik, W. Wong, S. Yue, E. Irissou, J.G. Legoux, Mechanical behavior of Ti cold spray coatings determined by a multi-scale indentation method, *Mater. Sci. Eng. A*. 530 (2011) 253–265.
- [120] S.H. Zahiri, W. Yang, M. Jahedi, Characterization of cold spray titanium supersonic jet, *J. Therm. Spray Technol.* 18 (2008) 110–117.
- [121] A.P. Alkhimov, V.F. Kosarev, S. V. Klinkov, The features of cold spray nozzle design, *J. Therm. Spray Technol.* 10 (2001) 375–381.
- [122] T. Schmidt, F. Gaertner, H. Kreye, New developments in cold spray based on higher gas and particle temperatures, *J. Therm. Spray Technol.* 15 (2006) 488–494.
- [123] N. Chawla, K.K. Chawla, *Metal matrix composites*, 2nd ed., Springer New York Heidelberg Dordrecht London, 1991.
- [124] Y. Nishida, *Introduction to metal matrix composites : Fabrication and recycling*, Springer Tokyo Heidelberg New York Dordrecht London Library, 2001.
- [125] N. Natarajan, V. Krishnaraj, J.P. Davim, *Metal Matrix composites - Synthesis, Wear characteristics, machinability study of MMC brake drum*, Springer Cham Heidelberg New

York Dordrecht London Ó, 2014.

- [126] Y. Zhou, Z. Sun, Crystallographic relations between Ti_3SiC_2 and TiC , *Mater. Res. Innov.* 3 (2006) 286–291.
- [127] M. Mohanty, R.W. Smith, Lightweight TiC/Ti wear-resistant coatings for lightweight structural applications, *J. Therm. Spray Technol.* 4 (1995) 384–394.
- [128] H.O. Pierson, *Handbook of refractory carbides and nitrides: properties, characteristics, processing, and applications*, Westwood, N.J.: Noyes Publications, 1996.
- [129] J. Yuan, Y. Zhu, X. Zheng, H. Ji, T. Yang, Fabrication and evaluation of atmospheric plasma spraying $WC-Co-Cu-MoS_2$ composite coatings, *J. Alloys Compd.* 509 (2011) 2576–2581.
- [130] Y.S. Wu, D.C. Zeng, Z.W. Liu, W.Q. Qiu, X.C. Zhong, H.Y. Yu, S.Z. Li, Microstructure and sliding wear behavior of nanostructured Ni_60-TiB_2 composite coating sprayed by HVOF technique, *Surf. Coatings Technol.* 206 (2011) 1102–1108.
- [131] R.M. Mahamood, E.T. Akinlabi, Laser metal deposition of functionally graded Ti_6Al_4V/TiC , *Mater. Des.* 84 (2015) 402–410.
- [132] W.Y. Li, G. Zhang, C. Zhang, O. Elkedim, H. Liao, C. Coddet, Effect of ball milling of feedstock powder on microstructure and properties of TiN particle-reinforced Al alloy-based composites fabricated by cold spraying, *J. Therm. Spray Technol.* 17 (2008) 316–322.
- [133] S.A. Alidokht, *Cold spray deposition of Ni-WC composite coatings and their sliding and erosive wear behaviour*, McGill University, 2018.
- [134] S.A. Alidokht, P. Manimunda, P. Vo, S. Yue, R.R. Chromik, Cold spray deposition of a Ni-WC composite coating and its dry sliding wear behavior, *Surf. Coatings Technol.* 308 (2016) 424–434.
- [135] W.Y. Li, G. Zhang, H.L. Liao, C. Coddet, Characterizations of cold sprayed TiN particle reinforced Al_{2319} composite coating, *J. Mater. Process. Technol.* 202 (2008) 508–513.
- [136] M. Yandouzi, P. Richer, B. Jodoin, SiC particulate reinforced $Al-12Si$ alloy composite coatings produced by the pulsed gas dynamic spray process: Microstructure and properties, *Surf. Coatings Technol.* 203 (2009) 3260–3270.
- [137] Y. Zhang, Y. Epshteyn, R.R. Chromik, Dry sliding wear behaviour of cold-sprayed $Cu-MoS_2$ and $Cu-MoS_2-WC$ composite coatings: The influence of WC , *Tribol. Int.* 123 (2018)

296–306.

- [138] Y. Zhang, J. Michael Shockley, P. Vo, R.R. Chromik, Tribological behavior of a cold-sprayed Cu-MoS₂ composite coating during dry sliding wear, *Tribol. Lett.* 62 (2016) 1–12.
- [139] S. Dosta, M. Couto, J.M. Guilemany, Cold spray deposition of a WC-25Co cermet onto Al7075-T6 and carbon steel substrates, *Acta Mater.* 61 (2013) 643–652.
- [140] M. Couto, S. Dosta, M. Torrell, J. Fernández, J.M. Guilemany, Cold spray deposition of WC-17 and 12Co cermets onto aluminum, *Surf. Coatings Technol.* 235 (2013) 54–61.
- [141] F. Sevillano, P. Poza, C.J. Múñez, S. Vezzù, S. Rech, A. Trentin, Cold-sprayed Ni-Al₂O₃ coatings for applications in power generation industry, *J. Therm. Spray Technol.* 22 (2013) 772–782.
- [142] K. Spencer, D.M. Fabijanic, M.X. Zhang, The influence of Al₂O₃ reinforcement on the properties of stainless steel cold spray coatings, *Surf. Coatings Technol.* 206 (2012) 3275–3282.
- [143] H. Koivuluoto, G. Bolelli, A. Milanti, L. Lusvarghi, P. Vuoristo, Microstructural analysis of high-pressure cold-sprayed Ni, NiCu and NiCu + Al₂O₃ coatings, *Surf. Coatings Technol.* 268 (2015) 224–229.
- [144] E. Irissou, J.G. Legoux, B. Arsenault, C. Moreau, Investigation of Al-Al₂O₃ cold spray coating formation and properties, *J. Therm. Spray Technol.* 16 (2007) 661–668.
- [145] K.J. Hodder, J.A. Nychka, A.G. McDonald, Comparison of 10 μm and 20 nm Al-Al₂O₃ metal matrix composite coatings fabricated by low-pressure cold gas dynamic spraying, *J. Therm. Spray Technol.* 23 (2014) 839–848.
- [146] T. Peat, A. Galloway, A. Toumpis, P. McNutt, N. Iqbal, The erosion performance of particle reinforced metal matrix composite coatings produced by co-deposition cold gas dynamic spraying, *Appl. Surf. Sci.* 396 (2017) 1623–1634.
- [147] J.M. Shockley, H.W. Strauss, R.R. Chromik, N. Brodusch, R. Gauvin, E. Irissou, J.G. Legoux, In situ tribometry of cold-sprayed Al-Al₂O₃ composite coatings, *Surf. Coatings Technol.* 215 (2013) 350–356.
- [148] J.M. Shockley, S. Descartes, E. Irissou, J.G. Legoux, R.R. Chromik, Third body behavior during dry sliding of cold-sprayed Al-Al₂O₃ composites: In situ tribometry and microanalysis, *Tribol. Lett.* 54 (2014) 191–206.
- [149] H.Y. Lee, Y.H. Yu, Y.C. Lee, Y.P. Hong, K.H. Ko, Cold spray of SiC and Al₂O₃ with soft

- metal incorporation: A technical contribution, *J. Therm. Spray Technol.* 13 (2004) 184–189.
- [150] X.K. Suo, Q.L. Suo, W.Y. Li, M.P. Planche, H.L. Liao, Effects of SiC volume fraction and particle size on the deposition behavior and mechanical properties of cold-sprayed AZ91D/SiCp composite coatings, *J. Therm. Spray Technol.* 23 (2014) 91–97.
- [151] R. Fernandez, B. Jodoin, Cold Spray Aluminum–Alumina Cermet Coatings: Effect of Alumina Content, *J. Therm. Spray Technol.* 27 (2019) 603–623.
- [152] S. Grigoriev, A. Okunkova, A. Sova, P. Bertrand, I. Smurov, Cold spraying: From process fundamentals towards advanced applications, *Surf. Coatings Technol.* 268 (2015) 77–84.
- [153] K.I. Triantou, D.I. Pantelis, V. Guipont, M. Jeandin, Microstructure and tribological behavior of copper and composite copper+alumina cold sprayed coatings for various alumina contents, *Wear.* 336–337 (2015) 96–107.
- [154] A. Sova, V.F. Kosarev, A. Papyrin, I. Smurov, Effect of ceramic particle velocity on cold spray deposition of metal-ceramic coatings, *J. Therm. Spray Technol.* 20 (2011) 285–291.
- [155] A. Sova, A. Papyrin, I. Smurov, Influence of ceramic powder size on process of cermet coating formation by cold spray, *J. Therm. Spray Technol.* 18 (2009) 633–641.
- [156] I. Hutchings, P.H. Shipway, *Tribology: Friction and Wear of Engineering Materials*, 2nd ed., Oxford : Butterworth-Heinemann, 1992.
- [157] B. Bhushan, *Principles and applications of tribology*, Second, John Wiley & Sons Inc., 2013.
- [158] G. Maurice, The third-body approach: A mechanical view of wear, *Wear.* 100 (1984) 437–452.
- [159] G. Stachowiak, *Wear - Materials, mechanisms and practice*, John Wiley & Sons Inc., 2006.
- [160] M. Godet, Third-bodies in tribology, *Wear.* 136 (1990) 29–45.
- [161] R.R. Chromik, H.W. Strauss, T.W. Scharf, Materials phenomena revealed by in situ tribometry, *Jom.* 64 (2012) 35–43.
- [162] R.R. Chromik, Y. Zhang, Nanomechanical testing of third bodies, *Curr. Opin. Solid State Mater. Sci.* 22 (2018) 142–155.
- [163] B. Venkataraman, G. Sundararajan, Correlation between the characteristics of the mechanically mixed layer and wear behaviour of aluminium, Al-7075 alloy and Al-MMCs, *Wear.* 245 (2000) 22–38.

- [164] ASM Metals Handbook. Volume 18, Friction, lubrication and wear technology, ASM International, Materials Park, OH, USA, 1998.
- [165] G. Straffelini, Friction and wear : Methodologies for design and control, Springer, 2015.
- [166] F.P. Bowden, D. Tabor, The friction and lubrication of solids, Oxford : Clarendon Press, 1986.
- [167] Z. Ghar, K. Heinz, Microstructure and Wear of Materials, Elsevier Science Publishers B.V., 1987.
- [168] J.T. Burwell, C.D. Strang, On the empirical law of adhesive wear, *J. Appl. Phys.* 23 (1952) 18–28.
- [169] K. Holmberg, A. Matthews, Coatings Tribology: Properties, Techniques and Applications in Surface Engineering, Elsevier B.V, 2009.
- [170] M. Dragon-Louiset, On a predictive macroscopic contact-sliding wear model based on micromechanical considerations, *Int. J. Solids Struct.* 38 (2001) 1625–1639.
- [171] N. Fillot, I. Iordanoff, Y. Berthier, Wear modeling and the third body concept, *Wear.* 262 (2007) 949–957.
- [172] Y. Berthier, M. Godet, M. Brendle, Velocity accommodation in friction, *Tribol. Trans.* 32 (1989) 490–496.
- [173] H. Dong, A. Bloyce, P.H. Morton, T. Bell, Surface engineering to improve tribological performance of Ti–6Al–4V, *Surf. Eng.* 13 (2014) 402–406.
- [174] Y.S. Mao, L. Wang, K.M. Chen, S.Q. Wang, X.H. Cui, Tribo-layer and its role in dry sliding wear of Ti-6Al-4V alloy, *Wear.* 297 (2013) 1032–1039.
- [175] T.F.J. Quinn, Oxidational wear, *Wear.* 18 (1971) 413–419.
- [176] G. Straffelini, L. Maines, The relationship between wear of semimetallic friction materials and pearlitic cast iron in dry sliding, *Wear.* 307 (2013) 75–80.
- [177] F.H. Stott, The role of oxidation in the wear of alloys, *Tribol. Int.* 31 (1998) 61–71.
- [178] A. Erdemir, A crystal chemical approach to the formulation of self-lubricating nanocomposite coatings, *Surf. Coatings Technol.* 200 (2005) 1792–1796.
- [179] A. Erdemir, A crystal-chemical approach to lubrication by solid oxides, *Tribol. Lett.* 8 (2000) 97–102.
- [180] G.M. Hamilton, Explicit equations for the stresses beneath a sliding spherical contact, *Proc. Inst. Mech. Eng. Part C J. Mech. Eng. Sci.* 197 (1983) 53–59.

- [181] H.D. Alamdari, M. Gariépy, S. Savoie, R. Schulz, M. Amiriyan, C. Blais, Dry sliding wear behavior of Fe₃Al and Fe₃Al/TiC coatings prepared by HVOF, *Wear*. 342–343 (2015) 154–162.
- [182] H. Ghazanfari, C. Blais, H. Alamdari, M. Gariépy, S. Savoie, R. Schulz, Characterization of dry-sliding wear of HVOF coatings made of Fe₃Al powders reinforced with sub-micrometer TiC particles produced by combustion synthesis, *Surf. Coatings Technol.* 360 (2019) 29–38.
- [183] G. Rasool, M.M. Stack, Wear maps for TiC composite based coatings deposited on 303 stainless steel, *Tribol. Int.* 74 (2014) 93–102.
- [184] G. Rasool, S. Mridha, M.M. Stack, Mapping wear mechanisms of TiC/Ti composite coatings, *Wear*. 328–329 (2015) 498–508.
- [185] H. Chen, Y. Du, D. Wang, C. Zhang, G. Yang, B. Liu, Y. Gao, S. Shi, TiC/Ti₃AlC₂-Co plasma-sprayed coatings with excellent high-temperature tribological properties, *Ceram. Int.* 44 (2018) 22520–22528.
- [186] M. Yandouzi, E. Sansoucy, L. Ajdelsztajn, B. Jodoin, WC-based cermet coatings produced by cold gas dynamic and pulsed gas dynamic spraying processes, *Surf. Coatings Technol.* 202 (2007) 382–390.
- [187] X.T. Luo, C.J. Li, Large sized cubic BN reinforced nanocomposite with improved abrasive wear resistance deposited by cold spray, *Mater. Des.* 83 (2015) 249–256.
- [188] J. Kusinski, S. Kac, G. Szwachta, S. Dosta, J. Garcia-Forgas, E.P. Georgiou, Wear resistance of the Ti/TiC coatings deposited by means of supersonic cold gas spray technique, *TMS 2014 Suppl. Proc.* (2014) 1173–1180.
- [189] Y. Du, H. Chen, G. Yang, B. Liu, Y. Gao, H. Luo, Effect of cobalt content on high-temperature tribological properties of TiC-Co coatings, *Ceram. Int.* 44 (2018) 14186–14194.
- [190] H. Zhou, C. Li, H. Yang, X. Luo, G. Yang, W. Li, T. Hussain, C. Li, Pores structure change induced by heat treatment in cold-sprayed Ti₆Al₄V coating, *J. Therm. Spray Technol.* 28 (2019) 1199–1211.
- [191] H. Fukanuma, N. Ohno, B. Sun, R. Huang, In-flight particle velocity measurements with DPV-2000 in cold spray, *Surf. Coatings Technol.* 201 (2006) 1935–1941.
- [192] C.A. Schneider, W.S. Rasband, K.W. Eliceiri, NIH Image to ImageJ: 25 years of image

- analysis, *Nat. Methods.* 9 (2012) 671–5.
- [193] K. Araci, D. Mangabhai, K. Akhtar, *Production of titanium by the Armstrong Process®*, Elsevier Inc., 2015.
- [194] Hysitron TI 950 Triboindenter User Manual Revision 9.3.0314 Hysitron Incorporated, 2014.
- [195] C.F.-C. Anthony, *Nanoindentation*, 3rd ed., New York : Springer, ©2011.
- [196] G. Oliver, W.C. Pharr, An improved technique for determining hardness and elastic modulus using load and displacement sensing indentation experiments, *J. Mater. Res.* 7 (1992) 1564–1583.
- [197] J. Krier, J. Breuils, L. Jacomine, H. Pelletier, Introduction of the real tip defect of Berkovich indenter to reproduce with FEM nanoindentation test at shallow penetration depth, *J. Mater. Res.* 27 (2012) 28–38.
- [198] E. Brandl, F. Palm, V. Michailov, B. Viehweger, C. Leyens, Mechanical properties of additive manufactured titanium (Ti-6Al-4V) blocks deposited by a solid-state laser and wire, *Mater. Des.* 32 (2011) 4665–4675.
- [199] E. Brandl, A. Schoberth, C. Leyens, Morphology, microstructure, and hardness of titanium (Ti-6Al-4V) blocks deposited by wire-feed additive layer manufacturing (ALM), *Mater. Sci. Eng. A.* 532 (2012) 295–307.
- [200] J. Cizek, O. Kovarik, J. Siegl, K.A. Khor, I. Dlouhy, Influence of plasma and cold spray deposited Ti Layers on high-cycle fatigue properties of Ti6Al4V substrates, *Surf. Coatings Technol.* 217 (2013) 23–33.
- [201] L.E. Murr, S.A. Quinones, S.M. Gaytan, M.I. Lopez, A. Rodela, E.Y. Martinez, D.H. Hernandez, E. Martinez, F. Medina, R.B. Wicker, Microstructure and mechanical behavior of Ti-6Al-4V produced by rapid-layer manufacturing, for biomedical applications, *J. Mech. Behav. Biomed. Mater.* 2 (2009) 20–32.
- [202] H. Assadi, H. Kreye, F. Gärtner, T. Klassen, Cold spraying - A materials perspective, *Acta Mater.* 116 (2016) 382–407.
- [203] W. Sun, A.W.Y. Tan, I. Marinescu, W.Q. Toh, E. Liu, Adhesion, tribological and corrosion properties of cold-sprayed CoCrMo and Ti6Al4V coatings on 6061-T651 Al alloy, *Surf. Coatings Technol.* 326 (2017) 291–298.
- [204] J.I. Qazi, O.N. Senkov, J. Rahim, A. Genc, F.H. (Sam) Froes, Phase transformations in Ti-

- 6Al-4V-xH alloys, *Metall. Mater. Trans. A.* 32A (2001) 2453–2463.
- [205] W.D. Nix, H. Gao, Indentation size effects in crystalline materials: A law for strain gradient plasticity, *J. Mech. Phys. Solids.* 46 (1998) 411–425.
- [206] I. Sen, S. Roy, M.F.X. Wagner, Indentation response and structure-property correlation in a bimodal Ti-6Al-4V Alloy, *Adv. Eng. Mater.* 19 (2017) 1–12.
- [207] G.B. Viswanathan, E. Lee, D.M. Maher, S. Banerjee, H.L. Fraser, Direct observations and analyses of dislocation substructures in the α phase of an α/β Ti-alloy formed by nanoindentation, *Acta Mater.* 53 (2005) 5101–5115.
- [208] T.B. Britton, H. Liang, F.P.E. Dunne, A.J. Wilkinson, The effect of crystal orientation on the indentation response of commercially pure titanium: Experiments and simulations, *Proc. R. Soc. A Math. Phys. Eng. Sci.* 466 (2010) 695–719.
- [209] W. Sun, A.W.Y. Tan, N.W. Khun, I. Marinescu, E. Liu, Effect of substrate surface condition on fatigue behavior of cold sprayed Ti6Al4V coatings, *Surf. Coatings Technol.* 320 (2017) 452–457.
- [210] C.M. Lewandowski, N. Co-investigator, C.M. Lewandowski, Powder metal technologies and applications, *ASM Int. Mater. Park. OH.* 7 (2015) 2762.
- [211] M. Winnicki, A. Małachowska, G. Dudzik, M. Rutkowska-Gorczyca, M. Marciniak, K. Abramski, A. Ambroziak, L. Pawłowski, Numerical and experimental analysis of copper particles velocity in low-pressure cold spraying process, *Surf. Coatings Technol.* 268 (2015) 230–240.
- [212] D. Goldbaum, Micromechanical testing of cold sprayed Ti splats and coatings, McGill University, 2012.
- [213] D. MacDonald, A. Nastik, B. Jodoin, Understanding adhesion, in: *Cold-Spray Coatings Recent Trends Futur. Perspect.*, Springer, 2018: pp. 421–450.
- [214] M.J. Donachie, Jr., *Titanium - A Technical Guide*, ASM International, Materials Park, OH, USA, 2000.
- [215] J. Capus, Conventional PM still a challenge for titanium and alloys, *Met. Powder Rep.* 69 (2014) 18–20.
- [216] S. Hadke, R.K. Khatirkar, S.K. Shekhawat, S. Jain, S.G. Sapate, Microstructure evolution and abrasive wear behavior of Ti-6Al-4V Alloy, *J. Mater. Eng. Perform.* 24 (2015) 3969–3981.

- [217] S.C. Lim, J.H. Brunton, The unlubricated wear of sintered iron, *Wear*. 113 (1986) 383–393.
- [218] B. Dubrujeaud, M. Vardavoulias, M. Jeandin, The role of porosity in the dry sliding wear of a sintered ferrous alloy, *Wear*. 174 (1994) 155–161.
- [219] H. Dong, T. Bell, Tribological behaviour of alumina sliding against Ti6Al4V in unlubricated contact, *Wear*. 225–229 (1999) 874–884.
- [220] K.M. Chen, X.X. Li, J.Q. Liu, S.Q. Wang, Y. Zhou, Q.Y. Zhang, Mild and severe wear of titanium alloys, *Tribol. Lett.* 61 (2016) 1–9.
- [221] G. Straellini, A. Molinari, Dry sliding wear of ferrous PM materials, *Powder Metall.* 44 (2003) 248–252.
- [222] L. Ceschini, G. Palombarini, G. Sambogna, D. Firrao, G. Scavino, G. Ubertalli, Friction and wear behaviour of sintered steels submitted to sliding and abrasion tests, *Tribol. Int.* 39 (2006) 748–755.
- [223] A. Leyland, A. Matthews, On the significance of the H/E ratio in wear control: A nanocomposite coating approach to optimised tribological behaviour, *Wear*. 246 (2000) 1–11.
- [224] M. Vardavoulias, The role of hard second phases in the mild oxidational wear mechanism of high-speed steel-based materials, *Wear*. 173 (1994) 105–114.
- [225] M.A. Islam, Z.N. Farhat, Effect of porosity on dry sliding wear of Al-Si alloys, *Tribol. Int.* 44 (2011) 498–504.
- [226] A.P. Mercer, I. Hutchings, The influence of atmospheric humidity on the abrasive wear of metals, 103 (1985) 205–215.
- [227] X.H. Cui, Y.S. Mao, M.X. Wei, S.Q. Wang, Wear Characteristics of Ti-6Al-4V Alloy at 20-400°C, *Tribol. Trans.* 55 (2012) 185–190.
- [228] X.X. Li, Y. Zhou, X.L. Ji, Y.X. Li, S.Q. Wang, Effects of sliding velocity on tribo-oxides and wear behavior of Ti-6Al-4V alloy, *Tribol. Int.* 91 (2014) 228–234.
- [229] J.C. Anderson, K.D. Leaver, R.D. Rawlings, J.M. Alexander, *Materials Science*, 4th ed., London: Van Nostrand Reinhold, 1990.
- [230] M.N. Gardos, The effect of anion vacancies on the tribological properties of rutile (TiO_{2-x}), *Tribol. Trans.* 31 (1988) 427–436.
- [231] M.N. Gardos, H.S. Hong, W.O. Winer, The effect of anion vacancies on the tribological properties of rutile (TiO_{2-x}), part II: Experimental evidence, *Tribol. Trans.* 33 (1990) 209–

220.

- [232] M.N. Gardos, Magnéli phases of anion-deficient rutile as lubricious oxides. Part I. Tribological behavior of single-crystal and polycrystalline rutile ($\text{Ti}_n\text{O}_{2n-1}$), *Tribol. Lett.* 8 (2000) 65–78.
- [233] M. Woydt, A. Skopp, I. Dörfel, K. Witke, Wear engineering oxides/antiwear oxides, *Tribol. Trans.* 42 (1999) 21–31.
- [234] Y. Zi-Run, H. Hai-Xiang, C.F. Jiang, W.M. Li, X.R. Liu, S. Lyu, Evaluation on dry sliding wear behavior of (TiB+TiC)/Ti-6Al-4V matrix composite, *Int. J. Precis. Eng. Manuf.* 18 (2017) 1139–1146.
- [235] H.J. Kim, C.H. Lee, S.Y. Hwang, Fabrication of WC-Co coatings by cold spray deposition, *Surf. Coatings Technol.* 191 (2005) 335–340.
- [236] H. Assadi, H. Kreye, F. Gärtner, T. Klassen, Cold spraying – A materials perspective, *Acta Mater.* 116 (2016) 382–407.
- [237] C.C. Degnan, P.H. Shipway, J.V. Wood, Elevated temperature sliding wear behaviour of TiC-reinforced steel matrix composites, *Wear.* 251 (2002) 1444–1451.
- [238] V.N.V. Munagala, T.B. Torgerson, T.W. Scharf, R.R. Chromik, High temperature friction and wear behavior of cold-sprayed Ti6Al4V and Ti6Al4V-TiC composite coatings, *Wear.* 426–427 (2019) 357–369.
- [239] N.M. Melendez, V. V. Narulkar, G.A. Fisher, A.G. McDonald, Effect of reinforcing particles on the wear rate of low-pressure cold-sprayed WC-based MMC coatings, *Wear.* 306 (2013) 185–195.
- [240] R. Maestracci, A. Sova, I. Smurov, P. Bertrand, M. Jeandin, Kinetics of composite coating formation process in cold spray: Modelling and experimental validation, *Surf. Coatings Technol.* 318 (2016) 309–314.
- [241] D.W. Richerson, W.D. Carruthers, L.J. Lindberg, Contact stress and coefficient of friction effects on ceramic interfaces, in: *Surfaces Interfaces Ceram. Ceram. — Met. Syst.*, 2012: pp. 661–676.
- [242] T.B. Torgerson, M.D. Harris, S.A. Alidokht, T.W. Scharf, S.M. Aouadi, R.R. Chromik, J.S. Zabinski, A.A. Voevodin, Room and elevated temperature sliding wear behavior of cold sprayed Ni-WC composite coatings, *Surf. Coatings Technol.* 350 (2018) 136–145.
- [243] A.T. Alpas, J. Zhang, Effect of microstructure and counterface material on the sliding wear

- resistance of particulate reinforced aluminum matrix composites, *Met. Mater. Trans. A.* 25 (1994) 969–983.
- [244] Q.Y. Zhang, Y. Zhou, X.X. Li, L. Wang, X.H. Cui, S.Q. Wang, Accelerated formation of tribo-oxide layer and its effect on sliding wear of a titanium alloy, *Tribol. Lett.* 63 (2016).
- [245] L. Du, C. Huang, W. Zhang, T. Li, W. Liu, Preparation and wear performance of NiCr/Cr₃C₂-NiCr/hBN plasma sprayed composite coating, *Surf. Coatings Technol.* 205 (2011) 3722–3728.
- [246] Q.Y. Zhang, X.H. Cui, L. Wang, X.X. Li, S.Q. Wang, K.M. Chen, Comparative study of wear behaviors of a selected titanium alloy and AISI H13 steel as a function of temperature and load, *Tribol. Trans.* 57 (2014) 838–845.
- [247] M. Lubas, J.J. Jasinski, M. Sitarz, L. Kurpaska, P. Podsiad, J.J. Jasinski, Raman spectroscopy of TiO₂ thin films formed by hybrid treatment for biomedical applications, *Spectrochim. Acta - Part A Mol. Biomol. Spectrosc.* 133 (2014) 867–871.
- [248] Z. Geng, S. Li, D.L. Duan, Y. Liu, Wear behaviour of WC-Co HVOF coatings at different temperatures in air and argon, *Wear.* 330–331 (2015) 348–353.
- [249] Z. Geng, S. Hou, G. Shi, D. Duan, S. Li, Tribological behaviour at various temperatures of WC-Co coatings prepared using different thermal spraying techniques, *Tribol. Int.* 104 (2016) 36–44.
- [250] J. Michael Shockley, C. Desrayaud, R.R. Chromik, S. Descartes, Significance of Al₂O₃ particle morphology in the microstructure evolution of cold-sprayed Al-Al₂O₃ during unconstrained high-pressure torsion, *Mater. Sci. Eng. A.* 684 (2017) 510–516.
- [251] H. Dong, T. Bell, Tribological behaviour of alumina sliding against Ti6Al4V in unlubricated contact, *Wear.* 225–229 (1999) 874–884.
- [252] P. Mi, T. Wang, F. Ye, Influences of the compositions and mechanical properties of HVOF sprayed bimodal WC-Co coating on its high temperature wear performance, *Int. J. Refract. Met. Hard Mater.* 69 (2017) 158–163.

Appendix A

Grain size calculation below wear track

To characterize the subsurface microstructure below the wear tracks, SEM images of the worn cross sections were taken at different magnifications as shown in the Fig. A1. To determine the average grain size in the UFG region, SEM images of the UFG region were exported into ImageJ and the boundary of the grain was traced (indicated by a red arrow in Fig. A2) using a polygon selection tool as shown in Fig. A2. The area of the grain was determined and equated to the area of the circle, to calculate its diameter. This diameter was considered as the size of the grain or grain size. At least 60-100 grains were measured and averaged to determine the average grain size.

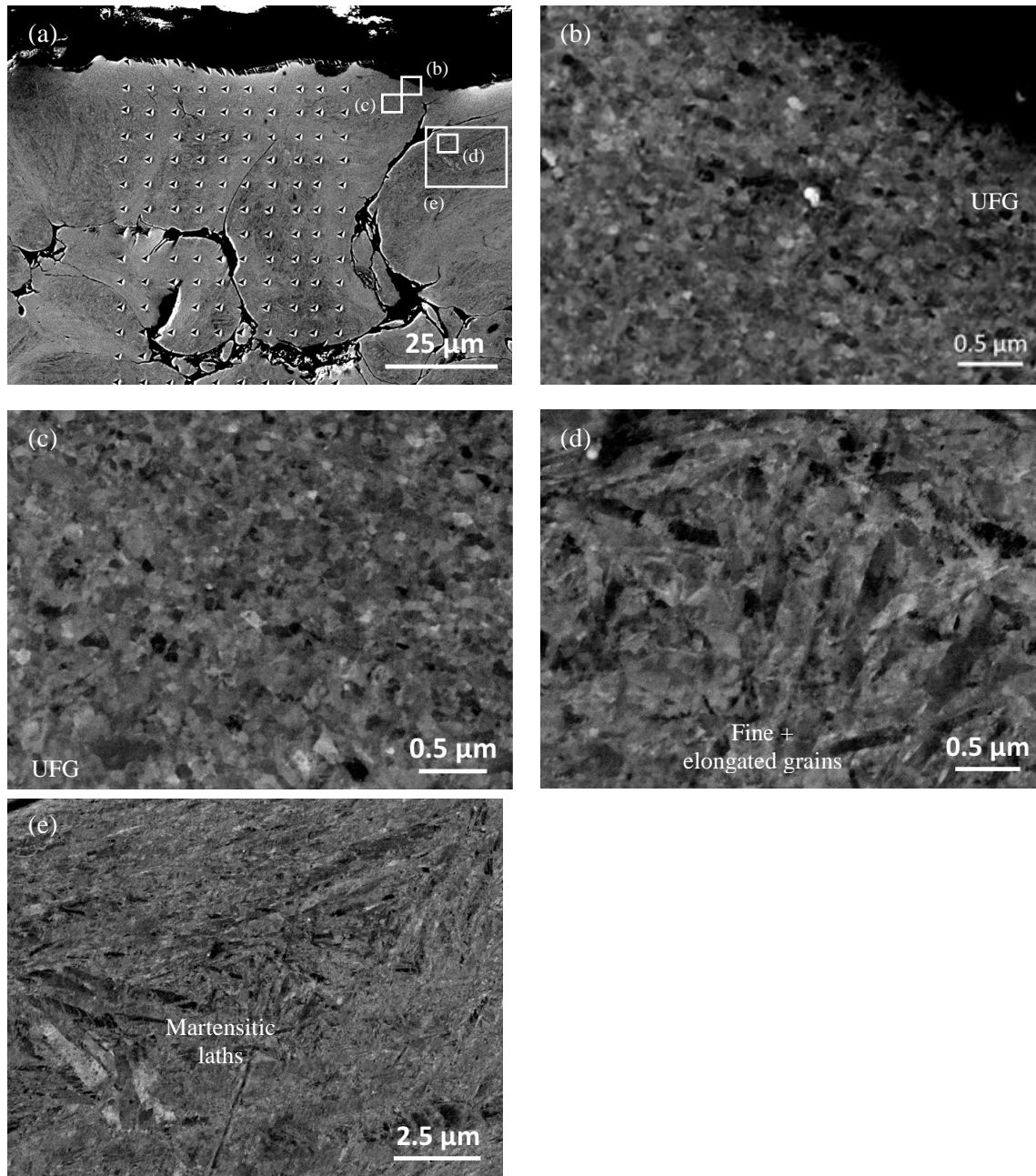


Fig. A1: ECCI of the wear track cross-section of Ti6Al4V coating (a) subsurface (b)&(c) near the surface showing UFGs (d) FG region showing fine and elongated grains (e) showing martensitic lath microstructure.

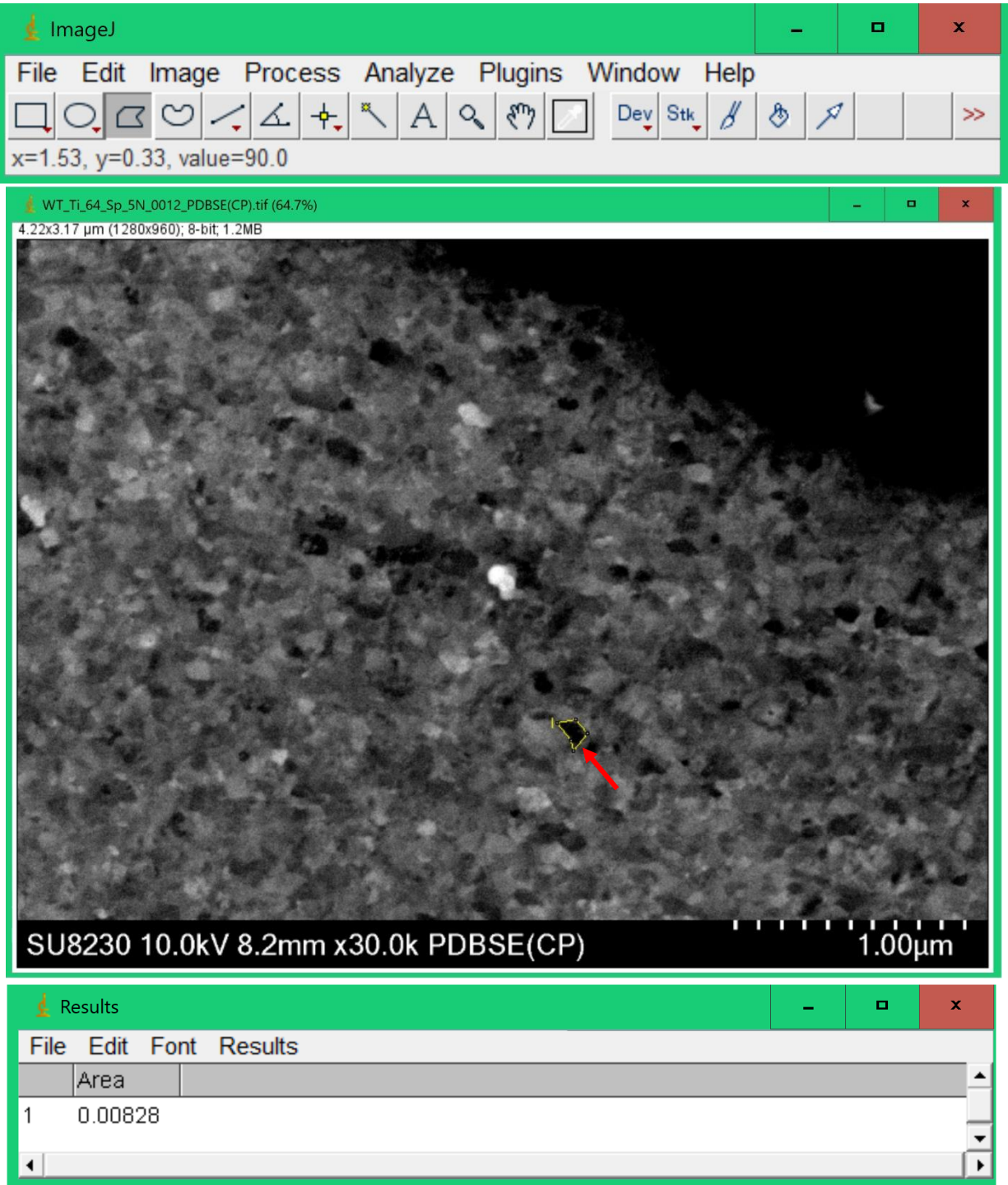


Fig. A2: Grain size measurement of the UFGs below the wear track of Ti6Al4V